Photoinduced Charge Transfer at Metal Oxide/Oxide Interfaces Prepared with Plasma Enhanced Atomic Layer Deposition

by

Manpuneet Kaur

A Dissertation Presented in Partial Fulfillment
of the Requirements for the Degree
Doctor of Philosophy

Approved April 2016 by the
Graduate Supervisory Committee:

Robert Nemanich, Chair
Sandwip Dey
Peter Crozier
Candace Chan

ARIZONA STATE UNIVERSITY

May 2016

ABSTRACT

$LiNbO_3$ and ZnO have shown great potential for photochemical surface reactions and specific photocatalytic processes. However, the efficiency of $LiNbO_3$ is limited due to recombination or back reactions and ZnO exhibits a chemical instability in a liquid cell. In this dissertation, both materials were coated with precise thickness of metal oxide layers to passivate the surfaces and to enhance their photocatalytic efficiency. $LiNbO_3$ was coated with plasma enhanced atomic layer deposited (PEALD) ZnO and Al_2O_3, and molecular beam deposited TiO_2 and VO_2. On the other hand, PEALD ZnO and single crystal ZnO were passivated with PEALD SiO_2 and Al_2O_3.

Metal oxide/$LiNbO_3$ heterostructures were immersed in aqueous $AgNO_3$ solutions and illuminated with ultraviolet (UV) light to form Ag nanoparticle patterns. Alternatively, Al_2O_3 and SiO_2/ZnO heterostructures were immersed in K_3PO_4 buffer solutions and studied for photoelectrochemical reactions. A fundamental aspect of the heterostructures is the band alignment and band bending, which was deduced from *in situ* photoemission measurements.

This research has provided insight to three aspects of the heterostructures. *First*, the band alignment at the interface of metal oxides/$LiNbO_3$, and Al_2O_3 or SiO_2/ZnO were used to explain the possible charge transfer processes and the direction of carrier flow in the heterostructures. *Second*, the effect of metal oxide coatings on the $LiNbO_3$ with different internal carrier concentrations was related to the surface photochemical reactions. *Third* is the surface passivation and degradation mechanism of Al_2O_3 and SiO_2 on ZnO was established. The heterostructures were characterized after stability tests

using atomic force microscopy (AFM), scanning electron microscopy (SEM), and cross-section transmission electron microscopy (TEM).

The results indicate that limited thicknesses of ZnO or TiO_2 on polarity patterned $LiNbO_3$ (PPLN) enhances the Ag^+ photoinduced reduction process. ZnO seems more efficient than TiO_2 possibly due to a higher carrier mobility. However, an increase of the ZnO thickness ($\geq$ 4 nm) reduced the effect of the PPLN substrate on the Ag nanoparticle pattern. For the case of Al_2O_3 and SiO_2/ZnO heterostructures, SiO_2 remains intact through 1 h stability tests. Unlike SiO_2, Al_2O_3 shows surface degradation after a short stability test of a few minutes. Thus, SiO_2 provides improved passivation over Al_2O_3. A detailed microscopy analysis indicates the underneath ZnO photocorrodes in the SiO_2/ZnO samples, which is possibly due to transport of ions through the SiO_2 protective layer.

This dissertation is dedicated to the memory of my father.

"Never give up on a dream just because of the time it will take to accomplish it.
The time will pass anyway."

- *Earl Nightingale*

ACKNOWLEDGMENTS

First, I would like to express my gratitude towards Dr. Robert J. Nemanich to give me an opportunity to work in his lab, and for the assistance and encouragement he provided me during my Ph.D. at ASU. Without his motivation and tremendous support, it wouldn't have been possible to finish this up. He is inspirational and an invaluable source of knowledge. Without any doubt, I will keep benefiting from his advising in the years to come.

I greatly appreciate the assistance of my committee members, Dr. Peter Crozier, Dr. Sandwip Dey, and Dr. Candace Chan. I acknowledge their contribution and suggestions to the development of this work and thank them for serving as my committee.

It was pleasure to work with such an amazing group of people at the Nanoscience Laboratory (NSL). I would like to thank Dr. Fu Tang and Dr. Chiyu Zhu for customizing the ALD system and training on the MBD system that I have extensively used in this research. Franz Koeck deserves special thanks for his endeavors. I would like to extend special appreciation to Dr. Jialing Yang and Dr. Brianna Eller for collaboration and insightful discussions. I would also like to thank Xingye Yang, Joe Shammas, Yu Yang, Aaron Papagalos, Mei Hao for their support and contribution to this work. I am glad I got opportunities to assist Christie Trimble, Trevor Van Engelhoven, Brandon Palafox, and Veronica Meeks. I would like to acknowledge Dr. Yang Sun, Dr. Xin Liu, Dr. Tianyin Sun, and Dr. Anna Zanewski for their support and great team work.

It was delightful experience to collaborate with other graduate research groups at ASU. I want to thank Qian Cheng and Qianlang Liu for their collaboration on different

projects. Working with both of them was an inspiration. In particular, Dr. Crozier, Dr. Chan, Dr. Dan Buttry, and Dr. Xihong Peng, I appreciate your thoughtful discussions to accomplish the projects that are an integral part of this dissertation. I would like to thank Andrew Copple for providing an insight to the density functional theory.

In addition, I acknowledge the assistance of experts at the LeRoy Eyring Center for Solid State Science. I would like to thank Dr. Barry Wilkens for Rutherford Back Scattering Spectroscopy (RBS) characterization, Dr. Emmanuel Soignard for assistance with x-ray reflectivity (XRR) and x-ray diffraction (XRD), Dr. Kenneth Mossman for training me on scanning electron microscopy (SEM), and Dr. Diana Convey and Dr. David Wright for their support with XRD and sample dicing. I cannot forget to thank all the staff at the Center for Solid State Electronics Research (CSSER). Special thanks to Stefan Myhajlenko for his commendable management, Jerry Eller for assistance with Lesker #3 e-beam, Arthur Handugan, Carrie Sinclair, and Paul Boland. I also want to thank Dr. Shariar Anwar for giving me access to the materials science laboratory.

This research has been financially supported by the National Science Foundation (DMR – 1206935), the Arizona Board of Regents, and the Flexible Display Center.

Finally, I want to thank my family and friends. My father is no longer with me but I owe a debt of gratitude to him. I would like to thank him for all the sacrifices he made and for letting me dream big while I was growing up in a small village. I don’t have enough words to express my gratitude to my mother and brother for their unwaivering support and affection and my sister-in-law for being a great friend. In addition, I would like to thank all my friends here in the United States and in India. I am fortunate to have you all in my life.

TABLE OF CONTENTS

Page

CHAPTER Page

LIST OF TABLES

Table Page

LIST OF FIGURES

Figure Page

Figure Page

Figure Page

Figure Page

Figure Page

Figure Page

Figure Page

Figure Page

Figure Page

Figure Page

Figure Page

INTRODUCTION

CHAPTER 1. PHOTOCHEMICLA REACTIONS ON OXIDES

Photochemical reactions can be used to remove industrial waste and chemicals from water and for water splitting to produce hydrogen fuel. For photochemical reactions, the illuminated above band gap light on the material excite electron-hole pairs, which migrate to the surface and react with chemical species and convert solar energy into chemical energy [1, 2, 3, 4, 5]. Photocatalysis is a process that is defined by two simultaneous reactions, reduction and oxidation (redox), usually on a solid photocatalyst surface. The commonly used photocatalyst materials are metal oxides and ferroelectrics. The requirements for photochemical reactions to occur at the solid-liquid interface are: (i) the redox potential of the chemical species should be within the photocatalyst bandgap, (ii) chemically stable solid photocatalyst, and (iii) high surface reaction rate of chemical species and photoexcited carriers.

Semiconductors and ferroelectrics are the promising materials for photocatalysis processes to provide new approaches to mitigate environmental pollution and energy problems. During the last decades, various materials, such as metal oxides (TiO_2, ZnO and ZrO_2) [1- 3, 6], sulfides (CdS) [1, 7], nitrides [1, 8] and ferroelectrics ($LiNbO_3$ and $BaTiO_3$) [3, 4, 5, 9-11] have been explored. However, the applications of photocatalyst materials are limited due to (i) high carrier recombination rates, and (ii) chemical instability. To enhance the photocatalyst efficiency it is critical to reduce the charge recombination and enhance the stability. Despite the wide band gap ferroelectrics are emerging as efficient photocatalysts, which is attributed to their chemical stability and internal electric field. On the other hand, ZnO has the highest reported photocatalytic

efficiency among metal oxides due to a high optical absorption coefficient but it has the disadvantage of chemical instability. A number of efforts have been made to improve the efficiency of ferroelectric and ZnO photocatalysts. Among the number of different methods the formation of optimized heterostructures has been extensively explored [12-15]. For ZnO, a passivation layer on the surface can increase the stability and thus increase the efficiency. Consequently, for ferroelectrics, metal oxide charge transfer layer at the surface can (i) reduce recombination due to surface states, and (ii) increase photoexcited charge separation. The heterostructure formation can protect the photocatalysts photocorrosion and enhance charge separation that also reduces the recombination.

I. Oxides as Photocatalysts and Charge Transfer Layers:

Metal oxides have been the primary materials for photocatalysis to produce hydrogen (H_2) fuel. The commonly used metal oxides for photocatalytic processes include ZnO, TiO_2 and ZnO/TiO_2 heterostructures due to their high reaction rate and appropriate band gap [1, 2, 16-19]. On the other hand, ferroelectrics such as $LiNbO_3$ and $BaTiO_3$ have been studied for photochemical reactions to remove dye molecules from water, and to pattern metal nanoparticles using reduction and oxidation processes [4, 5, 9-11, 20]. The wide band gap of ZnO, TiO_2, $LiNbO_3$ and $BaTiO_3$ makes them an efficient photocatalyst in UV illumination but the performance in visible light is significantly reduced [6, 12, 20].

To enhance the photochemical reaction efficiency various material properties have been explored. The first is the oxides with high absorption coefficient and low photoexcited carrier recombination rate. Absorption coefficient is a material property that

increases with the increase in band gap [4]. Among the metal oxides and ferroelectrics, ZnO and $LiNbO_3$ are the materials with high absorption and low recombination rate [7, 16]. Second is the use of larger surface area for photochemical reactions where ZnO, TiO_2 and $LiNbO_3$ powders and nanowires have been employed [4, 9, 17, 21, 22]. However, the photogenerated carriers are confined in close proximity, which can lead to increase the carrier recombination and back reactions. The material properties change substantially going from bulk to ultra-thin films and nanostructures (nanowires and nanoparticles). With the reduction in size, materials possess different optical, electrical, mechanical and chemical properties as compared to the bulk due to changes in surface properties and quantum confinement effects [23, 24]. Third is to use internal electric field of ferroelectrics [4, 9], such as in $LiNbO_3$ and $BaTiO_3$, to separate the photoexcited carriers, which can reduce the carrier recombination and enhance the photochemical reaction rate.

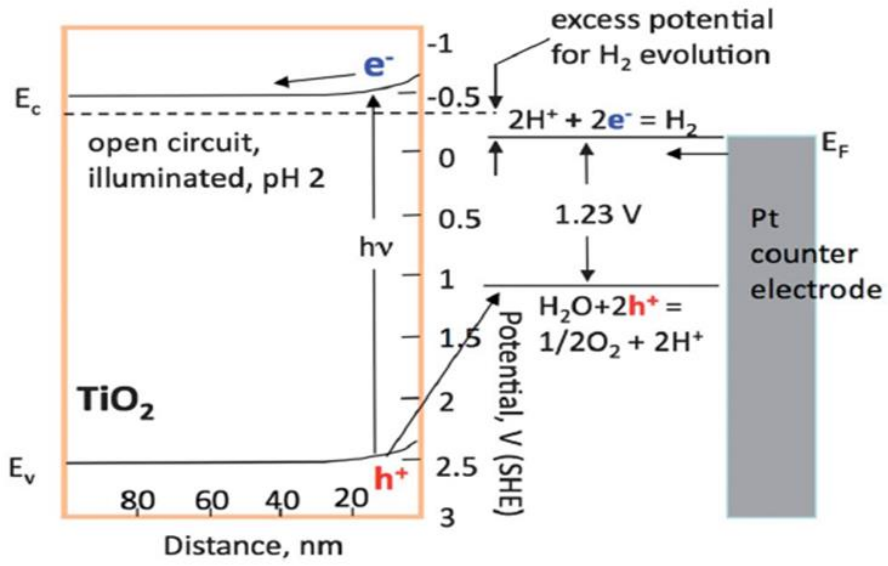

Figure 1.1. Schematic of H^+ and H_2O oxidation and reduction potential with respect to TiO_2 band gap [7].

Semiconductors are the conventional materials that have been widely considered for photocatalysis. A significant body of work has investigated ferroelectrics for photochemical reactions that show a similar efficiency to semiconductors due to the internal electric field of ferroelectrics [4]. The effect of the internal electric field is subject to change depending on the interfaces, including the electrolyte/ferroelectric and semiconductor/ferroelectric interfaces. Other than the bulk properties of photocatalyst materials, interfaces play a significant role in controlling the reduction and oxidation reactions. The photocatalyst materials are ideally chemically stable while satisfying the chemical species redox potential and band gap alignment. As shown in Figure 1.1, the photoinduced chemical species undergo photochemical reactions on the surface of the photocatalyst, provided the redox potential of species is within the photocatalyst band gap [1, 4, 5].

Other than photoelectrochemical process, photoinduced metal nanoparticle deposition is a process that is widely used to understand the photochemical reaction efficiency. This process is commonly used for ferroelectric surface photochemical reactions, where either reduction or oxidation process contributes to the formation of metal nanoparticles [25-30]. The surface of the ferroelectric is covered with electrolyte solution and illuminated with the UV light above the band gap of the ferroelectric. The photoexcited carriers near the surface of ferroelectrics migrate to the surface and cause the oxidation and reduction reactions. Photoinduced nanopattern formation on polarity patterned lithium niobate (PPLN) has been studied by a number of groups, Sun *et. al.* [25, 26], Park *et. al*. [27], and Haussmann *et. al.* [28]. They have shown the formation of Ag nanowires on domain boundaries and Ag nanoparticles that form preferably on positive

domains. Ag nanoparticle deposition is enabled by photoexcited electrons that reduce Ag^+ ions in aqueous $AgNO_3$ solution. Shown in Figure 1.2 are the reduction potential of Ag^+ to Ag, the oxidation potential of OH^- and H_2O, and the band gap position of $LiNbO_3$, Al_2O_3, TiO_2, ZnO and VO_2 [29, 30]. The pattern of the photoinduced Ag nanoparticles on the PPLN surface is influenced by the availability of photoexcited charge carriers near the surface [5, 26, 29]. The charge transfer metal oxide thin films with suitable band alignment and properties can enhance the photoexcited charge availability at the surface and thus can increase the density of Ag nanoparticles.

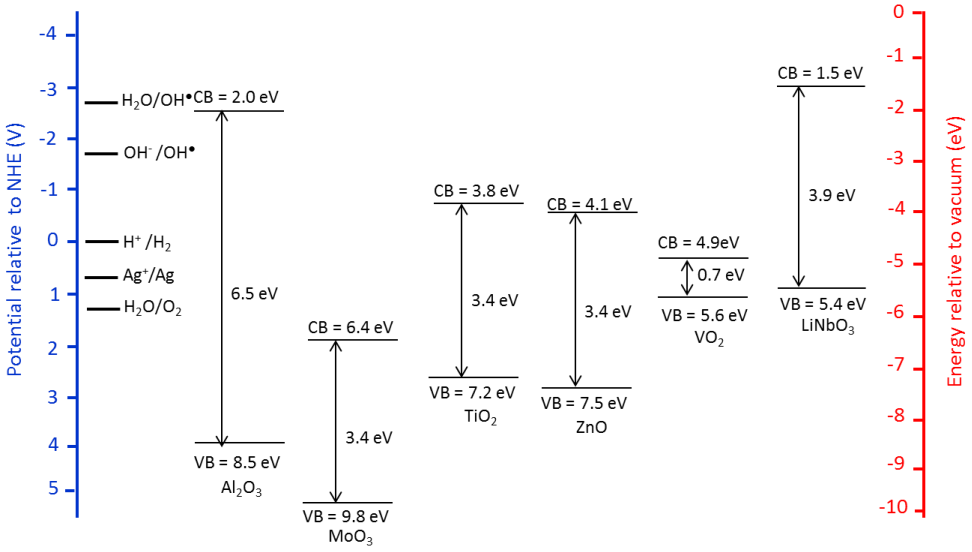

Figure 1.2. Redox potential of H_2O, hydroxyl ion (OH^-) and Ag^+ vs NHE with respect to $LiNbO_3$ negative (–c) and positive (+c) domain, and Al_2O_3, MoO_3, TiO_2, ZnO and VO_2 CBM and VBM position relative to vacuum level.

In this research, ZnO and $LiNbO_3$ have been used as photocatalysts. Despite having high efficiency for photochemical reactions, ZnO has been shown to be chemically unstable in the electrolyte solution. To overcome the issue of ZnO photocorrosion, a chemically stable metal oxide material can be used as a passivation

layer. In the case of $LiNbO_3$, the interface states, and Stern layer can limit the photochemical reactions. Metal oxide layers on $LiNbO_3$ can be used to enhance the photochemical efficiency. The interfaces for metal oxide/ZnO and metal oxide/$LiNbO_3$ for photochemical efficiencies are discussed in detail here.

II. ZnO:

Zinc oxide is a polar metal oxide that exhibits the highest polarization (0.05 C/m^2) among the wurtzite metal oxides and nitride semiconductors. Zinc oxide is a versatile material which is employed in the form of thin films, nanowires and nanoparticles, and it has been used in numerous applications such as an active channel material, a transparent conducting oxide (TCO), sensors, electron transfer layer, catalysts and UV light absorption materials [25, 26]. The numerous applications of ZnO are attributed to the wide band gap (3.3 eV), high exciton binding (60 meV) [24, 31], high absorption coefficient, and high carriers concentration (10^{17} – 10^{20} cm^{-3}) and mobility. The n-type character of ZnO, which is still an area of research, has been attributed to a number of effects including interstitial hydrogen, impurities and oxygen vacancies [32]. Different forms of ZnO, such as nanoparticles and thin films are interlayered between the active material (which generates electron-hole pairs) and cathodes as charge transfer layers [33].

Zinc oxide is a II-VI semiconductor which exists in the wurtzite, zinc blende or rocksalt crystal structure. At ambient conditions, the wurtzite hexagonal structure of ZnO is thermodynamically stable. Zinc blende ZnO is usually observed on cubic substrates and the rocksalt structure is obtained at relatively high pressure. The wurtzite hexagonal structure of ZnO belongs to the $P6_3mc$ space group in the Hermann-Mauguin notation and consists of a hexagonal unit cell with c/a ratio of 1.63, where c = 0.52 nm and a =

0.33 are the lattice constants. However, the c/a ratio observed experimentally in zinc oxide is smaller than the ideal value for hexagonal structure. The wurtizte ZnO structure, shown in Figure 1.3, consists of two alternate planes of O^{2-} and Zn^{2+} perpendicular to the c-axis. The O^{2-} and Zn^{2+} are terahedrally coordinated in a non-centrosymmetric structure, which is favorable for pyroelectric and piezoelectric properties.

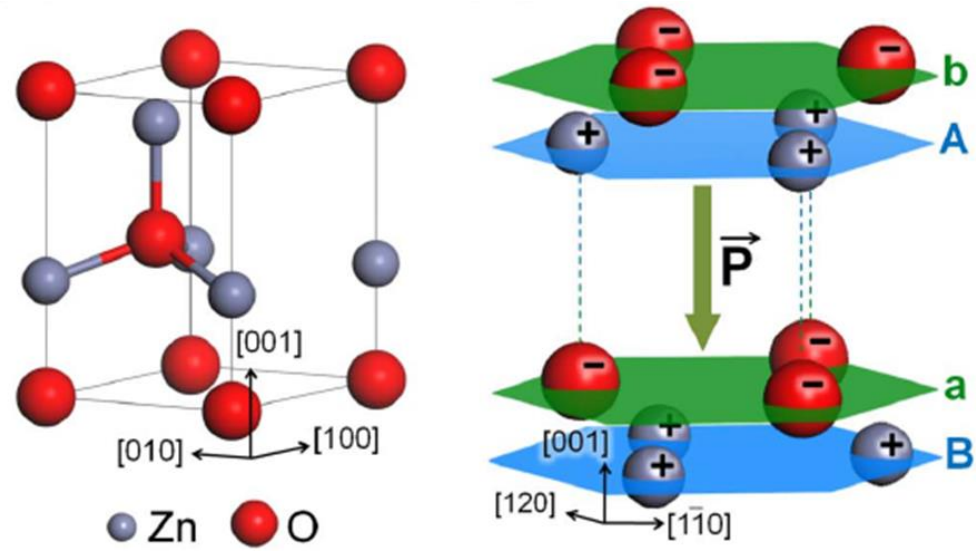

Figure 1.3. (a) ZnO unit cell, including the tetrahedral-coordination between Zn and its neighboring O. (b) ZnO has a noncentrosymmetric crystal structure that is made up of alternate layers of positive and negative ions, leading to spontaneous polarization $\vec{P}$ [34].

The single crystalline ZnO is polar in nature with alternate O and Zn planes. However, ZnO thin films are usually polycrystalline. The properties of ZnO thin films are sensitive to deposition techniques. Most commonly used deposition methods for ZnO are pulsed laser deposition (PLD), molecular beam epitaxy (MBE), sol-gel, sputtering, thermal evaporation, chemical vapor deposition and atomic layer deposition [24, 32]. The deposition processes for ZnO have evolved with the enhanced demands to control the interfaces and intrinsic properties of the films. In the last decade, studies using ALD

processes have led to a revolution in interface chemistry control, which solely initiates the reactions at the substrate surfaces [35, 36]. The PEALD ZnO process is discussed in detail in the PEALD section (Chapter 2). During the last few years, ALD and PEALD ZnO have shown improvement in properties; for example, the mobility can be increased to 60 $cm^2\ V^{-1}\ s^{-1}$ with carrier concentration of $10^{18}\ cm^{-3}$ at ≤150 °C [37, 38, 39]. Also, ALD deposited ZnO thin films have shown high crystal quality [40, 41].

III. $LiNbO_3$:

Lithium niobate ($LiNbO_3$) is a ferroelectric material that exhibits of both pyroelectric and piezoelectric properties [42]. It possesses the highest spontaneous polarization (0.71 C/m^2) among the ferroelectric materials. The spontaneous polarization is the reversible polarization which persists in the absence of an electric field. An applied mechanical stress parallel to the spontaneous polarization generates surface charge through the piezoelectric effect [42]. The properties of $LiNbO_3$ include transparency over a wide wavelength light, and large piezoelectric and optical coefficients. The unique properties of ferroelectric $LiNbO_3$ have opened the windows for various applications such as nonlinear optical, surface acoustic wave, wave guides, and electro-optic devices.

$LiNbO_3$ exhibits different crystal structures in the ferroelectric and paraelectric phases. In the ferroelectric phase, lithium niobate is classified with the 3*m* point group and *R*3*c* space group [43, 44]. The crystal structure of $LiNbO_3$ has trigonal structure, with a hexagonal base that has "c" and "a" parameters of 13.8631 Å and 5.14829 Å, respectively. The general formula (ABO_3) of $LiNbO_3$ is the same as perovskites; however, it does not the possess perovskite structure. In the paraelectric phase, $LiNbO_3$ crystal structure is centrosymmetric and exhibits a second order phase transition below

the Curie temperature [45]. The stacked sequence of $LiNbO_3$ along the c-axis has three types of octahedral: LiO_6, NbO_6 and vO_6, where the "v" represents vacant sites. The Li and Nb ions are stacked between the oxygen layer planes along the c-axis. A high applied voltage can switch the polarization of $LiNbO_3$ and form domains with opposite polarity [46]. The cations of Li and Nb are displaced along the *c*-axis, and the induced stress results in $LiNbO_3$ spontaneous polarization. The displacement of Li and Nb cations from centrosymmetric position in a direction parallel to the *c*-axis results only in antiparallel (180°) domains in $LiNbO_3$ crystals. Spontaneous polarization ($\vec{P}_{sp}$) generated bound charge is given as:

$$\sigma = \vec{P}_{sp} \,.\, \hat{c} \qquad (1)$$

The unscreened polarization bound charge in $LiNbO_3$ results in tilted conduction and valence bands due to the electric field [47]. The surface bound charge is compensated either by excess free carriers in the polar materials or screened by external charge carriers or adsorbed species [20, 48]. Thus, the commonly occurring screening can be divided into two categories, i.e. internal and external screening. The internal screening includes free carriers and ionized defects or impurities. On the other hand, the external screening arises from surface states and adsorbed charged molecules, radicals and ions at the surface. Both screening mechanisms are shown in Figure 1.4.

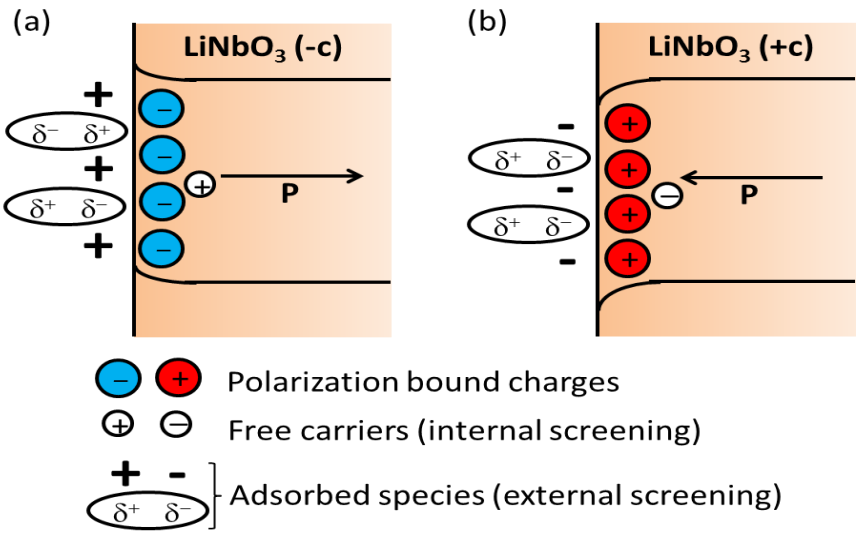

Figure 1.4. Schematic of ferroelectric $LiNbO_3$ shows (a) negative polarization bound charge on -c domain and (b)positive polarization bound charge on +c domain. In $LiNbO_3$, due to lack of free carriers in bulk, the surface is externally screened with oppositely charged adsorbed species by forming a Stern layer.

The internal screening mechanism leads to the charge accumulation near the surface and thus contributes to surface band bending. The internally screened surface exhibits a change in work function due to the surface band bending. The external screening mechanism leads to the formation of a sheet of opposite charges at the surface, which results in a surface dipole layer. The surface dipole layer can alter the surface electronic properties by changing the electron affinity and the work function of a surface [29]. In the case of $LiNbO_3$, external screening dominates over internal screening due to the low internal carrier concentration (10^{12} cm^{-2}). The external screening modulates the electron affinity of adjoining positive and negative domains, Figure 1.5.

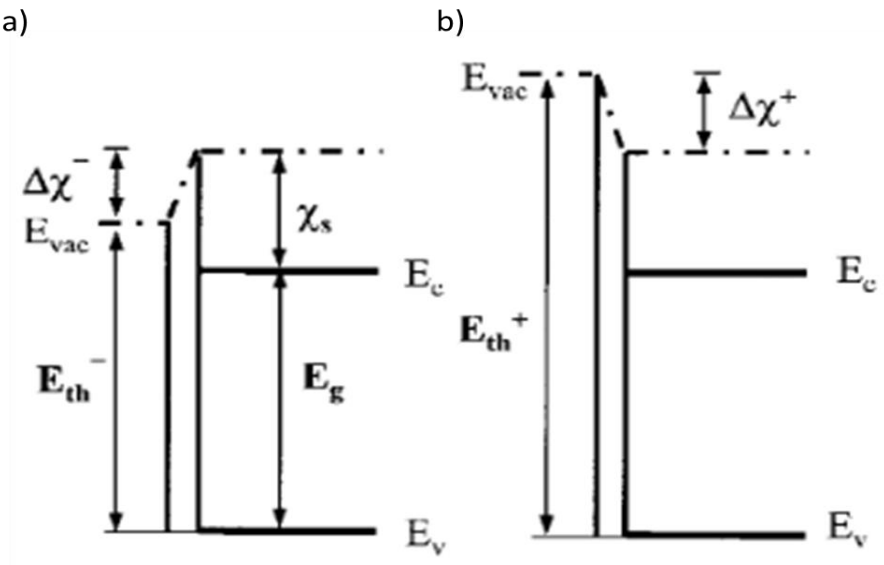

Figure 1.5. External screening results in a surface dipole that changes the electron affinity on the surface of the polar ferroelectric. $X_{s,}$ E_g, E_{th} and $\Delta\chi$ is the electron affinity, band gap, photothreshold, and electron affinity difference, respectively. The subscript (-) represents the negative domain and (+) represent positive domain [29].

Materials, such as $LiNbO_3$ and $BaTiO_3$, are among the group of ferroelectrics with bandgaps that may enable photocatalytic processes and exhibit an internal electric field that can lead to separation of the photoexcited carriers. Consequently, surface photochemical reactions display enhanced efficiency for these materials [7, 8, 20]. Specifically, enhanced reduction efficiency has been shown on positive $LiNbO_3$ and $BaTiO_3$ domain surfaces for photoinduced metal nanoparticle deposition [7, 20, 25, 26, 49].

IV. Charge Transfer in Heterostructures:

Heterostructures have advantages of reducing surface states, enhancing photoexcited carrier separation and in some cases, modulating the internal electric field to affect the charge transfer direction. These properties enhance the charge separation and

increase the photocatalytic efficiency. Metal oxide and ferroelectric heterostructures have been studied extensively for various applications such as photocatalysis, solar cells, and memory devices [7, 49-53]. The requirement of transparency and work function matching limits the selection of electron transfer layer. An interface of heterostructures plays a key role in the charge transfer process and charge transfer direction in semiconductor/ferroelectric, and passivation layer /semiconductor heterostructures [7]. The electron transport is initiated with the exposure of UV light photons of energy ($h\nu > E_g$) above the band gap of the photoactive material.

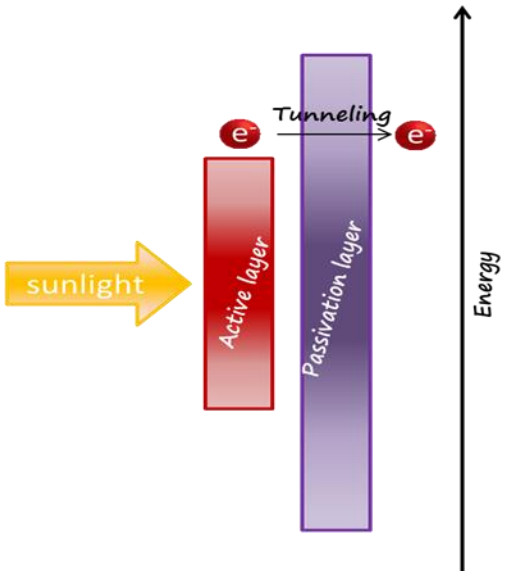

Figure 1.6. Schematic of active layer covered with thin passivation layer allowing an electron tunneling.

In this research two processes are discussed in detail: (i) the effect of SiO_2 and Al_2O_3 as passivation layers on ZnO surfaces, and (ii) the charge transfer in metal oxide/$LiNbO_3$ heterostructures. In the first study, the wide band gap insulators allow the penetration of illuminated light with negligible absorption. In the second study, the top metal oxide layer can overcome the charge recombination due to reduced interface states

and faster photoexcited charge separation. Although, ZnO is a potential candidate as an efficient photocatalyst; however in some of the electrolyte solutions ZnO is chemically unstable and undergoes photooxidation [16, 54]. The chemical instability is a hindrance for use as a photocatalyst. Thus, a chemically stable wide band gap material can be used as a passivation layer to protect the ZnO surface. Various methods have been developed to improve the performance of ZnO such as using a family of carbon, semiconductor, and wide band gap passivation layers [16, 55-58]. The unique properties of carbon, such as good electrical properties, corrosion resistance and stability, effectively improve the efficiency of ZnO [2, 16]. For example, graphene on top of ZnO can act as an electron reservoir for ZnO photo-excited electrons and also slows the electron-hole recombination rate due to faster electron transport from ZnO to the graphene surface [3, 59]. Wide band gap materials such as SiO_2, HfO_2 and Al_2O_3 may be suitable as a passivation layer because of their chemical and photo stability in the electrolytes. Al_2O_3 has been explored as a passivation layer for photocatalysis processes; however, the passivation efficiency is not in agreement for all the studies. Some studies show Al_2O_3 is chemically stable and protects the photocatalyst [60], while others show degradation of the Al_2O_3 [61]. The inconsistencies in the results can be attributed to the quality of Al_2O_3, the type of electrolyte and the specific application. The passivation layer is required to be thin, and free of pinholes and cracks to allow electron tunneling from the active material (ZnO) to the surface of the passivation layer and to prevent the photocorrosion of active layer in water and electrolyte solution. A schematic is shown in Figure 1.6.

In the second process, the ferroelectric polarization field, the metal oxides properties, and the band alignment at the heterostructure interface controls the pattern of

metal nanoparticle pattern on the surface. Polarity patterned lithium niobate (PPLN) substrates lead to spatially separated oxidation and reduction on –c and +c domain surfaces, respectively, which reduces the back reaction of carriers [7]. However, to further enhance the efficiency of surface reduction and/or oxidation on $LiNbO_3$, metal oxide charge transfer layer can be used. Burbure *et. al.* have studied the effect of TiO_2 on $BaTiO_3$ photochemical reaction using Ag metal deposition. They have shown on $TiO_2/BaTiO_3$ surfaces (i) the pattern on the surface of heterostructure is controlled by the polarization of $BaTiO_3$ [49, 52], (ii) photoinduced charge transfer to the surface [49, 52], and (iii) the Ag nanoparticle deposition is independent of TiO_2 crystal phase [52]. The charge transfer from $BaTiO_3$ to TiO_2 is attributed to the band alignment, Figure 1.7. Inoue *et. al.* have reported the use of TiO_2 and NiO films on PPLN that enhanced the photodecomposition of water on one type of domain (+c and –c) surface. The effect of band alignment charge transfer from ferroelectric to metal oxide surface is applicable only if the carrier concentration does not screen the photoexcited carrier flow. Once the carrier concentration in metal oxide becomes high enough to screen the ferroelectric photoexcited carrier flow, the Ag nanoparticle pattern diminishes.

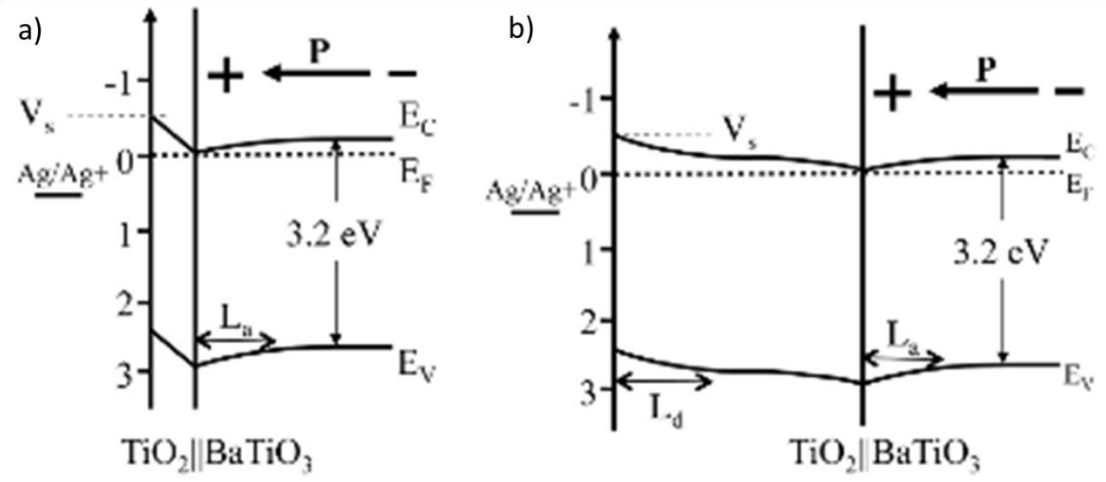

Figure 1.7. Band alignment of a) thin (15 nm) TiO_2 on $BaTiO_3$ and b) thick (100 nm) TiO_2 on $BaTiO_3$ [49].

Other than the band alignment assisted charge transfer and metal oxide carrier concentration screening in semiconductor and ferroelectric heterostructure, the charge accumulation at the interface due to ferroelectric polarization bound charge also needs to be considered. The accumulated charge at the interface can generate electric field, which can affect the flow of photoexcited carriers in ferroelectrics. Cagin *et. al.* have studied the polarization induced charge in ZnO in ZnO/ferroelectric capacitor structure. The calculated induced charge in ZnO was 10^{13} cm^{-2} [51]. An induced interface charge can cause upward or downward band bending in semiconductors. The charge accumulation and band bending at the interface of ZnO/ferroelectric is shown in Figure 1.8. The effect of band bending and depletion or accumulation layer is more prominent in thick films or bulk; however, in thin films the bands do not fully relax [7]. Schwinkendorf *et. al.* have shown the accumulation of 2DEG at the interface of ZnO/PZT ferroelectric field effect transistor (FeFET) [51]. They have explained the switching behavior of FeFET with the formation of electron trap layer in ZnO at the interface of ZnO/PZT heterostructure. The amount of charge accumulated at the interface is controlled by the applied voltage. Consequently, the stored charge causes the permanent on/off in FeFET structure. In case of polar oxide/ferroelectric FETs, the polarization is given by a combination of spontaneous polarization and the stress induced effect:

$$P_{piezoelectric} = P_{sp} + (e_{31} - e_{33}\frac{C31}{C33})(\varepsilon_x + \varepsilon_y) \qquad (2)$$

where, P_{sp} is the spontaneous polarization, e_{31} and e_{33} are piezoelectric coefficients, and C_{31} and C_{33} are elastic constants.

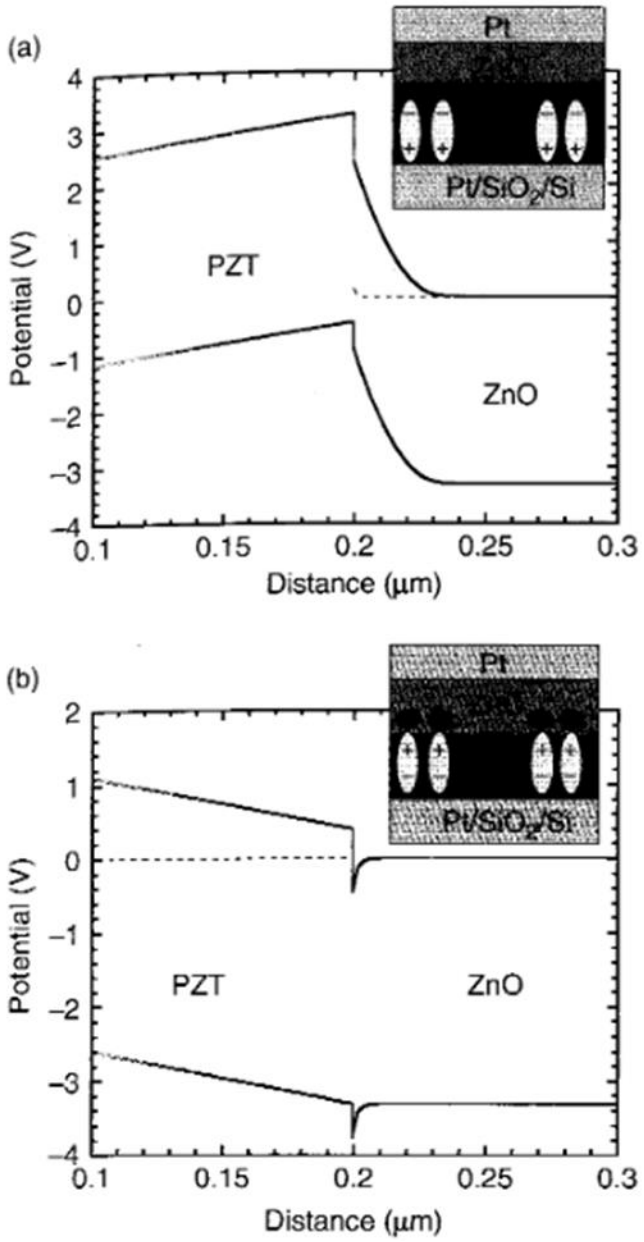

Figure 1.8. Calculated band diagram for a PZT/ZnO capacitor structure with PZT polarization in differing directions (a) and (b) [51].

V. Photoindued Metal Depositions:

The Ag nanoparticle pattern after photoinduced deposition is among one of the methods to study the surface photoreduction. The surface of the photocatayst is immersed with an aqueous $AgNO_3$ solution and illuminated with the UV light of energy higher than

the band gap of photoactive material to excite carriers near the surface. The photoexcited electrons and holes can cause reduction and oxidation of available chemical species at the surface. Photoinduced Ag nanoparticle deposition is the result of a reduction reaction. Presumably, the reduction and oxidation reactions occur in equilibrium. The occurrence of reduction process indicates the existence of balancing oxidation process. Figure 1.9 details the reduction and oxidation process on PPLN surfaces.

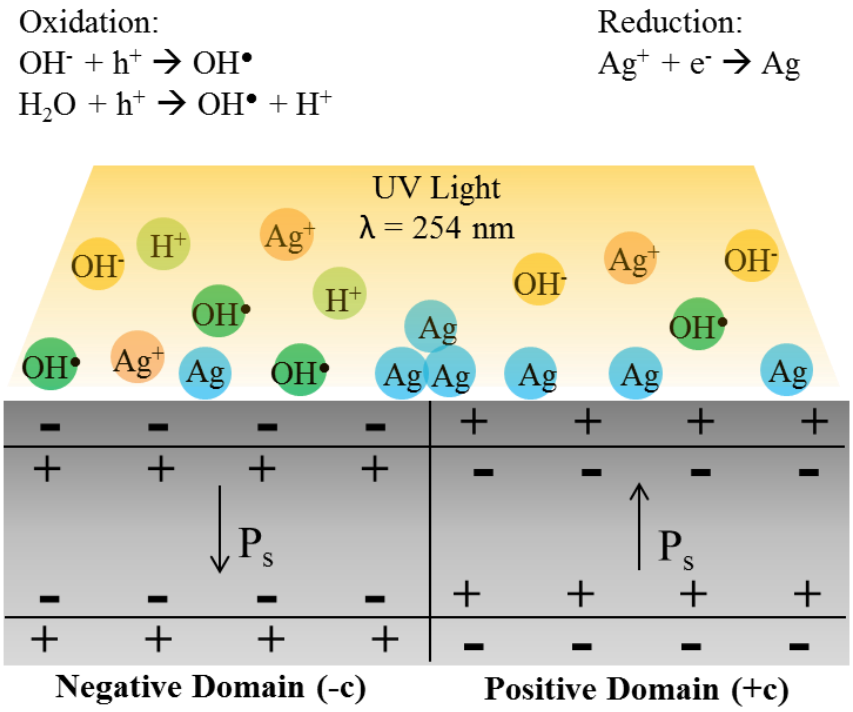

Figure 1.9. Schematic of photoinduced Redox reactions on $LiNbO_3$ -c and +c domain surface with UV light (l = 254nm, E = 4.2eV) illumination above the band gap of $LiNbO_3$. Favorable oxidation and reduction reaction on -c and +c domain surfaces, respectively, are shown above.

VI. Dissertation Approach:

This thesis is focused on two studies: (i) photochemical reactions using Ag nanoparticle deposition and the effect of interface band alignment of metal

oxides/ferroelectrics heterostructures, and (ii) Al_2O_3 and SiO_2 as passivation layers on ZnO. The band alignments are studied using x-ray and ultraviolet photoelectron spectroscopy (XPS and UPS). For photochemical reactions, surfaces of metal oxide/PPLN heterostructures were immersed with $AgNO_3$ solution and illuminated with UV light. The metal oxides were deposited using plasma enhanced atomic layer depiction (PEALD) and molecular beam deposition (MBD).

Chapter 2 and 3 discusses the deposition process, PEALD and MBD, in detail. In this research, films of ZnO, Al_2O_3 and SiO_2 were deposited using PEALD and other metal oxides (VO_2 and TiO_2) were deposited using MBD.

Chapter 4 and 5 introduces the characterization techniques of XPS, UPS, AFM and PFM are used to deduce the band alignment of heterostructures, and to characterize the surface topography and piezoelectric effect of ferroelectrics.

Photoinduced Ag nanoparticle deposition was used to characterize the effect of ZnO thickness on PPLN surface photochemical reactions in Chapter 6. AFM was used to characterize the pattern of Ag nanoparticles. Enhanced efficiency of Ag^+ ions was observed on 1, 2 nm ZnO/PPLN surfaces as compared to PPLN surfaces while PPLN controls the nanoparticle pattern on the surface. However, a further increase in ZnO thickness causes the decrease in photochemical reactions as the charge carriers in ZnO screens the photoexcited carriers in PPLN.

Chapter 7 focuses on the interface studies of metal oxides (ZnO, TiO_2, VO_2 and Al_2O_3)/$LiNbO_3$ heterostructures using XPS. Interface studies provide an insight to the band alignment and the mechanism of photoexcited charge transfer from PPLN to the metal oxide surface. Photoinduced Ag nanoparticle deposition was carried out on the

heterostructure and characterized using AFM to determine the effect of different metal oxides on photoreduction of Ag^{+}

Chapter 8 is the study of Al_2O_3 and SiO_2 passivation and degradation mechanism on ZnO. PEALD ZnO and single crystals of ZnO were used in this research. The band offsets of passivation layers and ZnO were calculated using UPS and XPS before the electrochemical measurements in phosphate electrolyte solution. AFM and SEM were used to analyze the surfaces and TEM was used do the cross-sectional characterization of heterostructures after electrochemical measurements.

In the end, Chapter 9 summarizes the important results and also presents opportunities for future studies based on this research.

References:

[1] A. Kudo, Y. Miseki, "Heterogeneous photocatalyst materials for water splitting" Chem. Soc. Rev. 38 (2009) 253-278.

[2] A. Paracchino, V. Laporte, K. Sivula, M. Grätzel, E. Thimsen, Highly active oxide photocathode for photoelectrochemical water reduction, Nature materials. 10 (2011) 456-461.

[3] F. E. Osterloh, "Inorganic nanostructures for photoelectrochemical and photocatalytic water splitting" *Chem. Soc. Rev.* **42** (2013) 2294.

[4] L. Li, P. A. Salvador and G. S. Rohrer, "Photocatalysts with internal electric field", *Nanoscale* **6** (2014) 24.

[5] M. Stock, and S. Dunn, "Influence of the Ferroelectric Nature of Lithium Niobate to Drive Photocatalytic Dye Decolorization under Artificial Solar Light" *J. Phys. Chem.* **116**, 20854 (2012).

[6] Y. Wang, J. Liu, L. Liu, D.D. Sun, "Enhancing stability and photocatalytic activity of ZnO nanoparticles by surface modification of graphene oxide" Journal of nanoscience and nanotechnology 12 (2012) 3896-3902.

[7] J. F. Reber, M. Rusek, "Photochemical hydrogen production with platinized suspensions of cadmium sulfide and cadmium zinc sulfide modified by silver sulfide" *J. Phys. Chem.* **90** (1986) 824.

[8] K. Maeda, X. Wang, Y. Nishihara, D. Lu, M. Antonietti and K. Domen, "Photocatalytic Activities of Graphitic Carbon Nitride Powder for Water Reduction and Oxidation under Visible Light" *J. Phys. Chem.***113** (2009) 4940.

[9] M. Stock and S. Dunn, "$LiNbO_3$ – A New Material for Artificial Photosynthesis", *IEEE Transac. Ultrasonics Ferroelectrics Freq. Contr.* **58**, 0885 (2011).

[10] B. Zielinska, E. Borowiak-Palen, R. J. Kalenzuk, "Preparation and Characterization of Lithium Niobate as a Novel Photocatalyst in Hydrogen Generation" *J. Phys. Chem. Solids* **69** (2007) 236.

[11] K. Saito, K. Koga and A. Kudo, "Lithium Niobate Nanowires for Photocatalytic Water Splitting" *Dalton Trans.* **40** (2011) 3909.

[12] R. Sapkal, S. Shinde, T. Waghmode, S. Govindwar, K. Rajpure, C. Bhosale, "Photo-corrosion inhibition and photoactivity enhancement with tailored zinc oxide thin films" Journal of Photochemistry and Photobiology B: Biology. 110 (2012) 15-21.

[13] J. Jiang, X. Zhang, P. Sun, and L. Zhang, "ZnO/BiOI Heterostructures: Photoinduced Charge-Transfer Property and Enhanced Visible-Light Photocatalytic Activity" *J. Physical Soc. Chem.* **115** (2011) 20555.

[14] X. Hong, J. Kim, S. Shi, Y. Zhang, C. Jin, Y. Sun, S. Tongay, J. Wu, Y. Zhang and F. Wang, "Ultrafast charge transfer in atomically thin MoS2/WS2 heterostructures" *Nature Nanotech.* **9** (2014)

[15] X. Wang, L. Yin, G. Liu, L. Wang, R. Saito, G. Q. Lu and H. M. Cheng, "Polar interface-induced improvement in high photocatalytic hydrogen evolution over ZnO–CdS heterostructures" *Energy Envi. Sci.* **4** (2011) 3976.

[16] Y. Q. Cao, J. Chen, H. Zhou, L. Zhu, X. Li, Z. Y. Cao, D. Wu and A. D. Li, "Photocatalytic activity and photocorrosion of atomic layer deposited ZnO ultrathin films for the degradation of methylene blue", *Nanotech.* **26**, 024002 (2015).

[17] A. Fujishima, X. Zhang, D. A. Tryk, "TiO_2 photocatalysis and related surface phenomena" *Surface Science Reports* **63** (2008) 515.

[18] M. A. Lazar, S. Varghese and S. S. Nair "Photocatalytic Water Treatment by Titanium Dioxide: Recent Updates" *Catalysts* **2** (2012) 572.

[19] M. Liu, C. Nam, C.T. Black, J. Kamcev, L. Zhang, "Enhancing Water Splitting Activity and Chemical Stability of Zinc Oxide Nanowire Photoanodes with ultrathin titania shells", *J. Phys. Chem. C.* 117 (2013) 13396-13402.

[20] Y. Cui, J. Briscoe, and S. Dunn, "Effect of Ferroelectricity on Solar-Light-Driven Photocatalytic Activity of $BaTiO_3$ --- Influence on the Carrier Separation and Stern Layer Formation" *Chem. Mater.* **25** (2013) 4215.

[21] B. Zielinska, E. Borowiak-Palen, R. J. Kalenzuk, "Preparation and Characterization of Lithium Niobate as a Novel Photocatalyst in Hydrogen Generation" *J. Phys. Chem. Solids* **69** (2007) 236.

[22] U. Ozgur, Y. I. Alivov, C. Liu, A. Teke, M. A. Reshchikov, S. Dogan, V. Avrutin, S.J. Cho, and H. Morkoc, "A comprehensive review of ZnO materials and devices" *J. Appl. Phys.* **98**, (2005) 041301

[23] Z. L. Wang, "Zinc Oxide Nanostructures: Growth, Properties and Applications" *J. Phys. Condens. Matt.* **16**, R829-R858 (2004).

[24] A. Janotti and C. G. V. D. Walle, "Fundamentals of Zinc Oxide as a Semiconductor", *Rep. Prog. Phys.* **72**, 126501 (2009).

[25] Y. Sun, R. J. Nemanich, "Photo-induced Ag deposition on periodically poled lithium niobate: Concentration and intensity dependence" *J. Appl. Phys.* **109**, 104302 (2011).

[26] Y. Sun, B. S. Eller, and R. J. Nemanich, "Photoinduced Ag deposition on periodically poled lithium niobate: Wavelength and polarization screening dependence" *J. Appl. Phys.* **110**, 084303 (2011).

[27] Y. S. Park, J. H. Kim, and W. Yang, "Comparison Study of Metal Nanoparticles Grown on Polarity Patterned Ferroelectrics by Scanning Probe Microscopy" *Surf. Interface Anal.* **44** (2012) 759.

[28] A. Haussmann, P. Milde, C. Erler, and L. M. Eng, "Ferroelectric Lithography: Bottom-up Assembly and Electrical Performance of a Single Metallic Nanowire" *Nano Lett.* **9** (2009) 2.

[29] W. C. Yang, B. J. Rodriguez, A. Gruverman, and R. J. Nemanich, *Appl. Phys. Lett.* **12**, (2004) 2316.

[30] Y. Xu, S. A. A. Schoonen, "The absolute energy positions of conduction and valence bands of selected semiconducting minerals" *American Mineralogist* **85** (2000) 543–556.

[31] P. Barquinha, R. Martins, E. Fortunato, "Advances in GaN and ZnO-based Thin Film, Bulk and Nanostructured Materials and Devices" Vol. *156* (Ed: S. J. Pearton), Springer , New York **2012** , 435.

[32] U. Ozgur, Ya. I. Alivov, C. Liu, A. Teke, M. A. Reshchikov, S. Dogan, V. Avrutin,S. J. Cho, and H. Morkoç, "A comprehensive review of ZnO materials and devices", *Appl. Phys. Rev.* **98** (2005) 041301.

[33] J. C. Moore, R. Louder and C. V. Thompson, "Photocatalytic Activity and Stability of Porous Polycrystalline ZnO Thin-Films Grown via a Two-Step Thermal Oxidation Process", *Coatings* **4**, 651-669 (2014).

[34] T. S. Herng, A. Kumar, C. S. Ong, Y. P. Feng, Y. H. Lu, K. Y. Zeng & J. Ding, "Investigation of the non-volatile resistance change in noncentrosymmetric compounds" *Nature Specific Reports* **2** (2012) 587.

[35] S. M. George, A. W. Ott, and J. W. Klaus, "Surface chemistry for atomic layer growth Source" *J. Phys. Chem*. **100**, 13121 (1996).

[36] H. B. Profijt, S. E. Potts, M. C. M. van de Sanden, and W. M. M. Kessels, "Plasma-Assisted Atomic Layer Deposition: Basics, Opportunities, and Challenges" *J. Vac. Sci. Technol.* **A 29** (2014) 5

[37] E. Fortunato, P. Barquinha, and R. Martins, "Oxide Semiconductor Thin-Film Transistors: A Review of Recent Advances", *Adv. Mater*. **24**, 2945-2986 (2012).

[38] R. L. Hoffman, B. J. Norris and J. F. Wager, "ZnO-based transparent thin-film transistors", *Appl. Phys. Lett*. **82**, 5 (2003).

[39] N. Huby, S. Ferrari, E. Guziewicz, M. Godlewski and V. Osinniy, "Electrical behavior of zinc oxide layers grown by low temperature atomic layer deposition", *Appl. Phys. Lett.* **92**, 023502 (2008).

[40] P. C. Rowlette, C. G. Allen, O. B. Bromley, A. E. Dubetz and C. A. Wolden, "Plasma-Enhanced Atomic Layer Deposition of Semiconductor Grade ZnO Using Dimethyl Zinc", *Chem. Vap. Dep.* **15**, 15-20 (2009).

[41] S. H. Park, C. S. Hwang, H. S. Kwack, J. H. Lee, and H. Y. Chu, "Characteristics of ZnO thin films by means of plasma-enhanced atomic layer deposition", *Electrochem. Solid State Lett.* **9**, G299-G301 (2006).

[42] M. E. Lines and A. M. Glass, *Principles and Applications of Ferroelectrics and Related Materials* (Clarendon, Oxford, 1977).

[43] D. A. Scrymgeour, V. Gopalan, A. Itagi, A. Saxena, and P. J. Swart, "Phenomenological theory of a single domain wall in uniaxial trigonal ferroelectrics: lithium niobate and lithium tantalite," *Phys. Rev. B* **71**, 184110 (2005).

[44] S. C. Abrahams, E. Buehler, W. C. Hamilton, and S. J. Laplaca, "Ferroelectric lithium tantalate—III. Temperature dependence of the structure in the ferroelectric phase and the para-electric structure at 940°K" *J. Phys. Chem. Solids* **34**, 521 (1973).

[45] K. Kitamura, J. K. Yamamoto, N. Iyi, S. Kimura, and T. Hayashi, "Stoichiometric $LiNbO_3$ single crystal growth by double crucible Czochralski method using automatic powder supply system," *J. Cryst. Growth* **116**, 327 (1992).

[46] H. Franke, "Li+ Ionic-Conductivity in $LiNbo_3$" *Phys. Status Solidi A* **83** (1984) K73.

[47] W. C Yang, B. J. Rodriguez, A. Gruverman, and R. J. Nemanich, *J. Phys.: Condens. Matter*, **17**, S1415 (2005).

[48] S. V. Kalinin, D. A. Bonnell, T. Alvarez, X. Lei, J. H. Ferris, Q. Zhang and S. Dunn, "Atomic Polarization and Local Reactivity on Ferroelectric Surfaces: A New Route toward Complex Nanostructures", *Nano Lett.* 2, 589 (2002).

[49] N. V. Burbure, P. A. Salvador, and G. S. Rohrer, "Photochemical Reactivity of Titania Films on $BaTiO_3$ Substrates: Origin of Spatial Selectivity" *Chem. Mater.***22** (2010) 5823.

[50] P. Schwinkendorf, M. Lorenz, H. Hochmuth, Z. Zhang, and M. Grundmann, "Interface charging effects in ferroelectric ZnO–BaTiO3 field-effect transistor heterostructures", *Phys. Status Solidi A* 211 (2014) 166.

[51] E. Cagin, D. Y. Chen, J. J. Siddiqui, and J. D. Phillips, "Hysteretic metal-ferroleectric-semiconductor capacitors based on PZT/ZnO heterostructures" *J. Phys. D* **40** (2007) 2430.

[52] N. V. Burbure, P. A. Salvador and G. S. Rohrer, “Photochemical Reactivity of Titania Films on $BaTiO_3$ Substrates: Influence of Titania Phase and Orienation”, *Chem Mater*. **22** (2012) 5831.

DEPOSITION TECHNIQUES:

CHAPETR 2. PLASMA ENHANCED ATOMIC LAYER DEPOSITION:

I. Introduction:

The term atomic layer deposition (ALD) is derived from atomic layer epitaxy (ALE). ALD has also been termed as atomic layer growth (ALG), atomic layer evaporation, molecular layer epitaxy (MLE), molecular deposition, molecular lamination, molecular layering (ML), and chemical layering [1]. According to the literature, the origin of the ALD process remains controversial as the process has been independently demonstrated by two groups in the 1960s and 1970s. Self-limiting gas and substrate reactions were reported by Aleskovskii's group from Russia in 1964 [2] and Suntola's group from Finland in 1974 under the names molecular layering and atomic layer epitaxy (ALE) [3], respectively. Conversely, in most of the journals Suntola's group is recognized as pioneering the reaction chemistry of atomic layer deposition [4]. The only difference in the processes developed by these two groups was the use of reactants and the materials deposited. The Finland group carried out the deposition process using element reactants: Zn/S, Sn/O_2 and Ga/P to deposit ZnS, SnO_2 and GaP in their first report [3] and compound reactants: the $TaCl_5/H_2O$ and $Zn(Mn)Cl_2/H_2S$ and $AlCl_3/H_2O$ to deposit Ta_2O_3, ZnS and Al_2O_3 as described in several patents [5,6]. The deposition process developed by the group from Russia involved $TiCl_2/H_2O$ to deposit TiO_2 and $GeCl_4/H_2O$ to deposit GeO_2 [3].

In the 1990s ALD processes were successfully adapted by the semiconductor industry to improve the quality of high-k films for microelectronic technologies consequently reducing gate tunneling [7]. An atomic level control of thickness and the ability to modulate materials properties in ALD processes brought attention to various high-k materials. In the last decade, ALD research has expanded to include metal nitrides [8, 9, 10], metal sulphides [10, 11] and elemental metals [10, 12, 13]. As ALD research has expanded, a number of reviews have discussed ALD applications in semiconductor devices [14, 15], photocatalysis [16-22], nanopatterning [23, 24], and solar cells [25, 26]. ALD is a low temperature process and most of the materials deposited are amorphous. Thus, the atomic layers do not follow substrate epitaxy as suggested by the name ALE

[10]. The name "atomic layer deposition", which dates back to the 1990s, more accurately specifies the nature of the process [10].

ALD is a self-limiting sub monolayer two-step process, in which the metal precursor and the reactant gas are separated with a N_2 purge step. Unlike chemical vapor deposition (CVD), in ALD the reactants saturate the surface in real time [1, 7, 10, 12, 13, 27-35]. As shown in Figure. 2.1, ALD is a four step process: in the first step the surface saturated with a precursor pulse; the second step is the N_2 purge to remove the excess precursor and gaseous byproducts; the third step is the oxygen reactant reaction to replace the ligands; and the fourth step is the N_2 purge to remove the excess oxygen and gaseous byproducts and to prepare the surface for next cycle. The thickness of films is controlled by the number of cycles, where one cycle of ALD typically deposits 0.5-2.5 Å thickness. Consequently, the ALD deposition mechanism leads to uniform and conformal ultra-thin films.

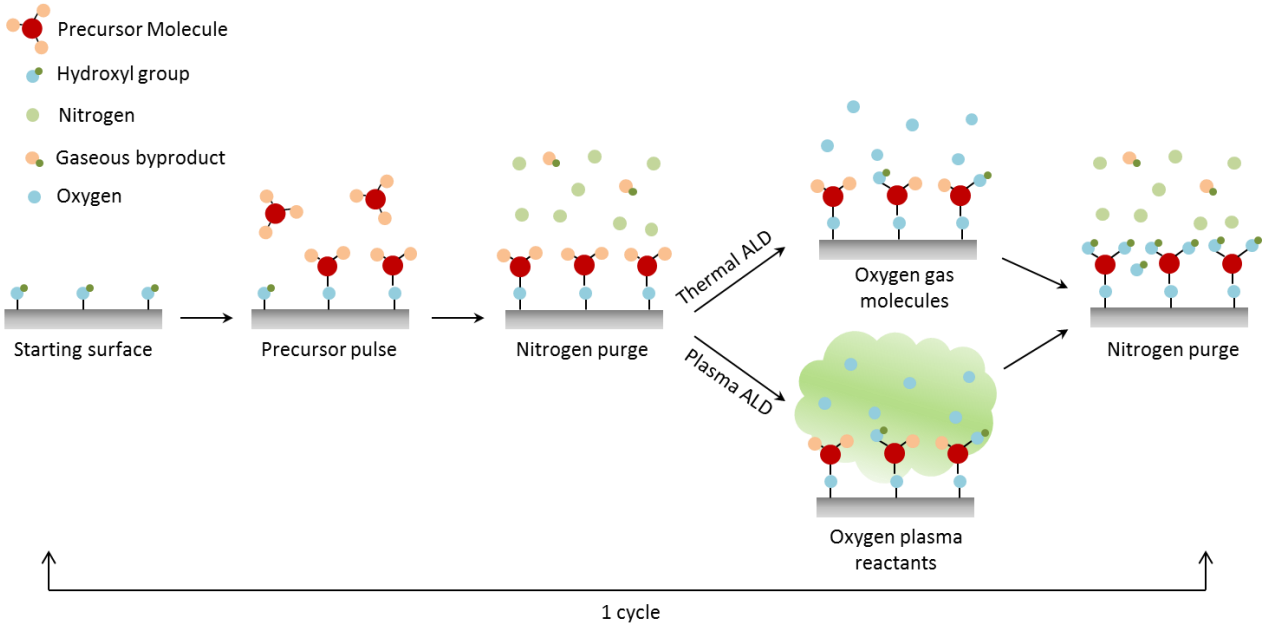

Figure 2.1. Schematic of an ALD process, showing the four step process for one cycle of thermal or plasma enhanced ALD.

Plasma-Enhanced Atomic Layer Deposition (PEALD) is a modified form of conventional ALD in which plasma generated reactants are used to exchange reactions with ligands [35]. This process was first time reported at Philips Research Laboratories in Eindhoven, the Netherlands, in 1991 by De Keijser and Van Opdorp [36]. They deposited

GaAs using remote microwave plasma to generate hydrogen radicals that drive surface reactions with GaM_3 and AsH_3. However, the interest in PEALD expanded in the mid-1990s, when the semiconductor industry explored it for microelectronics of non-planar surfaces [37, 38]. Following Sherman's patent on the PEALD process in 1996, Rossnagel's group reported PEALD of metal (Ta and Ti) films in 2000 [39].

II. Categories of Atomic Layer Deposition:

Atomic layer deposition processes have evolved in the last two decades, and various forms of ALD have been conceptualized using different gaseous reactants or adding molecular energy during deposition. In this introduction metal compounds are termed as "precursors" and the non-metal gaseous vapors are termed as "reactants".

A. Thermal ALD:

The conventional ALD process is usually termed as "thermal ALD". The surface reactions of precursor and water vapor or oxygen gas are driven by thermal energy without the assistance of plasma or generated radicals. Usually, the thermal ALD deposition process requires slightly higher deposition temperatures (150 ºC - 500 ºC). The most common materials that have been deposited using thermal ALD systems are metal oxides (Al_2O_3, TiO_2, ZnO, ZrO_2, HfO_2, and Ta_2O_5) [1, 11, 41], metal nitrides (TiN, TaN, and W_2N) [7, 8, 9, 25, 41], and sulfides (ZnS and CdS) [8, 11]. Thermal ALD provides uniform coverage on 3D surfaces [10]; however, the thermal energy requirement to drive surface reactions has drawbacks. For example, flexible electronics that require low temperature deposition cannot sustain a typical thermal ALD process due to the high deposition temperature [35]. On the other hand, the low reactivity of O_2 gas or H_2O with precursors, such as β-diketonates, guanidinates, amidinatesand (substituted) cyclopentadienes, limits the materials that can be used in thermal ALD process [10, 35]. To overcome the issues of conventional ALD processes, plasma enhanced ALD and energy enhanced ALD processes have been successfully employed.

B. Plasma-Enhanced ALD:

A plasma-enhanced or plasma-assisted ALD process is a modified conventional ALD process, in which water vapor or gaseous molecules are replaced with plasma generated atomic gaseous species and radicals, Figure 2.1. The plasma generated highly reactive species facilitate surface reactions with ligands during the reactant step. PEALD

has merits over thermal ALD, in that it allows deposition at low temperatures and opens an avenue for low reactivity precursors while allowing film properties modulation. Some of the initial PEALD thin films were elemental metals prepared using metal precursor molecules and H_2 plasma, e.g. PEALD Ta using $TaCl_5$ and hydrogen plasma [35]. This was a breakthrough as metal deposition with conventional ALD was next to impossible. The interest in PEALD is increasing rapidly in semiconductor and non-semiconductor industries, which has led to the development of a large selection of precursors. PEALD provides versatility for applications that require a new set of ALD parameters that are not feasible with thermal ALD. The most commonly used plasma reactants include O_2, N_2, H_2, HF, NF_3, and NH_3 or combinations thereof, which can be used to deposit metal oxides, metal nitrides, metal fluorides, metal sulphides and metals. The most common materials that have been deposited successfully using PEALD are: metals (Ti, Ta, Al, Ru, Cu, Co, Ni, W), metal nitrides (TiN, TaN, RuTiN, $TiSi_xN_y$, $TaSi_xN_y$, W_2N, SiN_x), metal oxides (Al_2O_3, Ta_2O_5, Y_2O_3, ZrO_2, ZnO, HfO_2, $SrTiO_3$, $SrTa_2O_6$ and $SrBi_2Ta_2O_9$) [35]. Processes for PEALD of sulfides and fluorides are not as developed as those for oxides, nitrides and metals. The surface chemistry for metal fluorides can be developed using metal precursor molecules and fluorine radicals generated in an HF, F_2 or NF_3 plasma.

As the high reactivity of the plasma species is a source of energy in PEALD to initiate surface reactions, less thermal energy is required. According to the literature, PEALD materials exhibit improved properties, such as higher film density, lower impurity concentration and improved electronic properties. In addition, the high reactivity of plasma reactants provides the freedom to use a wider range of precursors including chemically stable precursors, such as β-diketonate, which show negligible deposition in thermal ALD chemical reactions [35].

C. Energy-Enhanced ALD:

As mentioned above PEALD is a form of EEALD which is defined in a few different ways. The concept is to enhance the surface energy, either using plasma generated radicals during a gaseous reactant step [41] or to incorporate a step of helium (He) plasma (or UV illumination), or molecular energy transfer after a gaseous reactant plasma step. For example, Potts *et. al.* have used plasma generated ions to increase the surface energy during TiO_2 deposition in the O_2 reactant step [41]. The EEALD TiO_2

films were prepared at room temperature with a high growth rate, using [Ti(Cpx)L3] precursors, which is not viable with thermal ALD. Another concept is to use excited molecules to transfer a significant and controlled energy pulse to surface species. The process may involve plasma-excited noble gases (He, Ne, Ar, Kr), which can transfer eVs of energy without chemical interactions. The additional energy could enable nucleation or crystal growth at temperatures lower than achievable by thermal ALD. The implementation is through an additional plasma pulse and purge that is included in the ALD cycle, Figure 2.2. The freedom to modulate PEALD processes has revolutionized thin film interfaces through precise control of chemistry, morphology, and crystallinity.

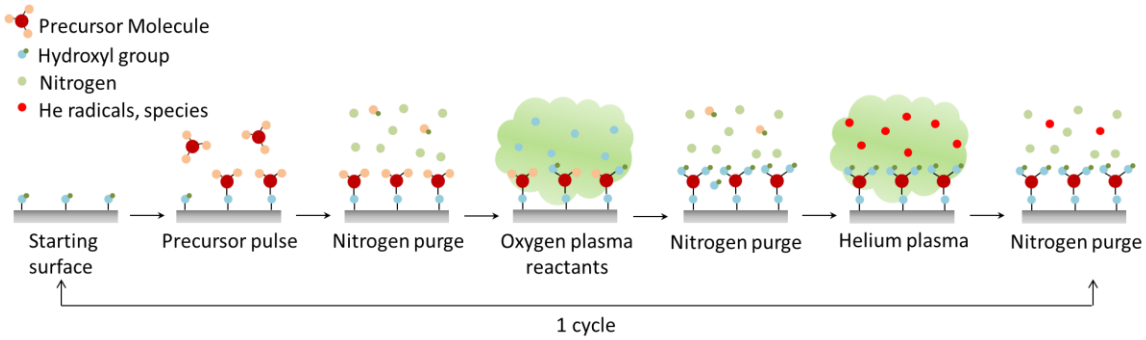

Figure 2.2. Schematic of an EEALD process, showing a six step process for one deposition cycle. Here, a helium plasma pulse following the oxygen pulse and nitrogen purge enhances the surface energy and allows the atoms to rearrange at the surface.

III. Plasma Basics:

Plasma is an electrically quasi-neutral (density of electrons is equal to the density of ions) collection of gaseous species of free and charged particles. The most common plasma generation method is to use an electric field to ionize gaseous species by accelerating and heating the electrons. The copper coil around the quartz tube generates an electrical field that ionizes the gas passing through it. The hot or high energy electrons (T_e ~ 3.5 x 10^4 K, ~3eV) excite the reactant gas and dissociate it into radicals, and ions. Despite the critical role of charged particles in the plasma, the density of charged particles is significantly lower (10^{-6}-10^{-3}) than the density of atomic oxygen radicals and expected O_2 neutrals(the densities of O_2 species in oxygen plasma are listed in Table 2.1). Therefore, the surface reactions are dominated by the high concentration of radicals. The formation of a positive charge space layer, also called a “plasma sheath”, between

the plasma boundary and the substrate surface, generates ions that are accelerated towards the surface. An increase in the velocity of ions enhances the energy of ions reaching the surface. The potential difference of the substrate surface (V_f) and plasma (V_p) is given as:

$$D.\ V_p\text{-}V_f = \frac{T_e}{2e} + \frac{T_e}{2e}\ln\left(\frac{m_i}{2\pi m_e}\right) \quad \ldots\ldots\ldots\ldots\ldots\ldots\ldots\ldots\ldots\ldots (1)$$

where, e is the electron charge, T_e is the electron energy in eV, m_e is the electron mass and m_i is the ion mass. Usually, the potential difference is a few times T_e. The potential difference can vary from <50 V to a few hundreds of volts depending on the plasma conditions and reactor configuration. The ion energy distribution vs ion energy plots of commonly used plasmas for PEALD (O_2, N_2 and H_2) is shown in Figure 2.3.

Table 2.1. Densities of plasma species in an O_2 plasma, as typically used in plasma ALD processes. Data are presented for two different pressures and the electron temperature, T_e, and energy, E_{ion}, of ions accelerated to the (grounded) substrate are also given. The data have been compiled for an inductively-coupled plasma operated at a source power of 500 W. The excited species O* and O_2* correspond to the lowest metastable states being O (^{1}D) and O_2 ($a^1\Delta g$), respectively. Reprinted from H. B. Profijt *et al.*, *J. Vac. Sci. Technol. A* 29, 050801 (2011) [42].

Pressure (mTorr)	O_2 (cm^{-3})	O (cm^{-3})	O_2* (cm^{-3})	O* (cm^{-3})	O_2^+ (cm^{-3})	O^+ (cm^{-3})	O^- (cm^{-3})	n_e (cm^{-3})	T_e (eV)	E_{ion} (eV)
10	3×10^{14}	7×10^{13}	4×10^{13}	4×10^{12}	5×10^{10}	4×10^{10}	2×10^{10}	2×10^{10}	2.8	15.3
100	3×10^{15}	1×10^{14}	3×10^{14}	5×10^{10}	4×10^{10}	1×10^{10}	3×10^{10}	3×10^{10}	2.1	10.8

The two mechanisms that account for PEALD processes are:

First, the high energy species in the plasma act as the reaction driving force independently of substrate thermal energy. The concentration of the species can be controlled by varying gas and plasma parameters, such as flow rate, pressure, power, etc. Thus, the energy provided to the surface and surface adsorbed molecules can be manipulated for PEALD and EEALD.

Second, the oxygen ions can act as a source of energy in PEALD and EEALD processes, which can accelerate the reaction rate and rearrange the adsorbed molecules.

Similar to the high energy species, the energy and density of ions can be manipulated by varying the gas and plasma parameters. Typically, the plasma sheath thickness and ion mean free path controls the collision of ions with the substrate surface. The surface ion bombardment can cause undesired damage to the surface, which may or may not be prevented depending on the reactor configuration.

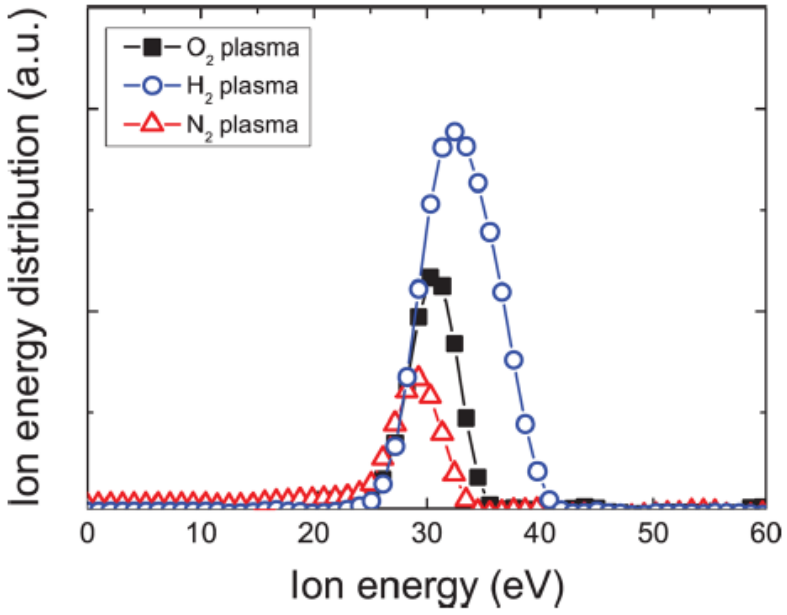

Figure 2.3. Ion energy distribution vs ion energy (eV) of O_2, H_2 and N_2 remote plasmas using a retarding field energy analyzer (RFEA). The operating plasma conditions are: pressure 8 mTorr and plasma power 100 W [40].

Types of Plasma Sources:

The plasma sources are usually differentiated by the way the plasma is generated or by the distance of the plasma source from the deposition surface. In general, three

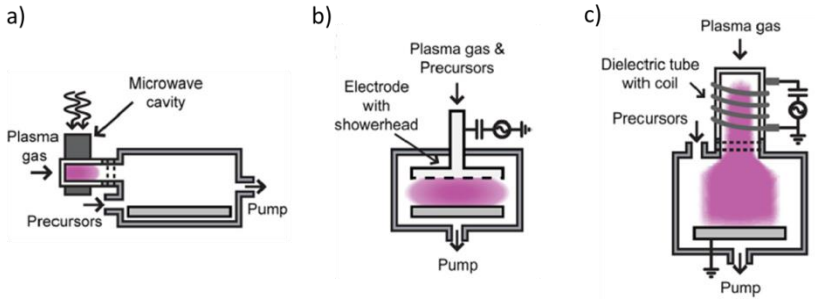

Figure 2.4. Schematic of a) radical-enhanced, b) direct and c) remote plasma sources [43].

types of plasma designs have been employed i.e. radical-enhanced, direct plasma and remote plasma.

Radical-enhanced Plasma: In this configuration, the plasma is generated far away from the ALD surface reactions zone, Figure 2.4 a). The plasma species flow from the plasma source to the substrate surface through tubing. This allows the electrons and ions to lose energy while undergoing multiple surface collisions and recombination. Consequently, the configuration is called radical-enhanced plasma. These plasma sources can be used in PEALD reactors and also for surface cleaning. The commercially available microwave surfatron [44] and the radiofrequency-driven radical-enhanced plasma system are sold by R*Evolution (MKS Instruments) [45] and Litmas RPS (Advanced Energy) [46].

Direct Plasma: The second configuration of plasma systems is the direct plasma. In this design, the plasma is generated between two parallel electrodes, and generally, the substrate is used as one of the electrodes. Typically one electrode is powered at 13.56 MHz radio frequency and the other electrode, usually the substrate, is grounded. In this case, the substrate sits directly on the electrode that participates generating the plasma. Therefore, this configuration is referred to as direct plasma. As the plasma species are generated in the proximity of the substrate surface, shorter pulse times are required during ALD processing. However, the high energy fluxes of plasma ions and radicals can induce surface damage.

Remote Plasma: In this configuration, the plasma is generated remotely from the reaction surface such that the substrate stage does not participate in plasma generation. This configuration is different from both above discussed radical enhanced and direct plasma. Unlike the radical enhanced plasma configuration, the plasma generation in a remote plasma is above the reaction surface. In contrast to direct plasma, for remote plasma the substrate and plasma conditions can be varied independently. The plasma composition and distance from the substrate surface provides the freedom to control the plasma properties. The operating flexibilities of remote plasma make it viable for surface cleaning and other R&D processes. Another advantage of remote plasma is the plasma source and deposition surface distance that allows *in situ* thickness measurement using spectroscopic ellipsometry. The inductively-coupled plasma (ICP) is the most commonly used plasma source in many of the commercially available PEALD systems [42, 47].

IV. PEALD Reactor Configuration:

A schematic of the customized PEALD reactor that was used to deposit thin films for this research is shown in Figure 2.5 a). The chamber is pumped to a base pressure of 8 x 10^{-8} Torr using a turbo pump backed with a mechanical pump; however, the mechanical pump is switched to a dry pump during processing. The ALD reactor has an ICP, i.e. a helical copper coil around a 32 mm diameter quartz tube, to generate a remote plasma ~12 inches above the reaction surface. The oxygen plasma is ignited with 13.56 MHz rf at 200 W while maintaining the O_2 gas pressure at 100 mTorr with a flow rate of 35 sccm. The O_2 gas pressure and flow rate, and plasma power is varied for some depositions to tune the thin film properties. The chamber is also heated to ~70 ºC during the PEALD processing to avoid chemical condensation at the chamber walls. As shown in Figure 2.5, the precursors are stored in stainless steel bubbler and each bubbler is maintained at a specific temperature according to the vapor pressure. The pipelines between the bubblers and chamber are also heated to prevent condensation. Argon gas is used as a carrier gas to deliver the precursor vapors from the bubbler to the chamber. Labview software is used to control the precursor time, N_2 purge and O_2 plasma pulse, and to combine the gas phase sequences to form ALD cycles. The system is installed with five precursors, i.e. Dimethylaluminum Isopropoxide (DMAI), Tetrakis(ethylmethylamino)hafnium (TEMAHf), Tri(dimethylamino)silane (TDMAS), Dimethyl Zinc (DMZ) and Gallium Acetylacetonate. The materials deposition using these precursors is discussed below.

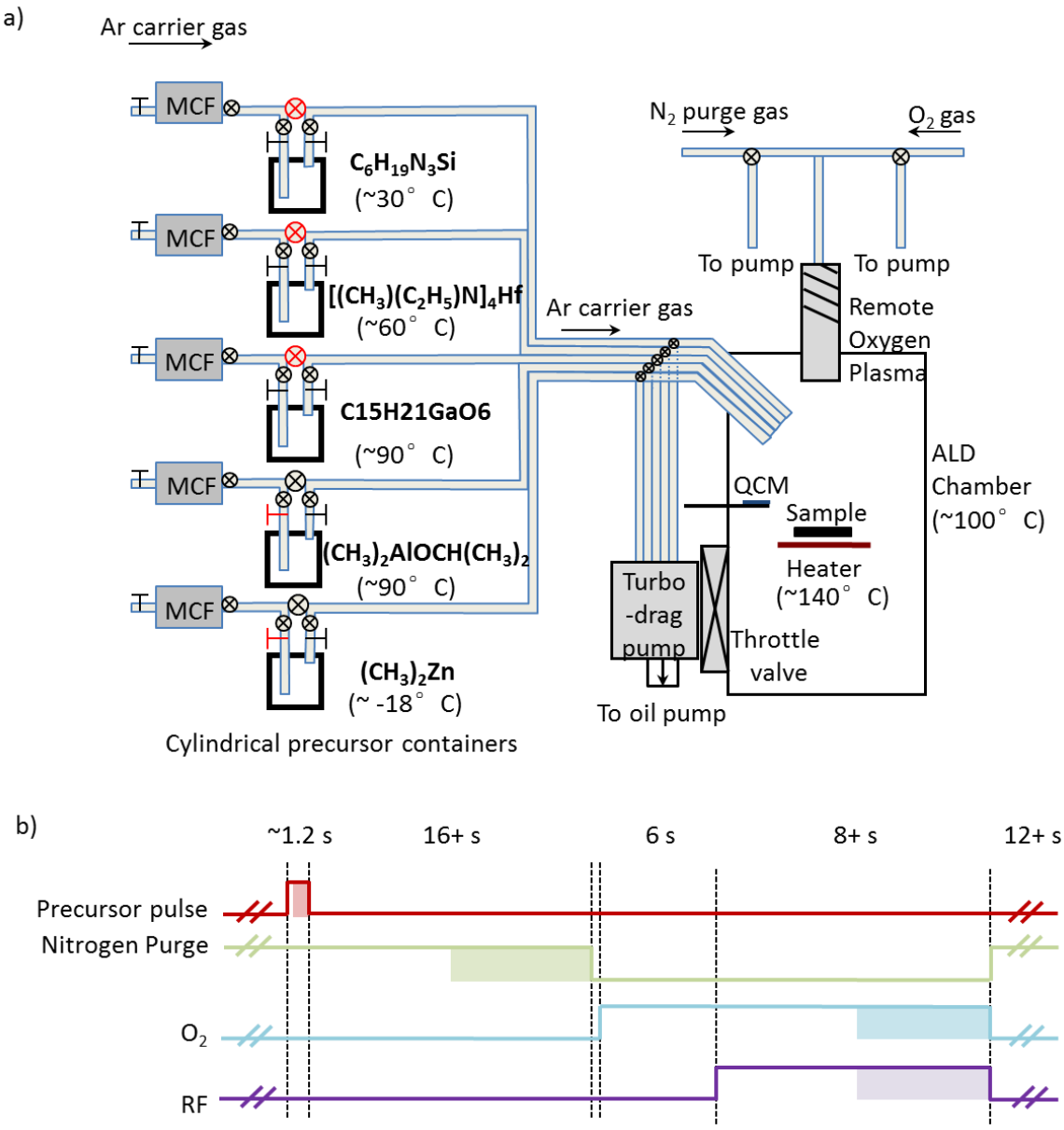

Figure 2.5. Schematic of a) ICP remote plasma ALD reactor and b) gas phase sequences for 1 PEALD cycle controlled using Labview software.

V. Growth Mechanisms of ALD:

The basic growth mechanism in all the ALD processes is similar but there is significant variation in the reaction rates and reactivity of the adsorbed metal precursor molecules and the reactant gas. However, the growth process depends on a number of factors, such as adsorption sites, precursor molecule size, precursor reactivity etc. The first step is the surface adsorption which is followed by the reactant gas exchange

reaction with ligands. Below are the different models of ALD growth process as described by Puurunen *et. al*. [10].

A. Surface Adsorption:

During the sequential steps of an ALD process, the atoms adsorb at the surface and the ALD surface adsorption mechanism can be divided into two categories,"physisorption" and "chemisorption" which differs on the basis of bond strength between adsorbing precursor molecule and the reactive surface sites, Figure 2.6.

Chemisorption: Chemisorption is a strong interaction of precursor molecule and substrate surface. A chemisorbed bond is formed between the adsorbed precursor molecule and surface site; thus, only a monolayer of precursor molecules can adsorb at the surface, Figure 2.6 a.

Physisorption: On the other hand, physisorption represents weak bonding of the adsorbed precursor molecules with minimal changes in the molecule structure, Figure 2.6 b. Because of the lack of chemical bond formation between the surface site and precursor molecule, the resultant adsorption can be a multilayer.

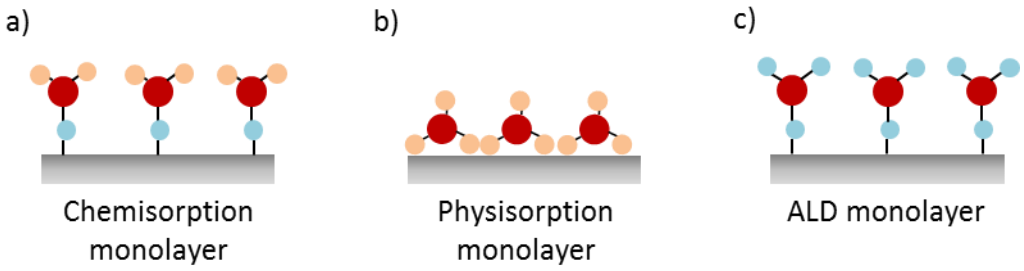

Figure 2.6 a) Chemisorbed monolayer of precursor molecules, b) Physisorbed monolayer at the reactive sites and c) ALD monolayer of material grown on the surface.

An ALD surface adsorption monolayer is different from the ALD layer thickness per cycle. An ALD monolayer is the thickness of material after the four step process. However, for the case of physisorption, a monolayer is an arrangement of precursor molecules in a close-packed array. Conversely, a chemisorbed monolayer is an arrangement of precursor molecules that bond at the surface reactive sites. For an ideal ALD process, chemisorption is the preferred surface adsorption mechanism.

As is evident, surface adsorption plays a critical role in the first step of an ALD process. The reaction mechanism between the precursor molecules and substrate surface can be irreversible or reversible in nature. Usually, chemisorption is either irreversible or reversible and in contrast, physisorption is always reversible. As per the definition, ALD is a self-limiting process, which indicates the molecules adsorbed at the surface should not desorb. Thus, the surface adsorption in ALD is limited to irreversible chemisorption. In ALD self-limiting surface reactions, chemisorption can be described by three mechanisms; ligand exchange, dissociation and association, Figure 2.7. The metal precursor molecule usually contains a metal atom bonded with ligand groups; the number of ligands is evident in the chemical composition. For instance, a molecule with 3 ligands can be represented as ML_3.

Ligand exchange: The first ligand exchange reaction is between the surface reactive site and one of the precursor molecule ligand, which reduced ML_3 to $–ML_2$ or $>ML_1$ (Figure 2.7 a). A metal molecule forms a bond at a surface reactive site while releasing ligand and adsorption site species as byproducts.

Dissociation: The second process chemisorption, i.e. dissociation, does not change the number of metal atoms adsorbed at the surface. In this step, the already released ligand forms a bond with another reactive surface site, Figure 2.7 b. Through this step, the released precursor molecule ligand can cover more than one surface reactive site.

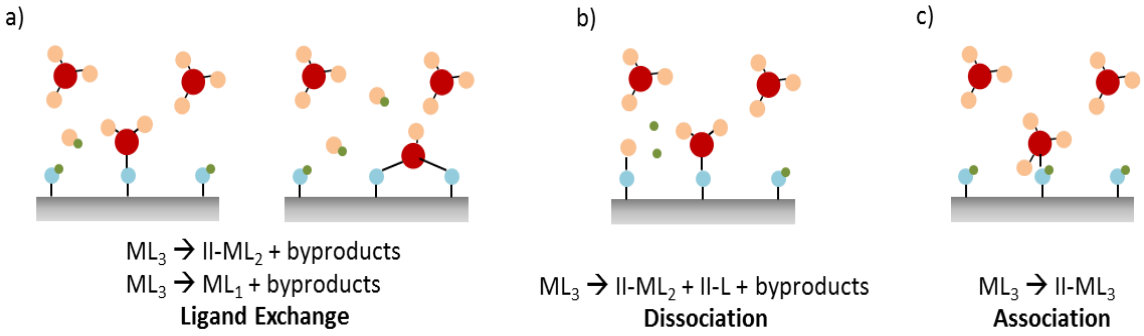

Figure 2.7. ALD chemisorption mechanisms by a) ligand exchange, b) dissociation and c) association.

Association: In case of association, the metal precursor molecule does not release any of the ligands; instead it forms an associated bond with a reaction site, Figure 2.7 c. Similar

to the second process, association does not change the number of metal molecules adsorbed at the surface.

Among the above three chemisorption mechanisms, ligand exchange is preferable for ALD processes. The removal of ligands as byproducts often reduces impurities and carbon concentration in the case of organometallic precursors.

B. Surface Coverage:

Surface coverage is critical to initiate uniform and conformal ALD thin films deposition. In theory, the preferable surface coverage is the chemisorbed precursor molecules in a close packed structure. However, in practice it is next to impossible to control the pattern of precursor molecules at the surface due to the steric hindrance of ligands and the preferred chemisorption at the surface reactive sites. The surface coverage described here is discussed in detail by Puurunen et. al. in references [10] and [48].

Steric Hindrance: Steric hindrance is caused by the ligands bonded to the precursor metal atom, where the ligands cover reactive sites and prevent chemisorption of other precursor molecules. This phenomenon is directly related to the size of the ligands. Large ligands prevent the chemisorption of other precursor molecules on the surface and small ligands can provide full adsorption on the surface reactive sites. In such cases, despite the fact that the surface saturation is regulated by the size of ligands, the surfaces are considered fully covered.

Surface Reactive Sites: The surface bonding sites depends on the substrate material. For the case of metal oxides, hydroxyl groups (–OH) or impurities can act as reaction sites. Some of the materials, such as metals, Si, SiO_2 etc., easily adsorb hydroxyl groups and others, such as the family of carbon materials etc, do not adsorb hydroxyl groups. Surface treatments using plasma or other functional groups can vary the number of surface sites. The surface treatments can be used to either increase or decrease the number of reactive sites. In spite of the empty space on the surface, the precursor molecules cannot adsorb if the surface lacks uniform coverage of reactive sites.

Unlike other deposition techniques, such as MBE, sputtering, and e-beam etc, the ALD growth rate is dependent on the precursor molecule size and on the surface reactive sites concentration. The surface reactive sites concentration also defines the “growth

mode" in ALD which is limited by surface nucleation. The non-uniformity or scarcity of surface reactive sites can lead to the formation islands (Volmer–Weber growth). Presumably, ALD thin films follow a two-dimensional growth (layer-by-layer growth, Frank–van der Merwe growth) which leads to the smooth surfaces. However, two-dimensional growth of a monolayer in ALD is usually less than a monolayer of material thickness. The third possible growth mode in ALD thin film deposition is "random deposition". All three modes are illustrated in Figure 2.8 a - c.

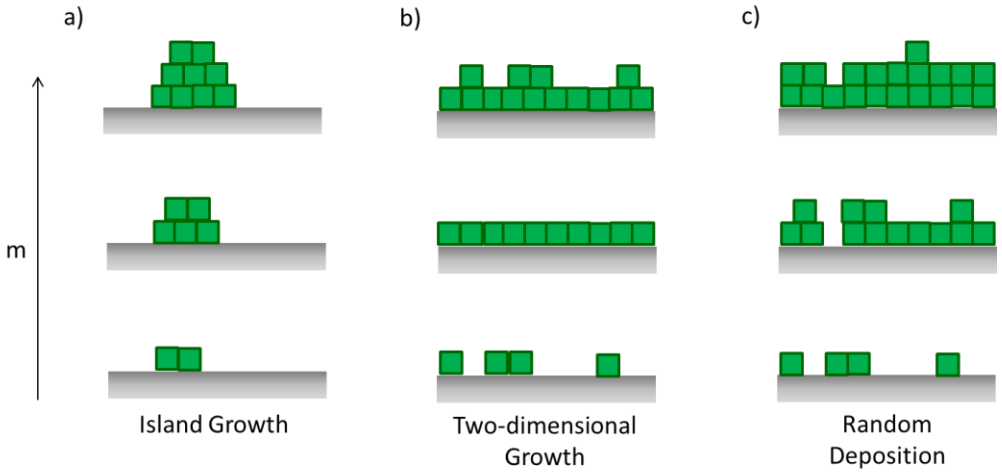

Figure 2.8. Schematic of possible growth mode in ALD with the increase in number of cycles: a) island growth, b) two-dimensional growth and c) random growth.

Island Growth: Island growth is the result of a scarce and non-uniform distribution of surface reactive sites, where with the deposition continues through the chemisorbed precursor molecules. Thus, islands form instead of a uniform thin film, Figure 2.8 a). However, the deposition can become continuous when the islands grow in size and coalesce to form a film.

Two-dimensional Growth: Two-dimensional growth is a layer-by-layer growth mode with the formation of one monolayer of material in each cycle. In spite of the common use of monolayer in ALD and two dimensional growth, the ALD monolayer is different from a monolayer of material. Thus, the ALD deposition process does not occur in monolayers of materials. Nevertheless, the ALD deposition follows the two-dimensional growth on uniformly distributed surface reactive sites.

Random Growth: Random Growth defines the chemisorption of precursor molecules, with equal probability to the available reactive sites. The self-terminating nature of ALD surface reactions results in uniform and smooth films. Random growth can be explained using two further depositions models, i.e. the shower model and the rain model, where the rain model describes the continuous deposition and the shower model describes the ALD growth. In rain model, the molecules stick to the surface where they first hit and there is no surface diffusion. In the shower model, random deposition is defined as a shower of precursor molecules on the surface which involves self-termination reactions and faster layer closure. The later leads to the growth of low roughness films compared to the rain model.

The ALD growth mode for the first monolayer varies with the surface reactive site density which is determined by the substrate top surface. It is likely that the reactive site density will change with the increase in number of cycles. For example, the initial island growth could change to uniform thin layer formation with an increase in the number of cycles. Figure 2.9 shows a TEM image of Al_2O_3 islands reconstruction into uniform thin film as the number of ALD cycles increase from 15 to 30.

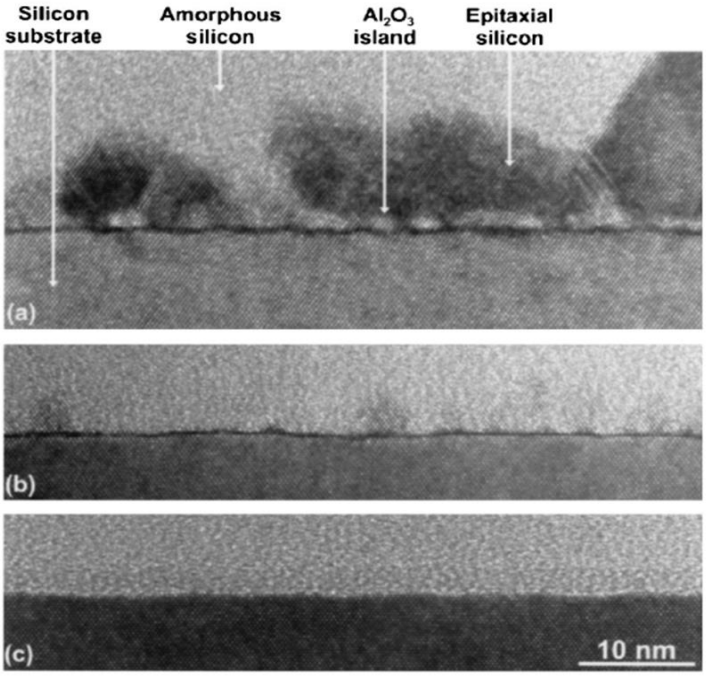

Figure 2.9. TEM cross-sectional image of thermal ALD Al_2O_3 covered with SiO_2 after a) 15 cycles, b) 20 cycles and c) 30 cycles [47].

C. Growth Rate:

In the ALD growth model, the deposition is described by the materials as growth per cycle (GPC). It is assumed that the ALD GPC should remain constant and the thickness should show a linear increase with the number of cycles. However, the GPC can change as the ALD initial growth may be surface coverage limited. In some cases, the initial cycles have lower or higher GPC before the GPC becomes constant. The variation in GPC with the number of ALD cycles is discussed in the following:

Linear Growth Rate: To obtain a linear growth rate the number of cycles, two conditions play important roles. First, the concentration of reactive sites remains constant with the increase in number of cycles. Second, the steric hindrance conditions are the same in each cycle, i.e. the number of ligands per adsorbed precursor molecule are the same.

Surface Enhanced Growth Rate: In surface enhanced growth rate, the GPC is higher initially and becomes constant in the steady state regime. The higher growth rate corresponds to a higher density of reactive sites on the surface.

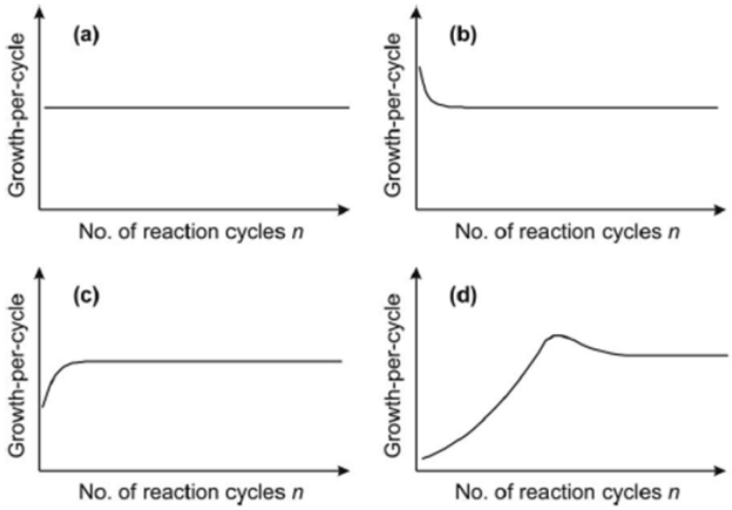

Figure 2.10. ALD growth rate per cycle (GPC) with the increase in number of cycles shows a) linear growth, b) surface enhanced growth, and surface inhibited growth c) type 1 and d) type 2) [10].

Surface Inhibited Growth Rate: In surface inhibited growth rate, the growth rate is lower in the beginning than in the steady state regime. Opposite to surface enhanced growth rate, a lower concentration of reactive sites results in the lower GPC. This behavior is commonly described as type 1 surface inhibited growth rate. In type 2 surface inhibited

growth rate, the GPC increases with the increase in number of cycles in the beginning and reaches maximum before it decreases and becomes constant in the steady state regime.

The growth rate in all ALD processes is also temperature dependent. The range of temperature, where the constant GPC is viable, is called the "ALD Growth Window", Figure 2.11. This is an important term in ALD processes which is related to self-limited growth. The growth rate may be either higher or lower, below and above the growth window depending on specific surface processes. Usually, the processing temperature is selected in between the growth window. Temperature is an important parameter to determine the concentration and type of species adsorbed on the surface and also to inhibit the surface reactions. The reactive sites concentration can also be affected with the variation in temperature. The usual behavior of GPC with temperature is discussed as following:

Decrease in GPC: A decrease in GPC is observed either below or above the growth window temperature. At high temperatures, the GPC is reduced due to a reduction in the density of reactive sites and desorption of precursor molecules. However, at low temperatures, a decrease in GPC is an indication of incomplete reactions, where the thermal energy is lower than the amount of energy required to initiate chemical reactions between the reactive sites and precursor ligands, Figure 2.11.

Increase in GPC: An increase in GPC at low temperature may be due to precursor condensation at the surface. On the other hand, at high temperature, the precursor molecules decompose and initiate unwanted chemical reactions, thus the GPC increases but impurities may be incorporated in the films.

Constant GPC: A constant GPC is a result of uniform reactive site density and self-limiting reactions. In the constant GPC temperature range, the surface reactive site density remains unaffected and the thermal energy is sufficient to drive the surface reaction without causing surface desorption and precursor decomposition.

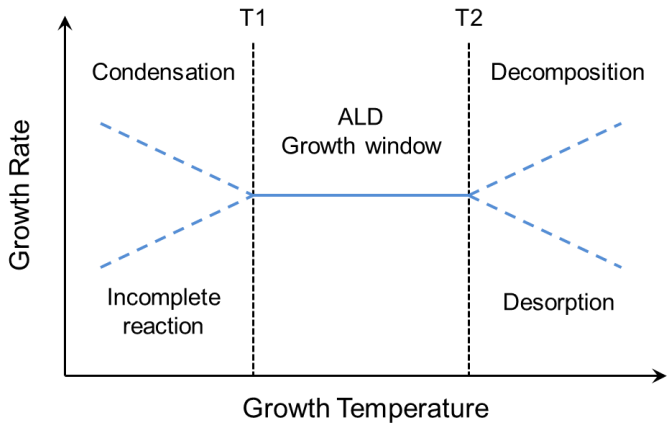

Figure 2.11. Growth rate vs growth temperature plot determines constant growth rate temperature range called "ALD growth window".

D. Effect of Plasma on the Growth Rate:

The observation of an enhanced growth rate with PEALD has been attributed to high reactivity of the plasma species and active oxygen that remains on the surface after the O_2 plasma step. Two plasma mechanisms that contribute to the enhanced growth rate are: (i) due to high reactivity of oxygen species [20], and (ii) increase in reactive sites due to surface active oxygen [49-52]. Remaining active oxygen on the surface may replace the ligands during the precursor pule, which forms additional adsorption sites for the incoming precursor molecules. In addition, the ligand replacement during the precursor pulse also helps to reduce the steric hindrance and expose additional reactive sites for

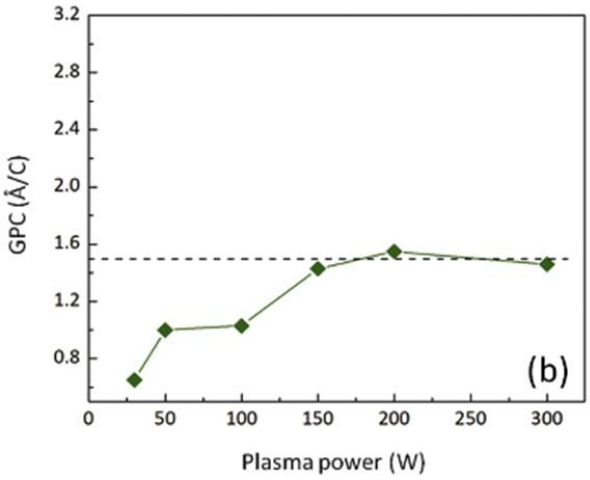

Figure 2.12. Al_2O_3 growth rate per cycle vs remote plasma power [53].

chemisorption [51]. The increase in adsorption sites for in O_2 plasma is similar, and possibly higher than the increase found using ozone assisted growth [54].

We have studied the PEALD growth of Al_2O_3 using DMAI and remote oxygen plasma. The GPC achieved in our studies is higher (30% - 80%) than thermal ALD Al_2O_3 using DMAI [53]. The increase in growth rate with increase in plasma power also corroborates the above hypothesis, Figure 2.12. Other studies, Lim *et. al.* and Koo *et. al.* have also shown a higher growth rate for PEALD Al_2O_3 using trimethyl(aluminum) (TMA) precursor [55, 56].

AFM was used to characterize the surface roughness for PEALD Al_2O_3 films deposited at 200 ºC and 25 ºC, respectively to analyze the effect of the increased growth rate on the surface morphology. Figure 2.13 shows the AFM scans of the Si substrate before Al_2O_3 deposition [Figure 2.13 a] and after 6 nm and 33 nm Al_2O_3 [Figure 2.13 b] and [Figure 2.13 c)], respectively. It is evident from AFM RMS that the increased growth rate does not impact the uniformity or conformity of PEALD films.

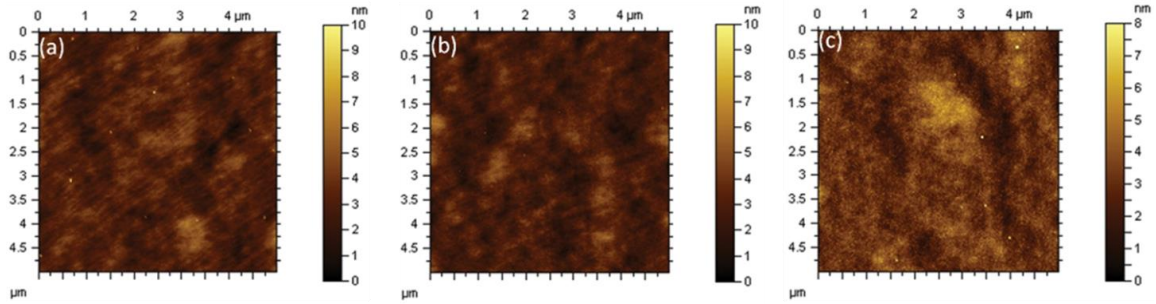

Figure 2.13. AFM image (5 µm x 5 µm) of a) Si substrate, b) as grown 6 nm PEALD Al_2O_3 at 200 ºC and c) as grown 33 nm PEALD Al_2O_3 at 25 ºC. The RMS roughnesses are ~0.77±0.05 nm, ~0.76±0.05 nm and ~0.86±0.05 nm, respectively [53].

VI. PEALD of Materials Used in this Research:

A. Aluminum Oxide using DMAI:

The following brief results for PEALD Al2O3 using DMAI have been published by Jialing Yang, Brianna S. Eller, Manpuneet Kaur, and Robert J. Nemanich in the Journal of Vacuum Science and Technology A.

Trimethyl(aluminum) (TMA) is extensively used precursor for thermal ALD Al_2O_3 [10, 60] . The binary reaction of TMA and water are well understood. Dimethyl aluminum isopropoxide (DMAI) has seldom been used in thermal ALD possibly because

of the unreliable results of PEALD growth rate using, the bonding configurations of Al atoms on the surface and the carbon content in the films [53, 55]. However, the non-pyrophoric nature of DMAI makes it a safe alternative to pyrophoric TMA. Langereis and Potts *et. al*. have reported possible DMAI surface adsorption and reaction with O_2 plasma as following [57, 53]:

$\|^{-}$ OH (ads) + ½ $[(CH_3)_2AlOCH(CH_3)_2]_2$ (g) → $\|^{-}$ $OAl(CH_3)OCH(CH_3)_2$ (ads) + CH_4(g)

$\|^{-}$ $OAl(CH_3)OCH(CH_3)_2$ (ads) + $9O^*$ (g) → $\|^{-}$ Al(OH) (ads) + $3CO_2$ (g) + $3H_2O$ (g)

And /or

$\|^{-}$ OH (ads) + ½ $[(CH_3)_2AlOCH(CH_3)_2]_2$ (g) → $\|^{-}$ $OAl(CH_3)_2$ (ads) + $HOCH(CH_3)_2$ (g)

$\|^{-}$ $OAl(CH_3)_2$ (ads) + $4O^*$ (g) → $\|^{-}$ Al(OH) (ads) + CO_2 (g) + H_2O (g)

The above both reactions suggest that after one complete ALD cycle the surface is terminated by hydroxyl (–OH) group and accessible for the chemisorption of DMAI molecules for the next cycle.

Results and Discussion:

1. *Growth window and Self-limiting growth:*

The self-limiting growth of Al_2O_3 was ensured with the optimized PEALD growth window, and DMAI dosing time and O_2 plasma time at 200 ℃ which is within the growth window. Figure 2.14 shows the growth window of DMAI to deposit Al_2O_3. The 20 nm of Al_2O_3 films were deposited on Si substrate in the temperature range of RT to 320 ℃ and characterized using RBS and XRR to measure the thickness. The constant growth rate (~1.5 Å/cycle) was obtained for the films grown from RT to 220 ℃. Our experimental growth rate is slightly higher than the reported growth rate, i.e. 1.0-1.2 Å/cycle, for DMAI. The discrepancies are related to the remaining active oxygen on the surface as discussed above. An inset Figure 2.14 shows the linear increase in the Al_2O_3 thickness with the increase in number of cycles at 200 ℃ which implies the growth rate is consistent throughout the thickness. The slight decrease in the growth rate at RT is most likely due to incomplete reaction as the growth rate increases with the increase in plasma exposure time. This behavior indicates the RT thermal energy was not sufficient

to complete the chemisorption reaction. The increase in the growth rate above 220 °C is attributed to precursor decomposition as discussed earlier in the ALD growth window.

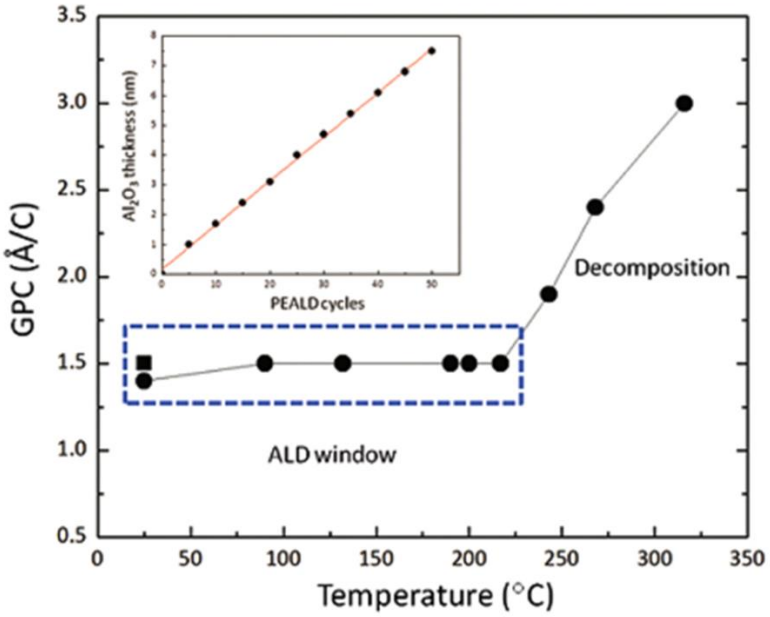

Figure 2.14. Al_2O_3 growth rate per cycle vs deposition temperature represents the PEALD growth window. A square indicates the increased growth rate at RT with the oxygen exposure time. The inset shows the increase in Al_2O_3 thickness with increase in number of deposition cycles [53].

To determine the growth window, the optimized parameters such as O_2 plasma, precursor dose and N_2 purge time of 8 sec, 0.6 sec and 40 sec were used. The selected parameters are above the experimental given numbers. As shown in the Figure 2.15, the Al_2O_3 growth rate saturates for O_2 plasma pulse of ≥6s, precursor dose of ≥0.2s and N_2 purge of ≥18s at 200 °C.

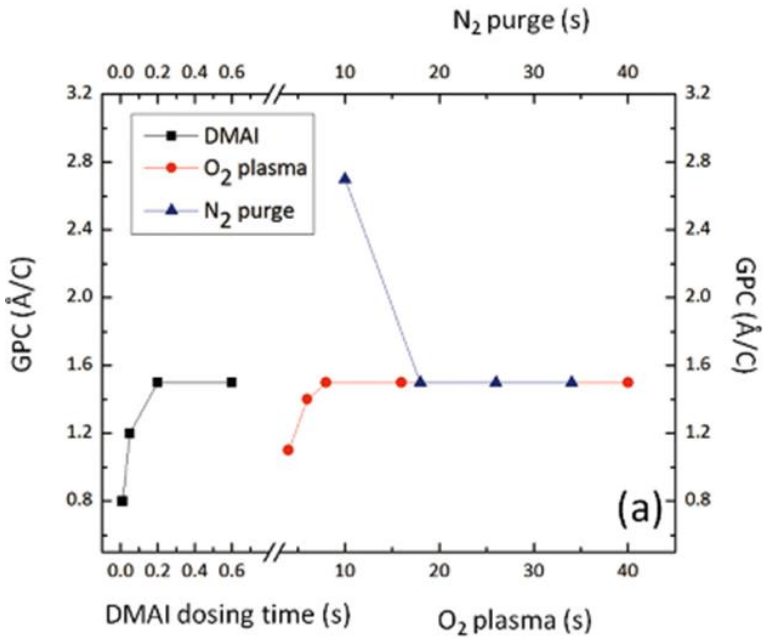

Figure 2.15. Al_2O_3 growth rate per cycle vs DMAI dose time, O_2 plasma time and N_2 purge time [53].

2. Al_2O_3 composition:

The Al_2O_3 thin film composition, such as Al atoms per cycle and mass density ratio were determined using RBS and XRR, respectively. Despite the RBS determined Al atoms per cycle at RT (3.9±0.2 atoms nm^{-2} $cycle^{-1}$) were ~26% less than at 220 °C (5.3±0.2 atoms nm^{-2} $cycle^{-1}$), the growth rates at both temperatures are similar. The density of Al_2O_3 deposited at RT (~2.7 g/cm^3) was also ~10% lower as compared to 220 °C (~3.0 g/cm^3); however, the O:Al ratio was higher at RT (2.1) than 220 °C (1.6). Consequently, the high concentration of O at low temperature deposition compensates for the lower Al concentration. The important results of Al_2O_3 deposited at room temperature (25 °C) and (200 °C) are summarized in Table 2.2.

Table 2.2: Al_2O_3 film properties on Si substrates grown by remote PEALD and DMAI at 25 °C and 200 °C [53].

PEALD	RT (25 °C)	200 °C
Growth per cycle	1.5 A/cycle	1.5 A/cycle
Al atoms per cycle^{-1}	3.9 ± 0.2 atoms nm^{-2} cycle^{-1}	15.3 ± 0.2 atoms nm^{-2} cycle^{-1}
Mass density	2.69 ± 0.04 g/cm^{-3}	2.96 ± 0.02 g/cm^{-3}
O/Al ratio	2.1 ± 0.1	1.6 ± 0.1
Refractive index (630 nm)	1.61 ± 0.01	1.63 ± 0.02
Band gap	6.9 ± 0.1 eV	6.7 ± 0.1 eV
Electron affinity	--	2.2 ± 0.1 eV

B. Silicon Oxide using TDMAD:

The SiO_2 deposition recipe using PEALD was developed by Dr. Brianna Eller in our group.

Despite its potential, the ALD of SiO_2 has challenging due to the low reactivity of Si precursors with H_2O at lower temperatures. Some techniques have been developed to enhance the reactivity, such as using high temperatures (>300°C), long reactant exposure times [27-29], or using pyridine and Al as catalyst [30-32]. High reactivity of oxygen plasma in PEALD is promising alternate to enhance the reactivity of precursors. A number of precursors including BDEAS (SiH2(NEt2)2) and TEOS ($Si(OEt)_4$) have been used to deposit PEALD SiO_2. However, high dosing time was required for low temperature deposition [1, 62]. For PEALD SiO_2 deposition in this research, tris(dimethylamino)silane (TDMAS) was explored and used which has high reactivity with H_2O_2 [58].

1. Experiment:

In this study, TDMAS was used to deposit SiO_2 on Si surfaces in PEALD chamber. The background pressure of chamber is ~$3.0x10^{-8}$ Torr. During deposition, oxygen plasma was ignited with 13.56 MHz rf-excitation applied at 200 W. The oxygen flow was maintained at 100 mTorr with a flow rate of 35 sccm. The precursor temperature was maintained at 33°C, and the pipelines between the bubbler and the chamber were heated to ~40°C to prevent precursor condensation. The pulse time of the TDMS was 1.6 sec, N2 purge gas was 40 sec and O_2 plasma was 8 sec. The SiO_2 was deposited at room temperature.

2. Results and Discussion:

The GPC as a function of timing sequence was modified for the precursor, oxygen plasma, and nitrogen purge for room temperature depositions. The deposition process demonstrated that the saturated growth rate was achieved with a precursor pulse time >1.6 sec and an O_2 plasma pulse time >16 sec. In addition, the nitrogen purge time of >30 sec ensured the removal of residual reactants, Figure 2.16. The relationship of growth rate with temperature was also investigated under saturation conditions. The results are shown in Figure 2.17, where the films were deposited using a precursor pulse time of 1.6 sec, oxygen plasma time of 8 sec, and nitrogen purge time of 30 s. It is evident from Figure 2.17 that the largest growth rate of 1.25Å/cycle was obtained at lower substrate temperatures. However, the growth window was not well defined. Increase in temperature resulted in a decrease of growth rate for temperatures <450°C. At higher temperatures, the dramatic increase of growth rate corresponds to the thermal decomposition of TDMAS. Thus the growth cannot be considered self-limiting.

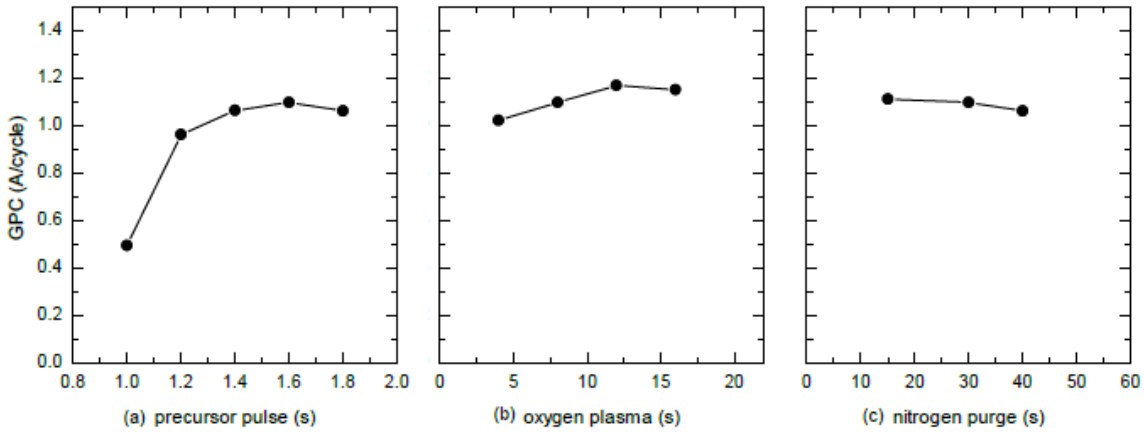

Figure 2.16. Growth rate per cycle (GPC) of ALD SiO_2 as a function of a) TDMAS, b) oxygen plasma time, and c) nitrogen purge time at 30 °C. The timing for each respective gas phase was 1.6 sec, 16 sec and 30 sec when not specified otherwise.

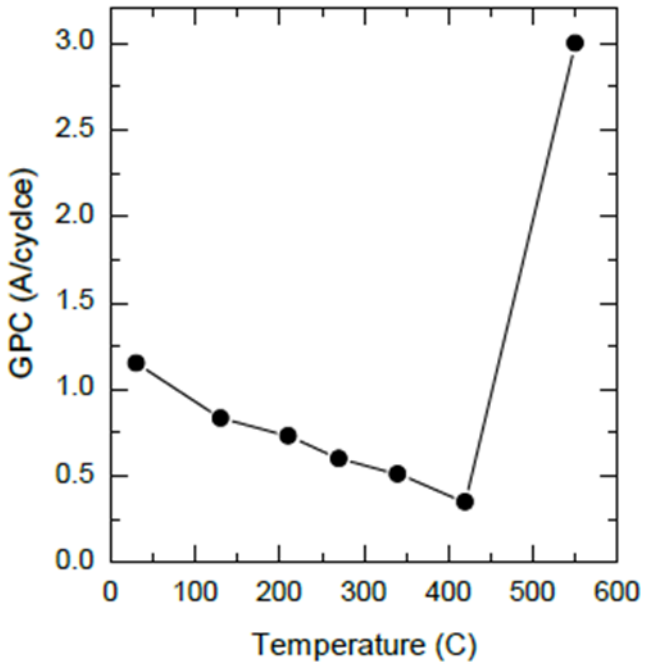

Figure 2.17. The growth rate per cycle (GPC) of PEALD SiO_2 at substrate temperatures varying from 30 to 550 °C with precursor pulse time of 1.6 sec, O_2 plasma time of 16 sec, and nitrogen purge time of 30 sec.

Table 2.3: SiO_2 content and deposition characteristics determined as by RBS and XPS. (Thickness measurements were confirmed with XRR; however, the sample deposited at 550°C did not provide reliable results, most likely due to contamination in the film.

Deposition Temperature (°C)	Growth Rate (Å/cycle)	Si:O ratio	Contamination (% conc.)
30	1.1	1:2	undetectable
270	0.6	1:2	undetectable
550	~3.0	1:2	~2% molybdenum ~2% nitrogen

In addition to the self-limiting and saturation experiments and characterizations, some measurements were conducted at three different temperatures (30 °C, 270 °C and 550 °C). Thick SiO2 layers were deposited for Rutherford backscattering (RBS) and x-ray reflectivity measurements (XRR) measurements. The results are summarized in Table 2.3. The temperature did not affect the stoichiometry or density of the films. However,

there was an increase in contamination for the thermally decomposed film, where small concentrations of nitrogen from the precursor and molybdenum from the sample holder were detected.

C. Zinc Oxide using DMZ:

1. Experiment:

A custom chamber with a base pressure of $5x10^{-8}$ Torr was used for PEALD ZnO deposition. The pressure during deposition is set to 100 mTorr using throttle valve between the chamber and the turbo pump. Because of the high vapor pressure of DMZ (5 x 10^2 Torr at 20 °C) it was necessary to cool the source using a chiller filled with ethylene glycol to -18 °C. Ar gas was used as a carrier gas with a flow rate of 50 standard cubic centimeters per minute (sccm) to transport DMZ from the bubbler to the chamber. The chamber walls were heated to 100 °C to avoid condensation of the precursor on the chamber walls. To ignite the remote O_2 plasma, 35 sccm ultrahigh purity grade O_2 gas flowed through the glass tube, positioned ~25 cm above the sample surface. The glass tube is inductively coupled with an rf-source at a power of 200 W and frequency of 13.56 MHz. The large distance from the oxygen plasma source to the sample act as a remote plasma and thus reduces the direct bombardment of substrate surface with oxygen ions and excited species. N_2 (research grade) purge gas flow of 50 sccm was used to separate the DMZ precursor and O_2 plasma pulse to avoid chemical vapor deposition (CVD) like reactions.

The p-Si substrates were cleaned ultrasonically for 10 min in acetone followed by 10 min in methanol to remove the hydrocarbons and exposed to an O_2 plasma for 8 sec to remove carbon and to prepare the surface for precursor chemisorption. The saturated surface termination with DMZ molecules and self-limiting growth of ZnO was ensured using different DMZ pulse times, O_2 plasma times and N_2 purge times. The ALD growth window of ZnO was ascertained doing the deposition from RT (25 °C) to 220 °C.

AFM was used to characterize the topography of nanocrystalline ZnO thin films. The density of the ZnO films was determined using x-ray reflectivity (XRR) to calculate the thickness from Rutherford backscattering (RBS). The film thickness was also confirmed with XRR values. X-ray diffraction (XRD) was used to characterize the crystal

structure vs deposition temperature. RBS measurements characterized the Zn and O composition in the ZnO films deposited at different temperatures. The film thicknesses were also calculated using XPS for thin films (< 5 nm), and the studies also corroborated the chemical states of the ZnO.

2. Results and Discussion:

Self-limiting growth and growth window of PEALD ZnO:

Self-limiting growth is the property of ALD that differentiates it from chemical vapor deposition (CVD), which makes it crucial to ensure self-limiting growth by varying the precursor pulse, N_2 purge and O_2 plasma pulse time. The precursor pulse time for saturated deposition was determined using different pulse times at 100 °C, which is within the growth window of PEALD DMZ ZnO. The following parameters were used for ZnO deposition: the precursor pulse time of 0.35 sec, N_2 purge time of 30 sec and O_2 plasma time of 8 sec, as the saturated ZnO growth rate is observed at these parameters, Figure 2.18. The O_2 plasma was excited with 200 W since the growth rate saturated at a plasma power $\geq$ 200 W. The self-limiting growth rate was confirmed with the linear increase in the film thickness with an increase in the number of cycles, measured using XPS for thin films and RBS and XRR for thick films, Figure 2.18.

The saturation of precursor chemisorption on the substrate surface during the first pulse is surface adsorption sites dependent, which can make the initial growth rate different for different substrates. The surface treatments, such as oxygen or hydrogen plasma, can be used to enhance surface adsorption sites. The Si substrate provides moderate growth rate for most of the precursors due to fast adsorption of oxygen and hydrogen on the surface that act as precursor adsorption sites. The thickness of ZnO thin films and thus the GPC was measured *in situ* using the Zn and Si XPS core level peak intensities. The relative increase of the Zn peak intensity and decrease of the Si peak intensity was used to calculate the thickness of the thin films. The XRR on ~20 nm ZnO and RBS data of thick films (~80 nm) was also used to calibrate the thickness measurements from XPS core level intensities. The observed ZnO growth rate within the growth window (85 °C and 180 °C) is ~2.1 Å/cycle, Figure 2.18. The growth window of

ZnO using standard plasma (200 W, 100 mTorr and 8 sec) and precursor pulse (0.35 sec) parameters is from 85 °C to 180 °C.

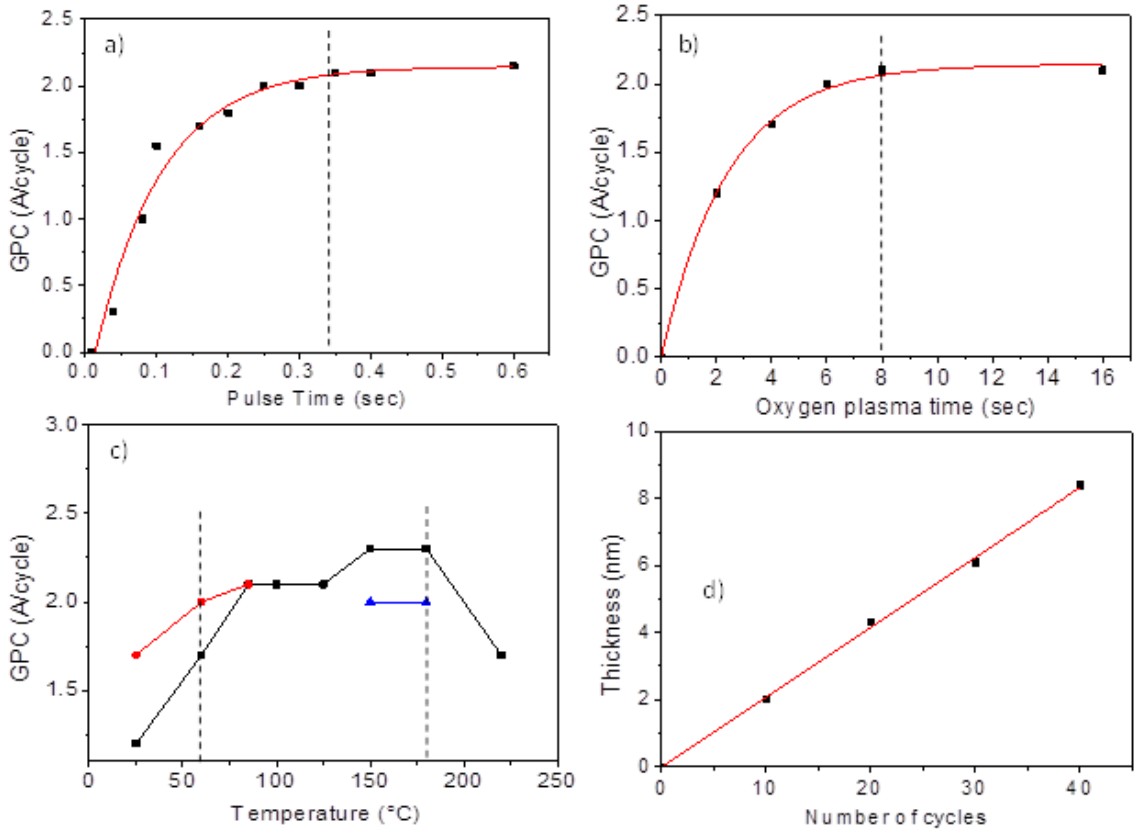

Figure 2.18. The deposition parameters of PEALD ZnO deposition using DMZ precursor are indicated. The saturated GPC at 100 ^{0}C a); saturated oxygen plasma time at 100 ^{0}C b); growth window of DMZ using oxygen plasma at standard deposition condition (black), the increase in growth rate with the increase precursor pulse time at RT and 60 ^{0}C and the decrease in growth rate with reduced oxygen plasma power (100W) at 150 ^{0}C and 180 ^{0}C (blue) c); and the linear increase in the thickness of ZnO film with the increase in number of cycles d).

As reported by Rowellete *et al.*, the DMZ precursor is inert with O_2 gas from 25 °C to 125 °C and the same was determined from our experiments [59]. The growth rate of ZnO is constant from 85 °C to 180 °C and comparatively lower below 85 °C and above 180 °C. An increase or decrease in the ALD growth rate above the growth window is usually ascribed to the decomposition or desorption of the precursor, respectively. Barnes *et al.* has studied the decomposition and desorption of DMZ and have shown

DMZ can desorb in the temperature range, ≥130 °C and ≤ 325 °C [59, 60]. The lower growth rate observed at temperatures above 180 °C, apparently signifies desorption of DMZ molecules. Conversely, desorption was not observed up to 180 °C. On the other hand, the lower growth rate below the growth window corresponds either to incomplete precursor chemisorption or to an incomplete oxidation reaction due to nsufficient thermal energy. Two experiments were performed to understand the surface reactions below the ZnO growth window; the first experiment was to increase the DMZ pulse time from 0.35 sec to 0.7 sec and the second was to increase the oxygen plasma time from 8 sec to 40 sec; the N_2 purge time was increased to 50 sec to prevent CVD like deposition. The increase in pulse time from 0.35 to 0.7 sec at 60 °C increases the GPC from 1.7 Å/cycle to 2.0 Å/cycle (Figure 2.18 c), which implies unsaturated chemisorption of DMZ molecules caused the low GPC. The ZnO growth rate was unaffected with an increase in oxygen plasma time. Above the growth window (at 150 °C and 180 °C), using standard deposition parameters, a slight increase in the GPC (from 2.1 Å/cycle to 2.4 Å/cycle) was observed. The GPC was reduced from 2.4 Å/cycle to 2.0 Å/cycle with oxygen plasma power of 100 W, i.e. half of the standard oxygen plasma power. This implies the high GPC was possibly due to an increase in thermal energy that increased the reaction rate of adsorbed oxygen plasma species with DMZ molecules. The tweaking in deposition parameters widens the growth window (60 °C – 180 °C) as compared to the standard deposition conditions.

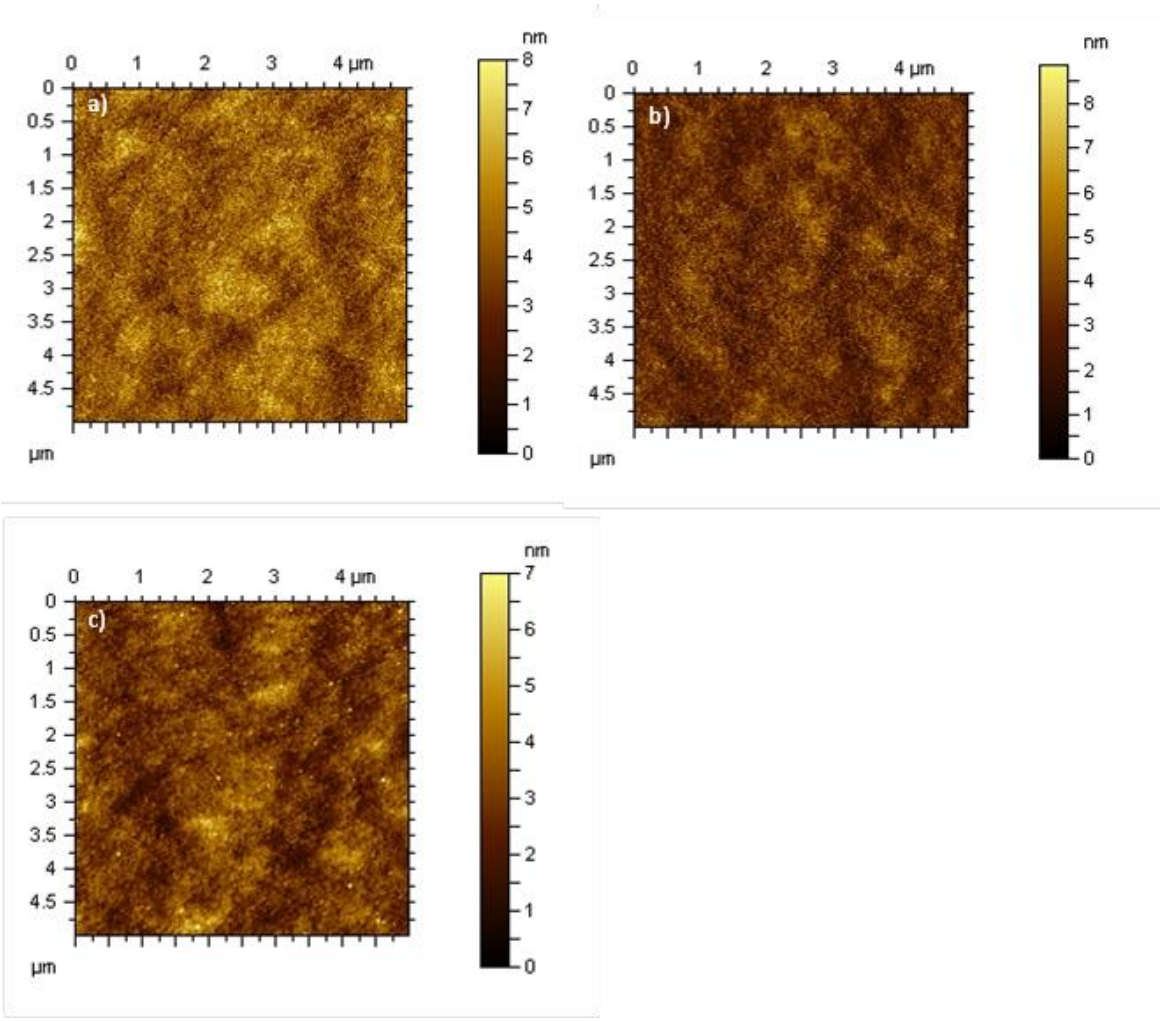

Figure 2.19. The AFM scans show the surface topography of ZnO 20 nm films deposited at a) 85 ^{0}C, b) 100 ^{0}C and c) 125 ^{0}C. The roughness for all the surfaces is measured as ~0.9 nm, irrespective of deposition temperature.

RBS data shows, the Zn:O atomic ratio was 1:1 irrespective of the deposition temperature within the growth window. It is evident from AFM imges, the ZnO deposition using DMZ and oxygen plasma source is conformal and uniform; the roughness for 20 nm thick films deposited within the growth window, irrespective of the deposition temperature, is ~ 0.9 nm (Figure 2.19).

Crystal structure of PEALD ZnO:

The crystal structure of ZnO is very sensitive to temperature, unlike Zn:O ratio and roughness, and varies from a-axis dominated orientation to c-axis orientation with the

variation in deposition temperature from 85 °C to 180 °C. As shown in Figure 2.20, the crystal structure of ZnO films has highest (2 -1 -1 0) peak at 85 °C; the orientation is mixed (a-axis and c-axis perpendicular to the plane) at 100 °C but c-axis growth begins to dominate over a-axis growth; the c-axis orientation dominates at 125 °C; and the well-oriented (0 0 0 2) films are deposited with the further increase in temperature i.e. at 180 °C. The crystal orientation, oxygen vacancies and impurities are considered to control the mobility and carrier concentrations.

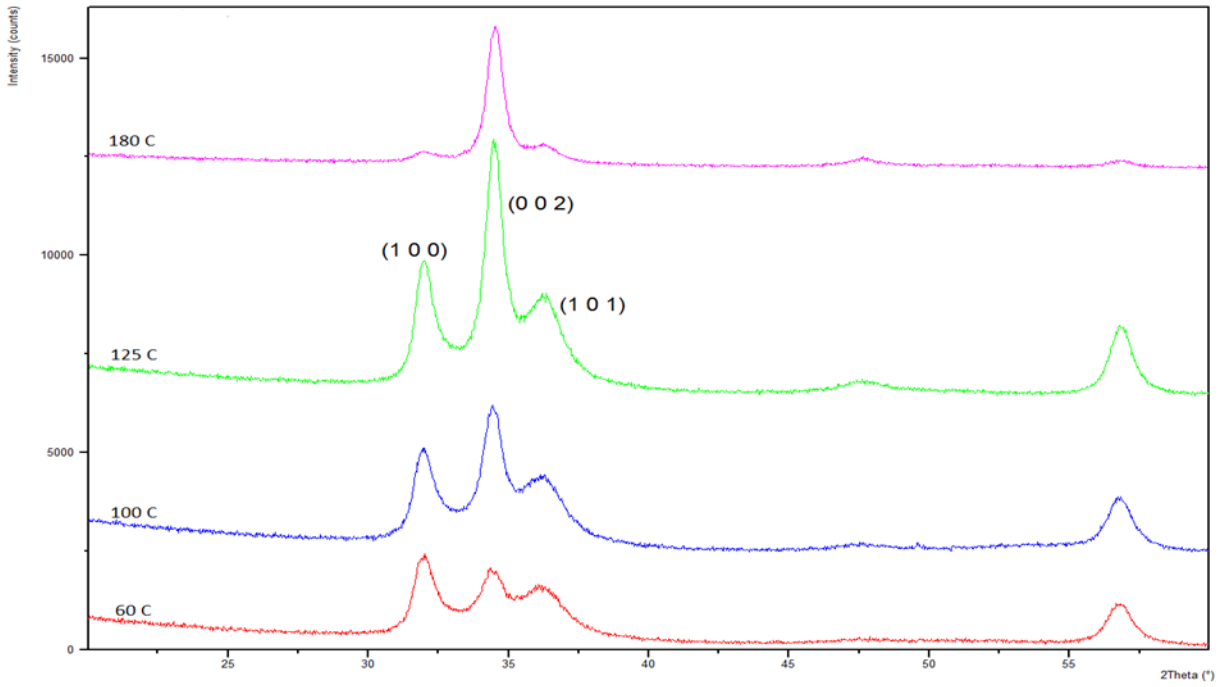

Figure 2.20. The grazing angle (ω = 0.5 degree) XRD scans of 20 nm ZnO deposited a) 85 ^{0}C, b) 100 ^{0}C, c) 125 ^{0}C and 180 ^{0}C. The change in crystal structure from mixed a-axis and c-axis orientation to c-axis orientation.

References:

[1] S. M. George, "Atomic Layer Deposition: An Overview" *Chem. Rev.* 110 (2010) 111–131

[2] T. Suntola, and J. Antson, U. S. Patent No. 4,058,43015 November, 3 1977.

[3] A. M. Shevjakov, G. N. Kuznetsova, and V. B. Aleskovskii, in Chemistry of High-Temperature Materials, Proceedings of the Second USSR Conference on High-Temperature Chemistry of Oxides, Leningrad, USSR, 26–29 November 1965 (Nauka, Leningrad, USSR, 1967), pp. 2 149–155, in Russian.

[4] T. Suntola, and J. Antson, U. S. Patent No. 4,058,43015 November, 3 1977.

[5] T. S. Suntola, A. J. Pakkala, and S. G. Lindfors, U.S. Patent No. 4,389,973 28 June 1983.

[6] T. S. Suntola, A. J. Pakkala, and S. G. Lindfors, U.S. Patent No. 4,413,022 1 November 1983.

[7] M. Leskel and M. Ritala, "Atomic Layer Deposition Chemistry: Recent Developments and Future Challenges" *Electronic Materials Angew. Chem. Int. Ed*. **42** (2003) 5548 –5554

[8] H. Kim, "Atomic layer deposition of metal and nitride thin films: Current research efforts and applications for semiconductor device processing" *J. Vac. Sci. Technol.* **B 21** 2003 1071

[9] V. Miikkulainen, M. Leskelä, M. Ritala, and R. L. Puurunen, "Crystallinity of inorganic films grown by atomic layer deposition: Overview and general trends" *Journal of Applied Physics* **113** (2013) 02130.

[10] R. L. Puurunena, "Surface chemistry of atomic layer deposition: A case study for the trimethylaluminum/water process" *J. Appl. Phys.* **97** (2005) 121301.

[11] N. P. Dasgupta, X. Meng, J. W. Elam, and A. B. F. Martinson, "Atomic Layer Deposition of Metal Sulfide Materials" *Acc. Chem. Res.* **48** (2015) 341−348.

[12] J. Hamalainen, M. Ritala, and M. Leskela, "Atomic Layer Deposition of Noble Metals and Their Oxides" *Chem. Mater.* **26 (**2014) 786−801.

[13] T. Tynell and M. Karppinen, "Atomic layer deposition of ZnO: a review" *Semicond. Sci. Technol.* **29** (2014) 043001.

[14] M. Knez, K. Nielsch, and L. Niinisto "Synthesis and Surface Engineering of Complex Nanostructures by Atomic Layer Deposition" *Adv. Mater.* **19** (2007) 3425–3438.

[15] H. Kim, H. Lee, W.J. Maeng, "Applications of atomic layer deposition to nanofabrication and emerging nanodevices", *Thin Solid Films* **517** (2009) 2563–2580.

[16] C. Detavernier, J. Dendooven, S. Pulinthanathu Sree, K. F. Ludwig and J. A. Martens, "Tailoring nanoporous materials by atomic layer deposition" *Chem. Soc. Rev.*, **40** (2011) 5242–5253.

[17] J. R. Bakke, K. L. Pickrahn, T. P. Brennan and S. F. Bent, "Nanoengineering and interfacial engineering of photovoltaics by atomic layer Deposition" *Nanoscale* **3** (2011) 3482–3508.

[18] J. Borges, and J. F. Mano, "Molecular Interactions Driving the Layer-by-Layer Assembly of Multilayers" *Advan. Func. Mater.* **114** (2014) 8883.

[19] Q. Peng, J. S. Lewis, P. G. Hoertz, J. T. Glass, and G. N. Parsons, "Atomic layer deposition for electrochemical energy generation and storage systems" *J. Vac. Sci. Technol.* **A 30 (**2012) 1

[20] D. M. King, X. Liang, A. W. Weimer, "Functionalization of fine particles using atomic and molecular layer deposition" *Powder Technology* **221 (**2012) 13–25.

[21] T. Singh, T. Lehnen, T. Leuning, and S. Mathur, "Atomic layer deposition grown MOx thin films for solar water splitting: Prospects and Challenges" *J. Vac. Sci. Technol.* **A 33 (**2015) 1.

[22] T. Wang, Z. Luo, C. Li and J. Gong, "Controllable fabrication of nanostructured materials for photoelectrochemical water splitting via atomic layer deposition" *Chem. Soc. Rev.* **43** (2014) 7469.

[23] X. Jiang and S. F. Bent, "Area-Selective ALD with Soft Lithographic Methods: Using Self-Assembled Monolayers to Direct Film Deposition" *J. Phys. Chem. C* 2009, *113,* 17613–17625.

[24] A. J. M. Mackus, A. A. Bol and W. M. M. Kessels, "The use of atomic layer deposition in advanced Nanopatterning" *Nanoscale* **6** (2014) 10941–10960.

[25] H. C. M. Knoops, M. E. Donders, M. C. M. van de Sanden, P. H. L. Notten, and W. M. M. Kessels, "Atomic layer deposition for nanostructured Li-ion batteries" *J. Vac. Sci. Technol*. **A 30** (2012) 1.

[26] J. Liu and X. Sun, "Elegant design of electrode and electrode/electrolyte interface in lithium-ion batteries by atomic layer deposition" *Nanotechnology* **26** (2015) 024001.

[27] S. M. George, A. W. Ott, and J. W. Klaus, "Surface chemistry for atomic layer growth Source" *J. Phys. Chem.* 100, 13121 (1996).

[28] C. H. L. Goodman and M. V. Pessa, “Title Atomic Layer Epitaxy” J. *Appl. Phys.* **60** (1986) R65.

[29] M. Leskela and M. Ritala, “ALD precursor chemistry: Evolution and future challenges” *J. Phys. IV* **9** (1999) Pr8/837.

[30] M. Leskela and M. Ritala, “Atomic layer deposition (ALD): from precursors to thin film structures” *Thin Solid Films* **409** (2002) 138.

[31] L. Niinisto, M. Ritala, and M. Leskela, “Synthesis of oxide thin films and overlayers by atomic layer epitaxy for advanced applications” *Mater. Sci. Eng. B* **41** (1996) 23.

[32] M. Ritala and M. Leskela, “Atomic layer epitaxy - a valuable tool for nanotechnology?” *Nanotechnology* **10** (1999) 19.

[33] T. Suntola, “Atomic Layer Epitaxy” *Acta Polytechnica Scandinavica-Electrical Engineering Series* **64** (1989) 242-270

[34] S. Haukka, E. L. Lakooma, and T. Suntola, “Adsorption controlled preparation of heterogeneous catalysts” *Stud. Surf. Sci. Catal*. **120A** (1999) 715.

[35] H. B. Profijt, S. E. Potts, M. C. M. van de Sanden, and W. M. M. Kessels, “Plasma-Assisted Atomic Layer Deposition: Basics, Opportunities, and Challenges” *J. Vac. Sci. Technol.* **A 29** (2014) 5.

[36] M. De Keijser and C. Vamn Opdorp, “Atomic Layer Epitaxy of Gallium Arsenide with the use of Atomic Hydrogen” *Appl. Phys. Lett.* **58** (1991) 1187.

[37] M. Verghese, J. W. Maes, and N. Kobayashi, Atomic layer deposition goes mainstream in 22nm logic technologies, http://www.solid-state.com (March 15, 2012).

[38] Tokyo Electron Limited website, http://www.tel.com (March 15, 2012)

[39] S.M. Rossnagel, A. Sherman, F. Turner, “Plasma-enhanced atomic layer deposition of Ta and Ti for interconnect diffusion barriers Source” *J. Vac. Sci. Techn.* B, **18** (2000) 2016-2020.

[40] A. Grill, Cold Plasmas in Materials Fabrication: From Fundamentals to Applications (Wiley-IEEE Press, New York, 1994).

[41] S.E. Potts, W.M.M. Kessels, “Energy-enhanced atomic layer deposition for more process and precursor versatility” *Coordination Chemistry Reviews* **257** (2013) 3254–3270

[42] H. B. Profijt, P. Kudlacek, M. C. M. Van de Sanden, and W. M. M. Kessels, “Ion and Photon Surface Interaction during Remote Plasma ALD of Metal Oxides” *J. Electrochem. Soc.* **158**, G88 (2011).

[43] S. B. S. Heil, J. L. van Hemmen, C. J. Hodson, N. Singh, J. H. Klootwijk, F. Roozeboom, M. C. M. van de Sanden, and W. M. M. Kessels, J. Vac. Sci. Technol. A 25, 1357 (2007).

[44] S. B. S. Heil, J. L. van Hemmen, C. J. Hodson, N. Singh, J. H. Klootwijk, F. Roozeboom, M. C. M. van de Sanden, and W. M. M. Kessels, "Deposition of TiN and HfO2 in a commercial 200 mm remote plasma atomic layer deposition reactor" *J. Vac. Sci. Technol*. A **25**, 1357 (2007).

[45] MKS website, http://www.mksinst.com (May 31, 2011).

[46] Advanced Energy website, http://www.advanced-energy.com/ (May 31, 2011).

[47] H. Kim and Il-Kwon Oh, "Review of plasma-enhanced atomic layer deposition: Technical enabler of nanoscale device Fabrication" *Jpn. J. Appl. Phys.* **53** (2014) 03DA01.

[48] R. L. Puurunen, W. Vandervorst, W. F. A. Besling, O. Richard, H. Bender, T. Conard, C. Zhao, A. Delabie, M. Caymax, S. D. Gendt, M. Heyns, M. M. Viitanen, M. de Ridder, H. H. Brongersma, Y. Tamminga, T. Dao, T. de Win, M. Verheijen, M. Kaiser, and M. Tuominen, "Island growth in the atomic layer deposition of zirconium oxide and aluminum oxide on hydrogen-terminated silicon: Growth mode modeling and transmission electron microscopy" *J. Appl. Phys.*, **96** (2004) 9.

[49] S. E. Potts, G. Dingemans, C. Lachaud, and W. M. M. Kessels, "Plasma-enhanced and thermal atomic layer deposition of Al2O3 using dimethylaluminum isopropoxide, [Al(CH3)(2)(mu-(OPr)-Pr-i)](2), as an alternative aluminum precursor" *J. Vac. Sci. Technol.* A 30, 021505 (2012).

[50] S. E. Potts,W. Keuning,E. Langereis,G. Dingemans, M.C.M. vandeSanden, and W. M. M. Kessels, "Low Temperature Plasma-Enhanced Atomic Layer Deposition of Metal Oxide Thin Films" *J. Electrochem. Soc.***157** (2010) P66.

[51] J. W. Lim and S. Yun, "Electrical properties of alumina films by plasma-enhanced atomic layer deposition" *Electrochem. Solid-State Lett.* **7** (2004) F45.

[52] S. B. S. Heil, P. Kudlacek, E. Langereis, R. Engeln, M. C. M. van de Sanden, and W. M. M. Kessels, "In situ reaction mechanism studies of plasma-assisted atomic layer deposition of Al2O3" *Appl. Phys. Lett.* **89** (2006) 131505.

[53] J. Yang, B. S. Eller, M. Kaur, and R. J. Nemanich, "Characterization of plasma-enhanced atomic layer deposition of Al2O3 using dimethylaluminum isopropoxide" *J. Vac. Sci. Technol.* A **32** (2014) 2.

[55] J. Koo, S. Kim, S. Jeon, H. Jeon, Y. Kim, and Y. Wen, "Characteristics of Al2O3 thin films deposited using dimethylaluminum isopropoxide and trimethylaluminum

precursors by the plasma-enhanced atomic-layer deposition method" *J. Korean Phys. Soc.* **48** (2006) 131.

[56] J. W. Lim and S. Yun "Electrical properties of alumina films by plasma-enhanced atomic layer deposition" *Electrochem. Solid-State Lett*.7, F45 (2004)

[57] E. Langereis, M. Creatore, S. B. S. Heil, M. C. M. van de Sanden, and W. M. M. Kessels, *Appl. Phys. Lett*. **89** (2006) 081915.

[58] B. B. Burton, S. W. Kang, S. W. Rhee, and S. M. George, "SiO2 Atomic Layer Deposition Using Tris(dimethylamino)silane and Hydrogen Peroxide Studied by in Situ Transmission FTIR Spectroscopy" *J. Phys. Chem. C* **113**, 8249 (2009).

[59] P. C. Rowlette, C. G. Allen, O. B. Bromley, A. E. Dubetz and C. A. Wolden, "Plasma-Enhanced Atomic Layer Deposition of Semiconductor Grade ZnO Using Dimethyl Zinc", *Chem. Vap. Dep.* **15** (2009) 15-20.

[60] T. M. Barnes, S. Hand, J. Leaf and C. A. Wolden, "ZnO synthesis by high vacuum plasma-assisted chemical vapor deposition using dimethylzinc and atomic oxygen", J. Vac. Sci. Tech. A **22** (2004)2118.

CHAPTER 3. MOLECULAR BEAM DEPOSITION:

I. Introduction:

Molecular beam deposition (MBD) is based on the principle of molecular beam epitaxy (MBE) experiment. MBE is an ultrahigh vacuum (UHV ~ 10^{-10} Torr) process to deposit epitaxial crystalline thin films. Kundsen cells are used as material source in MBE systems, which direct material to the substrate surface. Schoolar and Zemel *et. al.* were the first users of MBE, in 1964, to deposit lead sulfide [1]. The molecular beam for their system was produced by effusion cells. In late 1960s, the deposition technique was extended to deposit III-V semiconductors. Davey and Pankey *et. al.* deposited epitaxial gallium arsenide films in 1968 [2]. To date MBE III-V and II-VI films have been deposited for the applications of infrared imaging sensors and light emitting devices, etc. Lewis *et. al.* were the first ones to modify MBE hardware to use it as MBD to deposit dielectric materials [3-6]. The ultrahigh vacuum deposition method has advantages to reduce impurities, to deposit denser and mechanically stable films. The atomic or molecular beam is generated from the heated source. The flux distribution on the substrate surface is controlled by the substrate and source configuration.

II. MBD Reactor Configuration:

MBD system used in this research has a similar principle as MBE and MBD processes described above with a base pressure of 1 x 10^{-9} Torr. However, the sources used to evaporate the metal pellets were e-beam instead of using Knudsen or effusion cell and a background pressure of O_2 gas was maintained the background to deposit metal oxides.

Schematics of MBD chamber with top view and side view are shown in Figure 3.1 a) and b). The figure shows the three e-guns: vanadium, titanium and molybdenum, O_2 gas inlet, and sample and crucible positions. The chamber is pumped with a cryopump and a turbo-molecular pump to achieve the base pressure in the range of 10^{-9} Torr. Three e-beam guns are installed in the system have three different (Vanadium, Titanium, Molybdenum) metal sources. The e-guns are cooled using water jackets. Metal pellets in the crucibles are evaporated using e-beam aligned with magnets to focus at the center of the crucibles. Molybdenum crucible is installed with boron nitride crucible liner due to high thermal coefficient (138 W/(m·K)) of molybdenum. On the other hand, the thermal coefficient of vanadium and titanium is 30.7 W/(m·K) and 21.9 W/(m.K), respectively. The low thermal coefficient allows using the crucibles for vanadium ad titanium metals without crucible liners. This system can be used to deposit different oxidation states of vanadium oxide and molybdenum oxide by varying oxygen pressure and deposition temperature.

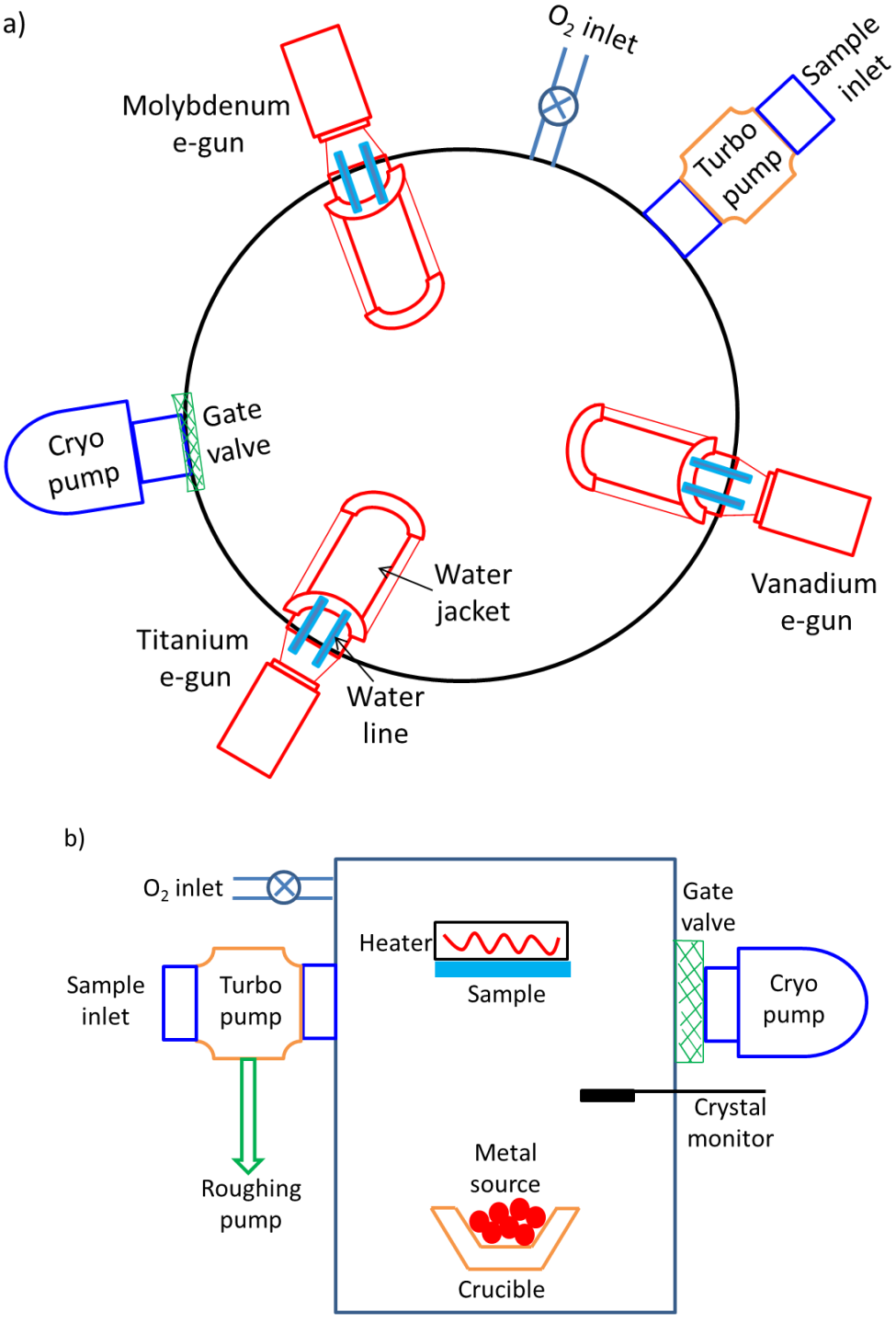

Figure 3.1. Schematic of MBD shows a) the top view of three guns: vanadium, titanium and molybdenum, cryo pump, oxygen inlet and turbo pump, and b) side view of sample and crucible position.

III. e-beam:

The e-guns installed in the chamber were purchased from MDC. The system includes e-vap CVS emission current controller and 10 kW power supply. An e-gun consists of two parts, an electron beam generator/emitter and the metal source, Figure 3.2. The emitter filament (tungsten) generates a beam of electrons by thermionic emission, which varies from 50 – 500 mA. The phenomenon of thermionic emission was demonstrated by Thomas A. Edison in 1883, where thermal energy is used to emit the electrons from a material while overcoming the work function. With the magnets installed on both sides of the emitter and crucible, the e-beam is confined and focused at the center of the source. An electron beam emitted from the filament is accelerated to high K.E. which provides high thermal energy to evaporate the metal source. The evaporation rate that is usually above the metal melting point determines the growth rate of metal oxides, which can be controlled by varying the emission current.

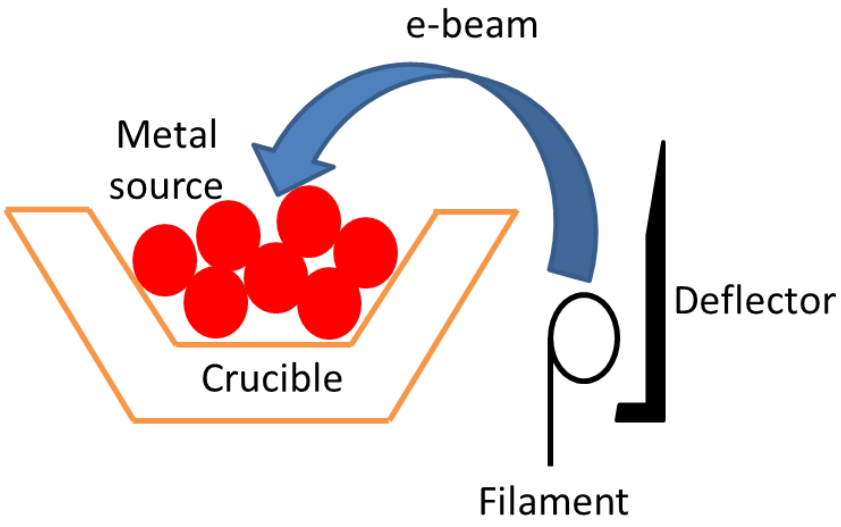

Figure 3.2. Schematic of emitter and crucible which shows the filament and e-beam path to the metal source.

IV. Oxides Deposition Mechanism:

To generate the electron beam, high voltage (HV) of 4.5 – 5.3 kV was applied between the e-gun filament and the metal source. The HV voltage used for vanadium, titanium and molybdenum metal sources was 4.5, 5.2 and 5.3 kV. In addition to the HV, emission current was increased to obtain the desired growth rate, which was ≤ 0.1 Å/sec for all the oxides. In a deposition method like MBD, the composition of metal oxide is controlled by the background oxygen and deposition temperature. Thus, the variation in oxygen pressure and deposition temperature can change vanadium oxide oxidation state. To obtain a specific oxidation states, the growth conditions are optimized. During the deposition, cryo pump is separated from the chamber using a gate valve Figure 3.1 a) and b). Consequently, turbo-molecular pump was used to maintain O_2 gas pressure for metal oxides deposition. The required oxygen gas pressure was different for different metal oxides. The oxygen pressure for VO_2 (vanadium (IV) oxide), TiO_2 and MoO_3 was 7×10^{-4}, 5×10^{-5} and 9×10^{-5} Torr, respectively. The vanadium, titanium and molybdenum metal sources were purchased from Alpha Aesar with 99.99%, 99.999% and 99.99% purity, respectively.

A. Vanadium Oxide:

Vanadium oxide has three oxidation states: VO_2 (vanadium (IV) oxide), V_2O_3 (vanadium (III) oxide) and V_2O_5 (vanadium (V) oxide). All the three oxidation states can be obtained using our MBD system. However, for this research, VO_2 was deposited and studied for band alignment and charge transfer properties in $VO_2/LiNbO_3$ and VO_2/PPLN heterostructures. With our MBD system VO_2 can be deposited at 450 °C and 550 °C and research grade O_2 gas pressure of 7×10^{-4}. The AFM scans of 55 nm VO_2 films deposited

at different temperatures are shown in Figure 3.3. It is evident from AFM scans, with the increase in deposition temperature the grain size also increases.

Vanadium (III) oxide can be deposited at 350 °C with O_2 gas pressure of 1 x 10^{-5} Torr; however, vanadium (V) oxide deposition requires 650°C and O_2 pressure in the rage of mTorr. With the O_2 gas pressure in mTorr, arcing becomes an issue in the vicinity of emitter which restricts the deposition of thick V_2O_5. Our prior research has studied the band alignment of stacked vanadium dioxide (VO_2) in HfO_2 and Si gate stack structure [7].

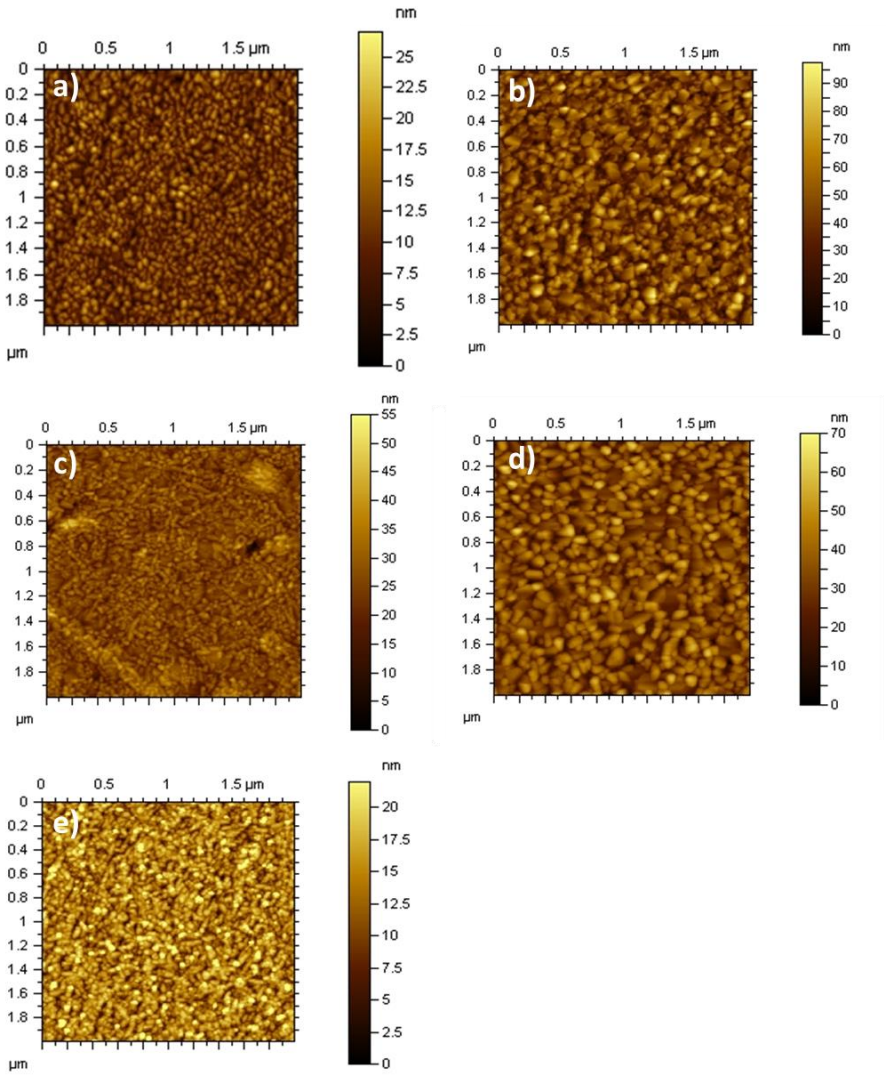

Figure 3.3. AFM images of 55 nm VO_2 on a) Si at 450 C, b) Si at 550 C, c) sapphire at 450 C, d) sapphire at 550 C, and e) PPLN at 550 C. The RMS of the VO_2 from AFM was 3.0, 13.1, 4.5, 8.3 and 3.5 nm, respectively.

B. Titanium Oxide:

Titanium (TiO_2) was used to determine the band alignment in $TiO_2/LiNbO_3$ and charge transfer in TiO_2/PPLN heterostructures. The deposition of TiO_2 could be achieved at comparatively lower temperature and oxygen pressure as compared to VO_2. For thin

thickness < 2 nm, TiO_2 can be deposited using two methods. First is to deposit Ti metal at RT and oxidize the thin film with oxygen and helium mixed plasma at 30 W, 100 mTorr, 200 °C for 2 min [8]. Second is to deposit TiO_2 at 250 °C while maintaining the background O_2 pressure at 5 x 10^{-5} Torr. However, to deposit thick films (> 2 nm) the second deposition method is preferred. With the increase in Ti metal, the oxidation of Ti with oxygen plasma is difficult due to penetration depth limit of oxygen plasma species.

C. Molybdenum Oxide:

Molybdenum oxide has multiple oxidation states and usually deposits in mixed oxidation states. MoO_3 is the highest work function (6.9 eV) material, which has been extensively used to transfer holes form organic materials and semiconductors in heterostructures. Usually, the evaporated molybdenum oxide is MoO_x ($x<3$) [9, 10]. The work function of molybdenum oxide decreases with the decrease in x [9]. MoO_x can be deposited in MBD system at various temperatures (RT – 250 °C) and oxygen pressure of 4 x 10^{-4}. Molybdenum pellets required highest emission current among the three metal sources in the MBD system. The emission current to evaporate molybdenum metal source was 200 – 200 mA.

References:

[1] R. B. Schoolar, J. N. Zemel, "Preparation of Single-Crystal Films of PbS" *J. Appl. Phys.* **35** (1964) 3

[2] J. E. Davey and T. Pankey, "Epitaxial GaAs films deposited by vacuum evaporation" *J. Appl. Phys.* **39** (1968) 1941.

[3] K. L. Lewis, A. M. Pitt, J. A. Savage, A. G. Savage, A. G. Cullis, and N. G. Chew, "Molecular Beam Techniques for optical thin film fabrication, Boulder Damage Symposium, Colorado, 1985.

[4] I. T. Muirhead, A. Miller, K.L. Lewis, J. Staromlynska, and K. Welford, "Molecular Beam Deposited Inteference Filters, *Tech. Dig. Series*, 6, Optical Interference Coatings, Optical Society of America, New York, 1988.

[5] K. L. Lewis, I. T. Muirhead, A. M. Pitt, and A. Miller," Thin Film Ultraclean Environments" *J. Vac. Sci. Technol.* **7** (1989) 3.

[6] K. L. Lewis, I. T. Muirhead, A. M. Pitt, A. G. Cullis, N. G. Chew, A. Miller, and T. J. Wyatt-Davies, "Molecular Beam Deposition of Optical Coatings and their Characterization" *Appl. Opt.* **28** (1989) 2785.

[7] C. Zhu, M. Kaur, F. Tang, X. Liu, D. J. Smith, and R. J. Nemanich, "Band alignment of vanadium oxide as an interlayer in a hafnium oxide-silicon gate stack structure" *J. Appl. Phys.* **112** (2012) 8.

[8] C. C. Fulton, G. Lucovsky and R. J. Nemanich, "Electronic states at the interface of Ti–Si oxide on Si(100)" *J. Vac. Sci. Technol.* **20** (2002) 1726.

[9] M. Vasilopoulou, A. M. Douvas, D. G. Georgiadou, L. C. Palilis, S. Kennou, L. Sygellou, A. Soultati, I. Kostis, G. Papadimitropoulos, D. Davazoglou, and P. Argitis, "The Influence of Hydrogenation and Oxygen Vacancies on Molybdenum Oxides Work Function and Gap States for Application in Organic Optoelectronics" *J. Am. Chem. Soc.* **134** (2012) 16178.

[10] C. Battaglia, S. M. Nicolas, S. D. Wolf, X. Yin, M. Zheng, C. Ballif, and A. Javery, "Silicon heterojunction solar cell with passivated hole selective MoOx contact" *Appl. Phys. Lett.* **104** (2014) 113902.

CHARACTERIZATION TECHNIQUES

CHAPTER 4. SCANNING PROBE MICROSCOPY:

I. Introduction:

Scanning probe microscopy uses a conducting or non-conducting tip mounted at the end of a cantilever, which moves back and forth to image the sample surface. The deflection experienced by the cantilever as it approaches the sample surface is measured by a laser reflection from the top of the cantilever, Figure 4.1. Scanning probe microscopy was discovered with the invention of scanning tunneling microscope (STM) in 1981by Swiss scientist Gerd Binnig and Heinrich Rohrer at IBM's Zurich. They were awarded the Noble Prize for the invention of STM in 1986 [1]. STM uses a conducting probe to tunnel electrons from sample to the tip and vice versa depending on the sign of the applied voltage. A bias applied between the sample and tip develops an electric field, which tunnels electrons when the distance between the tip and the sample surface is ~10 Å [1]. In STM, an image is created by the tunneling current that varies with the tip to sample distance. STM was limited to scan conducting or semiconducting surfaces. To overcome the limitations of STM, atomic force microscope (AFM) was discovered to image conducting as well as non-conducting surfaces. AFM can also be used for other applications such as atomic force microscopy (AFM) [3, 4, 5], piezoelectric force microscopy (PFM) [6, 7, 8], electrostatic force microscopy (EFM) [9, 10] and scanning kelvin probe microscopy (SKPM) [11, 12, 13], etc

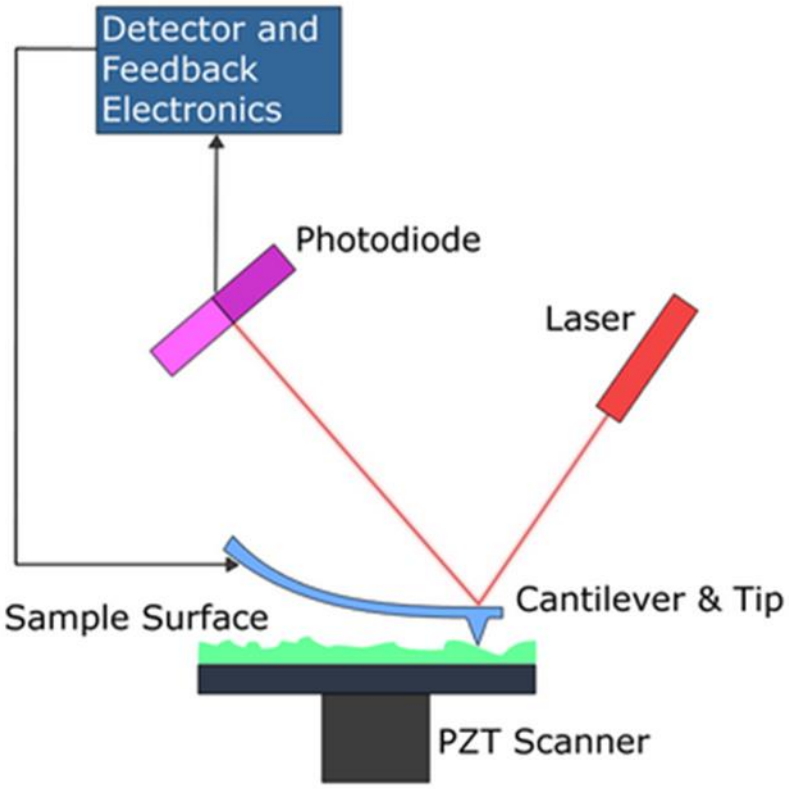

Figure 4.1. Schematic of scanning probe microscope [1].

II. Atomic Force Microscopy:

The atomic force microscope was developed by Binnig, Gerber and Quate in 1986 to image surface topography [3]. AFM consists of a cantilever with non-conducting probe tip which scans over the sample surface or the sample scans under the tip. The measured cantilever deflection of laser beam by photodiode sensor is sent to photodetector feedback loop to keeps the distance between the sample surface and tip constant, Figure 4.2. An electronic signal received by the computer from feedback loop controls the scanner position and from photodiode is converted into an image showing surface topography. The four quadrant photodiode generates voltage from each quadrant, which has amplitude directly related to the laser beam intensity. A voltage signal from each of

the four quadrants is added to get the total change in the laser beam intensity. AFM measures conducting and insulting surfaces at ambient pressure. In this research Asylum Research 3D MFP 3D is used, which scans the tip over the sample surface and has a floating sample stage to isolate the noise.

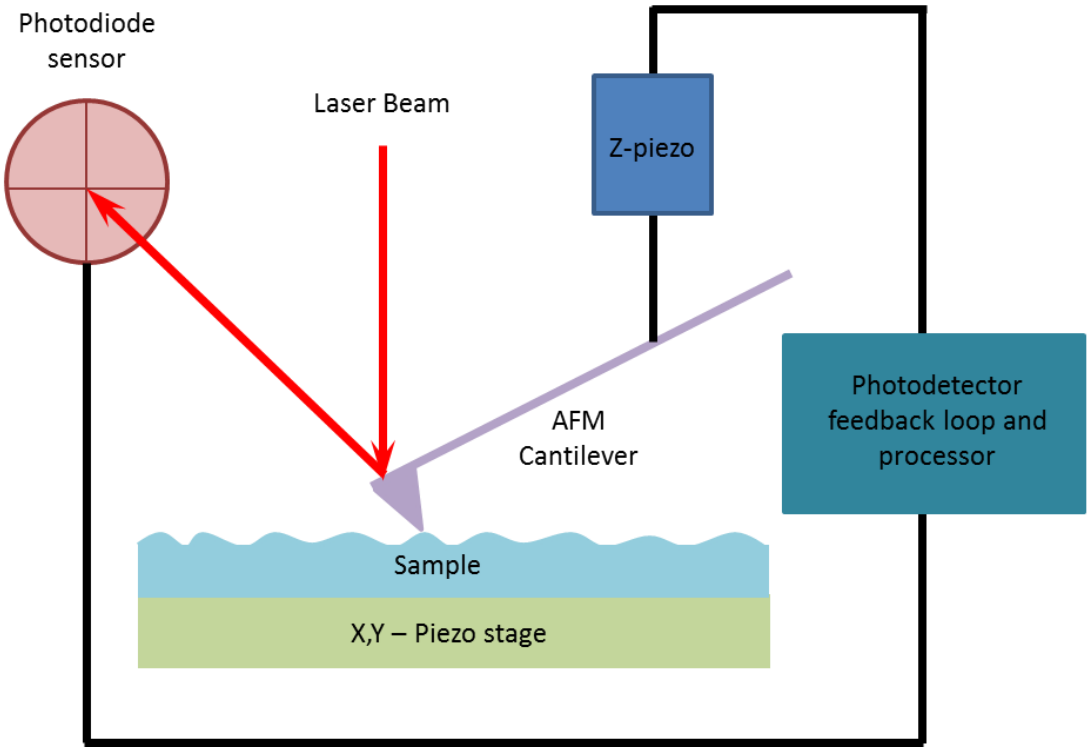

Figure 4.2. Schematic of AFM setup showing laser beam reflected from the back of the cantilever and the cantilever deflection is scanned by a four quadrant photodiode. Feedback loop processor converts the cantilever deflection into an image.

A. Probes:

AFM cantilevers are usually made of Si or Si_3N_4 in triangular or rectangular shape. The back of the cantilever is coated with reflective material to reflect the laser beam. A cantilever image and cross-sectional view is shown in Figure 4.3 (a) which also shows the cantilever length (L), thickness (T) and probe tip height (h). SEM image of a

tip with radius ~10 nm is shown in Figure 4.3. (b). In this research to scan AFM topography images, non-conducting Si probes of spring constant k = 13-77 N/m and the resonance frequency ~200 – 400 kHz are used.

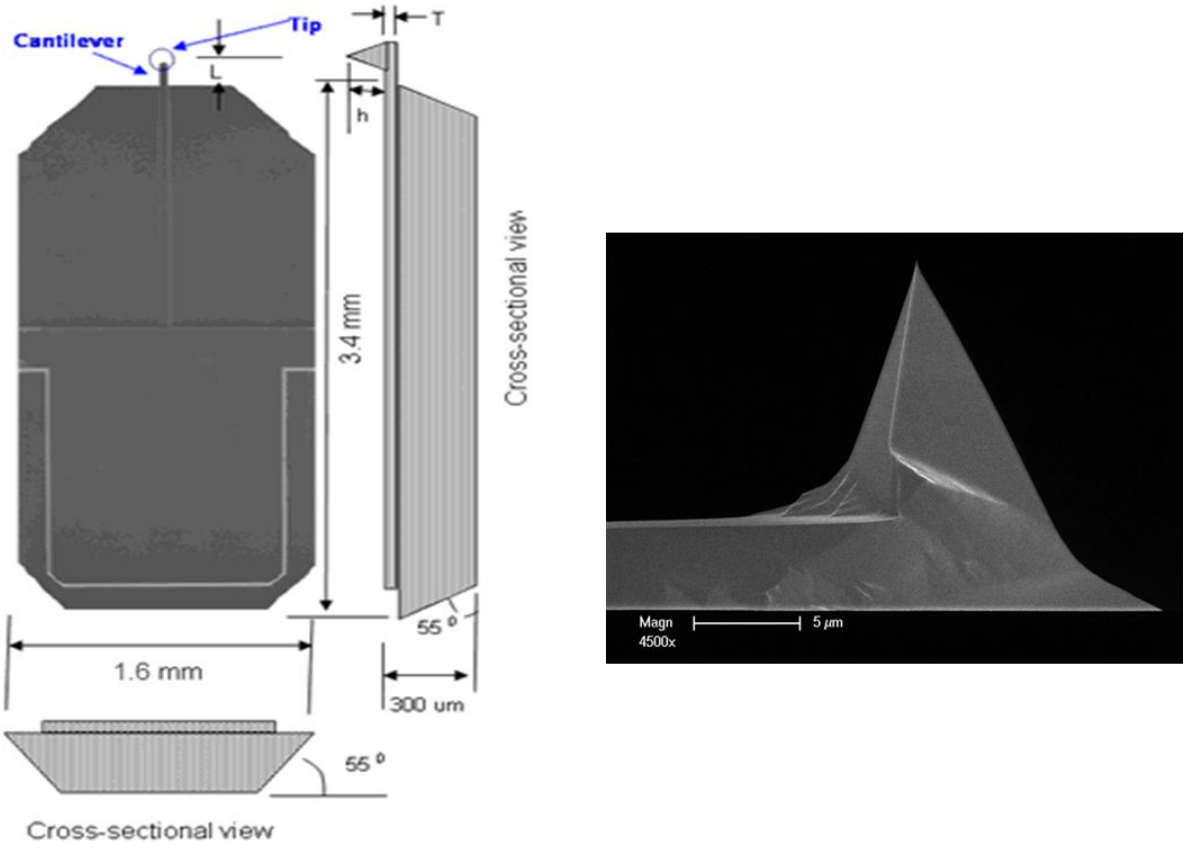

Figure 4.3 (a) Image and cross-sectional view of AFM probe showing cantilever, length, thickness and tip height (Nanoscience Instruments). (b) SEM image of a tip with radius ~ 10 nm (Bruker AFM probes).

B. Tip-Sample Interactions:

AFM cantilever deflection is the result of a force (10^{-11} N – 10^{6} N) between the tip and surface. The existence of Vander Waals, electrostatic, capillary and magnetic forces allow non-destructive imaging of the surface. For topography images, Vander Waals

attractive (long-range) and repulsive (short-range) forces exist between the tip and the sample. As the tip approaches the sample surface, the attractive and repulsive forces arise and show the same plot as Vander Waals interactions i.e. Force on the tip vs Distance, Figure 4.4. When the tip is far away from the surface weak attractive forces exist between the tip and the surface. As the tip comes close to the surface attractive forces increase and cause the downward movement of the tip until the tip comes so close to the surface where attractive forces starts decreasing. With the further decrease in the distance between the tip, the attractive interactions convert into repulsive forces. The

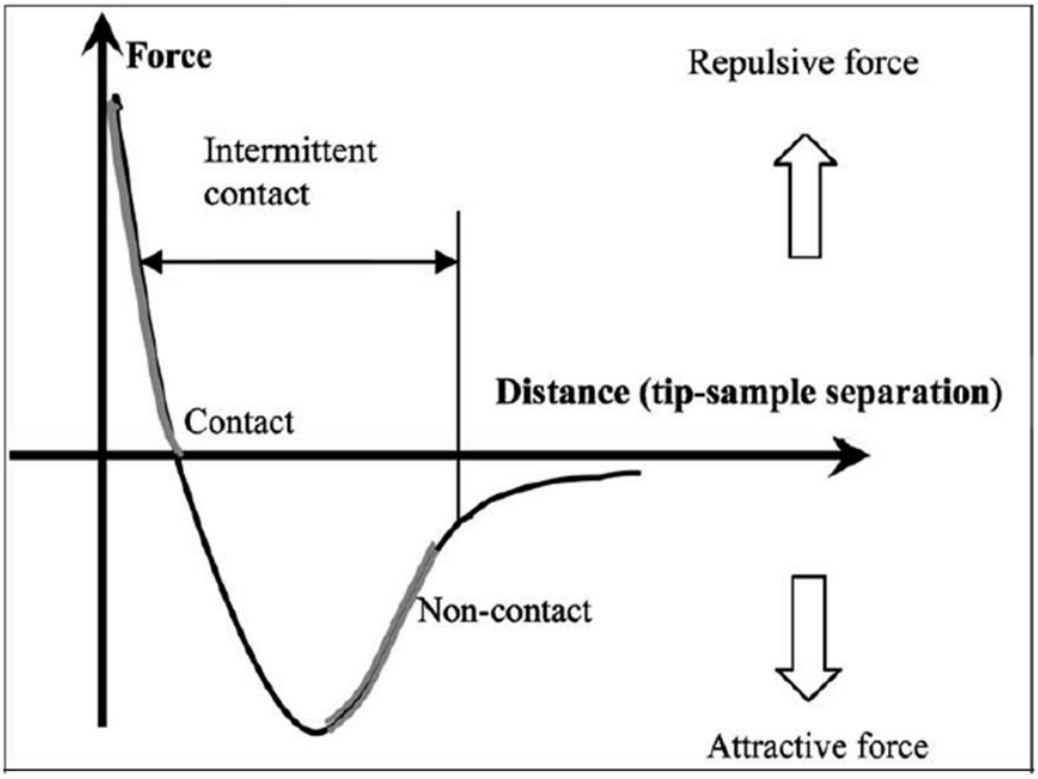

Figure 4.4. Force on the tip vs tip-sample distance shows a plot of attractive and repulsive forces between the tip and the sample. Non-contact AFM works in the attractive interactions region and contact AFM works in the repulsive interactions region.

nature of the interaction force is influenced by the sample surface and the distance between the tip and the sample. The tip-sample interaction forces other than the Vander Waals attractive and repulsive forces allow AFM to be used in other modes, Table 4.1.

Table 4.1 AFM tip-sample interactions and modes of operation.

Mode of Operation	Force of Interaction
Contact mode	Strong (repulsive)
Non-contact mode	Weak (attractive)
Tapping mode	Strong (repulsive)
Lateral force mode	Frictional forces
Magnetic mode	Sample magnetic field
Thermal scanning	Sample thermal conductivity

C. Operation Modes:

1. Contact AFM:

In contact mode, AFM operates in strong repulsive Vander Waals forces region, Figure 4.4, where tip makes a soft contact with the surface atoms. The cantilevers used for contact mode have spring constant (< 1 Nm) lower than the spring constant of surface atoms holding them together. Due to low spring constant, the force between the sample and the tip bends the cantilever and deflects the cantilever. Contact AFM can operate to create topography image in two modes: constant height mode and constant force mode.

Constant Height Mode:

In constant height mode, the cantilever is kept at constant height by applying constant voltage to the scanner. Since the scanner position is fixed, the cantilever deflect is used to generate the topography image. This mode can be used for very flat surfaces.

Constant Force Mode:

In constant force mode, the force between the tip and sample surface is kept constant by applying voltage to the scanner using feedback loop. The movement of the scanner along the z-direction due to applied voltage is used to generate topography image. In this case, the cantilever deflection does not contribute to topography image.

2. Tapping AFM:

In tapping mode, the tip-sample distance is kept between tens of Angstroms to hundreds of Angstrom and is made to oscillate at its resonance frequency (100 – 300 kHz). This mode operates in the attractive region of Vander Waals force vs distance plot. An oscillating tip makes an intermittent contact with the surface, experiencing free-amplitude of ~20 nm when the tip is in the air, and the tip amplitude decreases when it approaches to the surface. In scanning mode, when oscillating tip passes over the bump on the surface the cantilever oscillation amplitude decreases. However, when the tip passes over a trench the cantilever oscillation amplitude increases and approaches towards the free oscillation amplitude. In other words, the tip-sample interactions change the force on the tip with the change in sample-tip distance that changes the resonance frequency of the tip, Figure 4.5. The change in the oscillation frequency causes a change in the tip amplitude. A piezo-scanner attached to the cantilever keeps the tip oscillations amplitude constant at the set point value, using computer software, and adjusts the height of the scanner using

feedback loop. The voltage change measured from the piezo scanner to keep the z- height of the sample constant generates topography image.

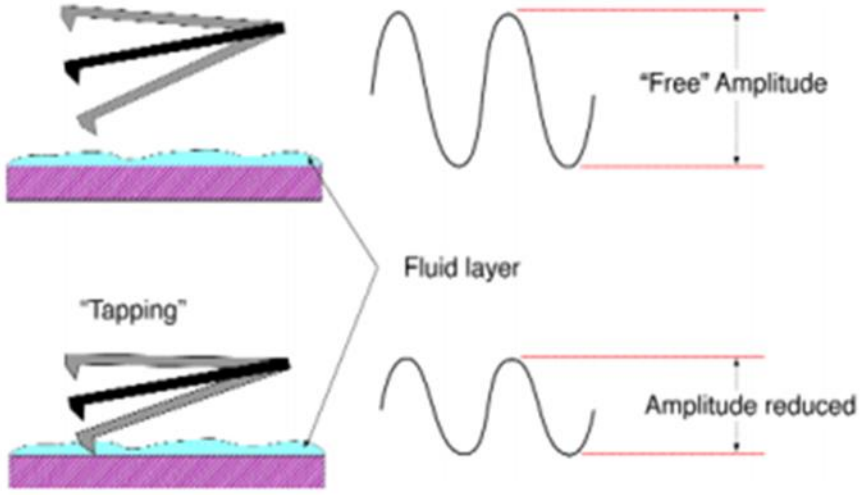

Figure 4.5. AFM cantilever oscillations amplitude in free air and in scanning mode at the set point value [15].

Tapping mode has advantages over the contact mode and can be used to scan rough surfaces and soft samples. The force used in the tapping mode per strike is ~0.5 nN, which is ~ 3 orders magnitude smaller than contact mode i.e. 100 nN. Unlike contact mode, lateral forces reduce drastically in the tapping mode due to intermittent contact with the sample, which increases the topography images resolution. High resolution AFM topography images of Ag nanoparticles on polarity patterned lithium niobate (PPLN) obtained in tapping mode is shown in Figure 4.6.

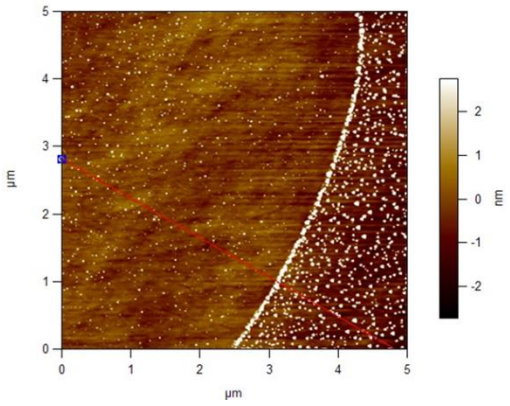

Figure 4.6. Tapping mode AFM topography image of Ag nanoparticles on PPLN.

III. Piezoresponse Force Microscope:

Piezoresponse force microscopy measures the electromechanical response (domain orientation, domain boundaries, piezoelectric hysteresis loop, piezoelectric constants and domain switching) of the sample when voltage is applied using a conductive tip. Guthner and Dransfeld were the first who studied piezoelectric properties of ferroelectric polymer using AFM in 1992 [25]. Over the years, the PFM was advanced and Gruverman et. al. presented results of nanoscale size poled domains on Barrium Titanate Oxide (BTO) and Lead Zirconate Titanate (PZT) in 1995 [26, 27]. After three years, Christman *et. al.* measured the piezoelectric constants using PFM [28]. In this research PFM is employed to study the alternate domain of polarity patterned lithium niobate (PPLN) substrate and ZnO/PPLN heterostructure.

PFM operates in contact mode, i.e. repulsive force region, when a tip with applied ac voltage raster over the sample surface. The ac voltage produces an electric field, which induces deformation in piezoelectric samples and causes cantilever deflection to generate PFM images. In PFM, topography and PFM images can be obtained simultaneously. An

experimental set-up of PFM used in this study is shown in Figure 4.7. The ac voltage applied to the tip is given as:

$$V_{tip} = V_{dc} + V_{ac} \quad (1)$$

where V_{tip} applied tip voltage, V_{dc} and V_{ac} are the dc and ac component of the applied voltage and

$$V_{ac} = V_0 \, Cos(\omega t) \quad (2)$$

where ω is the frequency at which the piezoelectric material contracts and expands.

In PFM, one frequency (~10 kHz) set value is required for ac modulation and another resonant frequency (45-115 kHz) set value is required for cantilever deflection. Two lock-in amplifiers, lock-in one and lock-in two, in Figure 4.9 are assigned to resonant frequency and ac modulation, respectively, to amplify frequency signals. Lock-in amplifier sets the tip deflection due to piezoelectric strain given as:

$$Z = Z_0 + A \, Cos \, (\omega t + \theta) \quad (3)$$

where Z_0 is the static surface displacement, A is piezoresponse amplitude at frequency ω and θ is the piezoresponse phase. Piezoresponse amplitude and phase generates amplitude and phase images, respectively. Phase images show the contrast in different orientation of spontaneous polarization of piezoelectric surfaces. Amplitude is the electromechanical deformation of the sample measured in nm/V. However, the amplitude signal is independent of polarization orientation except at the domain boundaries the value of amplitude is 0. PFM amplitude measurements can be used to determine the width of the domain boundaries. However, the domain width accuracy is questioned [20, 21].

A. Probes:

In PFM, conductive probes are used to apply tip voltage to the piezoelectric samples. The commonly used tips for PFM are Pt/Ir or diamond coated Si. Due to the contact mode operation of PFM, Pt/Ir conductive coating wears off quickly. Diamond coating thickness is ~ 1000 Å (0.1 Ω-cm, p-type) and are very expensive. These tips are expensive and non-uniform diamond coating has also been observed on Si tips [22, 23]. We have used n^+ Si tips (0.01-0.02 Ω-cm) coated with Pt/Ir from Nanosensors.

B. Contrast Mechanism in PFM Phase Image:

It is well know that all the ferroelectric materials are piezoelectric and shows reverse piezo effect when placed in an applied voltage. In ferroelectric materials, the piezoresponse is directly related to the polarization direction. For instance, when the applied electric field (generated by applied tip ac voltage) is parallel to the direction of the spontaneous polarization, $LiNbO_3$ domain expands in the direction of applied electric field i.e. applied voltage and piezoresponse are in 0° or 180° phase with each other. On the other hand, when the applied electric field is antiparallel to the direction of spontaneous polarization, $LiNbO_3$ domain contracts in the direction of applied electric field, i.e. applied voltage and piezoresponse are 180° out of phase with each other, Figure 4.7. The expansion and contraction of $LiNbO_3$ alternate domains with opposite spontaneous polarization causes color contrast in phase images.

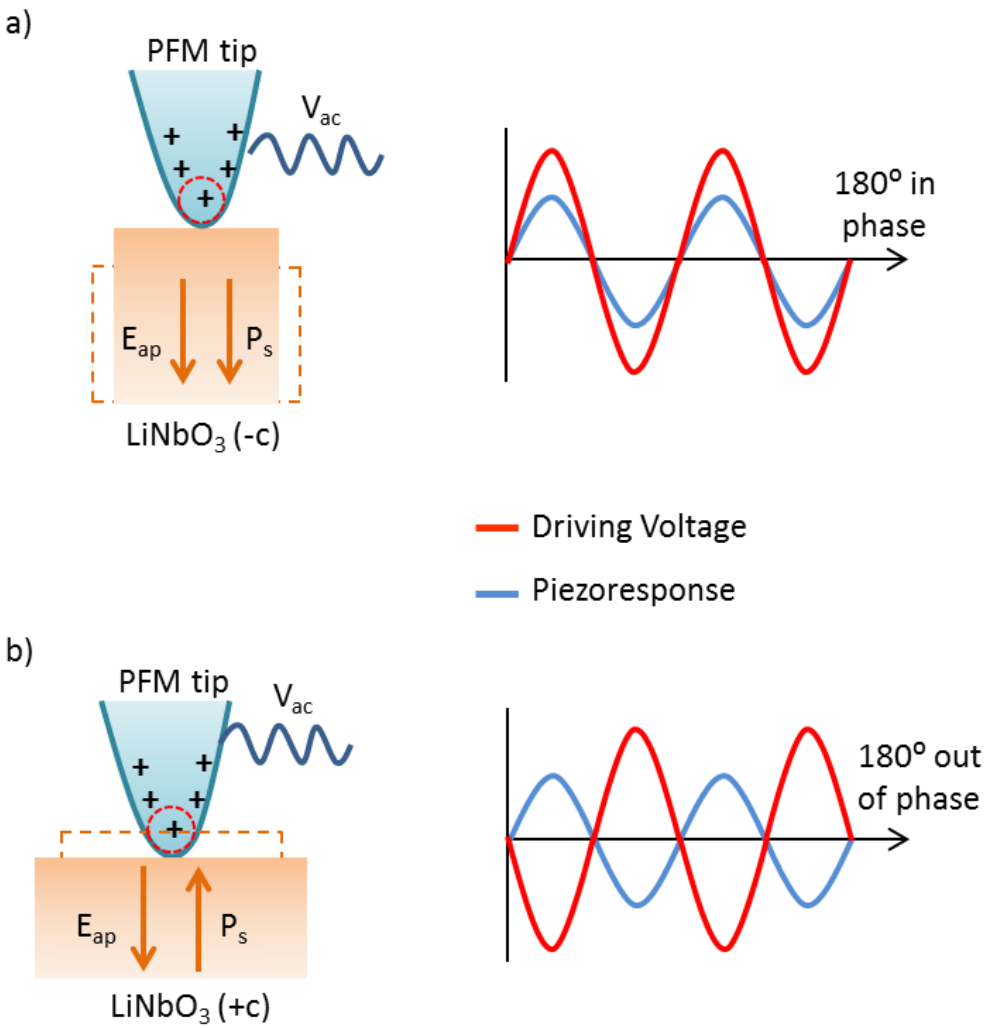

Figure 4.7. Schematic of piezoelectric effect in $LiNbO_3$ with applied tip voltage (V_{ac}). a) and b) $LiNbO_3$ negative domain (-c) and positive domain (+c) expands and contracts with the applied the applied electric field aligning parallel and antiparallel to spontaneous polarization, respectively. The applied voltage and piezoresponse are in 0° phase and 180° out of phase with each other when $LiNbO_3$ domain expands and contracts, respectively.

C. Operation Modes:

The local deformation of the sample, in vertical and horizontal direction, at the apex of the tip applies a force on the cantilever. Deflection of the cantilever is a force applied on the cantilever directly in the vertical direction when the sample underneath the tip expands or contracts. This is called vertical PFM due to the investigation of forces at the apex of the tip and movement of the cantilever directly in the vertical direction. Other than deflection of the cantilever, buckling or torsion investigates the forces applied on the cantilever in due to horizontal displacement and thus are associated to in-plane deformations, i.e. lateral displacement. Both deflection and torsion or buckling results in the movement of the cantilever in vertical direction which deflects the laser beam as shown in Figure 4.8. The cantilever displacement due to torsion or buckling can be used to detect in-plane polarization of domains which are not aligned at 180°.

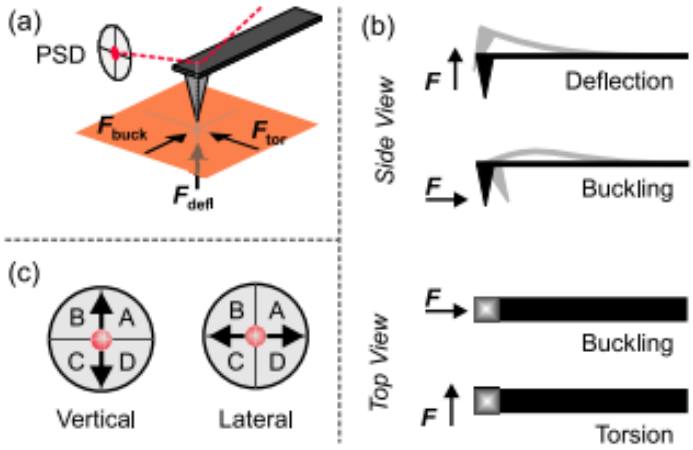

Figure 4.8. Schematic of the cantilever movement with an applied force at the apex of the tip duet to surface deformations. (a) shows the direction of deflection, buckling and torsion force with respect to the surface plane. (b) displays the side and top view of cantilever deflection with vertical (deflection) and lateral (buckling/torsion) forces. (c)

indicates the possible movement direction of laser beam reflecting from cantilever back [20]

This study involves PPLN samples with domains aligned at 180° which required the use of vertical PFM. Dual ac resonance tracking (DART) PFM is used to analyze the domains of PPLN using vertical mode.

Dart PFM:

PFM technique described above has limitations as the cantilever deflections are limited to a few picometers (pm) per volt. The small deflections are overshadowed by the noise from an optical lever, which is in the range of tens of pm. Thus the amplification of the signal is required to get accurate measurements using either high AC voltage or some other techniques. Usually, the modulation using high voltage is the most common method used to amplify the signal. However, high AC voltage generates large electric field that can switch the domains in case of ferroelectric materials and results cross talk between the topography and piezo signal [24, 25]. The other technique that has been developed to modulate the piezo signal is the use of cantilever contact resonance and is called DART PFM. The schematic of DART PFM is shown in Figure 4.9.

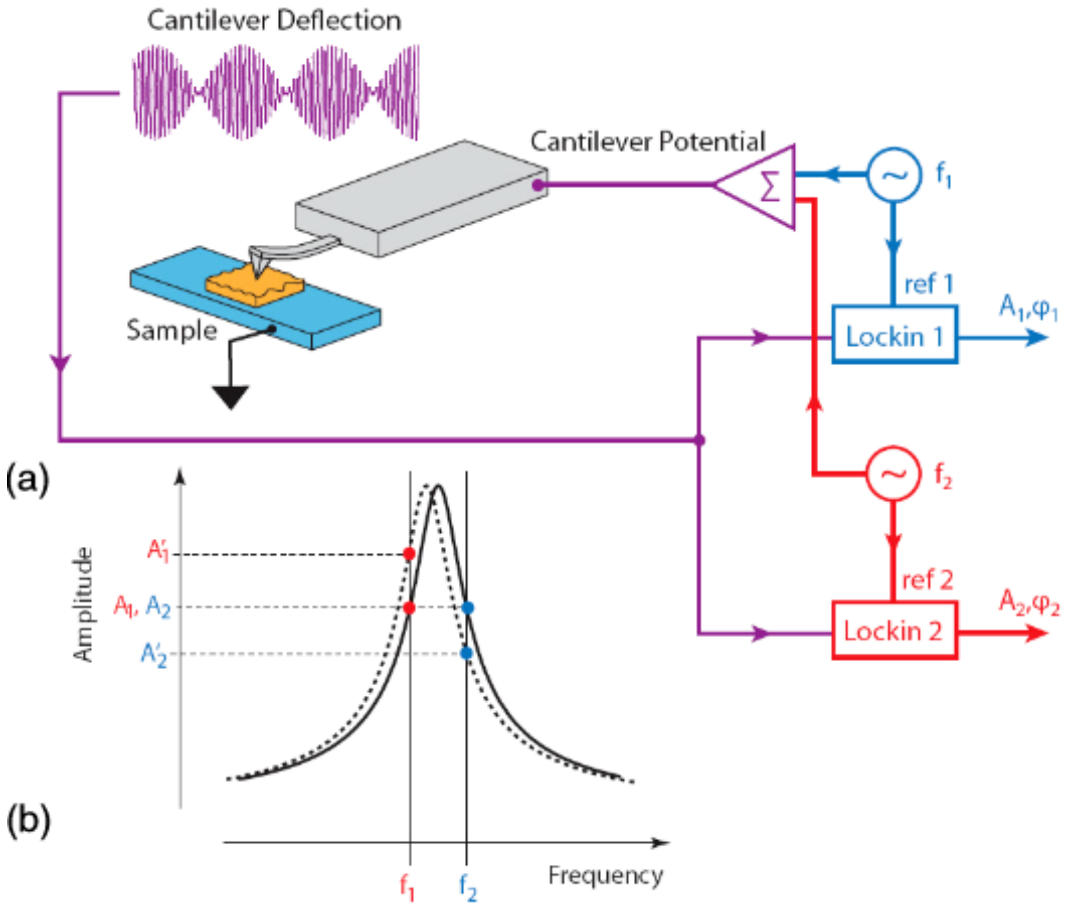

Figure 4.9 (a) Schematic Illustration of DART PFM. (b) The change in amplitude with dual resonance frequency [26].

In case of DART PFM, the drive frequency of the cantilever is adjusted tracking the contact resonance using a feedback loop. Unlike conventional PFM that uses phase frequency as the feedback loop response, DART uses the difference in the amplitudes of two different voltage frequencies that are applied at above and below the resonant frequency [27]. As shown in the schematic above (Figure 4.9), f_1 and f_2 are the two drive frequencies selected above and below the resonant frequency, respectively and A_1 and A_2 (solid black line) is the respective deflection amplitude. As the deflection changes the resonant frequency due to tip-sample surface force gradient, the deflection amplitude

changes to A_1' and A_2' (dotted black line). The amplitude difference (A_2'-A_1') is an input to a feedback loop to shift the drive frequency to make the new amplitude difference (A_2'-A_1') zero as the initial amplitude difference (A_2-A_1). DART PFM can be used on the samples to detect small piezo response on ferroelectric samples [28]. PFM phase images on PPLN domain ends is shown in Figure 4.10.

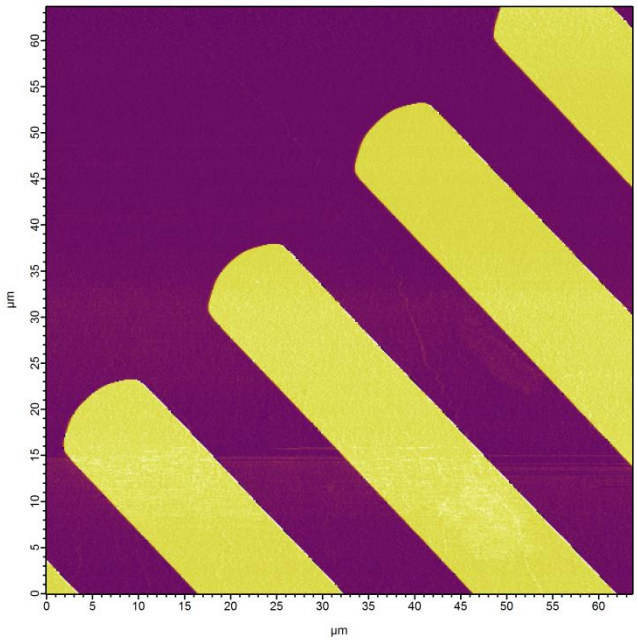

Figure 4.10. PFM phase image of PPLN showing positive domain ends and contrast in the positive (+c) and negative (-c) surface.

References:

[1] Scanning Probe Microscopy, Center for probing the nanoscale, Stanford University

[2] G. Binnig, C. F. Quate, and C. Gerber, "Atomic Force Microscope" *Phys. Rev. Lett.* **56** (1986) 930.

[3] N. Jalili, K. Laxminarayana "A review of atomic force microscopy imaging systems: application to molecular metrology and biological sciences", *Mechtronics* **14** (2004) 907.

[4] E. Meyers, "Atomic Force Microscopy", *Progress Surf. Sci.* **41** (1992) 3.

[5] C. B. Prater, P. G. Maivald, K. J. Kjoller and M. G. Heaton, "Tapping Mode Imaging Applications and Technology" *Veeco.*

[6] A. Gruverman, O. Auciello, and H. Tokumoto, "Scanning force microscopy for the study of domain structure in ferroelectric thin films" *J. Vac. Sci. Technol*. B **14** (1996) 602.

[7] A. Gruverman, O. Auciello, and H. Tokumoto, "Scanning force microscopy: Application to nanoscale studies of ferroelectric domains" *Integr. Ferroelectrics* **19** (1998) 49.

[8] O. Kolosov, A. Gruverman, J. Hatano, K. Takahashi, and H. Tokumoto, "Nanoscale Visualization and Control of Ferroelectric Domains by Atomic-Force Microscopy" *Phys. Rev. Lett*., **74** (1995) 4309.

[9] J. W. Hong, D. D. Kahng, J. C. Shin, H. J. Kim, and Z. G. Khim, "Detection and control of ferroelectric domains by an electrostatic force microscope" *J. Vac. Sci. Technol*. B **16** (1998) 2942.

[10] J. W. Hong, S. Park, and Z. G. Khim, "Measurement of hardness, surface potential, and charge distribution with dynamic contact mode electrostatic force microscope" *Rev. Sci. Instrum.* **70** (1999) 1735.

[10] M. Nonnenmacher, M. P. O'Boyle, and H. K. Wickramasinghe, "Kelvin Probe Force Microscopy" *Appl. Phys. Lett.* **58** (1991) 2921.

[11] M. Fujihira and H. Kawate, "Structural Study of Langmuir-Blodgett-Films by Scanning Surface-Potential Microscopy" *J. Vac. Sci. Technol.* B **12** (1994) 1604.

[12] M. M. Shvebelman, A. G. Agronin, R. P. Urenski, Y. Rosenwalks, and G. I. Rosenman, "Kelvin probe force microscopy of periodic ferroelectric domain structure in KTiOPO4 crystals" *Nano Lett*. **2** (2002) 455.

[15] C. B. Prater, P. G. Maivald, K. J. Kjoller, and M. G. Heaton, "Scanning Probe Microscopy .2. Scanning Technology and Applications" *Ameri. Lab.* **27** (1995) 50.

[16] P. Guthner, and K. Dransfeld, "Local Poling Of Ferroelectric Polymers by Scanning Force Microscopy" *Appl. Phys. Lett.* **61**, 1137-1139 (1992).

[17] A. Gruverman, O. Kolosov, J. Hatano, K. Takahashi, and H. Tokumoto, "Domain-Structure And Polarization Reversal In Ferroelectrics Studied By Atomic-Force Microscopy" *J. Vac. Sci. Technol.* B **13** (1995) 1095.

[18] A. Gruverman, O. Auciello, and H. Tokumoto, "Scanning force microscopy for the study of domain structure in ferroelectric thin films" *J. Vac. Sci. Technol.* B **14** (1996) 602

[19] J. A. Christman, R. R. Woolcott, A. I. Kingon, and R. J. Nemanich, "Piezoelectric measurements with atomic force microscopy" *Appl. Phys. Lett.* **73** (1998) 3851.

[20] E. Soergel, "Piezoresponse Force Microscopy (PFM)" *J Phys. D: Appl.Phys.* **44** (2011) 464003

[21] T. Jungk, A. Hoffmann, and E. Soergel, "Influence of the inhomogeneous field at the tip on quantitative piezoresponse force microscopy" *Appl. Phys. A* **86** (2007) 353.

[22] P. Niedermann, W. Haenni, N. Blanc, R. Christoph, and J. Burger, "Chemical vapor deposition diamond for tips in nanoprobe experiments" *J. Vac. Sci. Technol.* A **14** (1996) 1233.

[23] S. J. O'Shea, R. M. Atta, and M. E. Welland, "Characterization of Tips for Conducting Atomic-Force Microscopy" *Rev. Sci. Instrum*. **66** (1995) 2508.

[24] C. Harnagea, M. Alexe, D. Hesse and A. Pignolet, "Contact resonances in voltage-modulated force microscopy" *Appl. Phys. Lett.*, **83** (2003) 338.

[25] B. J. Rodriguez, C. Callahan, S. Kalinin, R. Proksch, "Dual-frequency resonance-tracking atomic force microscopy" *Nanotechnology*, **18** (2007) 475504.

[26] S. Kim, V. Gopalan and A. Gruverman, "Coercive fields in ferroelectrics: A case study in lithium niobate and lithium tantalite" *Appl. Phys. Lett.*, **80** (2002) 2740

[27] Piezoresponse force microscopy, *Asylum Research*.

[28] B. J. Rodriguez, S. V. Kalinin, J. Shin, S. Jesse, V. Grichko, T. Thundat, A. P. Baddorf and A. Gruverman, "Electromechanical imaging of biomaterials by scanning probe microscopy" *J. Struct. Biol.*, **153** (2006) 151.

CHAPTER 5. PHOTOEMISSION ELECTRON SPECTROSCOPY

I. Introduction:

Photoemission electron spectroscopy (PES) or photoelectron spectroscopy is an application of photoelectric effect, i.e. an incident photon can emit or ionize an electron from the surface, as explained by Albert Einstein in 1905. The excess photon energy than the amount of energy required to emit an electron is carried by an emitting electron in the form of kinetic energy (KE). PES is used to measure the kinetic energy of emitted photoelectrons to determine the binding energy (BE), which is used to examine the electronic structure of materials. Photoelectron spectroscopy can be divided into two categories, i.e. x-ray photoelectron spectroscopy (XPS) and Ultraviolet photoelectron spectroscopy (UPS), depending upon the photon energy source. The high energy x-rays are used to study the electronic profile of core level electrons and the technique is known as XPS, while low energy ultraviolet photons provide an electronic profile of valence electrons and the technique is termed as UPS. Both XPS and UPS characterizations are surface sensitive since the photon penetration depth is limited to few nanometers under the surface. Photoelectric effect defines the relationship between the kinetic energy (KE) and the binding energy (BE) of solids as:

$$BE = h\nu - KE - \phi_A \,, \tag{1}$$

where $h\nu$ is incident photon energy and ϕ_A is the analyzer work function. However, the detected BE in photoelectron spectroscopic system is different from equation (1) because the detected energy is referred to the vacuum level of the spectrometer and is given as:

$$BE = h\nu - KE - \phi_A + qV \tag{2}$$

where ϕ_A is the work function of analyzer, q is the elementary charge and V is the bias applied to either sample or analyzer. The applied bias provides photoelectrons sufficient energy to accelerate and overcome the analyzer work function and hence increases the collection of low energy electrons. Figure 5.1 illustrates the core level and valencne band electron emission with x-ray and ultraviolet photons.

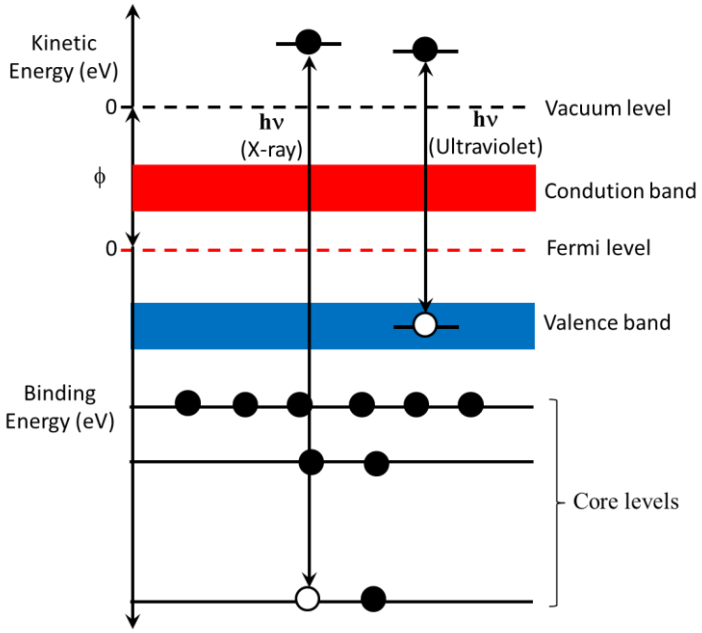

Figure 5.1. Energy level diagram of photoelectron emission in XPS and UPS.

Schematic of photoelectron microscopy is illustrated in Figure 5.2. Photoelectron spectroscopic system consists of photon source, energy analyzer and an electron multiplier detector in ultra-high vacuum (UHV). All the photoelectrons do not reach to the detector because of inelastic mean free path [1]. Recombination and scattering energy loses for most of the photo emitted electrons inhibit their surface escape. Consequently, the only electrons reach to the vacuum, which have sufficient kinetic energy to overcome the work function of the given material. However, some scattered electrons can escape to

the vacuum and contribute to the background spectrum. In front of the analyzer, the set of electrostatic lenses collect electrons and

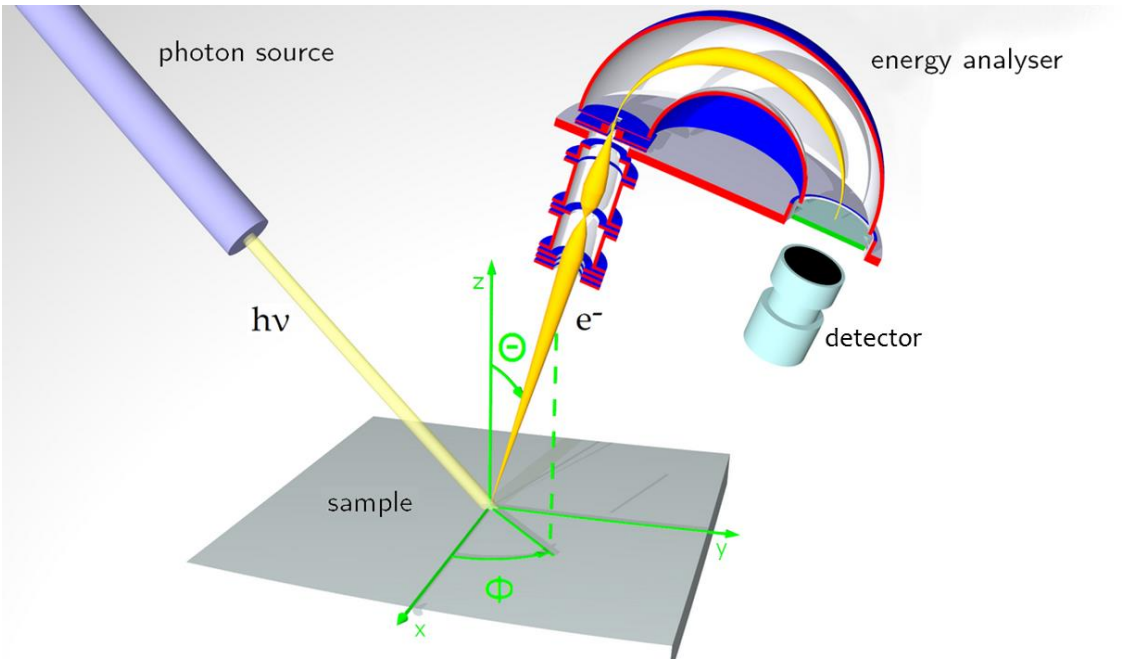

Figure 5.2. Schematic of photoelectron spectroscopy. Copyright: Photoemission spectroscopy (Wikipedia)

focus them on the entrance slit. The electric field is developed by applying bias to two hemispherical plates of the analyzer, which allows electrons with certain energy exit through the other slit to reach to the multiplier detector, where the electrons are accelerated and converted into current pulses.

II. X-ray Photoelectron Spectroscopy:

X-ray photoelectron spectroscopy is surface analysis method, as described above, which combines the x-rays surface irradiation and photoelectric effect. The other name used for XPS is Electron Spectroscopy for Chemical Analysis (ESCA), which was discovered by Kai Siegbahn in 1957 to study the chemical information instead of

elemental detection. XPS is used to characterize electronic structure, chemical oxidation states and atomic composition of the material being studied [2].

The commonly used metallic x-ray sources, to irradiate the surface to emit electrons, are aluminum (Al) and magnesium (Mg). X-rays are generated by bombarding Al or Mg anodes with electrons. A thoria coated iridium filament is heated to supply electrons, which are accelerated in a 15 kV electric field to be bombarded at water cooled metal anodes. Al and Mg anodes emit Al Kα (1486.6 eV) and Mg Kα (1253.6 eV) x-rays, respectively. Both, Al and Mg, sources are usually equipped and used in non-monochromatic systems due to wide x-ray beam and lower resolution to detect overlapping core levels and Auger peaks. However, monochromatic systems are equipped with only Al source, which achieves high resolution with added monochromator (a series of quartz crystals), which removes satellites and Bremsstrahlung [3]. A monochromatic XPS system (SCIENTA MX650), consists of SCIENTA SAX100, was used for most of the characterizations here. This system is installed with seven quartz crystals.

Monochromator: Concave shaped quartz crystals are used in a monochoromator to increase the surface area for x-rays incidence, which are diffracted satisfying Bragg's condition.

$$2\,d\,\mathrm{Sin}\theta = n\,\lambda \qquad (3)$$

where n is an integer, d is the distance between diffracting planes and λ is x-ray wavelength. The incident x-rays at an incidence angle $\theta_i \sim \theta_B$ can satisfy Bragg's diffraction condition. To focus the diffracted x-rays, concaved quartz crystal with radius 2R is tangentially aligned on Rowland's circle with radius R [4]. Quartz crystal and x-ray

source are placed on Rowland's circle which ensures the focus of diffracted x-rays will exist at another point on the circle [4,5]. Figure 5.3 shows the schematic of x-ray source, quartz crystal and sample on Rowland's circle. Rowland's circle sometimes is also called focus circle.

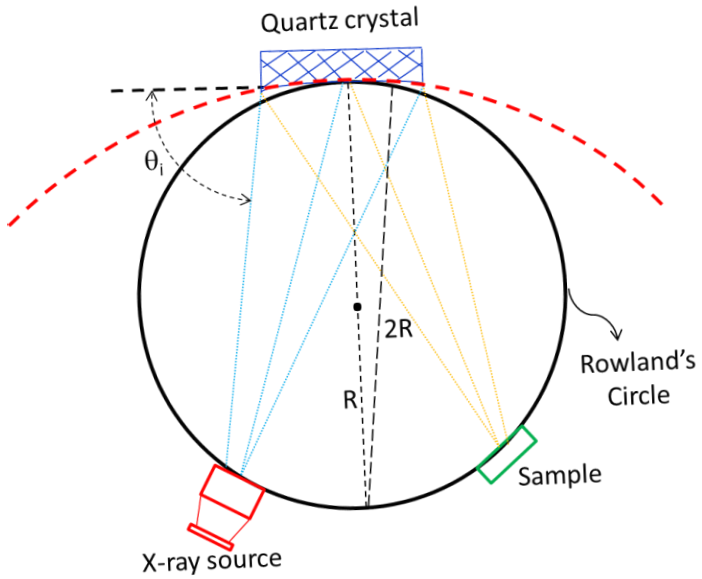

Figure 5.3. Schematic of Rowland's circle with positioned x-ray source, quartz crystal and sample.

Characterization:

1. **Core level Shift and Bonding:**

An XPS measured binding energy of core level electrons is used to determine the chemical oxidation and electronic states. The amount of energy required to remove electrons from core levels in elemental samples, such as Au [6], is supposed to be same in the absence of surface contamination and impurities. A small change in the core level peaks binding energy signifies the change in electronic environment of photoelectrons

and the change referred as core level shift. Another name used for core level shift is chemical shit. Quantitatively, chemical shift is the change in hybridization state with the nearest neighbor atoms and/or ionic/covalent bonding. For example, single crystalline Si substrate exposed to atmosphere forms thin film of SiO_2 on the surface. XPS shows two Si 2p peaks at 99 eV and 103.3 eV corresponding to Si and SiO_2, respectively. The core level binding energy can be used for further band alignment and band bending analysis.

2. **Thickness:**

Surface sensitivity of XPS enables it to determine the thickness of deposited or oxidized thin films. Hill *et. al.* calculated homogenous thin film thickness using Hill's equation in 1970 using the core level peak intensity of thin film and the substrate. Chiyu *et. al.* calculated SiO_2 thin film thickness on oxidized Si substrate using following equation [8].

$$t = \lambda_{SiO2} \, Sin\theta \, \ln\{1 + [(I_{SiO2} / R_{SiO2}) / I_{Si}]\} \quad (4)$$

where t is the SiO_2 thickness, θ is the angle between the photoelectrons emission direction and the sample surface i.e. 90^{o}, I_{SiO2} is the core level intensity of SiO_2 measured using XPS, I_{Si} is the core level intensity of Si measured using XPS and R_{SiO2} is the ratio of bulk SiO_2 and Si intensity i.e. 0.9392.

3. Chemical Composition:

As discussed earlier, all the emitted electrons do not reach to the detector which limits the direct comparison of XPS core level peak intensities and/or area. XPS intensities are also sensitive to the operating mode and instrumentation ability. Photoelectrons describe the electronic states of an element. With the change in the chemical composition the electronic states of an element also changes, which alters the

transition peak area from same and different elements. To eliminate the peak area discrepancies, the peak area for different elements and same element with different hybridization state to nearest neighbors must be scaled using atomic sensitivity factors. An atomic concertation percentage can determine the thin films composition that is calculated as [9]:

$$\text{Atomic \%} = [I_i^{exp} / S_i] / \sum_j^n [I_j^{exp} / S_j] \quad (5)$$

where I^{exp} is the core level intensity and S is the atomic sensitivity factor.

4. **Band Gap:**

XPS energy loss spectrum (ELS) can be used to determine the band gap. The O 1s core level is preferred to be measured for ELS spectrum due to smooth and broad spectral component of Plasmon loss related to it. A Plasmon peak is the result of a fraction of O 1s photoelectrons energy loss due to collective oscillations (Plasmons) and interband/intraband transitions [11,12]. The O 1s peak position is aligned to zero energy loss, the onset energy of electron excitation from valence band to conduction band measures the band gap of the material [13]. Figure 5.4 an ELS spectrum of PEALD Al_2O_3 O1s, used to calculate the band gap, i.e. 6.7$\pm$0.1 eV [14], which is comparable to ALD Al_2O_3 films band gap, i.e. 6.5 - 7.0 eV [12,15-17].

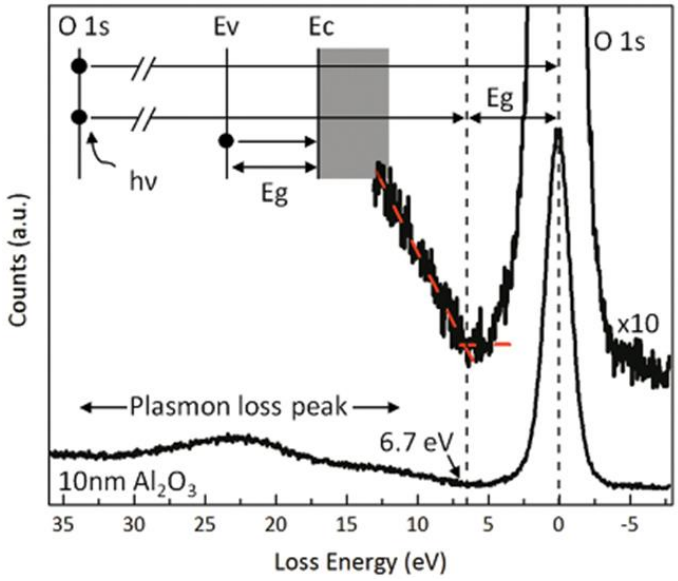

Figure 5.4. Oxygen 1s energy loss spectra from 10 nm PEALD Al_2O_3 on Si deposited at 200 °C. The zero loss energy represents O 1s peak position, E_v is the valence band maximum, E_c is the conduction band minimum and E_g is the band gap [14].

5. Other Peaks in XPS:

All peaks in an XPS spectrum are not the core level peaks created by photoelectrons emitted from the core levels of the nucleus. Along with the direct emission of photoelectrons with incident photons other phenomenon also occurs within the material and contributes to create XPS peaks. The most commonly known are the Auger peaks, satellite peaks, ghost peaks, shake-up peaks, and Plasmon peaks.

Auger Peaks: Auger peaks are often observed in XPS spectrum and the result of secondary electron emission with incident x-ray photons. As shown in Figure 5.5, the hole created by direct incident photon in the core level is filled by an energetic electron from higher energy level. An electron going from higher energy level to lower energy level releases energy, which in some cases is used as a kinetic energy for an another

electron to emit to the vacuum. Unlike photoelectrons, the energy of electrons participating in Auger peaks is independent of incident x-ray photon and does not satisfy equation (1) and (2). However, Auger peak position depends on the x-ray source material [18].

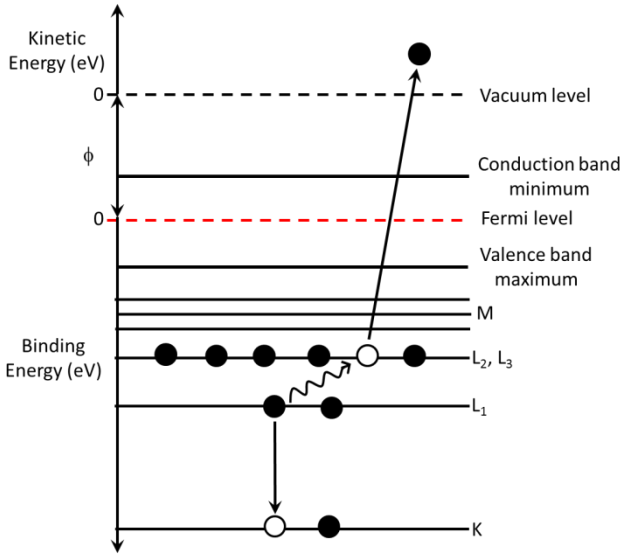

Figure 5.5. Energy diagram of Auger (KL1L2) process. X-ray photon emits and electron form orbital K, an electron from L1 fill the hole in K and transfer released energy in the form of KE to an electron in orbital L2, which contributes to create an Auger peak.

Satellite Peaks: Satellite peaks are observed near the core level peaks in XPS spectrum collected using non-monochromatic x-ray source. Origin of these peaks is the existence of several x-ray lines except Kα in non-monochromatic source.

Ghost Peaks: It is possible metal anode in XPS can get contaminated, such as with carbon, oxygen and in case of two anode system from the other source, and the accelerated electrons can hit at the other parts of the source interior [18]. When this happens, the x-ray core level peaks and ghost peaks are generated since the binding energy is referred to x-ray source energy. ***Plasmon Peaks:*** Plasmon peaks are energy loss

peaks of photoelectrons that lose their energy due to interband transitions and /or collective oscillation (Plasmons). As discussed earlier, these peaks can be used to determine the band gap of the material.

III. **Ultraviolet Photoelectron Spectroscopy:**

Unlike XPS, UPS system uses a noble gas plasma discharge generated photons. An electric field is used to accelerate electrons and ionize the gas to emit photons in a discharge lamp. In this research helium (He) gas of purity research grade (99.9999%) is used as photon source. Helium can produce two lines He(I) and He(II) of energy 21.22 eV and 40.82 eV, respectively. Line I corresponds to light photons produced from neutral atoms and line II corresponds to light photons produced from singly ionized atoms. A beam of photons (~3 mm) is focused to the material surface to emit photoelectrons. The low energy photons in UPS system allow emitting photoelectrons from valence band and the penetration depth is ~1 nm. Other than He gas, Ar and Ne can also be used to change the photon energy. Like He, Ar and Ne also generate two lines (I and II). The minimum energy photons are produced by Ar(I), i.e. 11.7 eV, and the maximum energy photons are produced by He(II), i.e. 40.8 eV [17]. Analyzer used here is VSW HA50. An UPS spectrum gives the valence band maximum with respect to the fermi level and electron affinity of the material being characterized.

Characterization:

1. Valence Band Maximum:

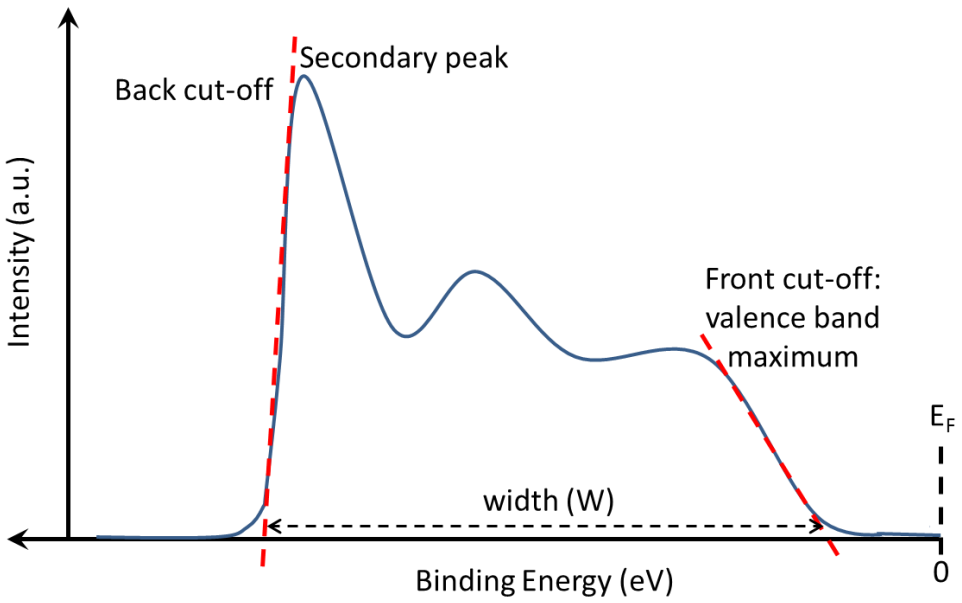

Figure 5.6. Schematic UPS spectrum showing valence band maximum with respect to Fermi level, back cut off, secondary peak and spectrum width.

An UPS spectrum gives the direct information of the valence band maximum (VBM) value. The front cut-off of the spectrum gives the position VBM with respect to the Fermi level, Figure 5.6.

2. **Electron Affinity**:

Electron affinity of a material is defined as the amount of energy released when an electron is added to a material. Using UPS, spectrum electron affinity value can be calculated using following equation:

$$\chi = h\nu - W - E_g \quad (6)$$

where, χ is the electron affinity, $h\nu$ is the ups source photon energy, W is the UPS spectrum width, E_g is the material band gap.

IV. Band Diagram:

The data measured using XPS and UPS can be used to determine the band diagram (band bending and band alignment) of a material. In case of a thin film (Al_2O_3) and substrate (ZnO) heterostructure, the valence band offset (VBO) method by Waldrop and Grant [20], and Kraut [21] is used in this study.

$$\Delta E_V = (E_{CL} - E_V)_{Al2O3} - (E_{CL} - E_V)_{ZnO} + \Delta E_{CL} \quad (8)$$

where ΔE_V is the VBO, E_{CL} is the XPS core level energy, E_V is the UPS VBM, $(E_{CL} - E_V)_{Al2O3}$ is the difference between the core level and VBM in Al_2O_3, $(E_{CL} - E_V)_{ZnO}$ is the difference between the core level and VBM in ZnO and ΔE_{CL} is the difference between Al_2O_3 and ZnO core level binding energy. The conduction band offset is calculated using the value of valence band offset using following equation:

$$\Delta E_C = E_{g,Al2O3} - E_{g,ZnO} - \Delta E_V \quad (9)$$

where ΔE_C is the conduction band offset, $E_{g,Al2O3}$ and $E_{g,ZnO}$ are band gap of Al_2O_3 and ZnO, respectively.

The process to determine the VBO in Al_2O_3 and ZnO is given in Figure 5.7. To draw a band diagram of ZnO and Al_2O_3 VBM, VBO and band bending is required. XPS is used to measure ZnO 2p and Al_2O_3 2p core levels and UPS is used to measure VBM of ZnO and Al_2O_3, which gives information of band bending and VBO at the interface of ZnO and Al_2O_3, respectively. VBO is calculated using equation 8 and band bending is calculated using following equation:

$$\text{Band Bending} = (E_{CL} - E_V)_{ZnO} + E_g - E_{CL} + E_C \quad (9)$$

where E_{CL} is the ZnO core level, E_V is the ZnO VBM, E_g is the ZnO band gap and E_C is the ZnO conduction band minimum. As reported by Waldrop [20] and Grant [21], the distance between the core level and VBM remains constant for a given material, which

implies the ZnO core level 2p and VBM shift in the same direction with same binding energy due to charges induced at the interface after Al_2O_3 deposition or change in internal carrier concentration of ZnO, Figure 5.8.

XPS data can independently determine the band bending since the VBM and core level difference remains constant.

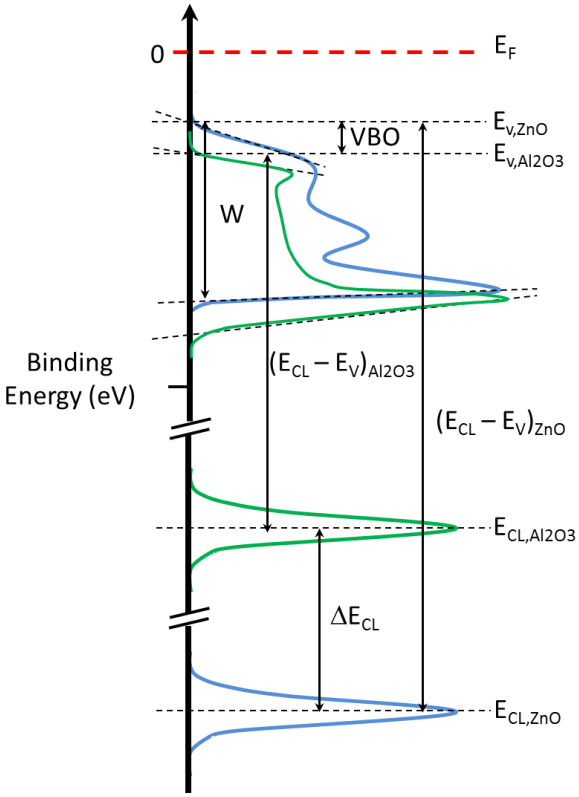

Figure 5.7. Schematic of VBO determinations in Al_2O_3 and ZnO heterostructure.

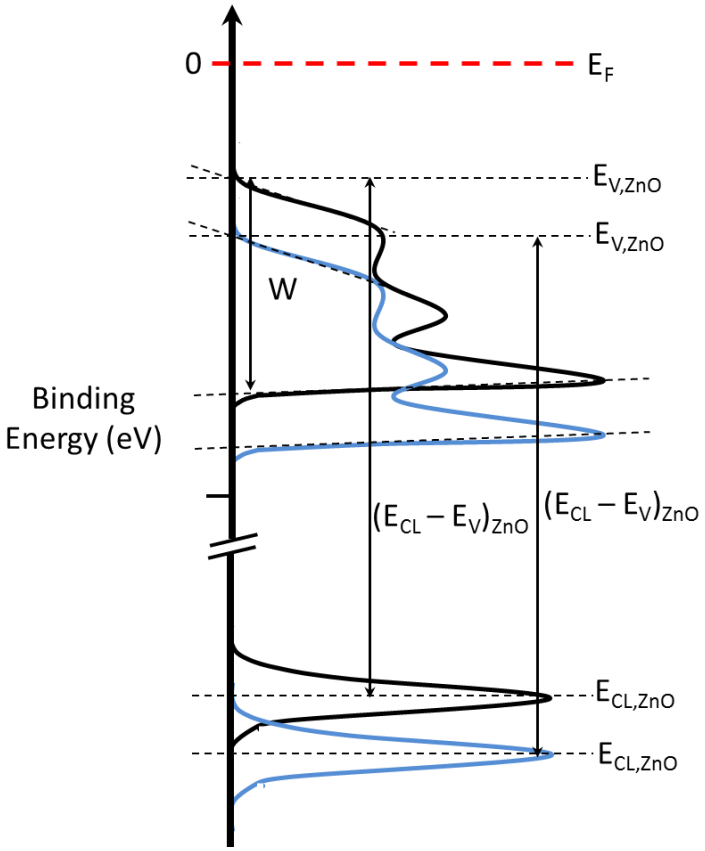

Figure 5.8. Schematic of change in ZnO core level and VBM and constant $(E_{CL} - E_V)_{ZnO}$.

References:

[1] D. Briggs, et. al., Practical Surface Analysis, Vol. 1 Auger and X-ray Photoelectron Spectroscopy, 2nd edition (John Wiley & Sons,West Sussex, 1990).

[2] C. C. Chusuei and D. W. Goodman, *Texas A&M University.*

[3] S. Zhang, L. Li and A. Kumar, "Materials Characterization Techniques" Taylor and Francis (2009).

[4] D. B. Wittry and N. C. Barb, "X-ray Crystal Spectrometers and Monochromators in Microanalysis", *Microsco. Microanal.* **7** (2001) 124.

[5] Z. W. Chen, Walter M. Gibson, and Huapeng, "Huang High Definition X-Ray Fluorescence: Principles and Techniques", *X-Ray Optics and Instrumentation* **2008** (2008) 318171.

[6] J.F. Moulder, W.F. Stickle, P.E. Sobol, K.D. Bomben, Handbook of X-ray photoelectron spectroscopy (Waltham: Perkin-Elmer Corporation, 1992).

[7] D. A. Cole, J. R. Shallenberger, S. W. Novak, R. L. Moore, M. J. Edgell, S. P. Smith, C. J. Hitzman, J. F. Kirchhoff, E. Principe, W. Nieveen, F. K. Huang, S. Biswas, and K. Jones, "SiO2 thickness determination by x-ray photoelectron spectroscopy, Auger electron spectroscopy, secondary ion mass spectrometry, Rutherford backscattering, transmission electron microscopy, and ellipsometry" *J. Vac. Sci. Technol.* B**18** (2000) 440–444.

[8] C. Zhu, M. Kaur, F. Tang, X. Liu, D. J. Smith, and R. J. Nemanich,"Band alignment of vanadium oxide as an interlayer in a hafnium oxide-silicon gate stack structure" *J. Appl. Phys.* **112** (2012) 084105.

[10] F. G. Bell and L. Ley, "Photoemission-Study of SiOx (0 Less-Than-or-Equal-to x Less-Than-or-Equal-to 2) Alloys" *Phys. Rev. B* **37**, 8383 (1988).

[11] H. Nohira, W. Tsai, W. Besling, E. Young, J. Petry, T. Conard, W. Vandervorst, S. De Gendt, M. Heyns, J. Maes, and M. Tuominen, "Characterization of ALCVD-Al2O3 and ZrO2 layer using X-ray photoelectron spectroscopy" *J. Non-Cryst. Solids* **303**, 83 (2002).

[12] M. Bär, M. Rusu, S. Lehmann, Th. Schedel-Niedrig, I. Lauermann, and M. C. Lux-Steiner, "The chemical and electronic surface and interface structure of CuGaSe2 thin-film solar cell absorbers" *Appl. Phys. Lett.* **93**, 232104 (2008).

[13] J. Yang, B. S. Eller, M. Kaur, and R. J. Nemanich, "Characterization of plasma-enhanced atomic layer deposition of Al2O3 using dimethylaluminum isopropoxide" *J. Vac. Sci. Technol. A* **32**, 021514 (2014).

[14] E. Bersch, S. Rangan, R. A. Bartynski, E. Garfunkel, and E. Vescovo, "Energy gap and band alignment for (HfO2)(x)(Al2O3)(1-x) on (100) Si" *Phys. Rev. B* **78** (2008) 085114.

[15]. Miyazaki, *J. Vac. Sci. Technol. B* **19** (2001) 2212.

[16] H. Y. Yu, M. F. Li, B. J. Cho, C. C. Yeo, M. S. Joo, D.-L. Kwong, J. S. Pan, C. H. Ang, J. Z. Zheng, and S. Ramanathan, *Appl. Phys. Lett.* **81** (2002) 376.

[17] "UVL Ultra-violet Source," *Thermo Electron Corporation* Application Note: AN30058_E (2008).

[18] Casa XPS, CasaXPS software Ltd. 2013.

[19] R. Smart, S. McIntyre, M. Bancroft, I. Bello *et al.*, *U. Hong Kong, Dept. Phys*.

[20] J. R. Waldrop and R. W. Grant, "Measurement of AlN/GaN (0001) heterojunction band offsets by x-ray photoemission spectroscopy" *Appl. Phys. Lett*. **68** (1996) 2879.

[21] E. A. Kraut, R. W. Grant, J. R. Waldrop and S. P. Kowalczyk, Heterojunction Band Discontinuities: Physics and Device Applications, edited by F. Capasso and G. Margaritondo (Elsevier, New York, 1987).

RESEARCH

CHAPTER 6. PHOTOCHEMICAL REACTION PATTERNS ON HETEROSTRUCTURES OF ZnO ON POLARITY PATTERNED LITHIUM NIOBATE

Abstract: The internal electric field in $LiNbO_3$ provides a driving force for heterogeneous photocatalytic reactions, where photoexcited holes or electrons can participate in redox reactions on positive and negative domain surfaces and at the domain boundaries. One of the methods to characterize the surface chemical reactivity is photoinduced Ag deposition by immersing the $LiNbO_3$ in an aqueous $AgNO_3$ solution and illuminating with above bandgap light. Reduction of Ag^+ ions leads to the formation of Ag nanoparticles at the surface, and a high density of Ag nanoparticles indicates enhanced surface photochemical reactions. In this study, an n-type semiconducting ZnO layer is deposited on polarity patterned $LiNbO_3$ (PPLN) to modulate the surface electronic properties and impact the surface redox reactions. After plasma enhanced atomic layer deposition (PEALD) of 1, 2, 4 and 10 nm ZnO thin films on PPLN substrates, the substrates were immersed in aqueous $AgNO_3$ and illuminated with above band gap UV light. The Ag nanoparticle density increased for 1 and 2 nm ZnO/PPLN heterostructures, indicating an enhanced electron density at the ZnO/PPLN surface. However, increasing the ZnO thickness beyond 2 nm resulted in a decrease of the Ag nanoparticle density and the formation of large clusters. The increase in nanoparticle density is related to the photoexcited charge density at the ZnO/PPLN interface and the presence of a weakly adsorbed Stern layer at the ZnO surface. The decrease in the

nanoparticle density for thicker ZnO is attributed to photoexcited electron screening in the ZnO layer that suppresses the electron flow from the $LiNbO_3$ to the ZnO surface.

I. Introduction:

Photochemical redox reactions have been used for various processes such as splitting water into H_2 and O_2 [1, 2], converting CO_2 and water into fuel [3] and removing organic and inorganic compounds from contaminated water [4, 5]. For photocatalytic processes involving semiconductors or oxides, above band gap light excites electrons and holes, which can transport to the surface and react with chemical species, provided that the redox potential of the reacting species is within the semiconductor or oxide bandgap [1, 2, 6]. The redox reaction rate is controlled by the number of carriers available at the surface, which is influenced by the recombination and generation rates. The recombination rate is affected by bulk defects and surface states, while the generation rate is controlled by the absorption of light near the surface of the photocatalyst.

A recent review discusses mechanisms where the internal electric field in ferroelectrics can separate photoinduced charge carriers and enhance the efficiency of photocatalytic processes [2]. Ferroelectric polarization and polar surfaces have been described as a source of internal fields [2]. Materials such as $LiNbO_3$ and $BaTiO_3$, are among the group of ferroelectrics with bandgaps that enable photocatalytic processes and that exhibit an internal electric field that can lead to separation of the photoexcited carriers. Consequently, surface photochemical reactions display enhanced efficiency for these materials [2, 6]. Specifically, enhanced reduction efficiency has been shown on positive $LiNbO_3$ and $BaTiO_3$ domain surfaces for photoinduced metal nanoparticle deposition [7, 8, 9].

Lithium Niobate ($LiNbO_3$) has previously been explored for photochemical efficiency in bulk, powder and nanowire forms [2, 3, 6, 9, 10, 11]. Polarity patterned $LiNbO_3$ crystalline surfaces have been used for photochemical reactions, where the reduction and oxidation reactions are spatially separated on the different polarity domains [2, 3, 6]. However, to improve the $LiNbO_3$ photochemical reaction efficiency, recent efforts have employed multi-phase $LiNbO_3$ nanowires [9], multi-crystalline powders ($LiNbO_3$ and $LiNb_3O_3$) [10], Fe doped $LiNbO_3$ [6] and Ag loaded $LiNbO_3$ [12]. Another method to improve the photochemical reaction efficiency is to use a semiconductor and ferroelectric heterostructure. Burbure *et. al.* have prepared $TiO_2/BaTiO_3$ heterostructures that led to an enhancement of the photochemical reaction efficiency. They demonstrated two phenomena: (i) photoinduced charge transfer from $BaTiO_3$ to the TiO_2 surface [13], and (ii) Ag^+ reduction that reflects the $BaTiO_3$ polarity pattern irrespective of TiO_2 crystal orientation [14]. The results indicated that the $BaTiO_3$ electric field controls the surface reactions of $TiO_2/BaTiO_3$ heterostructures. Here we investigate ZnO and ferroelectric lithium niobate ($LiNbO_3$) to form a semiconductor/ferroelectric heterostructure. The band gap of ZnO is 3.4 eV, which is less than the 3.9 eV bandgap of $LiNbO_3$. It has a much smaller spontaneous polarization of 0.05 C/m^2 [15], which can be neglected compared to the 0.71 C/m^2 spontaneous polarization of $LiNbO_3$ [16, 17]. The oxide heterostructures can serve two purposes: (i) reduction of defect states at the ferroelectric surface [18], and (ii) enhancement of the photoexcited charge separation process [14, 13]. The goal of this study is to modulate polarity patterned lithium niobate (PPLN) surfaces with ZnO thin films to understand how photocatalytic processes may be influenced by the heterostructure properties.

In $LiNbO_3$, the positive polarization charge terminated surface is termed as +c and the negative polarization charge terminated surface is termed as –c. In general, the polarization surface bound charge can be screened by free carriers, ionized impurities, defects (internal screening), charged adsorbed species, and/or surface states (external screening) [19, 20]. As shown in Figure 6.1, the polarization bound charge at $LiNbO_3$ surfaces is predominantly screened by external charges due to the low carrier concentration (10^{12} cm^{-3}) [17, 19]. The electric field induced by the polarization bound charge influences the photoinduced charge carrier density by displacing electrons towards the positive surface (+c) and holes towards the negative surface (–c).

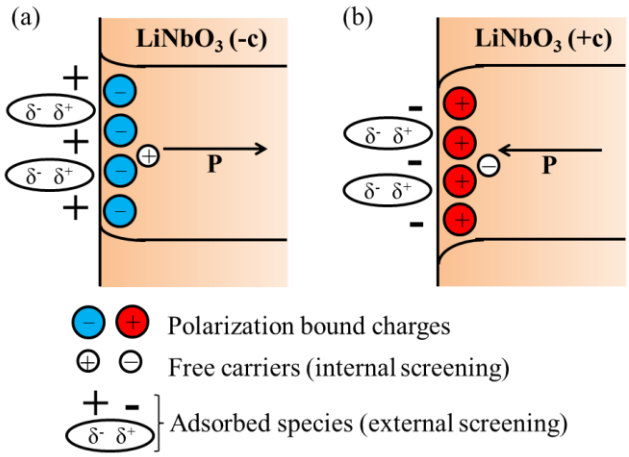

Figure 6.1. Schematic of ferroelectric $LiNbO_3$ shows (a) negative polarization bound charge on -c domain and (b) positive polarization bound charge on +c domain. In $LiNbO_3$, due to free carrier deficiencies in bulk, the surface is externally screened with oppositely charged adsorbed species by forming a Stern layer.

Among oxides, ZnO is a promising candidate as an electron transport layer due to its relatively high mobility and optical transparency. Wide band gap zinc oxide (ZnO)

thin films have been used for numerous applications in electronic and optical devices and have been more recently considered as photocatalysts and charge transfer layers in photovoltaic heterostructures [2-4, 24]. ZnO thin films and nanostructures can be used as efficient photocatalysts and are, in some cases, preferred over TiO_2 due to a higher absorption coefficient [5]. Despite the wide band gap, ZnO is typically an n-type semiconductor with a high internal carrier concentration ($1 \times 10^{16} - 1 \times 10^{18}$ cm^{-2}) [21-22]. The n-type character of ZnO, which is still an area of research, has been attributed to a number of effects including interstitial hydrogen, impurities and oxygen vacancies [22].

Photoinduced nanopattern formation on polarity patterned lithium niobate (PPLN) is a photocatalytic process that has shown Ag nanowire formation and preferred Ag nanoparticle deposition on domain boundaries and positive domains, respectively [7, 8, 11, 23]. Ag nanoparticle deposition is enabled by photoexcited electrons that reduce Ag^+ ions. Shown in Figure 6.2 are the reduction potential of Ag^+ to Ag, the oxidation potential of OH^- and H_2O, and the bandgap position of +c $LiNbO_3$, –c $LiNbO_3$ and ZnO [17, 24]. The structure and pattern of the photoinduced nanoparticle deposition on periodically poled ferroelectric materials is influenced by the availability of photoexcited charge carriers at the surface [6, 8, 17]. A major focus of this study is to examine the effect of ZnO film thickness on PPLN photochemical surface reactivity. This study addresses how the n-type carrier concentration and thickness of ZnO affects photoexcited electron transport from $LiNbO_3$ as evidenced by the observed Ag nanoparticle pattern and density

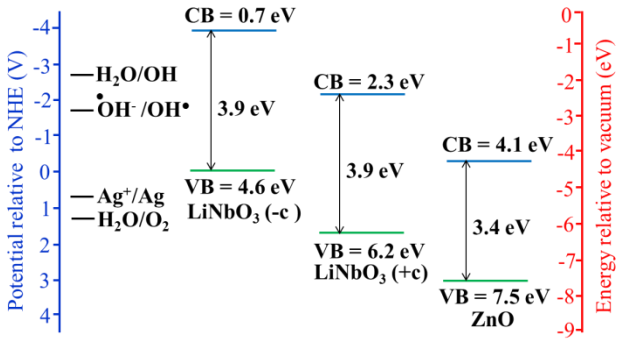

Figure 6.2. Redox potential of H_2O, hydroxyl ion (OH^-) and Ag^+ vs normal hydrogen electrode (NHE) with respect to $LiNbO_3$ negative (-c) and positive (+c) domain and ZnO conduction band minimum (CBM) and valence band minimum (VBM) position relative to vacuum level.

Plasma enhanced atomic layer deposition (PEALD) is a sub-monolayer deposition process that can achieve uniform, conformal ZnO thin films [25]. In this study, ZnO/PPLN heterostructures were prepared with various ZnO thicknesses (1, 2, 4 and 10 nm) using a PEALD process. To understand the photochemical reactivity of the ZnO/PPLN heterostructures, photoinduced deposition was carried out by illuminating the heterostructures with 254 nm (4.9 eV) and 350 nm (3.5 eV) UV light, which are above and below the band gap of $LiNbO_3$. The variation in the Ag nanoparticle pattern with the ZnO thickness provides insight into the charge transfer processes in ZnO/PPLN heterostructures and the photocatalytic redox reactions at the surface.

II. Experiment:

A. PEALD ZnO on PPLN:

This study employs plasma enhanced atomic layer deposition of ZnO thin films on periodically poled $LiNbO_3$ polished substrates which were purchased from Crystal Technologies. The 6 mm x 4 mm x 0.5 mm $LiNbO_3$ substrates were double side polished

with an ~20 μm period, lithographically patterned, polarity grating and c-axis surfaces with periodically arranged positive (+c) and negative (–c) domains separated by 180º domain boundaries. An ultrasonic chemical (acetone and methanol) clean was used to prepare the PPLN surfaces prior to PEALD. The ZnO thin films of different thicknesses (1, 2, 4 and 10 nm) were deposited at 130 ºC using dimethyl zinc (DMZ) as the precursor and oxygen plasma as the reactant with 0.35 second and 8 second exposures, respectively. The precursor and plasma steps were separated by 40 sec N_2 purge steps. The observed PEALD ZnO growth rate was determined to be ~2.1 Å/cycle using Rutherford Backscattering Spectrometry (RBS). The sub-monolayer two step atomic layer deposition requires reactive sites to initiate the reaction of the chemical precursor molecules at the substrate surface [26]. Prior to the PEALD process, the surface was treated with an O_2 plasma for 10 sec, to remove the surface adsorbed impurities that can act as reactive sites for PEALD nucleation. In addition, the initial plasma treatment provides a surface with reactivity similar to that after each growth cycle.

B. PFM of PPLN and ZnO/PPLN:

Piezo force microscopy (PFM) can be used to image the polarity domains of ferroelectric substrates. PFM detects the signal from the $LiNbO_3$ surface as it expands or contracts due to the converse piezoelectric effect induced by the applied potential. The $LiNbO_3$ domain expands or contracts if the applied electric field (E_{ap}) is parallel or anti-parallel to the spontaneous polarization (P_s), respectively (Figure 6.3). The spontaneous polarization of the +c or –c surfaces points toward or away from the surface, respectively. An Asylum Research Molecular Force Probe (MFP) 3D was used to image the domains in an ambient environment. PFM was performed before and after ZnO deposition with

conductive (Pt/Ir coated Si) tip probes (PPP-EFM, Nanosensors) of radius 30 ± 10 nm, spring constant of k = 0.5 to 9.5 N/m, resonance frequency between 45-115 kHz, and resistivity of 0.01 – 0.02 Ωcm. The periodic structure of PPLN is evident in the PFM phase image, where the color contrast represents the opposite polarity domains, Figure 6.4 a. After ZnO deposition on PPLN, a higher tip voltage (V_{ac}) was required to image the domains. The tip voltage used for PPLN and (1 nm – 10 nm) ZnO on PPLN was between ~250 mV to 950 mV. For each sample the tip voltage was adjusted to obtain the same cantilever signal from the photodetector. This signal is directly related to the material oscillation amplitude.

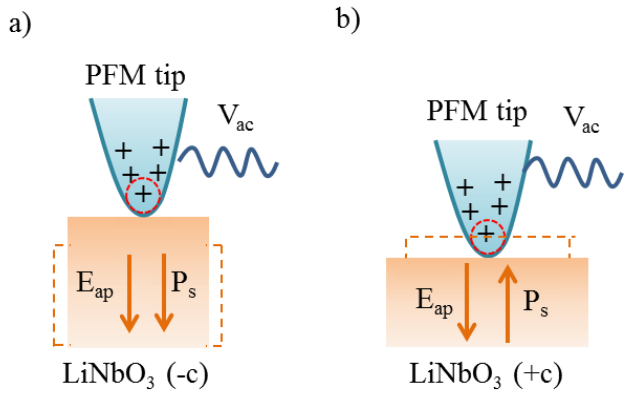

Figure 6.3. Schematic of piezoelectric effect in $LiNbO_3$ with applied tip voltage (V_{ac}). a) and b) $LiNbO_3$ negative domain (-c) and positive domain (+c) expands and contracts with the applied electric field aligning parallel and antiparallel to spontaneous polarization, respectively.

The electric field strength experienced by the ferroelectric material is affected by the top surface layer thickness (d) [26] and the presence of free carriers. For the case of a dielectric top layer, the electric field strength is inversely related to the thickness; however, for metals, the free carriers can completely screen the applied electric field.

Consequently, a semiconductor layer can reduce the applied electric field strength through an increase in thickness or through the free carrier concentration. For a dielectric between the PFM tip and surface, the electric field (E_{ap}) near the ferroelectric surface is given as [26]:

$$E_{ap} \propto V_{ac}/d \qquad (1)$$

where V_{ac} is the applied oscillating tip voltage and d is the distance from the tip to the ferroelectric surface. It is evident from equation (1) that with an increase in the distance between the tip and ferroelectric surface, the electric field strength experienced by the ferroelectric material decreases if V_{ac} is kept constant. The ZnO thickness increases the distance between the PFM tip and PPLN surface, and a higher tip voltage is required to obtain the same displacement.

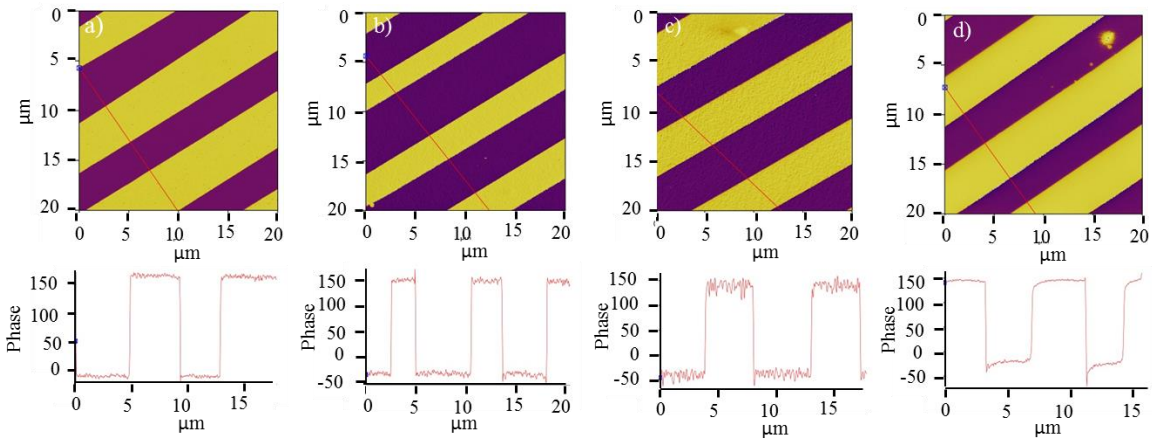

Figure 6.4. PFM phase image of a) bare PPLN, b) 1 nm ZnO/PPLN, c) 4 nm ZnO/PPLN and d) 10 nm ZnO/PPLN. The bottom phase vs width (µm) plots show 180° difference in the alternate opposite polarity domains of PPLN along the red line drawn on respective phase images.

C. Photoinduced Ag nanoparticle deposition on PPLN and ZnO/PPLN:

To establish the surface reactivity and charge transfer processes, Ag nanoparticle deposition was carried out on the ZnO/PPLN heterostructures and compared with the well-studied photoinduced deposition of Ag nano-patterns on bare PPLN [7, 8, 11, 23]. Prior to photoinduced deposition, the PPLN or ZnO/PPLN substrates were sonicated in methanol for 1 minute and dried with N_2 gas. The cleaned sample surfaces were covered with a 35 µL droplet of a 0.00001 M $AgNO_3$ solution and illuminated with 254 nm (4.9 eV) or 350 nm (3.5 eV) UV light of intensity ~1100 µW/cm^2 for 8 min. The illumination was obtained using a 100 W Hg lamp with line filters. After UV illumination, the samples were immersed in deionized water for 1 minute followed by a N_2 blow dry. The photoinduced Ag nanoparticle pattern was obtained using AFM in tapping mode, with non-conducting Si probes of spring constant k = 13-77 N/m and resonance frequency of ~200-400 kHz.

D. Electron Microscopy:

An aberration corrected JEOL ARM200F (200 kV) was employed to determine the thickness and crystallinity of the ZnO after Ag nanoparticle deposition for the 1 and 2 nm ZnO/PPLN heterostructures. The images were obtained using both bright field (BF) and high angle annular dark field (HAADF) configurations. Energy dispersive x-ray spectroscopy (EDX) was used to spatially locate the ZnO layers and identify the Ag nanoparticles.

III. Results:

A. Piezoelectric force microscopy (PFM) on PPLN and ZnO/PPLN surfaces:

PFM was used to measure the piezo response of PPLN +c and –c domains. As shown in the PPLN PFM phase scan in Figure 6.4 a, the alternate domains show color

contrast, differentiating the +c and –c domains. In addition, the PPLN domain contrast is also visible with 2 nm, 4 nm and 10 nm PEALD ZnO films, Figure 6.4 b – d. However, as the ZnO thickness was increased, a higher tip voltage (V_{ac}) was required to achieve the same tip displacement, Figure 6.5. The linear increase with thickness suggests that the screening is due to the dielectric layer thickness and the screening effect due to free carriers is not significant.

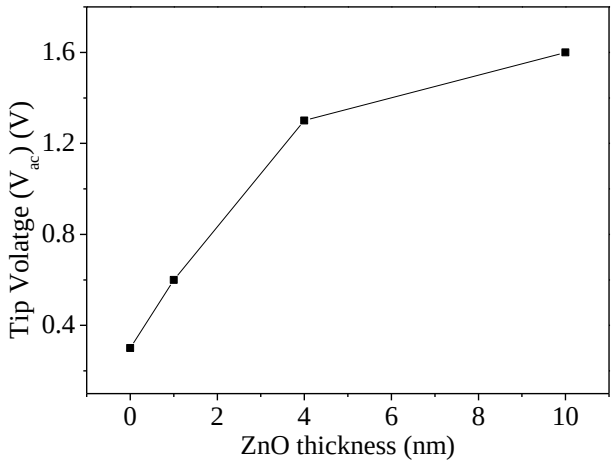

Figure 6.5. PFM tip voltage (V_{ac}) at 11 mV amplitude vs ZnO thickness plot shows the increase in V_{ac} with the increase in ZnO thickness.

B. Photoinduced Ag nanoparticle deposition on PPLN and ZnO/PPLN:

The resultant Ag nanoparticle patterns on PPLN and ZnO/PPLN heterostructures after photoinduced deposition are shown in Figures 6.6, 6.7 and 6.8. Two control experiments were conducted to exclude the possibility of unexpected surface reactions. In the first control experiment the PPLN sample was immersed in a 35 μL $AgNO_3$ solution in the absence of UV light. The AFM scan, in Figure 6.6 a, showed a smooth surface with an absence of Ag nanoparticles, which ruled out the possibility of direct reaction of ZnO with $AgNO_3$ in water. In the second control experiment, photoinduced Ag nanoparticle

deposition using 350 nm (3.5 eV) UV light illumination was performed on 2 nm ZnO/PPLN to analyze the contribution of electrons photoexcited in the ZnO. In this case, the photon energy is above the ZnO bandgap but below the $LiNbO_3$ bandgap. The AFM image shows sparse Ag nanoparticles irrespective of the +c and –c $LiNbO_3$ domains, Figure 6.6 b. This indicates the ZnO photoexcited electrons have a negligible contribution to the Ag^+ photoreduction.

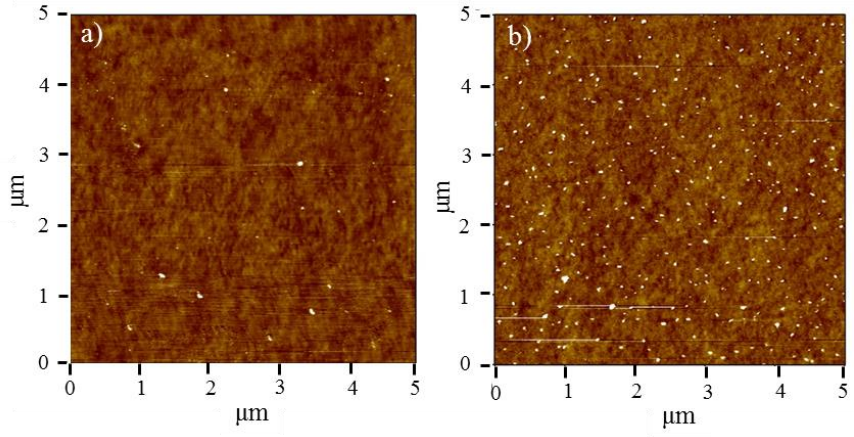

Figure 6.6. AFM scan of Ag nanopattern on 2 nm ZnO/PPLN a) with no UV light illumination and b) with 350 nm (3.5 eV) UV light illumination.

The AFM images of photoinduced Ag nanopatterns on PPLN and 1, 2, 4 or 10 nm ZnO on PPLN are shown in Figures 6.7 and 6.8. All photodepositions were conducted under similar conditions of UV wavelength, exposure time, intensity, and $AgNO_3$ concentration. The Ag nanoparticle patterns on the PPLN and ZnO/PPLN samples are summarized below:

Pattern of Ag nanoparticles on +c and –c domains: AFM images show the deposition of Ag nanoparticles is spatially enhanced on PPLN +c domains compared to –c domains, Figure 6.7 a. For the 1 nm ZnO on PPLN structures, an increased density of nanoparticles

was observed on both domains. A higher density of Ag nanoparticles was maintained on the +c domain surface compared to the –c surface, Figure 6.7 b. As the ZnO thickness increases to 2 nm, the nanoparticle density further increases on the negative domain and appears to be comparable to that on the positive domain. There is a notable change in the Ag nanoparticle pattern for ZnO films ≥ 4 nm, Figure 6.8 a – c. In this case, large agglomerated clusters are observed which are not evidently correlated with the domains.

Ag nanoparticles at domain boundaries: Preferential Ag nanoparticle deposition is observed along the domain boundaries on PPLN and on 1 and 2 nm ZnO/PPLN heterostructures. For 1 nm ZnO on PPLN the domain boundary nanoparticles are larger and show a higher density, Figure 6.7 b. The height vs width profiles of the AFM topography image shows the domain boundary width for 1 nm ZnO/PPLN is ~2 times (2.2 μm) larger than on bare PPLN (1 μm), Figure 6.7 d – e. In the AFM scan of the 2 nm ZnO/PPLN, the domain boundary nanoparticle density and width appears to be reduced compared to PPLN.

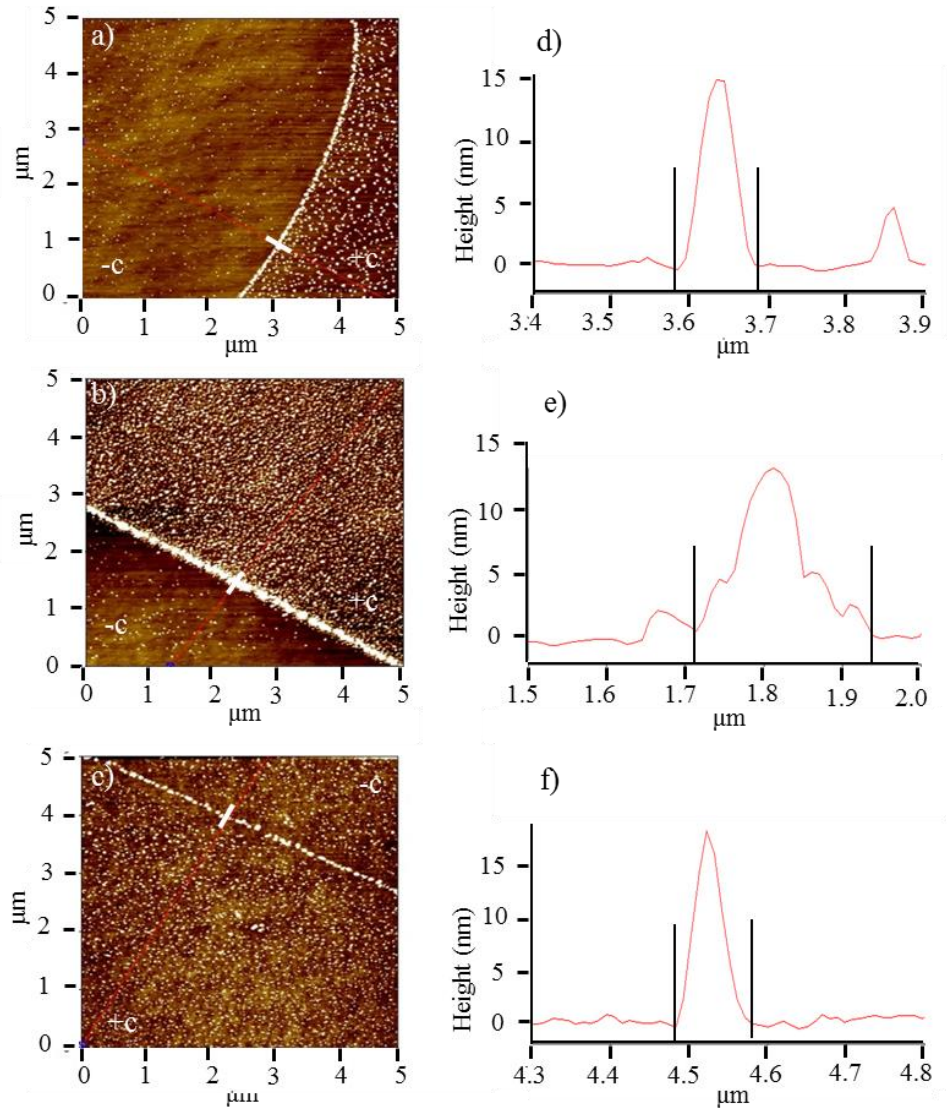

Figure 6.7. The AFM scans of photoinduced Ag nanoparticle pattern on a) bare PPLN, b) 1nm ZnO/PPLN and c) 2nm ZnO/PPLN. The –c and +c represents positive and negative domains of PPLN, respectively. The width and height profile across the domain boundary separating +c and –c domains shows the Ag nanoparticles size on d) bare PPLN, e) 1nm ZnO/PPLN and f) 2nm ZnO/PPLN.

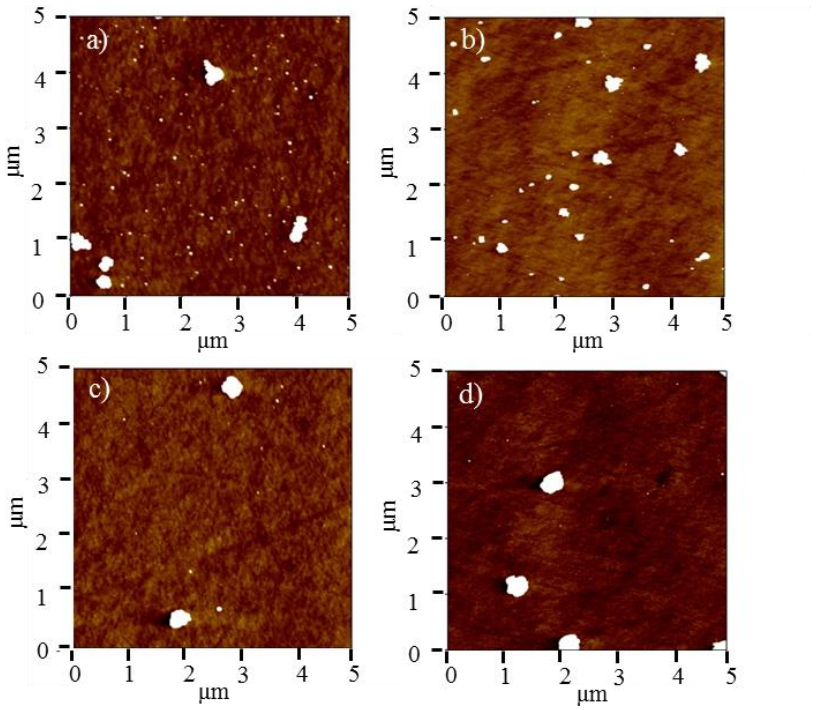

Figure 6.8. The AFM scans (5um x 5 um) of photo-induced Ag nanoparticle pattern on 4 nm ZnO/PPLN, a) using 254 nm UV light and b) 350 nm UV light, and 10 nm ZnO/PPLN, using c) using 254 nm UV light and d) 350 nm UV light.

C. Crystallinity and Thickness of ZnO on PPLN:

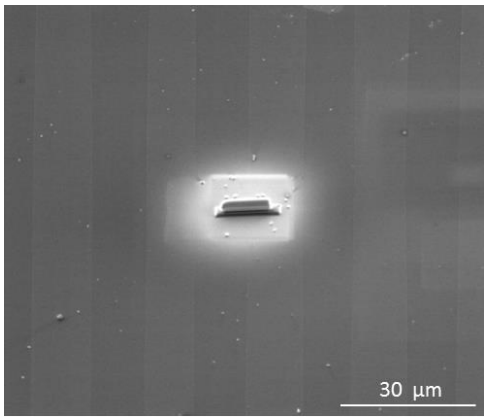

Figure 6.9. SEM image of TEM sample preparation. Light gray and dark gray parallel stripes are PPLN +c and –c domains with 180^0 opposite polarity.

The TEM cross-sections of polarity patterned $LiNbO_3$ were prepared with a domain boundary at the center as shown in Figure 6.9. The crystal structure and thickness of the PEALD 1 and 2 nm ZnO thin films are shown in the TEM images, Figure 6.10. The 2 nm ZnO films exhibit an amorphous structure, between the PPLN surface and Ag nanoparticles, as shown in Figure 6.10 b – d; however, the thicker ZnO films exhibit a crystalline structure [25]. Due to the amorphous structure, the ZnO cannot be differentiated from the amorphous carbon protective layer. The large particle clusters appear to correspond to domain boundary Ag nanoparticles on the 1 and 2 nm ZnO/PPLN, Figure 6.10 a – d. From the TEM images, the height of the nanoparticles at the domain boundaries and domain surfaces on both heterostructures is within the range (7–15nm) measured using AFM, Figure 6.7 e – h. Energy dispersive X-ray (EDX) scans and high angle annular dark field (HAADF) were performed on the same 2 nm ZnO/PPLN sample, Figure 6.11 a – b. The EDX scan shows the Zn K-shell peak confirming ZnO on the surface, Figure 6.11 a. On the same sample, the HAADF image and normalized EDX Zn K-shell peak intensities confirm the 2 nm ZnO thickness, Figure 6.11 b.

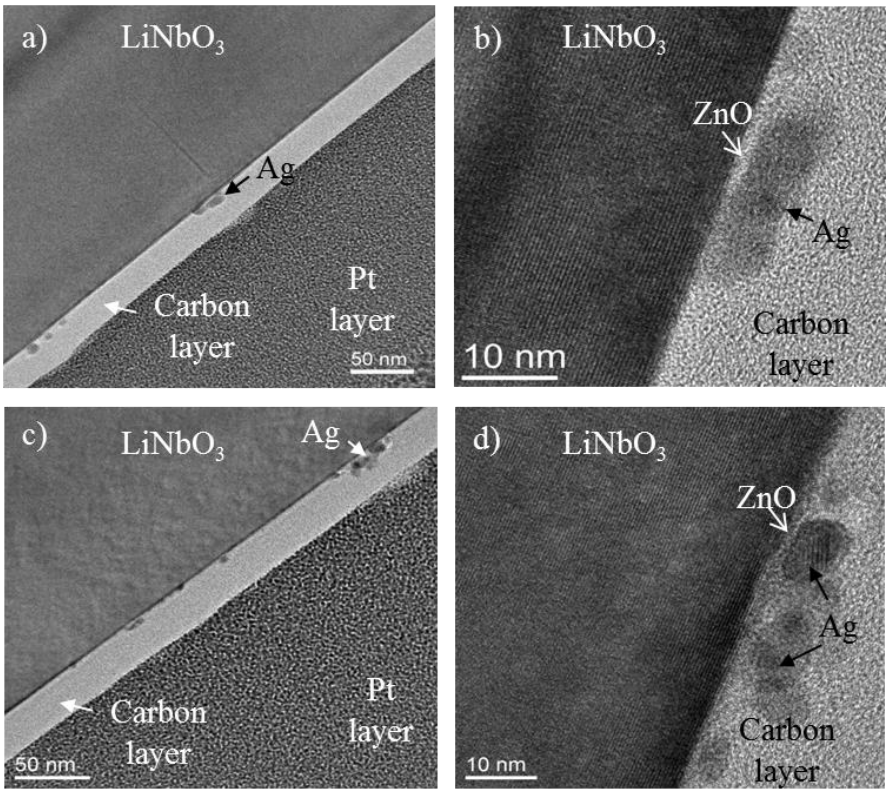

Figure 6.10. TEM images of the photo-induced deposition of Ag nanoparticles on a) and b) 1 nm ZnO/PPLN and c) and d) 2 nm ZnO/PPLN. In all TEM images, clustered Ag nanoparticles on PPLN are visible in all the images. ZnO thin films of thickness 1 nm and 2 nm are sandwiched between Ag nanoparticles and $LiNbO_3$ substrates in b) and d), respectively.

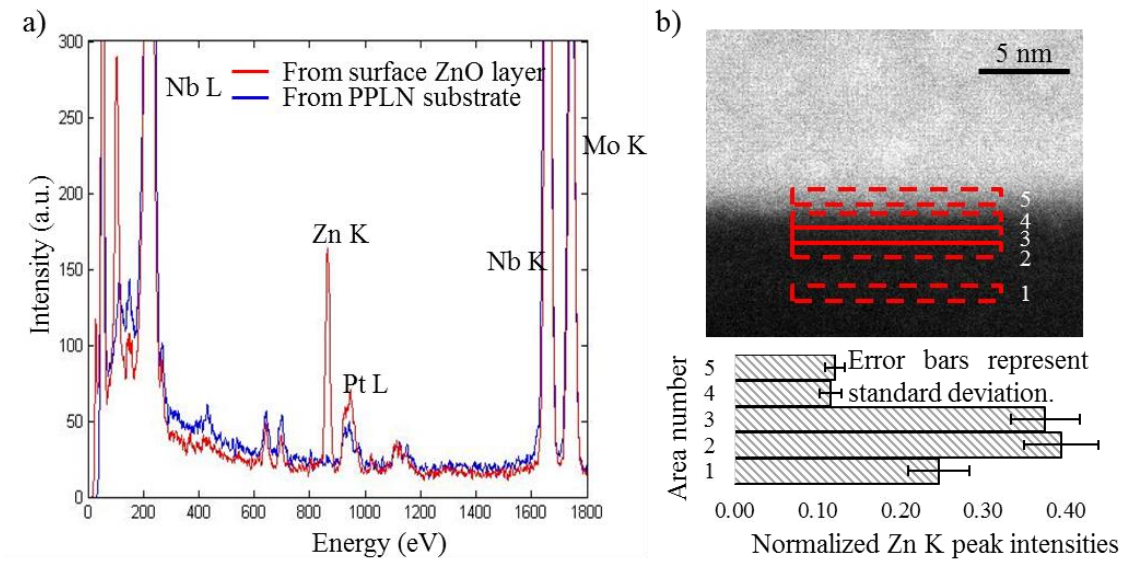

Figure 6.11. a) EDX spectra from both ZnO surface layer and from $LiNbO_3$ substrate showing Zn signal is only detected on the surface. Mo and Pt were introduced when the TEM sample was prepared using the focused ion beam. b) HAADF image of the 2 nm ZnO/PPLN sample and normalized EDX Zn K peak intensities in each area.

IV. Discussion:

The Ag nanoparticle pattern that develops on polarity patterned $LiNbO_3$, shown in Figure 6.12, is ascribed to the process of illumination with above bandgap photons (in this case 4.9 eV). The photoelectrons excited near the $LiNbO_3$ surface drift toward or away from the surface under the influence of the internal electric field and/or diffuse in all directions due to the thermal energies. The available electrons at the surface reduce Ag^+ to Ag which nucleates to form nanoparticles. The photoexcited holes oxidize water molecules to $OH^\bullet$ radicals and H^+ ions, and hydroxyl ions (OH^-) to $OH^\bullet$ radicals [6]. Prior work from our group has noted that the Stern layer can limit the concentration of

Ag^+ ions near the surface, which can lead to a reduced density of randomly deposited nanoparticles [8].

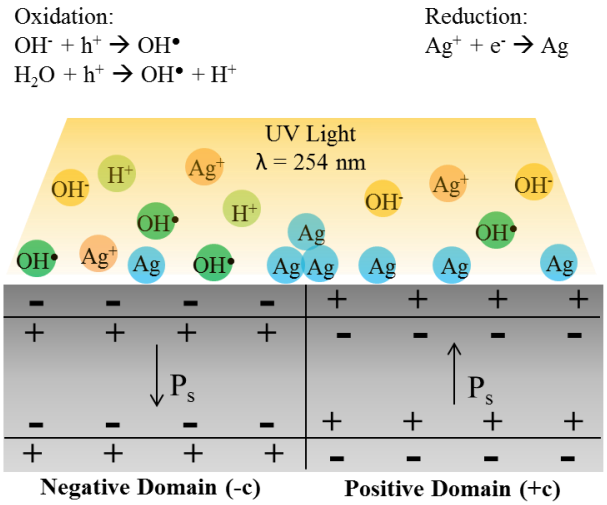

Figure 6.12. Schematic of photoinduced redox reaction on $LiNbO_3$ -c and +c domain surface with UV light (l = 254nm, E = 4.2eV) illumination above the band gap of $LiNbO_3$. Favorable oxidation and reduction reaction on -c and +c domain surfaces, respectively, are shown above.

In this research we observe that ZnO on PPLN results in a change of the Ag nanoparticle density and spatial distribution, indicating a change in the photoexcited electron availability at the surface. For 1 nm ZnO/PPLN heterostructures the overall Ag nanoparticle deposition is enhanced, and the selectivity is maintained. As the ZnO layer is increased to 2 nm, the Ag nanoparticle density on the –c domain surface becomes comparable to that on the +c domain surface. However, for ZnO thicknesses $\geq$ 4 nm, the reduction process changes completely. Here, agglomerated Ag clusters form on the surface with no apparent relationship to the $LiNbO_3$ domains and domain boundaries and the role of the $LiNbO_3$ domains and domain boundaries is no longer evident.

To understand the variation in Ag^+ reduction and the transport of photoexcited electrons from PPLN to the ZnO surface, we have considered the effects of the following three attributes: (i) the band alignment and interface states, (ii) the Stern layer, and (iii) screening due to photoexcited carriers in the ZnO.

A. Band Alignment of ZnO/$LiNbO_3$ and Interface States:

The favorable flow of photoexcited electrons and holes from one material to the other can be understood by the band alignment diagrams at the interface of a heterojunction [2, 27–29]. The reported average electron affinity of $LiNbO_3$ surfaces is 1.6 eV and that of ZnO is 4.1 eV [17, 24]. Applying Anderson's band alignment model, the ZnO conduction band minimum (CBM) is below the $LiNbO_3$ CBM, and electron transport is favored from $LiNbO_3$ to ZnO, Figure 6.13. According to prior work from our group, the +c and –c domain surfaces have different electron affinity because of the dipole generated by external screening (adsorbed charged molecules and/or ions) [17]. However, for ZnO/PPLN heterostructures, we have considered the average electron affinity of $LiNbO_3$ assuming that the polarization bound charges in PPLN are screened by charges at the ZnO interface. The actual band alignment will be modified by an interface dipole due to the specific interface bonding configuration.

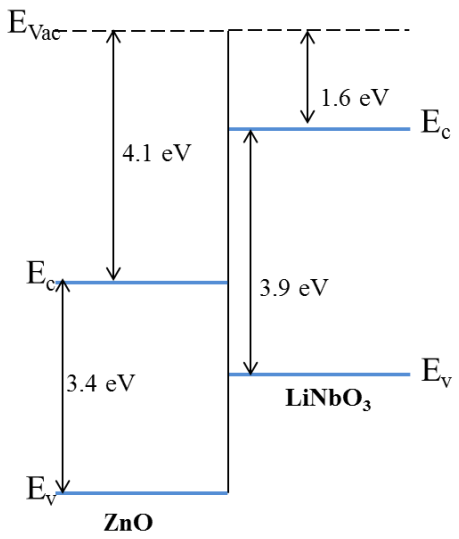

Figure 6.13. Anderson's band alignment model of ZnO and $LiNbO_3$. CBM and VBM of ZnO is below the CBM and VBM of $LiNbO_3$, which favors the electron migration from $LiNbO_3$ +c and -c to ZnO.

It is evident from the pattern of photoinduced Ag nanoparticles on 1 nm and 2 nm ZnO/PPLN heterostructures, that the pattern is controlled by electrons photoexcited in the PPLN. The overall increase in the density of nanoparticles indicates enhanced photoinduced electron migration to the surface. Mechanisms that can increase the electron migration are the reduction of recombination due to interface states, and the band alignment of ZnO/$LiNbO_3$.

B. Stern Layer:

The presence of a partially screened polarization charge will lead to the formation of a Stern layer at the surface of polar materials. The high ZnO electron carrier concentration (1×10^{-18} cm^{-3}) [21-22] apparently contributes to screening of the $LiNbO_3$ polarization bound charge. Consequently, the more effective screening alters the Stern layer composition compared to that for bare $LiNbO_3$. The Stern layer can affect the Ag^+

ion transport to the surface [8], and thus can affect the Ag nanopattern on the ZnO/PPLN heterostructures. For an $AgNO_3$ aqueous solution, the Stern layer consists of Ag^+, NO_3^-, OH^- and dipole water molecules, which can form a densely packed layer to screen the surface charge [8, 30]. The dense layer results in a barrier for Ag^+ ions to reach the surface. With an increase in the ZnO thickness the polarization screening is expected to be more efficient leading to a less dense Stern layer. The existence of a weak Stern layer on ZnO/PPLN heterostructures can enhance the reaction rate and thus increase the density of Ag nanoparticles on both (+c and -c) domain surfaces and domain boundaries.

C. ZnO Electron Screening:

It is well established that external screening is an effective way to compensate the polarization bound charge of $LiNbO_3$ [17]. For ZnO/$LiNbO_3$ heterostructures, photoexcited electrons in the ZnO layer can redistribute to effectively screen the polarization charge. Schwinkendorf *et. al.* and Cagain *et. al.* have studied the accumulation of an electron sheet layer in ZnO at the ZnO/$BaTiO_3$ positive domain interface for field effect transistors and the ZnO/lead zirconate titatnate (PZT) positive domain interface for capacitor structures [31, 32]. At the ZnO/$LiNbO_3$ positive domain interface, the positive polarization bound charge is screened by electrons in ZnO, which consequently reduces the internal electric field. In contrast, for bare PPLN, the incomplete external screening due to adsorbates results in an internal electric field that leads to electron drift to the positive surfaces. With the decrease of the internal electric field, electron diffusion dominates over electron drift, which reduces the Ag nanoparticle selectivity.

The 254 nm UV light used to illuminate ZnO/PPLN excites carriers in both ZnO and PPLN and 350 nm UV light excites carriers only in ZnO. As discussed above, the silver nanoparticle pattern is controlled by the photoexcited carriers in $LiNbO_3$ for 1 and 2 nm ZnO on PPLN. For $\geq$ 4 nm ZnO/$LiNbO_3$, the random pattern of large Ag nanoparticle clusters indicates the Ag cluster formation is independent of the PPLN domains. The large cluster formation is evident on the 4 nm ZnO/PPLN sample surface when photoinduced Ag deposition was performed using 3.5 eV UV illumination, presented in Figure 6.8 b. However, with the illumination of 4.9 eV UV on 4 nm ZnO/PPLN a higher density of small Ag nanoparticles is observed in addition to the clusters, shown in Figure 6.8 a. This indicates that the density of small particles is due to photoexcited electrons from the PPLN which transport to the ZnO surface and reduce Ag^+ ions. In contrast, for 10 nm ZnO/PPLN the absence of small nanoparticles indicates a negligible concentration of photoexcited electrons from the PPLN, in Figure 6.8 c – d. We suggest that the increase in the density of free electrons for the thicker ZnO layer screens the electron transport from PPLN. We note that the PFM images of ZnO/PPLN were not screened by the ZnO carrier concentration as the domains are displayed for all thicknesses, Figure 6.4. However, unlike the PFM measurements, the sample surfaces were illuminated with UV light during the photoinduced Ag deposition process, which photoexcites carriers in the ZnO and enhance the free carrier concentration. The formation of random Ag nanoclusters on both 4 and 10 nm ZnO/PPLN with the illumination of 254 and 350 nm UV light indicates the photoexcited electron density in the ZnO also contributes to the nanocluster formation.

V. Conclusions:

The Ag nanoparticle patterns formed on ZnO/PPLN heterostructures were examined to understand the effect of PEALD ZnO thin films on photoexcited electron transfer and photochemical reactions. AFM was employed to characterize the Ag nanopatterns on PPLN and ZnO/PPLN heterostructures. TEM and was used to verify crystal structure and thickness, and EDX was used for element detection to locate the ZnO thin film. We provide the evidence that 1-2 nm ZnO thin films on both +c and –c PPLN domains change the composition of the Stern layer and reduces the interface state density. We suggest that a weak Stern layer forms at the ZnO/PPLN surface as the PPLN polarization bound charge is screened by the ZnO carrier concentration. Thus, the Ag^+ ions can be more readily accessible to the photoinduced electrons to form Ag nanoparticles. On the other hand, the reduction of interface states can lower the carrier recombination rate and enhance the charge transport to the surface of the ZnO/PPLN surface. It is difficult at this time to say which process is dominant.

The electron diffusion process dominates over electric field assisted electron drift on –c domain surface covered with 1 nm and 2 nm ZnO, which enables an increase in the density of Ag nanoparticles. The band alignment of ZnO and $LiNbO_3$ is appropriate for electron transfer from $LiNbO_3$ to ZnO, which also contributes to enhancing the reaction rate at the surface. However, the thicker ($\geq$ 4 nm) ZnO films evidently impede charge migration from $LiNbO_3$ to the ZnO surface, irrespective of domain surface polarity. We suggest that screening by photoexcited charge carriers in the ZnO creates this effect. This study provides evidence that a limited thickness (< 4 nm) of ZnO on PPLN can increase the photoinduced reaction rate on +c and –c domain surfaces and at the domain

boundaries. A more extensive study could establish the effect of the band gap and band alignment of the metal oxide heterostructures on the photochemical processes.

References:

[1] A. Kudo and Y. Miseki, "Heterogeneous photocatalyst materials for water splitting", *Chem Socie. Rev.* **38** (2009) 253.

[2] L. Li, P. A. Salvador and G. S. Rohrer, "Photocatalysts with internal electric field", *Nanoscale* **6** (2014) 24.

[3] M. Stock and S. Dunn, "$LiNbO_3$ – A New Material for Artificial Photosynthesis", *IEEE Transac. Ultrasonics Ferroelectrics Freq. Contr.* **58**, 0885 (2011)

[4] A. Paracchino, V. Laporte, K. Sivula, M. Gratzel and E. Thimsen, "Highly active oxide photocathode for photoelectrochemical water reduction", Nature Matt. **10** (2011).

[5] Y. Q. Cao, J. Chen, H. Zhou, L. Zhu, X. Li, Z. Y. Cao, D. Wu and A. D. Li, "Photocatalytic activity and photocorrosion of atomic layer deposited ZnO ultrathin films for the degradation of methylene blue", Nanotech. **26**, 024002 (2015).

[6] M. Stock, and S. Dunn, "Influence of the Ferroelectric Nature of Lithium Niobate to Drive Photocatalytic Dye Decolorization under Artificial Solar Light",*J. Phys. Chem.* **116**, 20854 (2012).

[7] Y. Sun, R. J. Nemanich, "Photo-induced Ag deposition on periodically poled lithium niobate: Concentration and intensity dependence" J. Appl. Phys. **109**, 104302 (2011).

[8] Y. Sun, B. S. Eller, and R. J. Nemanich, "Photoinduced Ag deposition on periodically poled lithium niobate: Wavelength and polarization screening dependence" J. Appl. Phys. **110**, 084303 (2011).

[9] K. Saito, K. Koga and A. Kudo, "Lithium Niobate Nanowires for Photocatalytic Water Splitting" *Dalton Trans.* **40** (2011) 3909.

[10] B. Zielinska, E. Borowiak-Palen, R. J. Kalenzuk, "Preparation and Characterization of Lithium Niobate as a Novel Photocatalyst in Hydrogen Generation" *J. Phys. Chem. Solids* **69** (2007) 236.

[11] Y. S. Park, J. H. Kim, and W. Yang, "Comparison Study of Metal Nanoparticles Grown on Polarity Patterned Ferroelectrics by Scanning Probe Microscopy" *Surf. Interface Anal.* **44** (2012) 759.

[12] B. Zielinska, "Photocatalytic hydrogen generation with Ag-loaded $LiNbO_3$" *Mater. Sci.* **37** (2014) 911.

[13] N. V. Burbure, P. A. Salvador, and G. S. Rohrer, "Photochemical Reactivity of Titania Films on $BaTiO_3$ Substrates: Origin of Spatial Selectivity" *Chem. Mater.***22** (2010) 5823.

[14] N. V. Burbure, P. A. Salvador and G. S. Rohrer, "Photochemical Reactivity of Titania Films on $BaTiO_3$ Substrates: Influence of Titania Phase and Orienation", *Chem Mater*. **22** (2012) 5831.

[15] P. Gopal and N. A. Spaldin, "Polarization, piezoelectric constants, and elastic constants of ZnO, MgO, and CdO," *J. Elec. Mat***. 35** (2006).

[16] Y. Sun, J. H. Seo, C. J. Takacs, J. Seifter, and A. J. Heeger, "Inverted Polymer Solar Cells Integrated with a Low-Temperature-Annealed Sol-Gel-Derived ZnO Film as an Electron Transport Layer", *Adv. Mat.* **23**, 1679 (2011).
[17] W. C. Yang, B. J. Rodriguez, A. Gruverman, and R. J. Nemanich, Appl. Phys. Lett. **12**, 2316 (2004).

[18] Q. Gui, Z. Xu, H. Zhang, C.Cheng, X. Zhu, M. Yin, Y. Song, L. Lu, X. Chen, and D. Li, "Enhanced Photoelectrochemical water splitting performance of anodic TiO_2 nanotube arrays by surface passivation", *ACS Appl. Mater. Interfaces* **6** (2014) 17053.

[19] S. V. Kalinin, D. A. Bonnell, T. Alvarez, X. Lei, J. H. Ferris, Q. Zhang and S. Dunn, "Atomic Polarization and Local Reactivity on Ferroelectric Surfaces: A New Route toward Complex Nanostructures", Nano Lett. 2, 589 (2002).

[20] Y. Cui, J. Briscoe, and S. Dunn, "Effect of Ferroelectricity on Solar-Light-Driven Photocatalytic Activity of $BaTiO_3$ --- Influence on the Carrier Separation and Stern Layer Formation" *Chem. Mater.* **25** (2013) 4215.

[21] A. Janotti and C. G. V. D. Walle, "Fundamentals of Zinc Oxide as a Semiconductor", Rep. Prog. Phys. **72**, 126501 (2009).

[22] U. Ozgur, Ya. I. Alivov, C. Liu, A. Teke, M. A. Reshchikov, S. Dogan, V. Avrutin,S. J. Cho, and H. Morkoç, "A comprehensive review of ZnO materials and devices", *Appl. Phys. Rev.* **98** (2005) 041301.

[23] A. Haussmann, P. Milde, C. Erler, and L. M. Eng, "Ferroelectric Lithography: Bottom-up Assembly and Electrical Performance of a Single Metallic Nanowire" Nano Lett. **9** (2009) 2.

[24] Y. Xu, S. A. A. Schoonen, "The absolute energy positions of conduction and valence bands of selected semiconducting minerals" *American Mineralogist* **85** (2000) 543–556.

[25] P. C. Rowlette, C. G. Allen, O. B. Bromley, A. E. Dubetz and C. A. Wolden, "Plasma-Enhanced Atomic Layer Deposition of Semiconductor Grade ZnO Using Dimethyl Zinc", Chem. Vap. Dep. **15**, 15-20 (2009).

[26] S. E. Potts, G. Dingemans, C. Lachaud, and W. M. M. Kessels, *J. Vac. Sci. Technol. A* **30**, (2012) 021505.

[26] M. G. Cain, S. Dunn and P. Jones, "The measurement of ferroelectric thin films using piezo force microscopy", *NSTI-Nanotech.* **3** (2004)

[27] C. H. M. Chuang, P. R. Brown, V. Bulovic and M. G. Bawendi, "Improved performance and stability in quantum dot solar cells through band alignment engineering", *Nature Mater.* **13** (2014) 796.

[28] L. Yang, R. Zhou, J. Lan, Q. Zhang, G. Cao and J. Zhu, "Efficient band alignment for $Zn_xCd_{1-x}Se$ QD-sensitized TiO_2 solar cells", *J. Mater. Chem. A* **2** (2014) 3669.

[29] X. Lin, J. Xing, W. Wang, Z. Shan, F. Xu, and F. Huang, "Photocatalytic Activities of Heterojunction Semiconductors $Bi_2O_3/BaTiO_3$: A Strategy for the Design of Efficient Combined Photocatalysts" *J. Phys. Chem. C* **111** (2007)18288.

[30] D. Henderson and D. Boda, "Insights from theory and simulation on the electrical double layer", *Phys.Chem.Chem.Phys.* 11 (2009) 3822.

[31] P. Schwinkendorf, M. Lorenz, H. Hochmuth, Z. Zhang, and M. Grundmann, "Interface charging effects in ferroelectric ZnO–BaTiO3 field-effect transistor heterostructures", *Phys. Status Solidi A* 211 (2014) 166.

[32] E. Cagin, D. Y. Chen, J. J. Siddiqui, and J. D. Phillips, "Hysteretic metal-ferroleectric-semiconductor capacitors based on PZT/ZnO heterostructures" *J. Phys. D* **40** (2007) 2430.

CHAPTER 7. PHOTOEXCITED CHARGE TRANSPORT IN METAL OXIDES AND POLARITY PATTERNED LITHIUM NIOBATE HETEROSTRUCTURES

Abstract: Metal oxides are used as charge transfer layers in solar cells and photocatalytic electrode structures. The band gap and band alignment at the interface can influence the direction of charge transfer in heterostructures. In this research, 1.5 nm metal oxides (ZnO, TiO_2, Al_2O_3 and VO_2) were deposited on $LiNbO_3$ substrates for band alignment characterizations using XPS core level peaks. However, the metal oxides thicknesses were maintained to 1 and 2 nm on polarity patterned lithium niobate (PPLN) for photoinduced Ag nanoparticle deposition. The deduced band alignment of ZnO/$LiNbO_3$, TiO_2/$LiNbO_3$, Al_2O_3/$LiNbO_3$ and VO_2/$LiNbO_3$ shows conduction band offsets (CBOs) of 0.6, 0.8, 1.1 and 0.8 eV, respectively. The photoinduced Ag nanoparticle deposition on ZnO and TiO_2/PPLN heterostructures indicates the deposition follows the pattern of the PPLN but with enhanced Ag nanoparticle deposition for 1 nm thickness and comparable deposition on both domain surfaces for 2 nm thickness. For Al_2O_3/PPLN heterostructures, the Ag nanoparticle density is reduced with an increase in the Al_2O_3 thickness. On the other hand, VO_2/PPLN shows random deposition of Ag nanoparticles with reduced density irrespective of PPLN domains and domain boundaries. The Ag nanoparticle deposition on the heterostructures is in agreement with the determined electron flow from band alignment diagrams. The conduction band minimum (CBM) of ZnO, TiO_2 and VO_2 aligns below the CBM of $LiNbO_3$, thus favoring electron flow from PPLN to the surface. However, the Al_2O_3 CBM is above the $LiNbO_3$ CBM, which inhibits the electron through transport except electron tunneling.

I. INTRODUCTION:

The internal electric field of ferroelectric materials can improve photochemical reactions at surfaces [1-5], by reducing back reactions and recombination losses of photoexcited carriers. The effect is similar to that of a semiconductor p-n junction. Ferroelectrics are materials with a spontaneous polarization due to the different symmetry of the positive and negative atoms. $LiNbO_3$ exhibits the highest spontaneous polarization (0.71 C/m^2) [6] among ferroelectrics, and it has been established that the internal electric field can influence photochemical reactions. Specifically, the photoreduction efficiency of $LiNbO_3$ is similar to that for commonly used metal oxide photocatalysts [3].

Ferroelectric $LiNbO_3$ is a promising photocatalyst where the internal electric field has been explored to increase photoreaction efficiencies [3, 4, 26, 28]. To enhance the density of photoexcited carriers to participate in surface photoreduction, the ferroelectric surfaces can be covered with metal oxides to form oxide heterostructures. Enhanced photochemical reaction efficiencies have been established for oxide/ferroelectric heterostructures including $ZnO/LiNbO_3$ [29] and $TiO_2/BaTiO_3$ [1, 2]. For high efficiency, the metal oxide films should have (i) a suitable band alignment to allow the photoexcited charge transfer, (ii) a limited internal carrier concentration to prevent carrier screening of the ferroelectric internal field, and (iii) the limited thickness to prevent ferroelectric carrier screening.

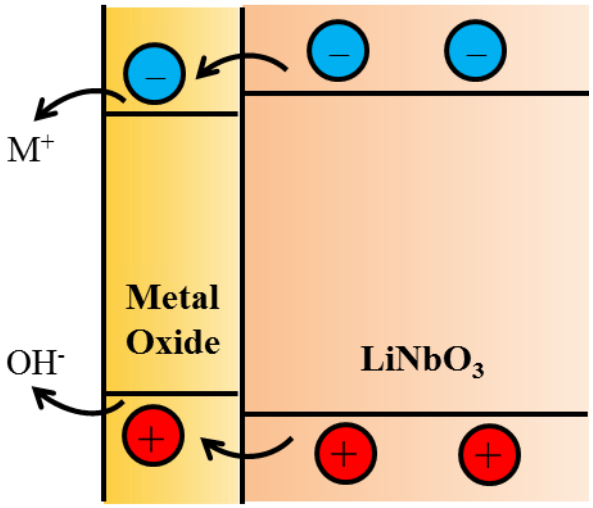

Figure 7.1. Schematic of photoexcited charge transfer in metal oxide/$LiNbO_3$ heterostructure to enable photochemical (metal ions, M^+, reduction and OH^- oxidation) surface reactions.

Metal oxides are among a group of widely used charge (electrons and holes) transfer materials in solar cells and photocatalytic electrodes. They have the advantage of optimally reducing surface states, allowing the charge transfer at the interface, and enhancing the charge separation [1, 2, 7-18]. ZnO and TiO_2/ferroelectric heterostructures have been explored to enhance the surface reactions. A schematic of the possible photoexcited charge transfer in metal oxide and ferroelectric heterostructures is shown in Figure 7.1. Metal oxides are divided into subcategories as per the charge transfer mechanism, (i) insulators (Al_2O_3 and SiO_2) [7-9], (ii) low electron affinity (ZnO, TiO_2, VO_2 and ZrO_2) materials [7, 9-16, 19] and (iii) high electron affinity (MoO_3 and WO_3) materials [7, 10, 16-18]. The focus of this study is to modify polarity patterned lithium niobate (PPLN) surfaces with Al_2O_3, ZnO, TiO_2 and VO_2 thin films to understand the effect of band alignment and metal oxide carrier concentration and mobility on surface

photochemical reactions. The electron affinity and band gap of these materials are shown in Figure 7.2.

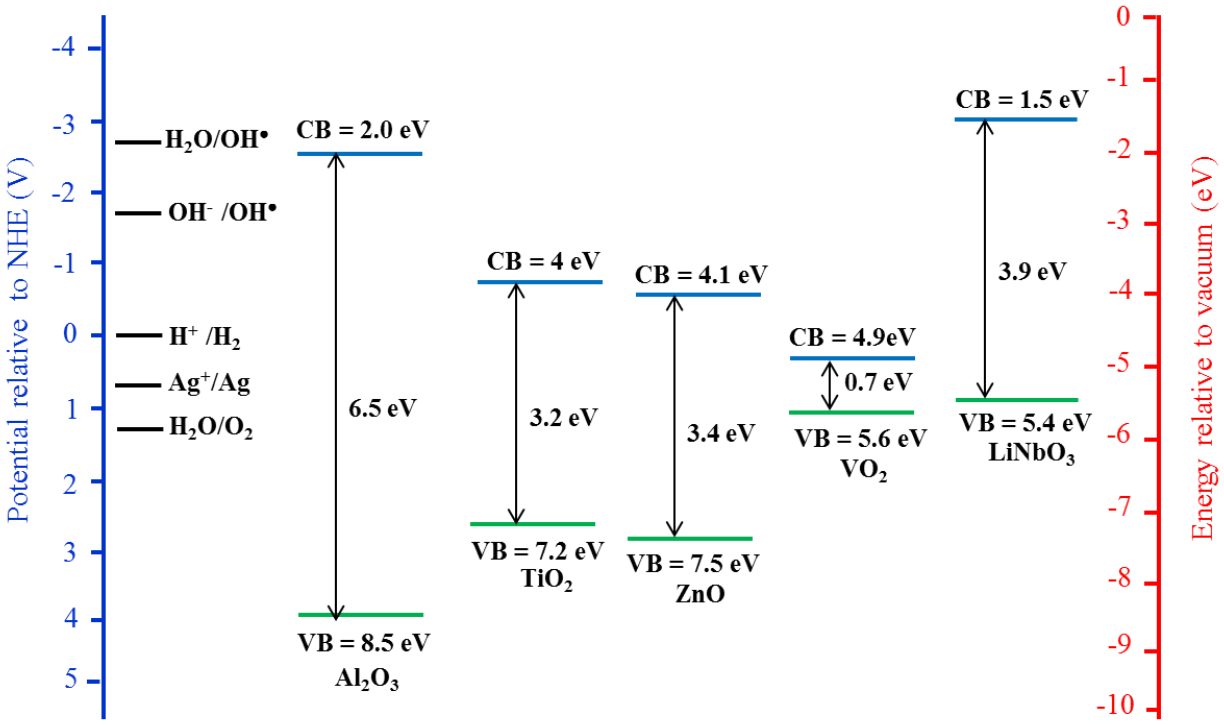

Figure 7.2. Redox potentials for H_2O, hydroxyl ion (OH^-) and Ag^+ ions with respect to $LiNbO_3$, and Al_2O_3, TiO_2, ZnO and VO_2 CBM and VBM position relative to vacuum level.

An approach to study the surface photochemical reactions and charge transfer process in heterostructures is to employ photoinduced metal deposition [1, 2, 29, 30-33]. The surface of the heterostructure is covered with an aqueous $AgNO_3$ solution and illuminated with UV light above the band gap of the carrier generating material. The carriers transport to the surface and cause photocatalytic oxidation or reduction. The potential for various redox reactions with respect to the band gap of the metal oxides and $LiNbO_3$ is also shown in Figure 7.2. For this research, Ag^+ reduction on metal

oxide/PPLN surfaces were studied to understand the electron transport in the metal oxide/ferroelectric heterostructures. Metal oxide thicknesses were limited to 1 nm and 2 nm to compare the electron migration with our prior work of charge transport through ZnO/PPLN heterostructures. The purpose of this study is to deduce the band alignment of metal oxide (ZnO, TiO_2, VO_2 and Al_2O_3)/$LiNbO_3$ heterostructure, the effect of band alignment on photoexcited carrier transport, and the effect of metal oxide carrier screening on the $LiNbO_3$ internal electric field.

II. Experiment:

A. Metal Oxide Deposition on PPLN: Polarity patterned lithium niobate (PPLN) substrates (6 mm x 4 mm x 0.5 mm) used in this study were purchased from Crystal Technologies. The substrates were double side polished with lithographically patterned ~20 μm period polarity gratings on c-axis surfaces. In this configuration the positive (+c) and negative (–c) domains are separated by 180 °C domain boundaries. An e*x-situ* ultrasonic chemical clean (acetone and methanol) was used on the PPLN substrates prior to deposition of Al_2O_3, TiO_2, ZnO or VO_2. The ZnO and Al_2O_3 layers were deposited using plasma enhanced atomic layer deposition (PEALD), and the TiO_2 and VO_2 were deposited using reactive molecular beam deposition. The ZnO and Al_2O_3 were deposited at 130 °C and 170 °C using dimethyl zinc (DMZ) and dimethyl(aluminum)isopropoxide (DMAI) precursors and oxygen plasma reactants. The respective 0.35 and 1.2 sec pulses of DMZ and DMAI were separated from 8 sec O_2 plasma (source of oxygen) generated at 200 W and 100 mTorr with 40 sec N_2 purge steps. The Rutherford backscattering spectroscopy (RBS) determined PEALD growth rate of ZnO and Al_2O_3 was 2.1 Å/cycle and 1.4 Å/cycle [20], respectively. For molecular beam deposition, metal pellets were

evaporated using an e-beam source and a background of O_2 gas as a reactant. The growth rate was controlled using a crystal monitor. To deposit TiO_2 on PPLN, O_2 pressure and substrate temperature were maintained at 1 x 10^{-4} Torr and 200 °C, and VO_2 was deposited at 450 °C, with an O_2 pressure of 7 x 10^{-4} Torr.

B. X-ray Photoelectron Spectroscopy: *In-situ* x-ray photoelectron spectroscopy (XPS) was used to measure the Nb and metal core level before and after 1.5 nm metal oxides deposition. For the XPS measurements 1 cm x 1 cm, double side polished, c-axis, single domain $LiNbO_3$ substrates (purchased from Crystal Technologies) were used. The x-rays were generated in UHV chamber (2 x 10^{-8} Torr) at 30 mA emission current and 15 kV accelerating voltage using monochromatic Al Kα (1486.6 eV) source. The XPS core level positions were used to determine the valence band offsets (VBO) following the approach given by Waldrop, Grant [34], and Kraut *et. al.*:

$$VBO = (E_{CL} - E_V)_{LN} - (E_{CL} - E_V)_{metal\ oxide} + \Delta E_{CL} \quad \ldots\ldots\ldots\ldots\ldots\ldots (1)$$

where, E_{CL} is the core level binding energy, E_V is the valence band minimum (VBM) binding energy, ΔE_{CL} is the difference of the Nb and metal core level binding energy, and $(E_{CL} - E_V)_{LN}$ and $(E_{CL} - E_V)_{metal\ oxide}$ are the differences of the binding energy and respective VBM of $LiNbO_3$ and metal oxides. In this case, the VBM positions are extracted from literature as the valence band spectra could not be measured due to charging during the measurements.

C. Photoinduced Silver Deposition and AFM: To understand the photoelectron transport of photoexcited electrons from $LiNbO_3$ through the metal oxide heterostructures, the density and pattern of the photoinduced Ag nanoparticle were observed with atomic force microscopy. After the metal oxide deposition, the substrates

were cleaned ultrasonically in methanol for 1 min. The surfaces were dried with N_2 gas and covered with 0.35 μl aqueous $AgNO_3$ solutions of concentration 0.00001 M and illuminated for 8 min using a 100 W Hg lamp with line filters. The UV light wavelength was 254 nm and the intensity was maintained at ~1100 $\mu W/cm^2$ during illumination. After photoinduced deposition the samples were immersed in deionized water for 1 min and dried with N_2 gas. The Ag nanoparticle pattern was imaged using atomic force microscopy (AFM). The AFM scan used a non-conducting Si cantilever of spring constant (k) 13-77 N/m and resonance frequency of ~200 – 400 kHz. The measurements were obtained using intermittent contact mode.

III. Results and Discussion:

A. Band Alignment of Metal Oxide/$LiNbO_3$:

To understand the band alignment of metal oxides (ZnO, TiO_2, Al_2O_3, VO_2) and $LiNbO_3$, the metal and Nb core levels in metal oxide/$LiNbO_3$ heterostructures were measured using XPS, Figure 7.3. Surface charging during XPS measurements, as the substrate is insulating $LiNbO_3$, resulted in a shift of all peaks towards higher binding energy. To calibrate the binding energy shift, the Nb $3d_{5/2}$ and C 1s core levels were measured for as-received and chemically cleaned $LiNbO_3$. All core levels were corrected by the difference of the measured C 1s peak and the standard value of 285 eV [34]. Using this method, the Nb peak was corrected to 206.8, which is close to the 207.0 eV value determined by Courths *et. al.* [36]. For the ZnO/$LiNbO_3$, TiO_2/$LiNbO_3$, Al_2O_3/$LiNbO_3$ and VO_2/$LiNbO_3$ heterostructures, the XPS metal core levels and Nb peaks were corrected to the value of the Nb peak from clean $LiNbO_3$. For example, in the case of

$ZnO/LiNbO_3$, the Nb $3d_{5/2}$ and Zn $2p_{1/2}$ original positions were 218.4 eV and 1031.6 eV,

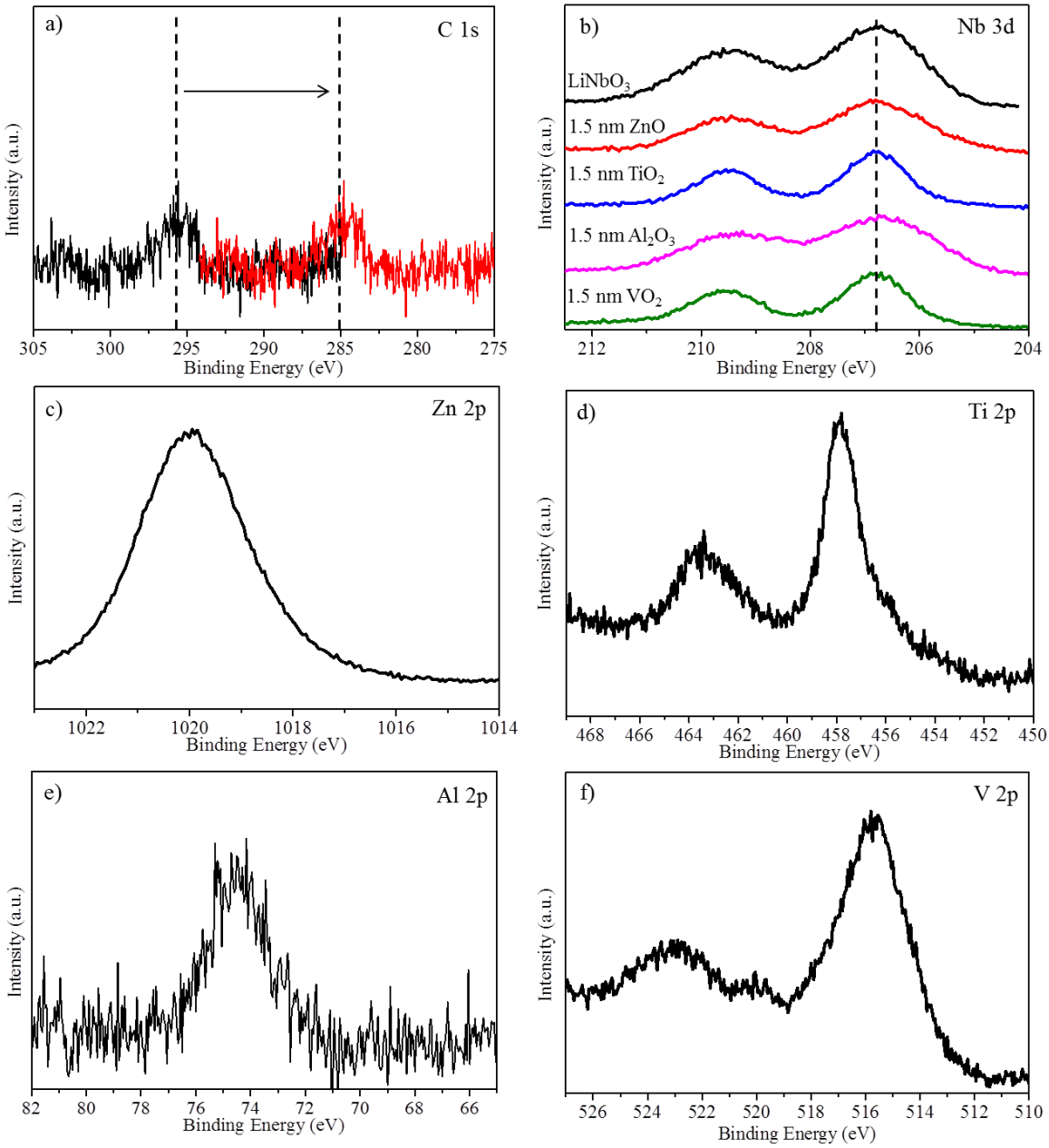

Figure 7.3. XPS core level of a) C 1s from as received (295.8) $LiNbO_3$ and calibrated (285 eV) from literature [36], b) Nb 3d peak for as received $LiNbO_3$, 1.5 nm $ZnO/LiNbO_3$, 1.5 nm $TiO_2/LiNbO_3$, 1.5 nm $Al_2O_3/LiNbO_3$ and 1.5 nm $VO_2/LiNbO_3$, c) Zn 2p, d) Ti 2p, e) Al 2p, and f) V 2p.

respectively. The Nb $3d_{5/2}$ peak was measured at 218.4 eV which is shifted by 11.6 eV to 206.8 eV. The same 11.6 eV value was used to shift the Zn $2p_{3/2}$ core level from 1031.6 to 1020.0 eV. The measured and corrected core level peak positions of the metals and Nb in $LiNbO_3$ for the heterostructures are listed in Table 7.1.

Table 7.1. XPS measured and corrected (in parentheses) peak positions of C1s, Nb 3d, Ti 2p, Al 2p and V 2p core levels. All the peak positions are in eV.

	C 1s	**Nb $3d_{5/2}$**	**Zn $2p_{3/2}$**	**Ti $2p_{3/2}$**	**Al 2p**	**V $2p_{3/2}$**
$LiNbO_3$	295.8 (285.0)	217.6 (206.8)	--	--	--	--
ZnO/$LiNbO_3$	--	218.4 (206.8)	1031.6 (1020.0)	--	--	--
TiO_2/$LiNbO_3$	--	217.3 (206.8)	--	468.3 (457.8)	--	--
Al_2O_3/$LiNbO_3$	--	219.3 (206.8)	--	--	86.9 (74.4)	--
VO_2/$LiNbO_3$	--	221.3 (206.8)	--	--	--	530.3 (515.8)

The VBMs with respect to Fermi level for metal oxides are used from literature to calculate VBOs of metal oxides and $LiNbO_3$ heterostructures band diagrams. The VBM of $LiNbO_3$, ZnO, TiO_2, Al_2O_3 and VO_2 is 3.0 [36], 3.1 [37], 3.1 [9], 4.5 [20] and 0.6 eV [19], respectively. Using equation (1) and the XPS core level values from Table 1, the calculated respective VBOs of ZnO/$LiNbO_3$, TiO_2/$LiNbO_3$, Al_2O_3/$LiNbO_3$ and VO_2/$LiNbO_3$ are 0.1, 0.1, 1.5 and 2.4 eV. The band gap and VBOs were further used to deduce the conduction band offsets (CBOs) for the metal oxide/$LiNbO_3$ heterostructures, Figure 7.4.

The band diagrams of the metal oxide/$LiNbO_3$ heterostructures in Figure 7.4 indicate the VBO and CBO at the interface. The interface band alignment can influence

the photoexcited carrier flow. ZnO and TiO_2 are two materials used in this study with a similar band gap and band alignment with $LiNbO_3$. The CBO for ZnO/$LiNbO_3$ and TiO_2 is 0.6 and 0.8 eV, respectively. Conduction band minimums (CBMs) of ZnO and TiO_2 align near the CBM of $LiNbO_3$ which indicates a favorable flow of photoexcited electron

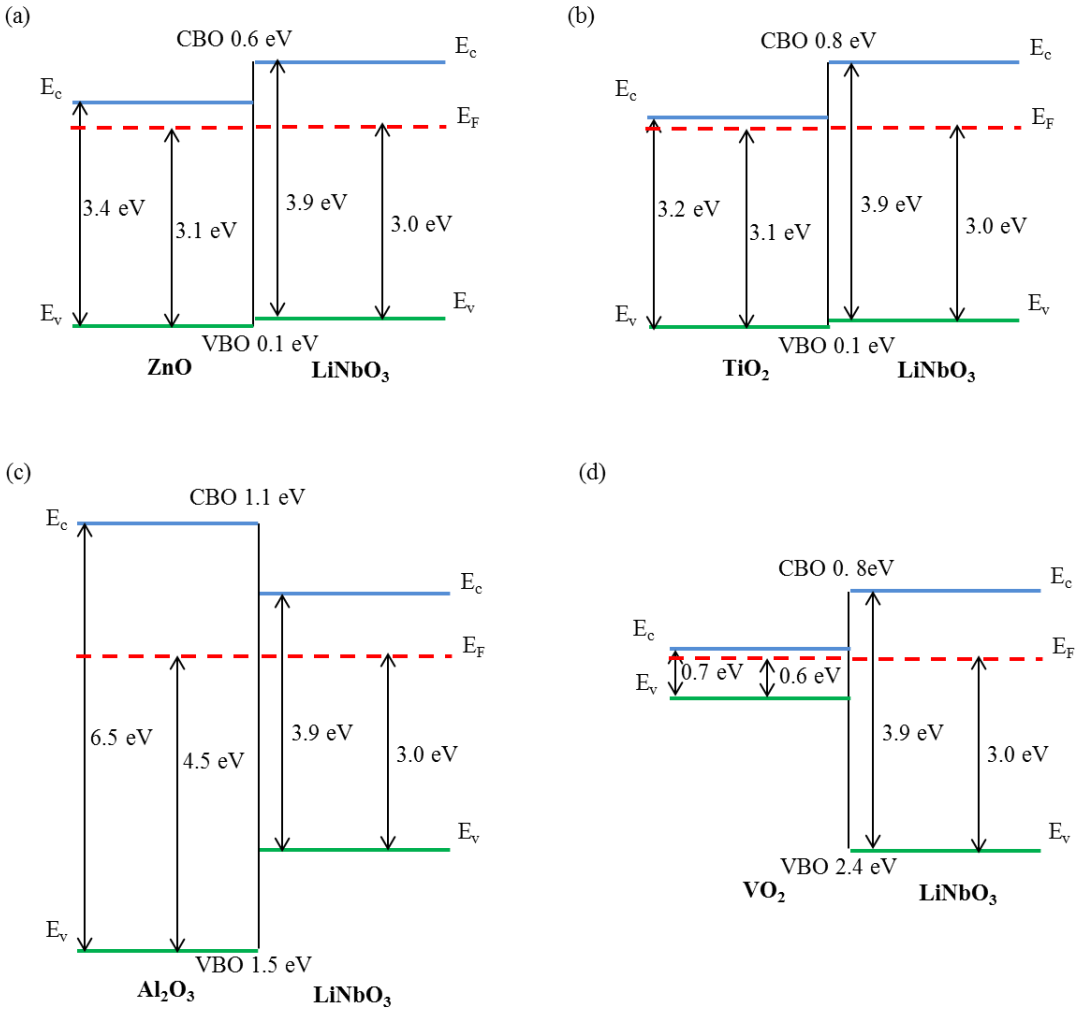

Figure 7.4. Band alignment shows the valence band offset (VBO) and conduction band offset (CBO) of a) ZnO/$LiNbO_3$, b) TiO_2/$LiNbO_3$, c) Al_2O_3/$LiNbO_3$, and VO_2/$LiNbO_3$ heterostructures.

from $LiNbO_3$ to ZnO and TiO_2 surfaces, Figure 7.4 a) and b). For Al_2O_3/PPLN, the band diagram, Figure 7.4 c), indicates the possible charge transfer process involves electron

tunneling. VO_2 is a small band gap material which has a CBM below the CBM of $LiNbO_3$, Figure 7.4 d), and signifies the electron transport from $LiNbO_3$ to the VO_2 surface.

B. Photoinduced Ag Deposition on Metal oxide/PPLN Heterostructures:

The heterostructure surfaces were immersed with aqueous $AgNO_3$ solution and illuminated with UV light (4.9 eV) above the bandgap of $LiNbO_3$ and the Ag nanoparticle pattern was recorded with AFM, Figures 7.5 and 7.6. The available electrons and holes at the surface due to drift and/or diffusion originate the surface redox reactions and control the Ag nanoparticle pattern. Prior work from our group by Sun *et. al.* have indicated that a dense Stern layer that can limit the availability of Ag^+ ions near the

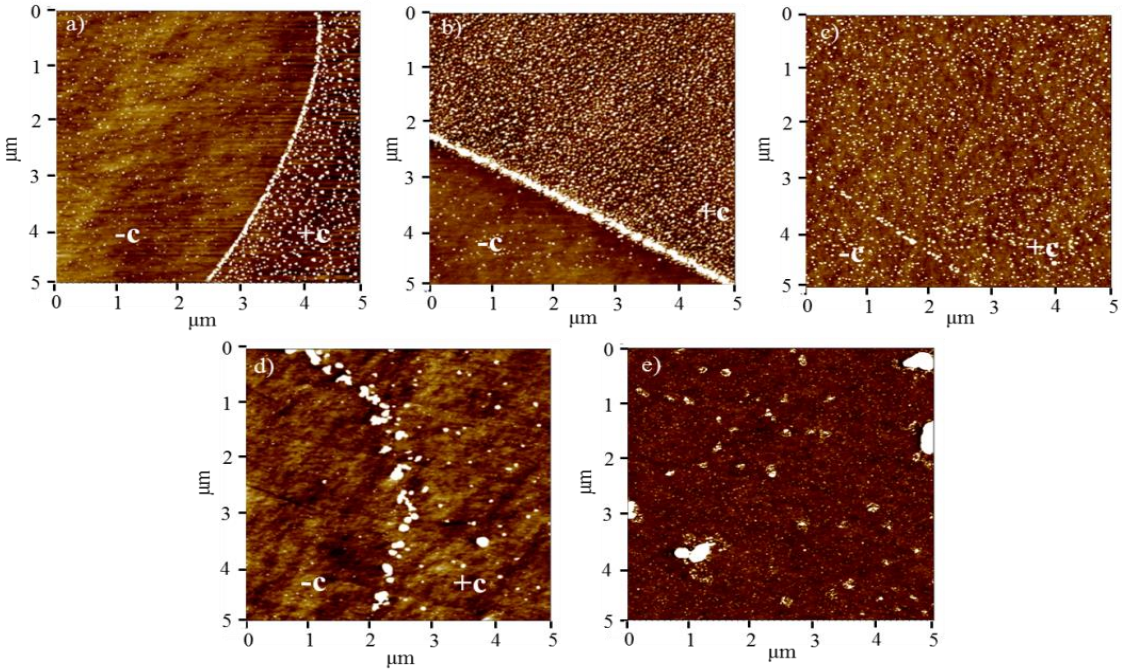

Figure 7.5. AFM scans after photoinduced Ag nanoparticle deposition on a) PPLN, b) 1 nm ZnO/PPLN, c) 1 nm TiO_2/PPLN, d) 1 nm Al_2O_3/PPLN, and e) 1 nm VO_2/PPLN.

which may be related to the reduced density of Ag nanoparticles [31]. We have observed in our previous work that the deposition of ZnO on PPLN possibly caused the formation of less dense Stern layer and reduced the surface states as the overall density of Ag nanoparticles on ZnO/PPLN heterostructures as compared to PPLN [29].

AFM topography images of photoinduced Ag nanoparticle patterns on PPLN and 1 and 2 nm (ZnO, TiO_2, Al_2O_3, VO_2)/PPLN heterostructures are shown in Figures 7.4 and 7.5. The Ag photoinduced deposition conditions, including $AgNO_3$ solution concentration, UV light wavelength and flux, were similar for all the samples. The Ag nanoparticle pattern on bare PPLN is used as a reference to compare changes in the Ag nanoparticle pattern on metal oxide/PPLN heterostructures. On bare PPLN, the Ag nanoparticle deposition is selective with increased density on +c domain surfaces and domain boundaries. The variation in the Ag nanoparticle pattern is described below:

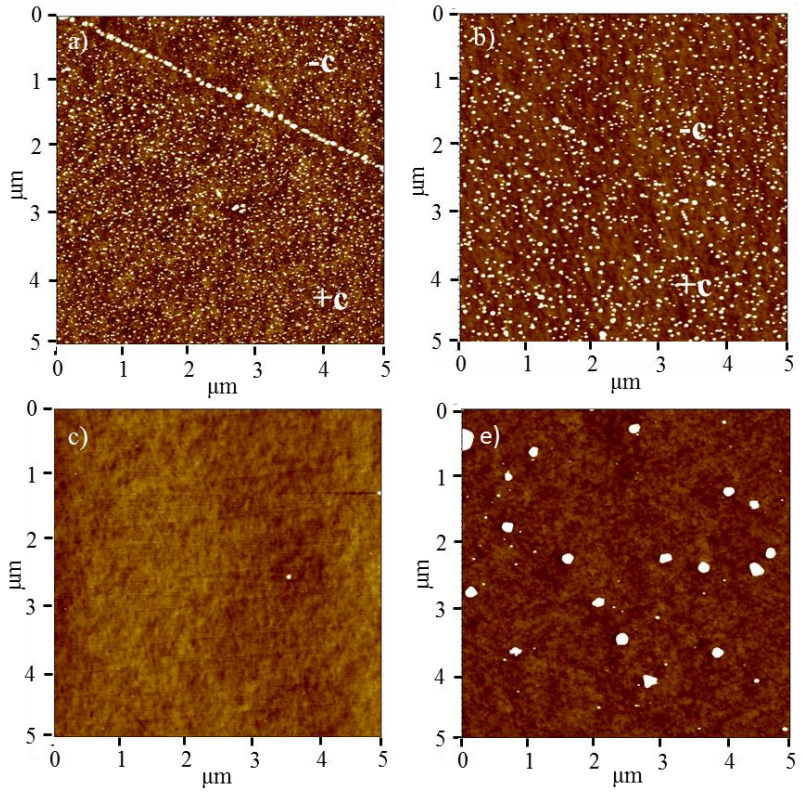

Figure 7.6. AFM scans after photoinduced deposition Ag on a) 2 nm ZnO/PPLN, b) 2 nm TiO_2/PPLN, c) 2 nm Al_2O_3/PPLN, and d) 2 nm VO_2/PPLN.

1 nm metal oxides/PPLN heterostructures: Unlike 1 nm ZnO/PPLN where the overall photoinduced Ag nanoparticle density is enhanced and the selectivity is similar to bare PPLN, 1 nm TiO_2/PPLN shows a loss of selectivity with comparable Ag nanoparticle density on +c and –c domain surfaces separated by larger particles at the domain boundaries, Figure 7.5 a) – c). In contrast, the overall density of Ag nanoparticles on 1 nm Al_2O_3/PPLN decreased compared to bare PPLN, Figure 7.5 d). The 1 nm VO_2/PPLN heterostructure shows random deposition of Ag nanoparticles on +c and –c domain surfaces and domain boundaries, Figure 7.5 d).

2 nm metal oxides/PPLN heterostructures: The Ag photoinduced pattern on 2 nm ZnO/PPLN and 2 nm TiO_2/PPLN shows a similar pattern with enhanced Ag deposition on –c domains and comparable density on +c domain surface, Figure 7.6 a) – b). However, on the 2 nm ZnO/PPLN heterostructure, the domain boundary is well defined, while on the 2 nm TiO_2/PPLN the domain boundary Ag nanoparticle deposition is sparse, The 2 nm Al_2O_3/PPLN shows essentially no Ag deposition on the surface Figure 7.6 c). The 2 nm VO_2/PPLN AFM surface indicates random deposition of Ag nanoparticles similar to the 1 nm VO_2/PPLN but with increased particle size, Figure 7.6 d).

The Ag nanopattern on 1 nm ZnO and TiO_2 on PPLN is different in terms of selectivity. The 1 nm ZnO/PPLN heterostructures maintain selectivity while showing an enhanced Ag nanoparticle density. On the other hand, 1 nm TiO_2 reduces the selectivity, and the Ag nanoparticle deposition on –c domain surfaces become comparable to +c domain surfaces. The pattern of Ag nanoparticles on 2 nm ZnO indicates the pattern is controlled by the PPLN domains and domain boundaries but with reduced selectivity. In contrast, on 2 nm TiO_2/PPLN, random deposition of nanoparticles occurs with no signs of domain boundary deposition. Despite the similar band alignment of ZnO and TiO_2 with $LiNbO_3$, the different Ag nanoparticle pattern indicates the material properties also influence the electron flow from PPLN to the metal oxide surface. In general, ZnO is reported as higher electron mobility material as compared to TiO_2 [18, 38-40]; however, some groups have reported the reverse behavior of electron mobility [41, 42]. In prior work by Hagfeldt *et. al.* the electron mobility of TiO_2 and ZnO was found to be the same [43]. Similarly, PEALD ZnO can have low carrier concentration than the ZnO thin films

deposited using other techniques due to higher reactivity of oxygen plasma species which reduce the impurities and oxygen vacancies [44]. Consequently, the TiO_2 thin films deposited using oxygen gas in MBD system can have higher carrier concentration as compared to PEALD ZnO. The discrepancies in ZnO and TiO_2 electron carrier concentration can be attributed to differences in the deposition processes. For this study, ZnO and TiO_2 were prepared using PEALD and MBD, respectively. Thus, we cannot exclude the difference in the properties of these two materials caused by the deposition processes. The internal carrier concentration of metal oxides can screen the electric field in $LiNbO_3$ and thus reduce the selectivity. The 1 nm TiO_2/PPLN shows a similar Ag nanoparticle pattern to that of 2 nm ZnO/PPLN. This behavior can be related to a higher reduction of interface states and/or more effective interface screening of the polarization by the free carriers in TiO_2.

The Ag nanoparticle pattern on 1 nm and 2 nm Al_2O_3/PPLN heterostructures corroborates that the electron transfer process is consistent with the heterostructure band alignment. The electron tunneling is expected to decreases exponentially with an increase in thickness [22]. The Ag nanoparticle density on Al_2O_3/PPLN indicates a decrease of the supply of electrons with the increase of Al_2O_3. The 1 nm Al_2O_3/PPLN shows a Ag nanoparticle pattern similar to PPLN but with reduced density. With the increase in Al_2O_3 thickness to 2 nm, the electron tunneling from PPLN to the Al_2O_3 surface is essentially blocked.

Unlike ZnO and TiO_2, 1 and 2 nm VO_2 shows random nanoparticle deposition. The carrier concentration of vanadium oxide is $10^{18} – 10^{19}$ cm^{-3} [45] is comparable to ZnO ($10^{18} – 10^{20}$ cm^{-3}) [45] and higher than TiO_2 (10^{17} cm^{-3}) [40]. As discussed above,

the high carrier concentration of the metal oxide layer can screen the internal electric field of $LiNbO_3$ and reduce the control of PPLN on Ag nanoparticle pattern formation. For this case, the electron diffusion dominates the electron drift, thus the Ag deposition does not show enhanced deposition of $LiNbO_3$ positive domains. With the increase in thickness, the photocarrier excitation in metal oxide layer screens the flow of photoexcited electrons from PPLN to the surface.

IV. Conclusions:

The x-ray photoemission spectroscopy results were used to determine the possible band alignment in metal oxide (Al_2O_3, ZnO, TiO_2 and VO_2)/$LiNbO_3$ heterostructures. The Ag nanoparticles deposition on these heterostructures establishes the effect of metal oxide/PPLN band alignment, and metal oxide carrier concentration on photoexcited charge transfer. For Al_2O_3/PPLN heterostructures, the charge transfer is limited by electron tunneling through the blocking Al_2O_3 layer. However, for ZnO/PPLN, TiO_2/PPLN and VO_2/PPLN the photoecited carriers can transport through the metal oxide film. We suggest with the increase in metal oxide thickness, the effect of metal oxide carrier concentration screening on PPLN internal electric field enhances and diminishes the selective Ag nanoparticle formation. The other effect that is evident in the experiments performed here is the diminished photoexcited carrier concentration from PPLN to the surface by the photoexcited carrier concentration with the increase in metal oxide thickness.

References:

[1] N. V. Burbure, P. A. Salvador and G. S. Rohrer, "Photochemical Reactivity of Titania Films on $BaTiO_3$ Substrates: Influence of Titania Phase and Orienation", *Chem Mater.* **22** (2012) 5831.

[2] N. V. Burbure, P. A. Salvador, and G. S. Rohrer, "Photochemical Reactivity of Titania Films on $BaTiO_3$ Substrates: Origin of Spatial Selectivity" *Chem. Mater.***22** (2010) 5823.

[3] L. Li, P. A. Salvador and G. S. Rohrer, "Photocatalysts with internal electric field", *Nanoscale* **6** (2014) 24.

[4] M. Stock, and S. Dunn, "Influence of the Ferroelectric Nature of Lithium Niobate to Drive Photocatalytic Dye Decolorization under Artificial Solar Light",*J. Phys. Chem.* **116**, 20854 (2012).

[5] Y. Cui, J. Briscoe, and S. Dunn, "Effect of Ferroelectricity on Solar-Light-Driven Photocatalytic Activity of $BaTiO_3$ --- Influence on the Carrier Separation and Stern Layer Formation" *Chem. Mater.* **25** (2013) 4215.

[6] W. C. Yang, B. J. Rodriguez, A. Gruverman, and R. J. Nemanich, Appl. Phys. Lett. **12**, 2316 (2004).

[7] S. Calnan, "Applications of Oxide Coatings in Photovoltaic Devices" *Coatings* **4** (2014) 162.

[8] E. Palomares , J. N. Clifford , S. A. Haque , T. Lutz , and J. R. Durrant, "Control of Charge Recombination Dynamics in Dye Sensitized Solar Cells by the Use of Conformally Deposited Metal Oxide Blocking Layers" *J. Am. Chem. Soc.* **125** (2003) 475.

[9] Y.W. Chen, J.D. Prange, S. Dühnen, Y. Park, M. Gunji, C.E. Chidsey, P.C. McIntyre, Atomic layer-deposited tunnel oxide stabilizes silicon photoanodes for water oxidation, Nature materials. 10 (2011) 539-544. (SiO2 and TiO2).

[10] S. Lattante, "Electron and Hole Transport Layers: Their Use in Inverted Bulk Heterojunction Polymer Solar Cells", Electronics **3**, 132-164 (2014).

[11] S. R. Ferreira, P. Lu, Y. J. Lee, R. J. Davis, and J. W. P. Hsu, "Effect of Zinc Oxide Electron Transport Layers on Performance and Shelf Life of Organic Bulk Heterojunction Devices" *J. Phys. Chem. C* **115** (2011) 13471.

[12] K. Stella, D. A. Kovacs, D. Diesing, W. Brezna, and J. Smoliner, "Charge Transport Through Thin Amorphous Titanium and Tantalum Oxide Layers" J. Electrochem. Society **158** (2011) 65.

[13] Y. J. Noh, S. I. Na, and S. S. Kim, "Inverted polymer solar cells including ZnO electron transport layer fabricated by facile spray pyrolysis", *Sol. Energ. Mat. Sol. C.* **117**, 139 (2013).

[14] Y. J. Kang, K. Lim, S. Jung, D. G. Kim, J. K. Kim, C. S. Kim, S. H. Kim and J. W. Kang, "Spray-coated ZnO electron transport layer for air-stable inverted organic solar cells", Solar Energy Mat. Solar Cells. **96,** 137-140, (2012).

[15] R. Sapkal, S. Shinde, T. Waghmode, S. Govindwar, K. Rajpure, C. Bhosale, "Photo-corrosion inhibition and photoactivity enhancement with tailored zinc oxide thin films" *Journal of Photochemistry and Photobiology B: Biology* **110** (2012) 15-21.

[16] L. Cattin, F. Dahou, Y. Lare, M. Morsli, R. Tricot, S. Houari, A. Mokrani, K. Jondo, A. Khelil, K. Napo and J. C. Bernede, "MoO3 surface passivation of the transparent anode in organic solar cells using ultrathin films" *J. Appl. Phys.* **105** (2009) 034507.
[17] J. Meyer, S. Hamwi, M. Kroger, W. Kowalsky, T. Riedl, A. Kahn, "Transition Metal Oxides for Organic Electronics: Energetics, Device Physics and Applications" *Adv. Mater.* 2012, 24, 5408.

[18] J. Meyer, S. Hamwi, T. Bulow, H. H. Johannes, T. Riedl, W. Kowalsky, "Highly efficient simplified organic light emitting diodes" Appl. Phys. Lett. 2007, 91, 113506.

[19] C. Zhu, M. Kaur, F. Tang, X. Liu, D. J. Smith, and R. J. Nemanich,"Band alignment of vanadium oxide as an interlayer in a hafnium oxide-silicon gate stack structure" *J. Appl. Phys.* **112** (2012) 084105.

[20] J. Yang, B. Eller, M. Kaur, and R. J. Nemanich, "Characterization of plasma-enhanced atomic layer deposition of Al2O3 using dimethylaluminum isopropoxide" *J. Vac. Sci. Technol.* **A 32** (2014) 021514.

[21] C. Thierfelder , S. Sanna, Arno Schindlmayr, and W. G. Schmidt, "Do we know the band gap of lithium niobate?" *Phys. Status Solidi* C **7** (2010) 362.

[22] G. Campet, J. Manaud, C. Puprichitkun, Z. Sun, P. Salvador, "Protection of photoanodes against photo-corrosion by surface deposition of oxide films: criteria for choosing the protective coating" *Active and Passive Electronic Components* **13** (1989) 175-189.

[23] A. Mang, K. Reimann, and St Rubenacke, "Band-Gaps, Crystal-Field Splitting, Spin-Orbit-Coupling, And Exciton Binding-Energies In Zno Under Hydrostatic-Pressure" Solid State Commun. 94, 251(1995).

[24] A. Janotti and C. G. V. D. Walle, "Fundamentals of Zinc Oxide as a Semiconductor", Rep. Prog. Phys. **72**, 126501 (2009).

[25] C. Ko and S. Ramanathan, "Observation of electric field-assisted phase transition in thin film vanadium oxide in a metal-oxide-semiconductor device geometry" *Appl. Phys. Lett.* **93** (2008) 252101.

[26] B. Zielinska, E. Borowiak-Palen, R. J. Kalenzuk, "Preparation and Characterization of Lithium Niobate as a Novel Photocatalyst in Hydrogen Generation" *J. Phys. Chem. Solids* **69** (2007) 236.

[27] M. Stock and S. Dunn, "$LiNbO_3$ – A New Material for Artificial Photosynthesis", *IEEE Transac. Ultrasonics Ferroelectrics Freq. Contr.* **58**, 0885 (2011).

[28] K. Saito, K. Koga and A. Kudo, "Lithium Niobate Nanowires for Photocatalytic Water Splitting" *Dalton Trans.* **40** (2011) 3909.

[29] M. Kaur, Q. Liu, P. Crozier, R. Nemanich, "Photochemical Reaction Patterns on Heterostructures of ZnO on Polarity Patterned Lithium Niobate"

[30] Y. Sun, R. J. Nemanich, "Photo-induced Ag deposition on periodically poled lithium niobate: Concentration and intensity dependence", J. Appl. Phys. **109**, 104302 (2011).

[31] Y. Sun, B. S. Eller, and R. J. Nemanich, "Photoinduced Ag deposition on periodically poled lithium niobate: Wavelength and polarization screening dependence", J. Appl. Phys. **110**, 084303 (2011).

[32] A. Haussmann, P. Milde, C. Erler, and L. M. Eng, "Ferroelectric Lithography: Bottom-up Assembly and Electrical Performance of a Single Metallic Nanowire" Nano Lett. **9** (2009) 2.

[33] Y. S. Park, J. H. Kim, and W. Yang, "Comparison Study of Metal Nanoparticles Grown on Polarity Patterned Ferroelectrics by Scanning Probe Microscopy" *Surf. Interface Anal.* **44** (2012) 759.

[34] J. Waldrop, R. Grant, "Measurement of AlN/GaN (0001) heterojunction band offsets by x-ray photoemission spectroscopy" *Appl. Phys. Lett.* **1996**, 68, 2879-2881.

[35] S. Kohiki, "Electron-energy-loss function of LiTaO3 and LiNbO3 by x-ray photoemission spectroscopy: Theory and experiment" *Physic. Rev. B* **57** (1998) 23.

[36] R. Courths, P. Steiner, H. Hochst, S. Hufner, " Photoelectron-Spectroscopy Investigation And Electronic-Properties Of $LiNbO_3$ Crystal-Surfaces" *Appl. Phys.* **21** (1980) 345.

[37] C. Zhu, D. J. Smith, R. J. Nemanich, "Band alignment of zinc oxide as a channel layer in a gate stack structure grown by plasma enhanced atomic layer deposition" *J. Vacc. Sci. Techn.* **30** (2012) 5.

[38] A. K. Chandiran, M. Abdi-Jalebi, M. K. Nazeeruddin, and M. Gratzel, "Analysis of Electron Transfer Properties of ZnO and TiO_2 Photoanodes for Dye-Sensitized Solar Cells" *ACS Nano* **8** (2014) 2661.

[39] Q. Zhang, C. S. Dandeneau, X. Zhou, G. Cao, "ZnO Nano-structures for Dye-Sensitized" *Solar Cells. Adv. Mater.* **21** (2009) 4087–4108.

[40] D. Eitan Barlaz and Edmund G. Seebauer, "Manipulation of carrier concentration, crystallite size and density in polycrystalline anatase TiO_2 via amorphous-phase medium range atomic order" *Cryst Eng Comm* **17 (**2015) 2101.

[41] M. Quintana, T. Edvinsson, A. Hagfeldt, G. Boschloo, "Comparison of Dye-Sensitized ZnO and TiO2 Solar Cells: Studies of Charge Transport and Carrier Lifetime" *J. Phys. Chem.* C**111** (2006) 1035–1041.

[42] Baxter, J. B.; Aydil, E. S. "Nanowire-Based Dye-Sensitized Solar Cells" *Appl. Phys. Lett.* 2005, 86, 53114.

[43] Hagfeldt, A.; Boschloo, G.; Sun, L.; Kloo, L.; Pettersson, H. "Dye-Sensitized Solar Cells" *Chem. Rev*. 2010, 110, 6595–6663.

[44] Ozgur, U.; Alivov, Y. I.; Liu, C.; Teke, A.; Reshchikov, M. A.; Dogan, S.; Avrutin, V.; Cho, S. J.; Morkoç, H. "A comprehensive review of ZnO materials and devices," *Appl. Phys. Rev.* 2005, **98**, 041301.

[45] D. Ruzmetov, D. Heiman, B. B. Claflin, V. Narayanamurti, and S. Ramanathan, "Hall carrier density and magnetoresistance measurements in thin-film vanadium dioxide across the metal-insulator transition" *Physical Review* B **79** (2009) 153107.

CHAPTER 8: PEALD Al_2O_3 AND SiO_2 PASSIVATION AND DEGRADATION MECHANISM ON ZINC OXIDE PHOTOELECTRODE

The photoelectrochemical characterizations, and TEM and SEM were performed by Qian Cheng and Qianlang Liu, respectively.

Abstract: Atomic layer deposited thin films provide uniform and conformal coverage, and thus can be efficiently used to deposit thin passivation layers on photoanodes and photocatalysts. ZnO is a high efficiency photocatalyst due to a high absorption coefficient, and it has been demonstrated for water splitting and water cleaning. However, chemical instability of ZnO hinders its use for photocatalysis process. Thus it is crucial to coat the ZnO surfaces to avoid direct contact with the electrolyte solution. In this paper, 1 and 2 nm PEALD Al_2O_3 or SiO_2 were deposited on 20 nm PEALD ZnO and single crystalline ZnO to study the stability and degradation mechanisms. The interface band alignment was determined by *in situ* photoemission and photochemical stability tests were performed and characterized with AFM, SEM, and TEM. The results indicate the VBO and CBO of Al_2O_3/ZnO are 1.1 eV and 2.2 eV, and SiO_2/ZnO is 2.5 eV and 3.2 eV, respectively. The Al_2O_3 passivation layer is unstable as it undergoes photocorrosion, which initiates from pinholes. On the other hand, SiO_2 shows improved passivation of ZnO from photoelectrochemcical measurements, AFM and SEM. However, the TEM results indicate the corrosion of underneath ZnO. The possible cause of photocorroison is the electrolyte ions transport through SiO_2

I. Introduction:

In order to reduce global warming and control the carbon emission, renewable energy is a viable option. The solar water splitting process to produce hydrogen fuel has been studied extensively [1 – 3]. The incident photons excite electron-hole pairs in a semiconductor photocatalyst, which are separated and migrate to the surface to react with an aqueous electrolyte solution. The reduction and oxidation reactions occur at the solid-liquid interface. Consequently, the band edges alignment with redox potentials play a critical in water splitting. For efficient reactions to prevail, both H^+/H_2 and OH^-/O_2 redox potentials must align within the bandgap, the reaction rate should be sufficient to prevent carrier recombination, and the photocatalyst should be chemically stable in an aqueous electrolyte [4].

Metal oxides (ZnO, TiO_2 and ZrO_2 etc) have been studied as photocatalysts for water splitting to generate hydrogen due to their suitable bandgap and appropriate band positions relative to the water redox potentials [1]. Despite the similar band gap, ZnO is preferred over TiO_2 because of its higher absorption coefficient [5-8]. However, photocorrosion of ZnO in an aqueous electrolyte solution makes it difficult to be used as a photoanode. High efficiency ZnO can be advantageous if the photocorrosion during chemical reactions can be prevented.

In a number of reviews, atomic layer deposited (ALD) films have been employed as passivation layers on chemically unstable photocatalyst surfaces [9-13]. The criteria for passivation layers are: (i) chemical stability in the electrolyte solution, (ii) efficient charge transport of photoexcited carriers to the electrolyte, and (iii) prevention of ions transport to the photocatalyst. Commonly used ALD passivation layers that have been studied for Si photoanodes include are Al_2O_3 [14], Ta_2O_5 [15] and TiO_2 [14, 16]. The

charge transfer mechanism, i.e. either transport or tunnel, through the passivation layer is determined by the band gap, band alignment and properties of the passivating material. The purpose of the passivation layer is to reduce the surface defects, or trap sites, to separate the chemically unstable photocatalyst from electrolyte solution and to enhance the efficiency of the photocatalytic processes [16-18].

Different thicknesses of TiO_2 have been used as a passivation layer on ZnO [19, 20]. The band gap of TiO_2 is comparable to the band gap of ZnO that allows absorption of the illuminated light in the TiO_2 and reduces the photoexcitation in ZnO. Also, the valence band (VB) edge of TiO_2 is slightly positive relative to ZnO, which favors transport of the TiO_2 photoexcited holes towards the ZnO and enhances the ZnO photocorrosion [15, 21]. To prevent these issues, the wide band gap materials, Al_2O_3 and SiO_2, can be used as passivation layers on ZnO. The wide band gap allows the transmission of most of the illuminated light to ZnO. Moreover, the absence of photoexcited carriers in a material like Al_2O_3 eliminates the possibility of hole transport to the ZnO layer.

Small band gap materials have also been studied to passivate ZnO [22]. However, the chemical instability and light absorption make them unfavorable to be used as protecting layers. For these reasons, the wide band gap Al_2O_3 and SiO_2 have been selected as passivation layers for ZnO in this study. Consequently, the VB edge of both oxides aligns below the ZnO VB edge, thus the possible carrier transport mechanism is tunneling. Al_2O_3 has been used as a protective layer on Fe_2O_3 [23], TiO_2 nanotubes [23], and WO_3 thin films [24]. Some of the studies have shown that Al_2O_3 is unstable in an aqueous solution [25] and others suggest it can protect the photocatalyst surface without

undergoing photocorrosion [14]. The inconsistency of Al_2O_3 as a passivation layer can be attributed to the different deposition methods and electrolyte conditions. The passivation layer is required to be thin, and free of pinholes and cracks to allow electron tunneling from the active material (ZnO) to the surface and to prevent the photocorrosion of the active layer in water or the electrolyte solution. To the best of our knowledge, there have not been any prior studies using SiO_2 for passivation of ZnO photoanodes.

In this research we propose to explore the interfacial properties and photocorrosion mechanisms of ZnO passivated with plasma enhanced atomic layer deposited (PEALD) Al_2O_3 and SiO_2 layers. The characterizations performed included photoelectron spectroscopy, photoelectrochemical stability, and microscopy (atomic force, scanning electron, transmission electron). PEALD is known to deposit uniform, conformal and pin-free high quality thin films, which makes it a good candidate among the known deposition processes [26]. The heterostructures which consisted of 20 nm ZnO thin films were also deposited using PEALD. A pinhole or defect on the surface of a protective layer can act as a corrosion site in the electrolyte solution during stability test, which can quickly grow and cause exfoliation of the whole passivation layer. Therefore, we can monitor the damage of the passivation layers and analyze the corrosion mechanisms through the change of photocurrent and microcopy characterizations. The demonstrated band alignments provide the band offsets at the interface of Al_2O_3 or SiO_2/ZnO and provide band bending information which may be related to the surface preparation and deposition processes. Also, the valence band maximum and conduction band minimum positions can be determined relative to the redox potentials from the band alignment diagrams.

II. Experiments:

A. ZnO substrate surface cleaning:

In this research, 1 cm x 1 cm x 2 mm single crystal ZnO wafers (MIT Corp) with both sides polished and cut along c-axis were used. The one side of the single crystal ZnO was O-face (0 0 0 -1) and the other side was Zn-face (0 0 0 1). The substrates were ultrasonically cleaned *ex situ* in methanol for 1 minute and dried with ultra-high purity (UHP) N_2 gas. ZnO substrates exposed to the atmosphere adsorbed a layer of –OH groups at the surface, which was removed prior to the deposition of PEALD SiO_2 and Al_2O_3 to form a clean interface between the passivation layer and photocatalyst. Various methods such as *ex situ* UV exposure and *in situ* He and O_2 mixed plasma have been reported to remove the layer of hydroxyl groups from the surface [23]. *In situ* surface cleaning is preferred over *ex situ* cleaning due to reduction of –OH groups and re-adsorption in UHV. In this study, the O-face of ZnO single crystal substrate was cleaned using *in situ* He:O_2 (80:20%) plasma at 310 °C for 40 minutes. The He:O_2 plasma gas pressure and power was maintained at 50 mTorr and 20 W, respectively, while the temperature was ramped at 1 degree/sec from 20 °C to 310 °C in He:O_2 gas at 50 mTorr. X-ray photoelectron spectroscopy (XPS) and Ultraviolet photoelectron spectroscopy (UPS) were used to measure the core (Zn, O and C), valence band maximum (VBM) and work function. On as received and plasma cleaned ZnO (0 0 0 -1). The absence of C 1s peak, reduction in shoulder O 1s peak, increase in the intensity of Zn 2p and increase in main O 1s peak indicate the removal of atmospheric carbon and –OH layer from the surface after He:O_2 plasma cleaning.

B. PEALD ZnO, Al_2O_3 and SiO_2 deposition:

PEALD is a two-step sub-monolayer process to deposit metals, metal oxides, nitrides and fluorides. To deposit metal oxides, remote oxygen plasma is used as a source of oxygen to oxidize metal precursor. The alternate two steps, metal precursor and oxygen plasma are separated by research grade nitrogen inert gas to avoid CVD-like reactions. This study employed 20 nm PEALD ZnO deposited on n-Si (1 0 0) one side polished substrate (0.5 mm x 1") and single crystal ZnO (0 0 0 -1), which are passivated with 2 nm and 4 nm PEALD Al_2O_3 or SiO_2. The Si substrate was ultrasonically cleaned in acetone and methanol for 10 minutes each to remove hydrocarbons from the surface. PEALD ZnO was deposited on n-Si followed by the 10 sec remote oxygen plasma clean, using 200 W power and 100 mTorr O_2 pressure at 130 °C, to remove the atmospheric adsorbed carbon. ZnO was deposited at 130 °C using dimethylzinc (DMZ) precursor and remote oxygen plasma pulse of 0.35 sec and 8 sec. The two pulses were separated by 40 sec N_2 purge. The observed growth rate of PEALD ZnO in our system is ~2.1 Å/cycle. PEALD Al_2O_3 and SiO_2 deposition was carried out using dimethyl(aluminum)isopropoxide (DMAI) and tris(dimethylamino)silane (TDMAS), respectively, and remote oxygen plasma. PEALD Al_2O_3 was deposited at 160 °C using 1.2 second DMAI pulse and SiO_2 was deposited at RT using 1.6 sec TDMAS pulse. The oxygen plasma time used for SiO_2 deposition was twice (16 sec) as compared to Al_2O_3 i.e. 8 seconds. The observed growth rate of Al_2O_3 and SiO_2 passivation layers is 1.8 A/sec and 1.1 Å/sec, respectively.

C. Ultraviolet and X-ray photoemission spectroscopy characterization:

In-situ x-ray photoelectron spectroscopy (XPS) and ultra-violet photoelectron spectroscopy (UPS) were used at various stages, Al_2O_3/ZnO and SiO_2/ZnO heterostructure formation to determine the elemental core levels, the valence band

maximum and the work function. PEALD Al_2O_3 and SiO_2 were annealed *in situ* at 400 °C in research grade N_2 gas (90 sccm, 60 mTorr) for 30 min and the core levels were measured before and after annealing. To investigate the cleaning process for the O-face ZnO substrate, the XPS and UPS measurements were performed on as received ZnO and plasma cleaned ZnO substrates. X-rays were generated using monochromatic Al Kα (1486.6 eV) source in UHV chamber at 30 mA emission current and 15 kV accelerating voltage. The carbon and oxygen core level (C 1s and O1s) were used to determine the presence of carbon and hydroxyl groups on the surface. The uncertainity in core level peak fitting can be up to ±0.1 eV. The shift in the core level peak positions was used to determine the change in band bending and deduced the valence band offsets.

UPS was also performed on as received single crystal and plasma cleaned ZnO and on as deposited and annealed PEALD Al_2O_3 and SiO_2 heterostructures. The He I (21.2 eV) radiation was generated from research grade He gas in a UHV chamber with base pressure 4×10^{-9} Torr. The helium discharge was excited with a 1 kV supply and a discharge current of 20 mA. The photoemitted electrons were dispersed using VSW 50 mm hemispherical analyzer with a resolution of ~0.1 eV. A negative bias of 8 V or 10 V was used to overcome the work function of the analyzer i.e. 4.4 eV. The UPS spectra provide the binding energy of the valence band maximum (VBM), i.e. given by the low binding energy cut off position relative to the Fermi level. The UPS spectrum can also provide the electron affinity, which is calculated as following:

$$\chi = h\upsilon - W - E_g \quad \ldots\ldots\ldots\ldots\ldots \quad (3)$$

where, hυ is the incident ultraviolet photon energy (21.2 eV), W is the width of the UPS spectrum from low binding energy cut-off to high binding energy cut-off and E_g is the band gap of the material.

The following method was used to determine the valence band offsets at the interface, which is given by Waldrop *et. al*. and Kraut *et. al.* [24]

$$\Delta E_V = (E_{CL} - E_V)_{ZnO} - (E_{CL} - E_V)_{dielectric} + \Delta E_{CL} \quad \ldots\ldots\ldots\ldots\ldots\ldots \quad (4)$$

where, E_V is the VBM binding energy, and ΔE_{CL} is core level binding energy difference between wide band gap passivation thin films and ZnO, $(E_{CL} - E_V)_{ZnO}$ is the difference between binding energy of Zn core level and ZnO VBM and $(E_{CL} - E_V)_{dielectric}$ is the difference between binding energy of passivation dielectric layer metal element core level and its VBM. The binding energy of metal element core level and VBM shifts in the same direction after PEALD deposition and annealing, the difference between them, i.e. $(E_{CL}\text{-}E_V)_{ZnO}$, remains constant and independent of band bending. The valence band offset (VBO) can be calculated using the semiconductor and dielectric core level binding energies. In this study, the VBO is calculated using the core level binding energy of Al_2O_3/ZnO and SiO_2/ZnO.

D. Electrochemical Characterization:

The electrochemical characterizations were performed with a potentiostat (Biologic SP-200) while using ZnO as an electrode. The counter electrode was a Pt wire and Ag/AgCl was a reference electrode. The single crystal ZnO sample was sealed with epoxy on the sides and at the back to avoid the direct contact of ZnO with the electrolyte solution. For the similar reasons, the 20 nm PEALD ZnO deposited on Si and FTO

substrates were sealed on the sides with Kapton tape. Indium metal was used as a back contact for ZnO. The epoxy sealed samples were immersed into the electrolyte solution (0.1 M K_3PO_4 buffer) with adjusted pH to 7 using H_3PO_4. A 450 W Xe solar simulator (Newport, model 66923) was used to acheive ~100 mW/cm^2 intensity of light. Linear sweep voltammetry (LSV) with a 10 mV/s scan rate and chronoamperometry (CA) were used to examine the light response and durability of ZnO samples coated with passivation layers.

E. AFM, SEM and TEM Characterization:

To explore the quality of SiO_2, Al_2O_3 and ZnO after photoelectrochemical process the surface was scanned using atomic force microscopy (AFM) and scanning electron microscopy (SEM) and cross-sectional images were characterized using transmission electron microscopy (TEM). AFM was performed on as deposited 4 nm Al_2O_3/ ZnO thin film / n-Si and 4 nm SiO_2/ ZnO thin film / n-Si before and after the stability test to examine the surface topography and understand the photocorrosion process. To confirm the results of AFM, the topography was also analyzed using SEM after stability tests on the same samples. An Asylum Research molecular force probe (MFP) 3D atomic force microscope (AFM) was used in tapping mode, with non-conducting Si probes of spring constant k = 13-77 N/m and the resonance frequency ~200 – 400 kHz, in ambient atmosphere to obtain the topography images.

An FEI Nova 200 field emission scanning electron microscope (SEM) was employed both to examine the surface morphology of the samples after stability tests and to prepare cross-sectional TEM samples with its inner integrated focused ion beam (FIB). A JEOL 2010F (200 kV) was used to acquire high resolution TEM images. Energy

dispersive x-ray spectroscopy (EDX) coupled to this microscope was also used for chemical analysis.

III. Results:

To determine the band alignment at the interface and to understand the charge transfer mechanism in wide band gap passivation layer and semiconductor heterostructure, we chose to study the band alignment of PEALD Al_2O_3/ZnO and PEALD SiO_2/ZnO interfaces using photoelectron spectroscopy, structural characterization using AFM, SEM and TEM.

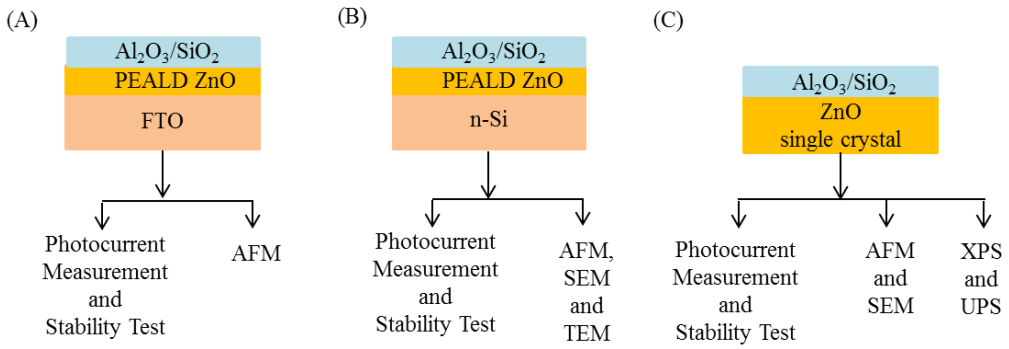

Figure 8.1. Passivation layer (Al_2O_3 and SiO_2) deposition on A) 20 nm PEALD ZnO/FTO, B) 20 nm PEALD ZnO/n-Si, and C) Single crystal ZnO.

For this study three different types of substrates, i.e. PEALD ZnO/FTO, PEALD ZnO/n-Si and ZnO single crystals, were used as described in the Figure 8.1. Selective measurements were done on each substrate coated with Al_2O_3 or SiO_2. The selectivity of characterization is decided based on the following factors. Samples with fluorine doped tin oxide (FTO) as substrate was selected due to high photocurrent results. However, the high roughness of FTO is an obstacle to determine the degradation of passivation layer through AFM. Thus the substrates with low surface roughness, 20 nm PEALD ZnO/n-Si

and single crystal ZnO were selected and compared for degradation mechanism. The ZnO thin films studies revealed that 4 nm SiO_2 could be an effective passivating layer, and the effectiveness of the protecting layer was also demonstrated in ZnO single crystal.

A. Al_2O_3/ZnO and SiO_2/ZnO band alignment:

To understand the band alignment at the interface between the ALD coatings and ZnO, XPS and UPS measurements were performed. Al_2O_3 and SiO_2 layers were deposited onto ZnO single crystals (O-terminated face) in order to have a well-controlled surface to study the effect of the ALD layer on band bending at the interface.

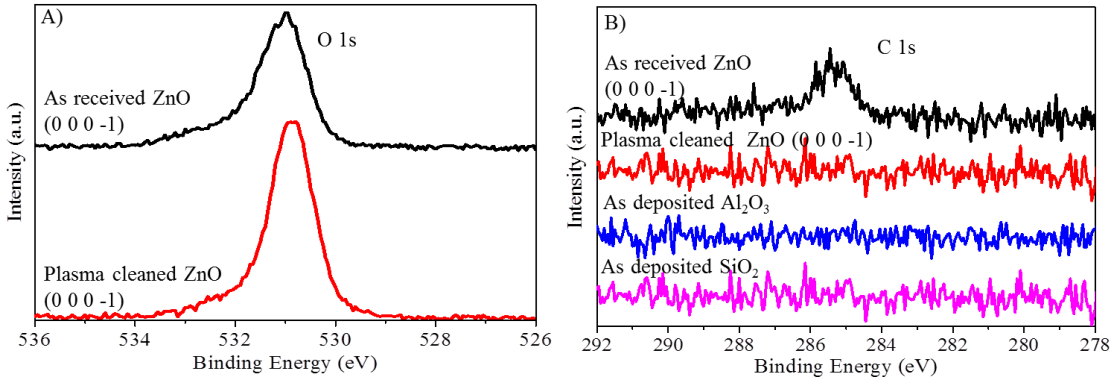

Figure 8.2. XPS of A) O 1s of as received and annealed Al_2O_3 and SiO_2 and B) C 1s of as received O-face ZnO and plasma cleaned O-face ZnO, as deposited Al_2O_3 and SiO_2 and.

In single crystal ZnO, band bending on the O-face is related to the surface adsorbed contaminants, such as carbon and hydroxyl layer, which can significantly affect the charge transfer to the surface in dielectric/ZnO heterostructures [25]. The defect states at the interface can act as charge trap regions and alter the charge tunneling from ZnO to the dielectrics. Thus surface cleaning is crucial prior to the deposition of PEALD dielectric thin films on O-face ZnO. Coppa et al. have studied the ZnO (0 0 0 -1) surface

cleaning using He:O_2 plasma at 525 °C [23]. However, because of the decomposition of ZnO single substrates used for this study cleaned at 525 °C, low temperature cleaning was required. To develop a cleaning process, different temperatures (310 °C - 500 °C) were used to determine the suitable annealing conditions without decomposing ZnO to clean O-face of ZnO. According to our experiments, annealing in He:O_2 mixed plasma at temperatures higher than 310 °C caused ZnO decomposition and desorption. The hydroxyl layer and carbon was removed effectively by annealing the substrate at 310 °C in He and O_2 mixed plasma. Post plasma cleaning, the O 1s and Zn $2p_{3/2}$ peaks increased in intensity and shifted 0.2 eV towards lower binding energies (Figure 8.2 a, 8.3 a), which indicated removal of surface donors. The diminished shoulder peak along with the ZnO O1s core level after surface cleaning indicated the removal of OH layer. The VBM binding energy for the as-received ZnO shifted from 3.4 eV to 3.2 eV after plasma cleaning (Figure 8.3 a), which is in agreement with the shift in the Zn 2p and O 1s core level binding energy in the XPS. The change in the Zn 2p core level indicates 0.2 eV downward band bending, considering the distance between the Zn core level and VBM is 1018.9 eV. After mixed plasma cleaning, the VBM position and XPS core levels moved toward the higher binding energy (0.2 eV) that signified the flat band in ZnO, which also indicated the decrease in donor surface states.

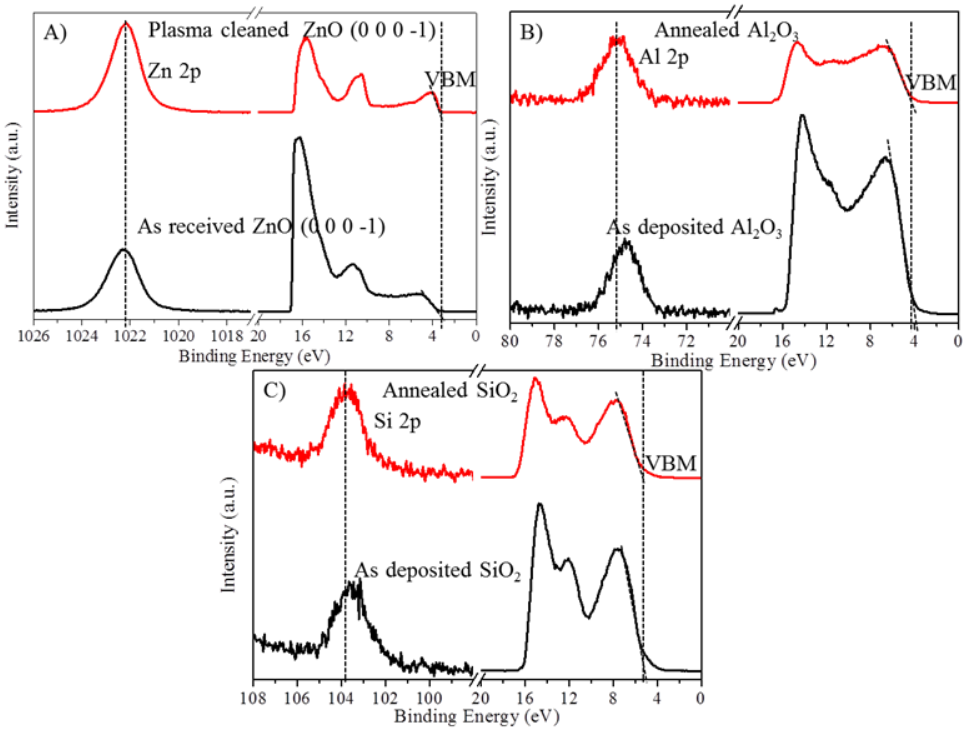

Figure 8.3 A) XPS of Zn $2p_{3/2}$ core level and UPS spectra of as received O-face ZnO, B) XPS of Al 2p core level and UPS spectra of as deposited and annealed Al_2O_3 and C) XPS of Si 2p core level and UPS spectra of as deposited and annealed SiO_2. The core level and VBM of ZnO shifts towards higher binding energy after plasma clean. However, the core level of Al and Si and VBM shifts towards the lower binding energy after Al_2O_3 and SiO_2 annealing.

The band bending is attributed to the accumulation or depletion layer near the interface to neutralize the surface charges. Ionized donors and free carriers accumulation/depletion generated the space charge layer, which induced upward or downward band bending. In case of ZnO, the surface adsorbed hydroxyl groups act as donors and makes the surface positively charged that causes the accumulation of free electrons and hence downward band bending is introduced in ZnO, as shown in Figure 8.4 a. The surface adsorption also affects the work function of the material. The increase

in the ZnO work function, i.e. from 4.3 to 4.5 eV, after surface cleaning is explained considering the donor nature of hydroxyl groups.

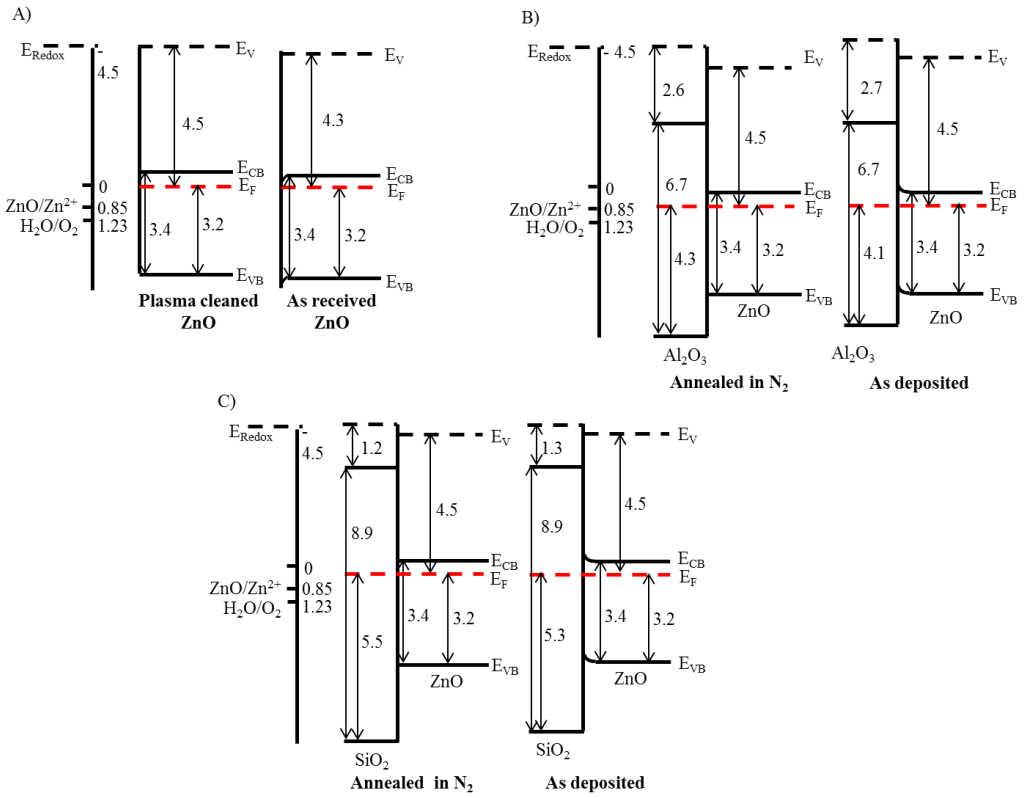

Figure 8.4. Redox potentials of water, ZnO and Al_2O_3 at RHE with respect to the vacuum level and Band diagram of a) as received ZnO (0 0 0 -1) and plasma ($He:O_2$) cleaned ZnO (0 0 0 -1), b) as deposited PEALD Al_2O_3/ZnO and annealed PEALD Al_2O_3/ZnO, and c) as deposited PEALD SiO_2/ZnO and annealed PEALD Al_2O_3/ZnO. The values in band diagrams and redox potentials are in eV.

The XPS and UPS data can be combined and used to draw the band alignment for heterostructures, which provide an insight to the valence and conduction band offsets at the interface and band bending. The data from XPS core level (Zn $2p_{3/2}$, Al 2p and Si 2p) peak positions and UPS (VBM and work function) for ZnO, Al_2O_3 and SiO_2, following each clean, deposition and annealing is concluded in Table 8.1. After the deposition of

~2.0 nm PEALD Al_2O_3 and SiO_2 on O-face ZnO, the Zn $2p_{3/2}$ core level shifts 0.4 eV and 0.5 eV towards the lower binding energy, Figure 8.3 b and c. Assuming the difference between the ZnO Zn 2p core level and VBM is constant (i.e. 1018.9 eV), 0.4 eV and 0.5 eV upward band bending was introduced in ZnO, as shown in Figure 8.4 b - c. The upward band bending demonstrates the negative charge in the PEALD films, which is compensated by the positive charges in the ZnO by inducing upward band bending. Presumably, the negative charge in PEALD films is due to the presence of interstitial oxygen and defects. Post-deposition annealing at 400 °C in research grade N_2 gas for 30 min removes the oxygen from thin PEALD and thus reduces the upward band bending in ZnO. The upward band bending and flat bands in ZnO after PEALD Al_2O_3 and SiO_2 and annealing are shown in Figure 8.4, which are calculated using XPS data.

Table 8.1: The table concludes the data from XPS core level (Zn $2p_{3/2}$, Al 2p and Si 2p) peak positions and UPS (VBM and work function) for ZnO, Al_2O_3 and SiO_2, following each clean, deposition and annealing.

Material	Zn $2p_{3/2}$ (eV)	O 1s (eV)	Si 2p (eV)	Al 2p (eV)	VBM (eV)	Work function (eV)
As received ZnO	1022.3	531	----	----	3.4	4.3
Plasma treated ZnO	1022.1	530.8	----	----	3.2	4.5
As deposited SiO_2	1021.9	----	103.5	----	5.3	5.1
Annealed SiO_2	1022.1	----	103.7	----	5.5	4.6
As deposited Al_2O_3	1021.8	----	----	74.6	4.0	5.4
Annealed Al_2O_3	1022.1	----	----	75.0	4.3	5.0

The measured band gap of amorphous PEALD Al_2O_3 using energy loss spectroscopy (EELS), in previous study, is 6.7 eV [26] and reported band gap of SiO_2 is 8.9 eV [27]. To determine the valence band offset of SiO_2/ZnO from equation 4, the experimental values of $(E_{CL} - E_V)_{ZnO}$, $(E_{CL} - E_V)_{SiO2}$ and ΔE_{CL} are used, which are determined as 1018.9 eV, 98.2 eV, – 920.7 eV, respectively. Similarly, the values of $(E_{CL} - E_V)_{ZnO}$, $(E_{CL} - E_V)_{Al2O3}$ and ΔE_{CL} for Al_2O_3/ZnO are measured as 1018.9 eV, 70.7 eV and – 947.1 eV, respectively. $(E_{CL} - E_V)_{Al2O3}$ and $(E_{CL} - E_V)_{Al2O3}$ values of as grown and annealed Al_2O_3 and SiO_2 and electron affinity of Al_2O_3 (2.6 eV) and SiO_2 (1.2 eV) from this study corroborates with the prior studies [27].The determined valence and conduction band offset of Al_2O_3/ZnO heterostructure is 1.1 eV and 2.2, and SiO_2/ZnO is 2.5 eV and 3.2.

It is evident from the band offsets in the band diagrams of Al_2O_3/ZnO and SiO_2/ZnO, the possible mechanism of photoexcited carrier transport from ZnO to the surface of Al_2O_3 and SiO_2 is tunneling.

B. Photoelectrochemical Characterization of Al_2O_3 and SiO_2 ALD coatings on PEALD ZnO:

LSV and CA measurements determine the current resulting from ZnO photoexcited holes transport to the electrolyte solution. The ZnO photocorrosion can also contribute to the photocurrent. The LSV measurement is shown in Figure 8.5 a) for 20 nm ZnO thin film. The stability test was performed using CA at a fixed potential of 0.3 V vs SCE to monitor the photocurrent generation over time. Due to thin ZnO film the current increase to the maximum and drops back to zero within a few minutes, Figure 8.5 a. The decay in the photocurrent generated by the ZnO photocorrosion is likely because

of the limited thickness of ZnO. The 4 nm Al_2O_3/ZnO shows the similar behavior as ZnO; however the increase and decrease in photocurrent is slower, Figure 8.5 a. On the hand, 4 nm SiO_2/ZnO shows the constant photocurrent with no significant change, Figure 8.5 a.

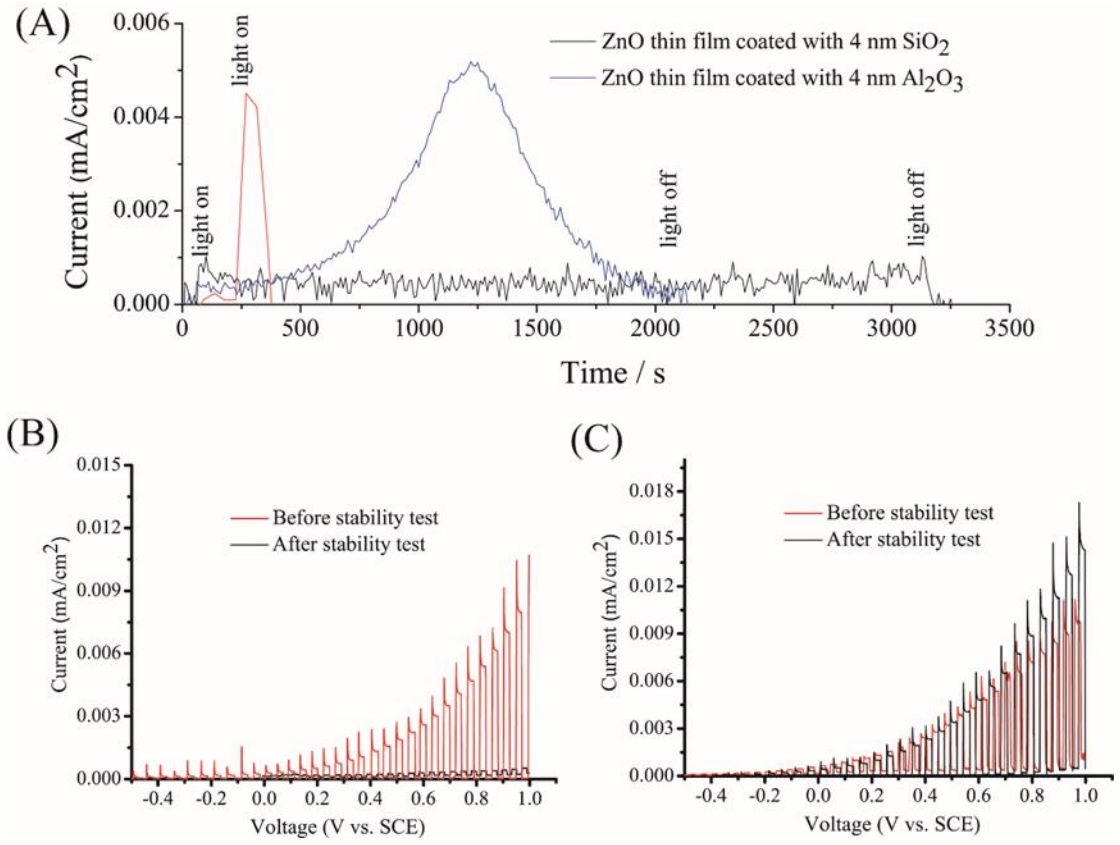

Figure 8.5. Comparison of 20 nm PEALD ZnO/FTO and passivated 20 nm PEALD ZnO/FTO with 4 nm Al_2O_3 and 4 nm SiO_2. (A) Stability test of all these three samples, the voltage was set at 0.3 V vs SCE, (B) comparison of LSV of ZnO sample coated with 4 nm Al_2O_3 before and after stability test, and (C) comparison of LSV of ZnO sample coated with 4 nm SiO_2 before and after stability test.

The LSV measurements on 4 nm Al_2O_3 or SiO_2 coated ZnO are shown in Figure 8.5 b and c before and after the stability test. The transient current spikes observed in the LSV plots are possibly due to the light turn on and off and/or from the increased charge transfer resistance due to the insulator ALD films tunnelling barrier. In case of the Al_2O_3/ZnO, the photocurrent was significantly smaller after the CA test (Figure 8.5 b), which indicates the dissolution of 20 nm ZnO due to photocorrosion. In contrast, the photocurrent before and after the CA test for the SiO_2/ZnO sample was similar, which suggests that SiO_2 layer was intact on 20 nm PEALD ZnO (Figure 8.5 c).

C. AFM and SEM Characterization:

To better understand these observations, AFM and SEM characterization were performed. To obtain a flat surface for AFM, ZnO films with ALD protecting layers of 4 nm were deposited onto n-Si substrates, which have ~ 20 times less surface roughness than FTO. The root mean square (RMS) roughness of the n-Si before and after the deposition of 20 nm PEALD ZnO was ~0.7 nm for the 5 μm x 5 μm scan; however, the RMS on FTO before and after ZnO deposition was ~15 nm. The AFM data for the Al_2O_3 coated film before and after the CA stability test is shown in Figure 8.6. The as-deposited Al_2O_3/ZnO/Si sample surface was flat, with roughness similar to the ZnO film (Figure 8.6 a). The CA and LSV plots for After CA testing, particles were observed on the surface in both AFM and SEM images due to the adhesion of phosphate salts from the electrolyte. Furthermore, pits of different sizes were observed on the surface of the samples after CA measurements of different durations. The AFM scan showed tiny pits ~ 6 nm deep on the surface after performing CA for 7 min, as shown in Figure 8.6 b. AFM on the surface after the 15 min stability test showed an increase in the width and depth of

pits (Figure 8.6 c). This indicates that the corrosion of the Al_2O_3 passivation layer initiated from tiny pin holes on the surface and expanded into large sized pits. To further confirm the corrosion mechanism, SEM characterization was performed on the same samples. It is evident from the SEM image (Figure 8.6 d) that Al_2O_3 surface after 7 min stability test has undergone severe damage with various darker contrast areas which were confirmed to be corrosion pits by TEM.

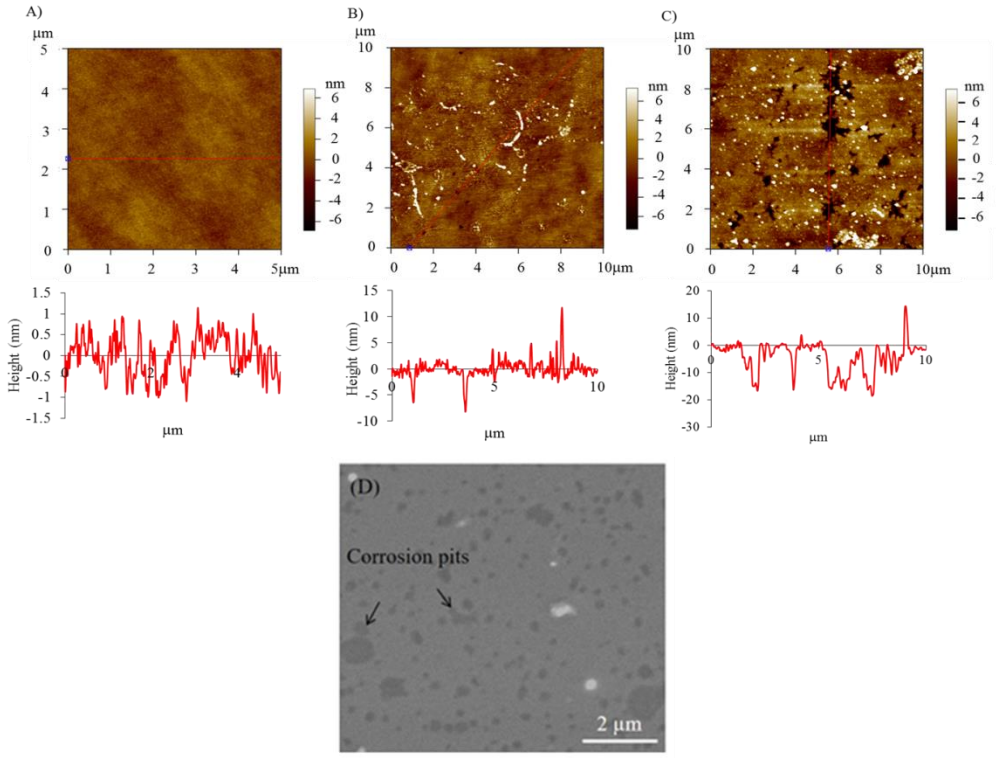

Figure 8.6. 4 nm Al_2O_3 coated 20 nm ZnO/n-Si (4A-PZS), AFM images of (A) before the stability test and (B) after stability test for 7 min and (C) after stability test for 15 min and the height and width profile for respective AFM topography image along the red line. (D) SEM image showing the surface morphology of the same sample after 7 min stability test.

On the other hand, AFM observation of the 4nm SiO_2/ZnO did not show obvious signs of degradation or pit formation (Figure 8.7 a - b). SEM observation of the SiO_2 passivated sample after 7 min of CA stability test (Figure 8.7 c) also showed an absence of pit formation.The surface remained as smooth as the sample prior to testing, even after performing CA for 1 hour (Figure 8.7 b and d), indicating that the SiO_2 layer was preserved.

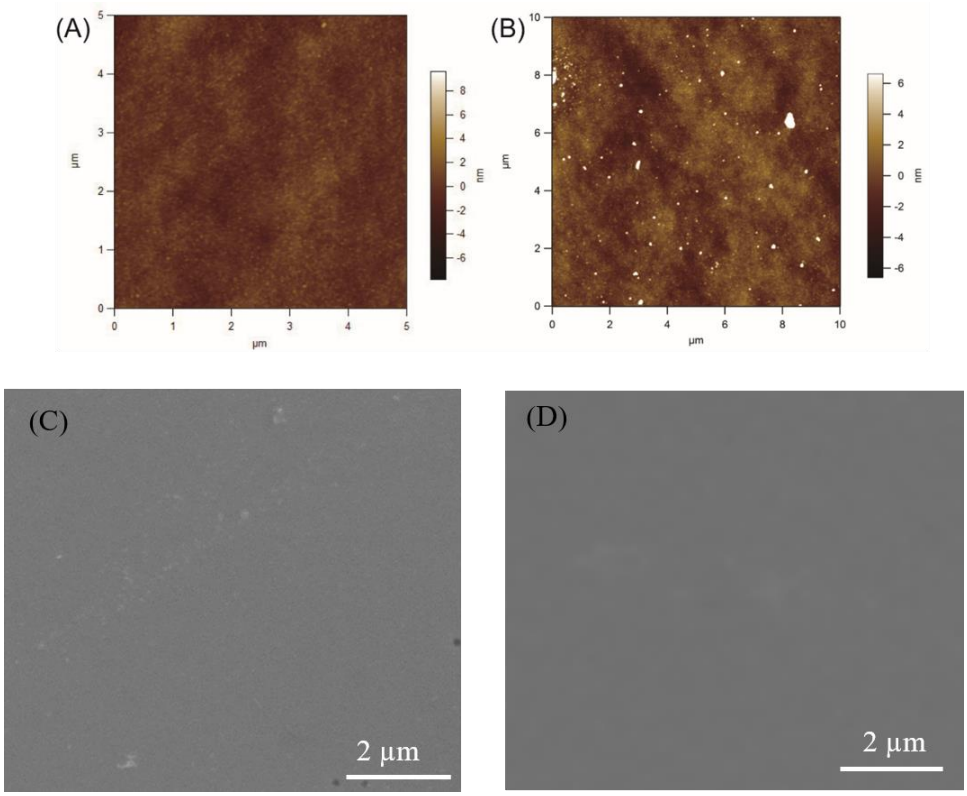

Figure 8.7. 4nm SiO_2 coated 20 nm ZnO on n-Si surface. AFM data for sample (A) as-prepared, (B) after 1 hour durability test. SEM image after CA for (C) 7 min, (D) 1h stability test.

D. TEM Characterization:

In order to understand and investigate the origin of pits observed in AFM and SEM scans, TEM characterization was crucial and thus performed on cross-sectioned Al_2O_3/ZnO/Si and SiO_2 /ZnO/Si samples. The crossectional TEM characterization provides an insight to the ZnO degradation mechanism the interface of passivation layers and ZnO. TEM sample was tilted to Si [0 1 1] zone axis to clearly show the interfacial structure.

For the Al_2O_3/ZnO/Si sample, a TEM sample was obtained across a few corrosion pits to compare the undamaged (Figure 8.8 a) and corroded (Figure 8.8 b) areas. TEM images show a thin amorphous layer between the Si substrate and ~21 nm PEALD ZnO. The observed thickness of Al_2O_3 layer is ~3 nm in the undamaged area, which is also confirmed by EDX. It is evident from TEM images that the ZnO is polycrystalline and Al_2O_3 layer is amorphous. Figure 8.8 b shows the corroded area where ZnO layer is reduced in thickness. The ZnO corrosion near the Si surface corresponds to the delamination behavior.

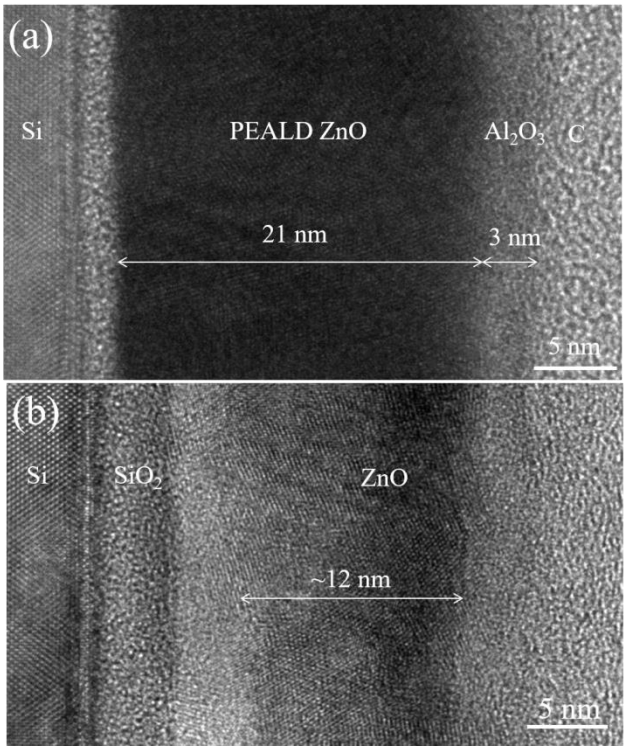

Figure 8.8. TEM images showing cross section microstructure of 4 nm Al_2O_3/ZnO/Si sample after 7 min of stability test from (a) uncorroded area and (b) corroded area.

Similar analyses were performed on the 4 nm SiO_2/ZnO/Si. From the CA, LSV, AFM and SEM results, this sample has shown negligible degradation. A TEM specimen was prepared from the sample that has been tested for stability for 1h. In TEM images, it is difficult to distinguish SiO_2 from amorphous carbon which indicates the amorphous nature of SiO_2, Figure 8.9 a. EDX was used to confirm the presence of the SiO_2 layer. A predominant Zn L peak is observed from intact ZnO layer, while Si peak dominates in the EDX scan that is acquired about 2 nm above the ZnO layer. The TEM from corroded area is also shown in Figure 8.9 b. In contrast to the Al_2O_3/ZnO/Si, a relatively uniform contrast is observed in the corroded ZnO area. This suggests the ZnO corrodes under the

SiO_2; however, the mechanism is different from Al_2O_3 passivation layer, which is discussed in the discussion section.

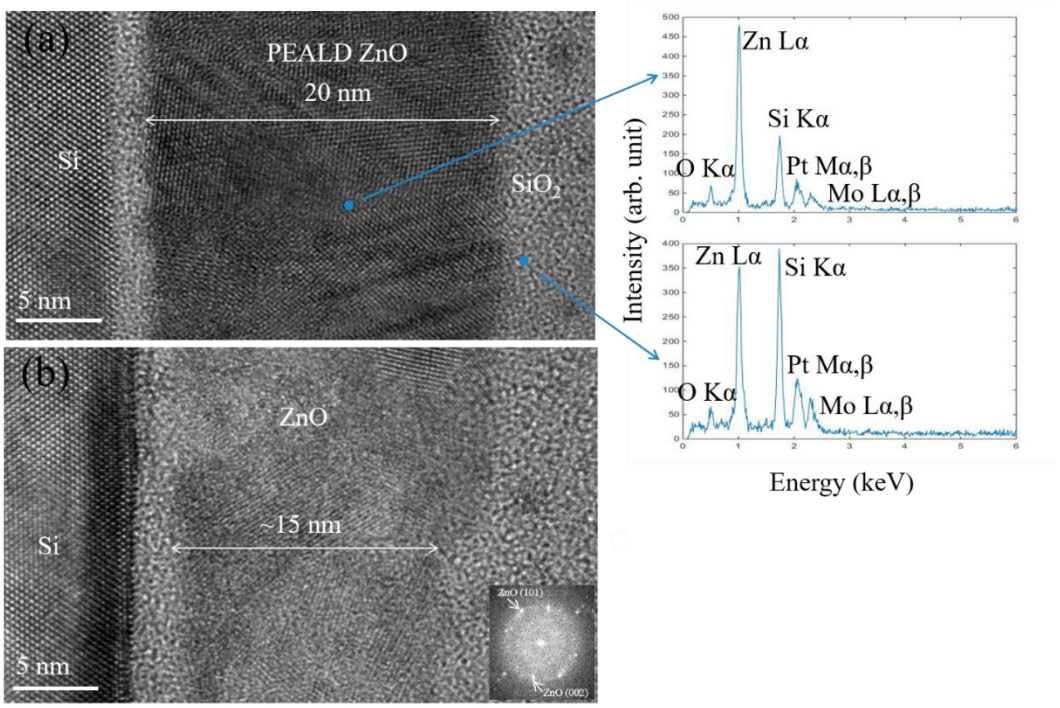

Figure 8.9. TEM images showing cross section microstructure of 4 nm SiO_2/ZnO/Si sample after 1h of stability test from (a) uncorroded area and (e) corroded area. EDX results from the ZnO layer and the top surface of the uncorroded area are also shown. The Pt and Mo peaks in the EDX spectrum come from the process of TEM sample preparation using FIB technique.

IV. Discussion:

A. Passivation effect of Al_2O_3 and SiO_2:

In order to understand the passivation of Al_2O_3 and SiO_2 on ZnO, the shape of the LSV and CA plots, and the surface topography images using AFM and SEM are analyzed. It is evident from photocurrent measurements that PEALD ZnO corrodes in less than 5 min, Figure 8.5 a. The possible cause of is the nanocrystalline structure as

shown in TEM (Figure 8.8 and 8.9). The wide bandgap and dielectric properties of Al_2O_3 and SiO_2 layers on ZnO generates an energy barrier for photoexcited carriers [Figure 8.4 b and 8.4 c]. Thus the photocurrent in LSV and CA plots shows a sharp decrease with an increase in thickness. The increase in thickness results in an exponential decrease of carrier tunneling, which is explained using the tunneling thickness of the dielectric layers. A suitable tunneling length for electrons has been shown to be ~2 nm [28].

The increase in photocurrent in the Al_2O_3/ZnO/FTO stability test, Figure 8.5 a, indicates ZnO is in direct contact with the electrolyte and thus photocorrosion contributes to enhance the photocurrent. It has been reported that Al_2O_3 passivation layer dissolves in hot water [29]. Consequently, it can be suggested that an Al_2O_3 can dissolve under the influence of photogenerated holes and water. To understand the photocorroison of protected ZnO and Al_2O_3 during photoelectrochemical measurements, AFM, SEM and TEM studies are crucial. The surface analysis with AFM and SEM scans show the Al_2O_3 surface has corrosion pits after photoelectrochemical measurements (Figure 8.6), which is possibly due to chemical instability and expanded corrosion initiated from pin holes. It appears Al_2O_3 corrosion rate is slower than ZnO. The TEM sample analysis of the corrosion pit showed the damaged ZnO, Figure 8.6 b, and EDX on the same sample confirms some of Al_2O_3 is preserved at the surface after the photoelectro-chemcial measurements.

In contrast to the Al_2O_3 dissolution issue, SiO_2 showed a higher stability for the same thicknesses. Unlike Al_2O_3, the SiO_2 layer showed a constant photocurrent which is an indication of intact SiO_2 on the surface. The same conclusion is also corroborated by the 1 h stability test measurements on 4 nm SiO_2/ZnO/FTO, which shows a negligible

increase in photocurrent. Thus, it seems that the 4 nm SiO_2 is sufficient for the passivation of the ZnO surface. However, the intact thick SiO_2 layer reduces the electron tunneling.

B. Degradation Mechanisms of Al_2O_3 and SiO_2:

The failure of wide band gap passivation layers is attributed to three factors: (1) pin holes, and (2) diffusion of electrolyte species through the passivating layer to the interface. The photocorrosion of the semiconductor or the damage of Al_2O_3 or SiO_2 passivation layer is either due to pin holes and surface defects or ion diffusion. The topography and cross-sectional characterization of Al_2O_3/ZnO/Si using AFM, SEM and TEM indicates the corrosion of Al_2O_3 and ZnO underneath. The favorable reaction for Al_2O_3 degradation with holes is similar to that of ZnO: [29]

$$2Al_2O_3 + 12h^+ \rightarrow 4Al^{3+} + 3O_2 \qquad (3)$$

The reaction of Al_2O_3 with water can cause thinning of the whole film. However, AFM and SEM shows non-uniform corrosion of the Al_2O_3/ZnO, which implies besides thinning, another photocorrosion process dominates in the passivation layer corrosion. A possible process for Al_2O_3 is pin holes and surface defects, which initiates the photocorrosion at the surface of Al_2O_3 and causes pit formation. A possible model of photocorrosion of Al_2O_3/ZnO is shown in Figure 8.10 (A). It was not possible to measure the surface corrosion pits of ZnO samples on FTO due to high surface roughness of FTO. In order to examine the corrosion mechanism, 20 nm PEALD ZnO/Si samples were coated with 4 nm SiO_2 or Al_2O_3. It is interesting to note that an exfoliation-like behavior was commonly observed in the areas where the most severe corrosion occured at the

interface between the n-Si substrate and ZnO, Figure 8.9 (B). Due to the wide band gap of ZnO and Al_2O_3, the photons with large wavelength penetrate ZnO and excite carriers in n-Si substrate. The photogenerated holes sweep to the interface of ZnO and Si and apparently cause ZnO corrosion. This leads to the exfoliation of ZnO at the Si/ZnO interface.

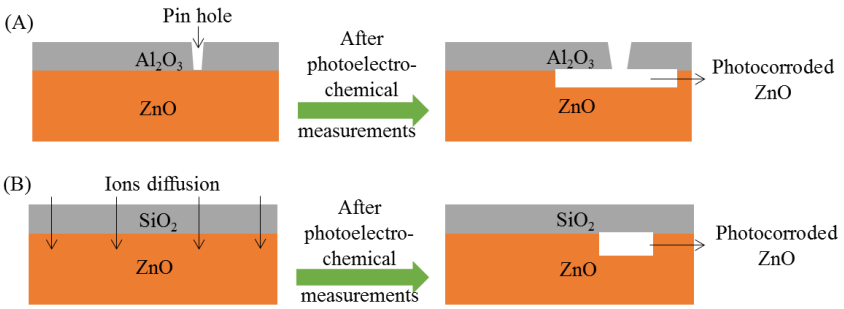

Figure 8.10. Photocorrosion mechanism of (A) Al_2O_3/ZnO due to electrolyte and ZnO direct contact through pin holes in Al_2O_3 layer and (B) SiO_2/ZnO due to ions diffusion through porous SiO_2 layer.

Tomkiewicz *et. al.* has studied the pitting of a 40-nm TiO_2 passivation layer on GaAs. The destruction mechanism of TiO_2 was explained with the diffusion of electrolyte species through films thinner than 40 nm to the interface of TiO_2 and GaAs and the reaction with holes dissolves the GaAs underneath the TiO_2 [30]. The intact TiO_2 film on top of the dissolved GaAs forms a bubble which ruptures due the pressure to form a pit [30, 31]. Similarly, the diffusion of electrolyte species has also been studied in SiO_2/Si ion diffusion field effect transistors (ISFET) [32]. The favorable migration of OH^- ions which has been reported in SiO_2 [32] suggests that OH^- can diffuse to the ZnO/SiO_2 interface and Zn^{2+} and O_2 can be released to the electrolyte through this same diffusion process. Although the sample surface is flat according to AFM and photocurrent is stable

in the stability test, the ZnO layer underneath still gets corroded. The photocorrosion mechanism of SiO_2/ZnO is shown in Schematic 3 (b). The stability and diffusion of electrolyte species through SiO_2 complicates the characterization and analysis of the corrosion process. Some of the surface areas are thin to allow the diffusion of ions, which initiate the corrosion to the underlying ZnO layer. Therefore, SiO_2 is different from Al_2O_3, even though the ZnO on both samples experiences corrosion. The rate of ZnO corrosion with SiO_2 passivation layers is very slow. The existing SiO_2 layer inhibits the direct contact between the ZnO and electrolyte, is more effective passivating the surface than Al_2O_3.

V. Conclusion

Al_2O_3 and SiO_2 were successfully deposited on ZnO single crystal and thin film sample and shows uniform coverage. ZnO samples coated with SiO_2 had better stability than samples coated with Al_2O_3. The failure of Al_2O_3 layers starts from defective sites or pin holes and expands to the underneath ZnO. Although the ZnO coated with SiO_2 shows better stability than Al_2O_3, the corrosion still occurs due to the diffusion of ions from electrolyte to the ZnO layer underneath.

References:

[1] K. Maeda, K. Teramura, D. Lu, T. Takata, N. Saito, Y. Inoue, K. Domen, "Photocatalyst releasing hydrogen from water" *Nature* **440** (2006) 295-295.

[2] M. Grätzel, "Photoelectrochemical cells" *Nature* **414** (2001**)** 338-344.

[3] Y. Sasaki, H. Nemoto, K. Saito, A. Kudo, "Solar water splitting using powdered photocatalysts driven by Z-schematic interparticle electron transfer without an electron mediator" *J. Physical Chem*. C **113** (2009) 17536-17542.

(4) M. G. Walter, E. L. Warren, J. R. McKone, S. W. Boettcher, Q. Mi, E. A. Santori, N. S. Lewis, "Solar water splitting cells" *Chem. Rev*. **110** (2010) 6446-6473.

[5] C. Han, M. Yang, B. Weng, Y. Xu, "Improving the photocatalytic activity and anti-photocorrosion of semiconductor ZnO by coupling with versatile carbon" *Physical Chem Chemical Phy*. **16** (2014) 16891-16903.

[6] A. Paracchino, V. Laporte, K. Sivula, M. Grätzel, E. Thimsen, "Highly active oxide photocathode for photoelectrochemical water reduction", *Nature materials*. **10** (2011) 456-461.

[7] Y. Wang, J. Liu, L. Liu, D.D. Sun, "Enhancing stability and photocatalytic activity of ZnO nanoparticles by surface modification of graphene oxide," *J nanosci nanotech*. **12** (2012) 3896-3902.

[8] Y. Cao, J. Chen, H. Zhou, L. Zhu, X. Li, Z. Cao, D. Wu, A. Li, "Photocatalytic activity and photocorrosion of atomic layer deposited ZnO ultrathin films for the degradation of methylene blue," *Nanotech*. **26** (2015) 024002.

[9] T. Singh, T. Lehnen, T. Leuning, S. Mathur, "Atomic layer deposition grown MOx thin films for solar water splitting: Prospects and challenges" *J. Vac. Sci. Tech.* A **33 (**2015**)** 010801.

[10] R. Sapkal, S. Shinde, T. Waghmode, S. Govindwar, K. Rajpure, C. Bhosale, Photo-corrosion inhibition and photoactivity enhancement with tailored zinc oxide thin films, Journal of Photochemistry and Photobiology B: Biology. 110 (2012) 15-21.

[11] S. Hu, N. S. Lewis, J. W. Ager, J. Yang, J. R. McKone, N. C. Strandwitz, "Thin-Film Materials for the Protection of Semiconducting Photoelectrodes in Solar-Fuel Generators" *J. Physic. Chem* C **119 (**2015) 24201-24228.

[12] N. G. Carratala, M. S. Prévot, K. Sivula, "Surface modification of semiconductor photoelectrodes" *Physical Chem. Chemical Phys.* **2015**.

[13] M. F. Lichterman, K. Sun, S. Hu, X. Zhou, M. T. McDowell, M. R. Shaner, M. H. Richter, E. J. Crumlin, A. I. Carim, F. H. Saadi, "Protection of inorganic semiconductors for sustained, efficient photoelectrochemical water oxidation" *Cataly. Today* **262 (**2016) 11-23.

[14] A. Abdulagatov, Y. Yan, J. Cooper, Y. Zhang, Z. Gibbs, A. Cavanagh, R. Yang, Y. Lee, S. George, "Al_2O_3 and TiO_2 atomic layer deposition on copper for water corrosion resistance", *ACS Appl. Mater. Interf.* 3 (2011) 4593-4601.

[15] C. Li, T. Wang, Z. Luo, D. Zhang, J. Gong, "Transparent ALD-grown Ta2O5 protective layer for highly stable ZnO photoelectrode in solar water splitting" *Chemic. Communic.* **51 (**2015) 7290-7293.

[16] Q. Gui, Z. Xu, H. Zhang, C. Cheng, X. Zhu, M. Yin, Y. Song, L. Lu, X. Chen, D. Li, "Enhanced photoelectrochemical water splitting performance of anodic TiO2 nanotube arrays by surface passivation" *ACS appl. Mat. Interf.* **6 (**2014) 17053-17058.

[17] M. Liu, C. Nam, C. T. Black, J. Kamcev, L. Zhang, "Enhancing water splitting activity and chemical stability of zinc oxide nanowire photoanodes with ultrathin titania shells" *J. Physical Chem.* C **117 (**2013) 13396-13402.

[18] Y. J. Hwang, C. Hahn, B. Liu, P. Yang, "Photoelectrochemical properties of TiO2 nanowire arrays: a study of the dependence on length and atomic layer deposition coating" *Acs Nano* **6 (**2012) 5060-5069.

[19] M. H. Lee, K. Takei, J. Zhang, R. Kapadia, M. Zheng, Y. Chen, J. Nah, T. S. Matthews, Y. Chueh, J. W. Ager, "p-Type InP Nanopillar Photocathodes for Efficient Solar-Driven Hydrogen Production" *Angewandte Chemie* **124 (**2012) 10918-10922.

[20] S. Hu, M. R. Shaner, J. A. Beardslee, M. Lichterman, B. S. Brunschwig, N. S. Lewis, "Amorphous TiO_2 coatings stabilize Si, GaAs, and GaP photoanodes for efficient water oxidation" *Science* **344 (**2014) 1005-1009.

[21] Y. Yang, D. S. Kim, Y. Qin, A. Berger, R. Scholz, H. Kim, M. Knez, U. Gösele, "Unexpected Long-Term Instability of ZnO Nanowires "Protected" by a TiO2 Shell" J. *Am. Chem. Soc.* **131 (**2009) 13920-13921.

[22] Y. Li, X. Zhang, S. Jiang, H. Dai, X. Sun, Y. Li, "Improved photoelectrochemical property of a nanocomposite NiO/CdS@ ZnO photoanode for water splitting" *Solar Energy Mater. Solar Cells* **132 (**2015) 40-46.

[23] F. L. Formal, N. Tétreault, M. Cornuz, T. Moehl, M. Grätzel, K. Sivula, "Passivating surface states on water splitting hematite photoanodes with alumina overlayers" *Chemical Sci* **2 (**2011) 737-743.

[24] W. Kim, T. Tachikawa, D. Monllor-Satoca, H. Kim, T. Majima, W. Choi, "Promoting water photooxidation on transparent WO3 thin films using an alumina overlayer" *Energy Env. Sci* **6 (**2013) 3732-3739.

[25] D. Barpuzary, Z. Khan, N. Vinothkumar, M. De, M. Qureshi, "Hierarchically grown urchinlike CdS@ ZnO and CdS@ Al2O3 heteroarrays for efficient visible-light-driven photocatalytic hydrogen generation" *J. Physical Chem.* C **116 (**2011) 150-156.

[26] S. M. George, "Atomic layer deposition: an overview" *Chem. Rev*. **110 (**2009) 111-131.

[23] B. Coppa, C. Fulton, P. Hartlieb, R. Davis, B. Rodriguez, B. Shields, R. Nemanich, "In situ cleaning and characterization of oxygen-and zinc-terminated, n-type, ZnO {0001} surfaces", *J. Appl. Phys*. **95** (2004) 5856-5864.

[24] J. Waldrop, R. Grant, "Measurement of AlN/GaN (0001) heterojunction band offsets by x-ray photoemission spectroscopy", *Appl. Phys. Lett*. **68** (1996) 2879-2881.

[25] H. Moormann, D. Kohl, G. Heiland, "Variations of work function and surface conductivity on clean cleaved zinc oxide surfaces by annealing and by hydrogen adsorption," *Surf. Sci*. **100** (1980) 302-314.

[26] J. Yang, B.S. Eller, M. Kaur, R.J. Nemanich, "Characterization of plasma-enhanced atomic layer deposition of Al2O3 using dimethylaluminum isopropoxide" *J. Vac. Sci. Tech.* A. **32** (2014) 021514..

[27] J. Yang, B. Eller, and R. Nemanich "Surface band bending and band alignment of plasma enhanced atomic layer deposited dielectrics on Ga- and N-face gallium nitride" J. Appl. Phys. **116** (2014) 123702.

[28] G. Campet, J. Manaud, C. Puprichitkun, Z. Sun, P. Salvador, "Protection of photoanodes against photo-corrosion by surface deposition of oxide films: criteria for choosing the protective coating," *Active Passive Electronic Comp*. **13** (1989) 175-189..

[29] A. Abdulagatov, Y. Yan, J. Cooper, Y. Zhang, Z. Gibbs, A. Cavanagh, R. Yang, Y. Lee, S. George, "Al2O3 and TiO2 atomic layer deposition on copper for water corrosion resistance," *ACS appl. Mater. Interf.* **3** (2011) 4593-4601.

[30] M. Tomkiewicz, J.M. Woodall,"Photoelectrolysis of water with semiconductor materials," J. *Electrochem. Soc*. **124** (1977) 1436-1440.

[31] A.J. Nozik, "Photoelectrochemistry: applications to solar energy conversion," *Annu. Rev. Phys. Chem*. **29** (1978) 189-222.

[32] A. Topkar, R. Lal, “Effect of electrolyte exposure on silicon dioxide in electrolyte-oxide-semiconductor structures,” *Thin Solid Films*. **232** (1993) 265-270.

CHAPTER 9: MODIFIED PLASMA ENHANCED ATOMIC LAYER DEPOSITION OF ZnO and Al_2O_3

Abstract: Plasma enhanced atomic layer deposition (PEALD) is a well-established deposition process to deposit smooth and uniform films for metal oxides. However, excess oxygen in the PEALD films does not favor the metal oxide electrical properties. Here we have employed helium plasma pulses in the PEALD deposition cycle for ZnO and Al_2O_3 and compared the films with without helium plasma. *In situ* XPS, and *ex situ* RBS, AFM and XRR were used to characterize the films. The results indicate removal of acceptor-like states (possibly excess oxygen) with incorporated helium plasma pulses. The effect is ascribed to rearrangement of the precursor molecules due to the energy provided by the helium plasma species.

I. Introduction:

Plasma enhanced atomic layer deposition (PEALD) is a novel deposition process to deposit uniform and conformal films for various applications [1, 2]. It has been extensively employed to deposit oxides including ZnO, Al_2O_3, HfO_2, SiO_2 and TiO_2 [1]. ZnO is a semiconductor material which has applications for electronic and optoelectronic devices due to its wide band gap, high carrier concentration and mobility, and transparency [3, 4]. For example, ZnO based thin film transistors and transparent conducting oxides on flexible and non-flexible substrates have been demonstrated. Similarly, Al_2O_3 have been considered for gate insulator application in electronic devices [5, 6]. Many of the properties of ZnO and Al_2O_3 rely on the deposition method and deposition temperature. With the continuing demands of thin films and flexible electronics, low roughness and low temperature processes are becoming mandatory requirements. In the last decade, the widely used low temperature process to deposit smooth and uniform films is plasma enhanced atomic layer deposition (PEALD) [1, 5]. However, the high reactivity of the oxygen plasma generated species can be detrimental to the electrical properties of ZnO and Al_2O_3 [7, 5]. Here, we propose a method to remove the excess oxygen from ZnO and Al_2O_3 using helium plasma pulses during PEALD deposition process. The films have been characterized with x-ray photoelectron spectroscopy (XPS), atomic force microscopy (AFM), x-ray reflectivity (XRR) and Rutherford Backscattering Spectroscopy (RBS).

The excess oxygen in ZnO thin films becomes negatively charged by trapping free electrons. Thus the conductivity and mobility of ZnO are reduced [8, 9]. In PEALD Al_2O_3, we have shown in prior studies that the adsorption of excess oxygen acts as acceptor, which shifts the core level peaks to lower binding energy [5]. To mitigate the adsorbed O_2 problem on ZnO nanowires Kind *et. al.* have used UV light illumination, which has successfully enhanced the ZnO conductivity [8]. We are adopting a similar approach for a PEALD ZnO deposition process to remove the excess oxygen during the deposition. Instead of using a source of UV light, a helium (He) plasma step is incorporated in the PEALD process after each oxygen plasma pulse. The He plasma generates UV photons of line I (21.2 eV) [10], where the intensity can be controlled by varying the He gas pressure [10].

II. Experiment:

The ZnO and Al_2O_3 thin films were deposited on 25.4 mm n-Si wafers in our customized PEALD system using dimethyl zinc (DMZ) and dimethyl(aluminum)isopropoxide (DMAI). During the deposition, the nitrogen purge gas, and oxygen and helium plasma ignition pressure was maintained at 100 mTorr using a throttle valve that separates the chamber and turbo pump. To pump the chamber, the turbo pump was backed with a one stage dry pump. DMZ is a high vapor pressure precursor, thus requires to be cooled to -18 °C. On the other hand DMAI is heated to 90 °C to be vaporized. The precursor vapors were transported from bubbler to the chamber using an Ar gas flow of 55 sccm for DMZ and 70 sccm for DMAI. To avoid condensation of precursor vapors, the pipelines and chamber walls were heated and maintained at ~100 °C. The N_2 purge gas flow was 50 sccm, and the O_2 and He gas flows were 35 sccm and 45 sccm, respectively. The remote O_2 and He plasmas were generated at 200 W and 13.54 MHz at ~25 cm above the deposition surface, which reduces the ion bombardment on the surface. Consequently, the O_2 and He plasma generated radical species and photons which reach the reaction surface. The oxygen and helium plasma pulse was 8 sec. Schematics of the He assisted PEALD process is shown in Figure 1. The ZnO was deposited at 130 °C and the Al_2O_3 was deposited at 170 °C. XPS was used to determine the core level positions, RBS was used to determine the thickness and

elemental ratios (Zn:O and Al:O), AFM was used to scan the surface topography, and XRR was used to determine the thickness and density.

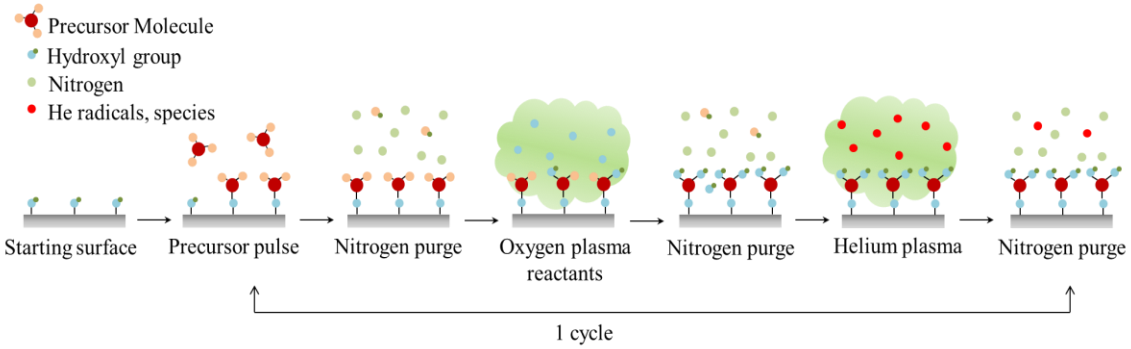

Figure 9.1. Schematic of He pulse induced plasma enhanced atomic layer deposition.

III. Results And Discussion:

The XPS core levels (O 1s, Zn 2p, Al 2p and Si 2p) after 10 PEALD cycles of ZnO or Al_2O_3 with and without He plasma pulse are shown in Figure 2. It is evident that all the core levels shift to higher binding energy after growth with He plasma pulses. The shift to higher binding energy is an indication of reduced acceptor-like states in the PEALD films. For instance, in our prior studies, the as-deposited Al core level position of 10 nm PEALD Al_2O_3 at 200 °C was 74.2 eV [5]. However, after a 600 °C anneal in N_2, the peak position shifts to 75.3 eV indicating the acceptor states were removed [5]. For He plasma assisted Al_2O_3 deposition, the Al core level position is 75.4 eV, which is at 0.9 eV higher energy than the Al core level of Al_2O_3 (74.5) deposited without He plasma pulse. Similarly, the XPS Zn core level positions in ZnO deposited with and without He plasma pulse are at 1022.0 eV and 1021.5 eV, respectively. The 0.5 eV shift of the Zn core level to higher binding energy is explained using the same concept of the removal of acceptor like states. A similar shift is also observed in the Si core level, Figure 2 c, f. The oxygen peaks in Figure 2 c and f are the combination of two peaks, from Si substrate and ZnO, and Si substrate and Al_2O_3, thus it is difficult to distinguish them.

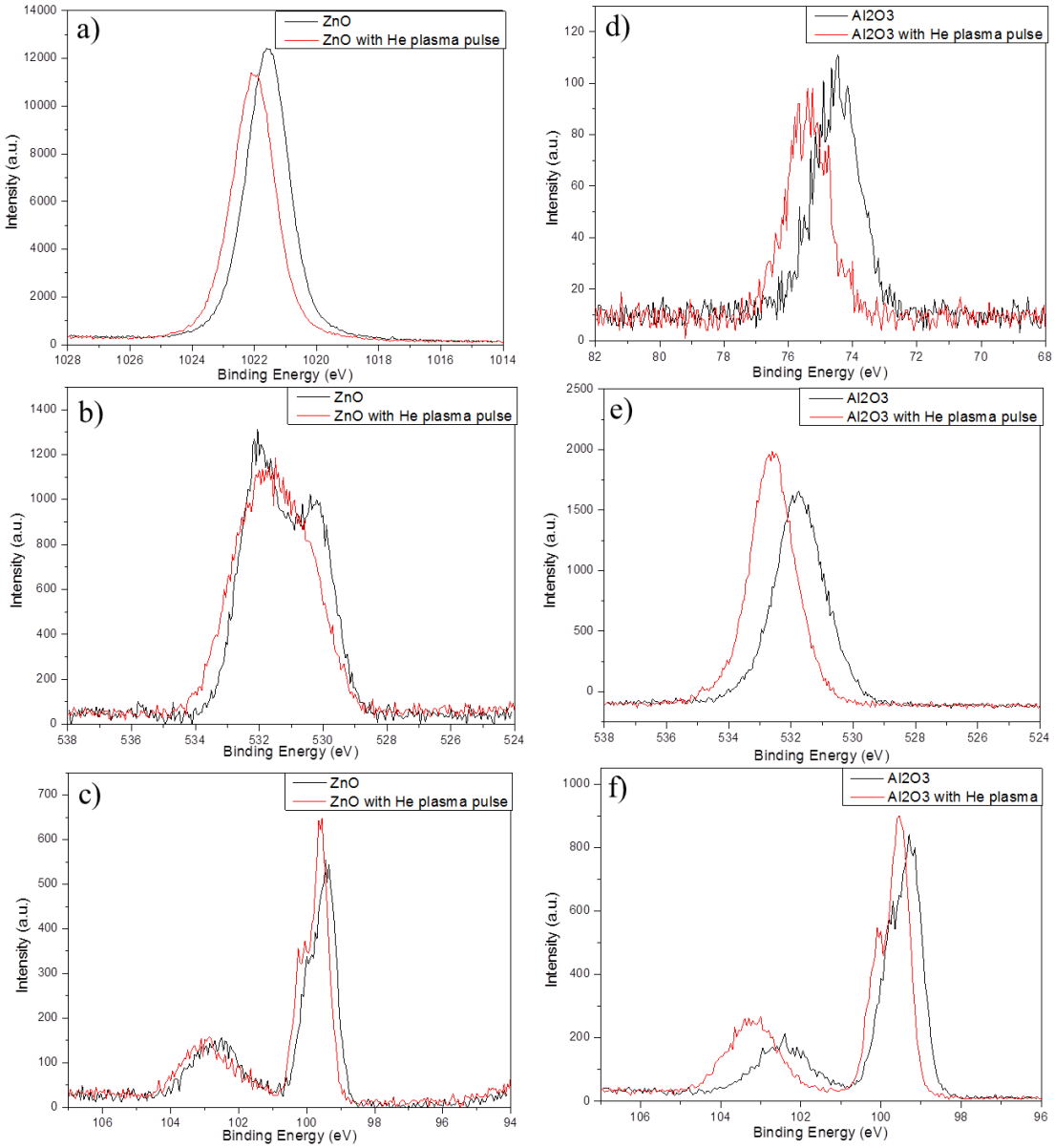

Figure 9.2. XPS core level of ZnO a) Zn 2p, b) O1s, and c) Si 2p of PEALD ZnO with and without He plasma pulse. XPS core level of Al_2O_3 d) Al 2p, e) O1s, and f) Si 2p with and without He plasma pulse.

The thick ZnO and Al_2O_3 films were deposited for the analysis using RBS, XRR and AFM. The results for all these characterizations are summarized in Table 1. It is evident from the AFM scans that the roughness of the ZnO and Al_2O_3 is similar for the PEALD deposition with and without He plasma, Figure 3. However, XRR shows a significant change (~10%) in the Al_2O_3 density. The thickness of the Al_2O_3 is slightly

reduced with the He plasma pulses, and consequently, the density increases. We conclude that the He plasma leads to a rearrangement the precursor molecules which cause the increase in density. On the other hand, the change in ZnO density is less as compared to Al_2O_3. The elemental ratio deduced from RBS suggests, the stoichiometry of ZnO and Al_2O_3 remains essentially the same, Zn:O = 1:1 and Al_2O_3 = 2:3, irrespective of the change in the deposition process.

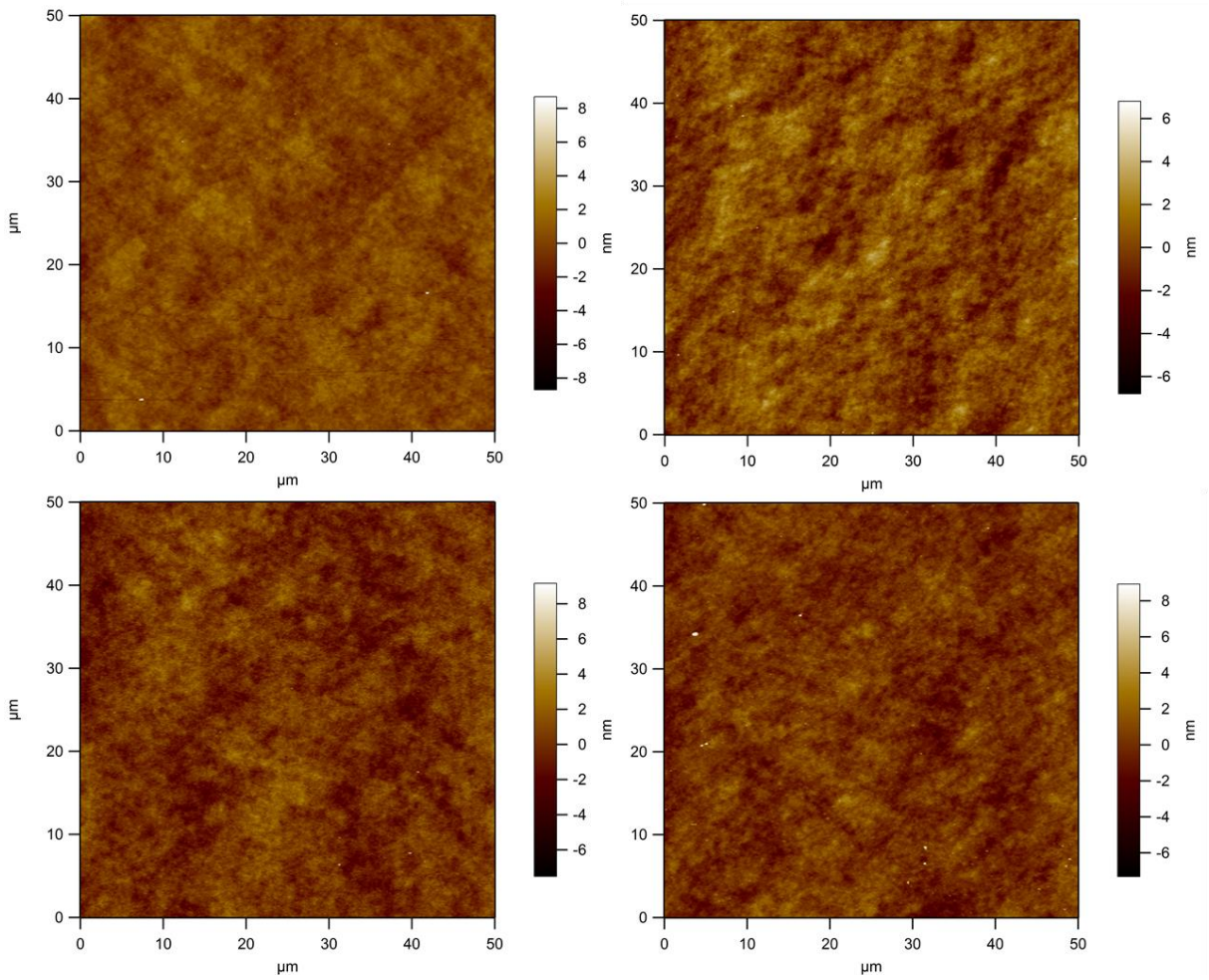

Figure 9.3. AFM scan of (a) PEALD ZnO (b) PEALD ZnO with He plasma pulse, (c) PEALD Al_2O_3, and (d) PEALD Al_2O_3 with He plasma pulse. The RMS obtained from AFM scans is 8.47, 8.6, 7.3 and 7.5 nm respectively

Table 9.1. This table concludes the RBS Zn:O and Al:O ratio, RBS thickness, AFM roughness, GPC, and XRR density and thickness for PEALD ZnO and Al_2O_3 films with and without helium plasma pulses.

Material Deposited	**Zn:O ratio** ±0.03/±0.04	**Al:O ratio** ±0.03/±0.04	**XRR density (g/cm^3)** (±0.02)	**RBS thickness (x 10^{17} $atoms/cm^2$)/XRR thickness (nm)** (±0.1)	**GPC (Å/cycle) from XRR**	**Roughness (nm)** ± 0.2 nm
100 cycles of ZnO	1:1	--	5.0	1.45/19.7	`1.96	8.47
100 cycles of ZnO with He plasma pulse	1:1	--	5.1	1.45/19.2	1.92	8.6
150 cycles of Al_2O_3	--	2:3	2.9	1.25/19.0	1.26	7.3
150 cycles of $Al2O_3$ with He plasma pulse	--	2:3	3.2	1.20/18.0	1.2	7.5

IV. Conclusions:

Helium plasma pulse assisted PEALD growth of ZnO and Al_2O_3 is compared with PEALD ZnO and Al_2O_3. The XPS core level positions indicate the removal of acceptor like states, possibly excess oxygen, which may be due to UV photons generated during the He plasma pulse. An increase in the Al_2O_3 density signifies the rearrangement of DMAI precursor molecules on the surface with energy provided by the He plasma species.

References:

[1] H. B. Profijt, S. E. Potts, M. C. M. van de Sanden, and W. M. M. Kessels, "Plasma-Assisted Atomic Layer Deposition: Basics, Opportunities, and Challenges" *J. Vac. Sci. Technol.* **A 29** (2014) 5.

[2] H. Kim and Il-Kwon Oh, "Review of plasma-enhanced atomic layer deposition: Technical enabler of nanoscale device Fabrication" *Jpn. J. Appl. Phys.* **53** (2014) 03DA01.

[3] Janotti, A.; Walle, C. G. V. D. Fundamentals of Zinc Oxide as a Semiconductor, *Rep. Prog. Phys.* 2009, **72**, 126501.

[4] Ozgur, U.; Alivov, Y. I.; Liu, C.; Teke, A.; Reshchikov, M. A.; Dogan, S.; Avrutin, V.; Cho, S. J.; Morkoç, H. A comprehensive review of ZnO materials and devices, *Appl. Phys. Rev.* 2005, **98**, 041301.

[5] J. Yang, B. S. Eller, M. Kaur, and R. J. Nemanich, "Characterization of plasma-enhanced atomic layer deposition of Al2O3 using dimethylaluminum isopropoxide". Vac. Sci. Technol. A **32** 2014 (2).

[6] E. Bersch, S. Rangan, R. A. Bartynski, E. Garfunkel, and E. Vescovo, "Band offsets of ultrathin high-kappa oxide films with Si" *Phys. Rev.* B **78**, 085114 (2008).

[7] S. Lee, S. Bang, J. Park, S. Park, W. Jeong, and H. Jeon, "The effect of oxygen remote plasma treatment on ZnO TFTs fabricated by atomic layer deposition" *Phys. Status Solidi* A **207** (2010) 1845.

[8] H. Kind, H. Yan, B. Messer, M. Law, and P. Yang, "Nanowire Ultraviolet Photodetectors and Optical Switches" *Adv. Mater*. **14** (2002) 158.

[9] S. Song, W. K. Hong, S. S. Kwon, and T. Lee "Passivation effects on ZnO nanowire field effect transistors under oxygen, ambient, and vacuum environments" *Applied Physics Letters* **92** (2008) 263109.

[10] R. Kawakami, A. Takeichi, M. Niibe, T. Inaoka, and K. Tominaga "Damage Characteristics of TiO2 Thin Film Surfaces Etched by Capacitively oupled Radio Frequency Helium Plasmas" *Jap. J. App. Phy.* **50** (2011) 08KD01.

[11] F. Tang, C. Zhu, D. J. Smith, and R. J. Nemanich, "Low temperature growth of high-k Hf–La oxides by remote-plasma atomic layer deposition: Morphology, stoichiometry, and dielectric properties" *J. Vac. Sci. & Tech. A* **30** (2012) 01A147.

CHAPTER 10. SUMMARY AND FUTURE WORK

I. Summary:

The interface band alignments, band offsets and properties of oxide heterostructures are crucial for carrier transport for various applications, such as photocatalysis, solar cells and electronics. This dissertation is focused on the study of heterostructure band alignments, photoexcited charge transport, and surface photochemical reactions. PEALD processes were employed to deposit metal oxides on $LiNbO_3$, polarity patterned lithium niobate (PPLN) and ZnO. As mentioned in the earlier, this research work has addressed three aspects.

First is the band alignment at the interface of metal oxides and $LiNbO_3$ or ZnO. These studies employed *in situ* x-ray photoelectron spectroscopy (XPS) and ultraviolet photoelectron spectroscopy (UPS) before and after the oxide deposition. The shift in the XPS core levels was used to determine the valence band offsets (VBOs) and conduction band offsets (CBOs) of metal oxides and $LiNbO_3$. On the other hand, the VBOs and CBOs of Al_2O_3 or SiO_2 on ZnO were determined using UPS measured valence band maximum (VBM) and XPS core level positions. Metal oxide/$LiNbO_3$ band diagrams show the favorable electron transport from $LiNbO_3$ to ZnO, TiO_2 and VO_2 and electron tunneling as the possible charge transfer through Al_2O_3. Band diagrams were developed that show the band bending in addition to the band offsets of as-deposited and processed PEALD films.

Second is the effect of metal oxide layers on the $LiNbO_3$ surface photochemical reactions. Different thicknesses (1, 2, 4, 10 nm) of PEALD ZnO were deposited on PPLN and results established that the internal carrier concentration at the interface screens the

effect of the internal electric field of PPLN. Thus the pattern of photoinduced Ag nanoparticle was no longer controlled by the PPLN internal electric field. Another effect that was observed in ZnO/PPLN heterostructures was the increased photoexcited carrier concentration with an increase of the ZnO thickness which screens the photoexcited carrier transport from the PPLN substrate. The photoinduced Ag nanoparticle deposition study on ZnO/PPLN indicates that the metal oxides suppress the surface states, and also reduce the effect of the internal electric field, which diminishes electron drift and enhances electron diffusion. Thus the Ag nanoparticle deposition is enhanced on –c $LiNbO_3$ domain surfaces. The TiO_2/PPLN heterostructures, show a similar effect as ZnO as reflected in the Ag nanoparticle deposition. The VO_2/PPLN shows a different Ag nanoparticle pattern as compared to ZnO and TiO_2. The results may reflect less than optimal higher carrier higher carrier concentration. For Al_2O_3/PPLN heterostructures, the insulating properties of Al_2O_3 reduces the photoinduced carrier tunneling from PPLN for thicknesses > 2 nm.

Third is the surface passivation and degradation mechanism of Al_2O_3 or SiO_2 on ZnO. In this study, PEALD Al_2O_3 and SiO_2 were deposited on 20 nm ZnO/n-Si and 20 nm ZnO/FTO which were characterized using AFM, SEM and TEM. The Al_2O_3 stability test was performed for 15 min and SiO_2 stability test was performed for 4 h. The degradation of 4 nm Al_2O_3 was evident in AFM and SEM surface scans. Unlike Al_2O_3, SiO_2 surfaces did not show signs of degradation. However, TEM characterization on both samples showed the degradation of the ZnO each with a different mechanism. TEM of the Al_2O_3/ZnO/n-Si indicated that photocorossion of ZnO is initiated through the Al_2O_3 pin holes which expose the ZnO directly to the electrolyte solution. In contrast, SiO_2

provides improved stability of ZnO; however, degradation of the underneath ZnO was attributed to diffusion of ions which were transported from the electrolyte solution during stability test.

II. Future Work:

The proposed future work consists of two areas: (A) to use $LiNbO_3$ and modified $LiNbO_3$ surfaces with PEALD films for photocatalytic processes for water splitting and photo-oxidation surface reactions, and (B) to extend the versatility of PEALD processes.

A. $LiNbO_3$ and Modified $LiNbO_3$ Surfaces for Photo-oxidation Reactions and Water Splitting:

The research discussed above has studied approaches for photoreduction reactions on $LiNbO_3$. Most of the studies suggest oxidation reactions occur in equilibrium with reduction reactions which are driven by photoexcited holes [1, 2]. However, to the best of our knowledge, there have not been prior studies that explored the hole driven surface reactions on $LiNbO_3$ or metal oxide/$LiNbO_3$. Thus it would be interesting to study the surface photo-oxidation reactions. To understand the role of holes in $LiNbO_3$ and metal oxide/$LiNbO_3$ heterostructures, the phtoto-oxidation dominated nanoparticle deposition processes can be used as described in the dissertation.

On the other hand, the most commonly used materials for photocatalytic processes to produce H_2 fuel or to clean water are semiconductors [1]. Other than semiconductors, only a few studies have been done to remove dye molecules from water using the internal electric field of ferroelectrics [2, 3]. The water splitting reactions are driven by both reduction and oxidation reactions. Earlier, Burbure *et. al.* have studied surface photoreduction reactions on $TiO_2/BaTiO_3$ [4]. We have shown a significant

increase in the surface photoreduction processes with ZnO or TiO_2 on PPLN in the research here. Presumably, with the enhanced photoreduction surface reactions, surface photo-oxidation also increases. In addition to using $LiNbO_3$ ferroelectric material that highest polarization among the ferroelectric materials, metal oxide/$LiNbO_3$ structures can also provide a significant increase in the photocatalysis efficiency. Thus, the metal oxide/$LiNbO_3$ heterostructures may be used for water splitting or water cleaning with enhanced efficiency.

B. Energy Enhanced Atomic Layer Deposition:

Other than studying the heterostructure interfaces, PEALD processes were an integral part of the research concluded here. The uniform and conformal deposition is certainly an advancement of ALD process that makes it favorable for electronic devices. Moreover, low temperature deposition with PEALD has been extensively reported in the last decade. However, the high reactivity of the oxygen plasma species incorporates excess oxygen which is evident in the form of acceptor like defects in the metal oxide films [5]. The PEALD capabilities may be expanded by incorporating pulses of He plasma to remove the excess oxygen during the deposition which may have a significant effect on the electrical properties of metal oxides (semiconductors and dielectrics).

UV light is known to desorb adsorbed oxygen from ZnO nanowires and to improve their electrical properties [6]. Specifically, helium plasma generates a UV line (I) of energy 21.2 eV which can be used after each oxygen plasma pulse possibly to remove the adsorbed excess oxygen on the surface. Other than using UV light photons, the effect of molecular energy provided by the novel gasses (He, Ne, Ar, Kr) pulses incorporated after oxygen or precursor pulse can be studied. The energy provided by the

non-reactive plasma species can enhance the nucleation or rearrange the precursor molecules and thus altering the materials properties and GPC.

References:

[1] L. Li, P. A. Salvador and G. S. Rohrer, "Photocatalysts with internal electric field", *Nanoscale* **6** (2014) 24.

[2] M. Stock, and S. Dunn, "Influence of the Ferroelectric Nature of Lithium Niobate to Drive Photocatalytic Dye Decolorization under Artificial Solar Light",*J. Phys. Chem.* **116**, 20854 (2012).

[3] Y. Cui, J. Briscoe, and S. Dunn, "Effect of Ferroelectricity on Solar-Light-Driven Photocatalytic Activity of $BaTiO_3$ --- Influence on the Carrier Separation and Stern Layer Formation" *Chem. Mater.* **25** (2013) 4215.

[4] N. V. Burbure, P. A. Salvador, and G. S. Rohrer, "Photochemical Reactivity of Titania Films on $BaTiO_3$ Substrates: Origin of Spatial Selectivity" *Chem. Mater.***22** (2010) 5823.

[5] J. Yang, B. S. Eller, M. Kaur, and R. J. Nemanich, "Characterization of plasma-enhanced atomic layer deposition of Al2O3 using dimethylaluminum isopropoxide" . Vac. Sci. Technol. A 32(2) 2014

[6] H. Kind, H. Yan, B. Messer, M. Law, and P. Yang, "Nanowire Ultraviolet Photodetectors and Optical Switches" *Adv. Mater*. **14** (2002) 158.

REFRENCES

A. Kudo, Y. Miseki, “Heterogeneous photocatalyst materials for water splitting” Chem. Soc. Rev. 38 (2009) 253-278.

A. Paracchino, V. Laporte, K. Sivula, M. Grätzel, E. Thimsen, Highly active oxide photocathode for photoelectrochemical water reduction, Nature materials. 10 (2011) 456-461.

F. E. Osterloh, “Inorganic nanostructures for photoelectrochemical and photocatalytic water splitting” *Chem. Soc. Rev.* **42** (2013) 2294.

L. Li, P. A. Salvador and G. S. Rohrer, “Photocatalysts with internal electric field”, *Nanoscale* **6** (2014) 24.

M. Stock, and S. Dunn, “Influence of the Ferroelectric Nature of Lithium Niobate to Drive Photocatalytic Dye Decolorization under Artificial Solar Light” *J. Phys. Chem.* **116**, 20854 (2012).

Y. Wang, J. Liu, L. Liu, D.D. Sun, “Enhancing stability and photocatalytic activity of ZnO nanoparticles by surface modification of graphene oxide” Journal of nanoscience and nanotechnology 12 (2012) 3896-3902.

J. F. Reber, M. Rusek, “Photochemical hydrogen production with platinized suspensions of cadmium sulfide and cadmium zinc sulfide modified by silver sulfide” *J. Phys. Chem.* **90** (1986) 824.

K. Maeda, X. Wang, Y. Nishihara, D. Lu, M. Antonietti and K. Domen, “Photocatalytic Activities of Graphitic Carbon Nitride Powder for Water Reduction and Oxidation under Visible Light” *J. Phys. Chem.***113** (2009) 4940.

M. Stock and S. Dunn, “$LiNbO_3$ – A New Material for Artificial Photosynthesis”, *IEEE Transac. Ultrasonics Ferroelectrics Freq. Contr.* **58**, 0885 (2011).

B. Zielinska, E. Borowiak-Palen, R. J. Kalenzuk, “Preparation and Characterization of Lithium Niobate as a Novel Photocatalyst in Hydrogen Generation” *J. Phys. Chem. Solids* **69** (2007) 236.

K. Saito, K. Koga and A. Kudo, “Lithium Niobate Nanowires for Photocatalytic Water Splitting” *Dalton Trans.* **40** (2011) 3909.

R. Sapkal, S. Shinde, T. Waghmode, S. Govindwar, K. Rajpure, C. Bhosale, “Photo-corrosion inhibition and photoactivity enhancement with tailored zinc oxide thin films” Journal of Photochemistry and Photobiology B: Biology. 110 (2012) 15-21.

J. Jiang, X. Zhang, P. Sun, and L. Zhang, "ZnO/BiOI Heterostructures: Photoinduced Charge-Transfer Property and Enhanced Visible-Light Photocatalytic Activity" *J. Physical Soc. Chem.* **115** (2011) 20555.

X. Hong, J. Kim, S. Shi, Y. Zhang, C. Jin, Y. Sun, S. Tongay, J. Wu, Y. Zhang and F. Wang, "Ultrafast charge transfer in atomically thin MoS2/WS2 heterostructures" *Nature Nanotech.* **9** (2014)

X. Wang, L. Yin, G. Liu, L. Wang, R. Saito, G. Q. Lu and H. M. Cheng, "Polar interface-induced improvement in high photocatalytic hydrogen evolution over ZnO–CdS heterostructures" *Energy Envi. Sci.* **4** (2011) 3976.

Y. Q. Cao, J. Chen, H. Zhou, L. Zhu, X. Li, Z. Y. Cao, D. Wu and A. D. Li, "Photocatalytic activity and photocorrosion of atomic layer deposited ZnO ultrathin films for the degradation of methylene blue", *Nanotech.* **26**, 024002 (2015).

A. Fujishima, X. Zhang, D. A. Tryk, "TiO_2 photocatalysis and related surface phenomena" *Surface Science Reports* **63** (2008) 515.

M. A. Lazar, S. Varghese and S. S. Nair "Photocatalytic Water Treatment by Titanium Dioxide: Recent Updates" *Catalysts* **2** (2012) 572.

M. Liu, C. Nam, C.T. Black, J. Kamcev, L. Zhang, "Enhancing Water Splitting Activity and Chemical Stability of Zinc Oxide Nanowire Photoanodes with ultrathin titania shells", *J. Phys. Chem. C.* 117 (2013) 13396-13402.

Y. Cui, J. Briscoe, and S. Dunn, "Effect of Ferroelectricity on Solar-Light-Driven Photocatalytic Activity of $BaTiO_3$ --- Influence on the Carrier Separation and Stern Layer Formation" *Chem. Mater.* **25** (2013) 4215.

B. Zielinska, E. Borowiak-Palen, R. J. Kalenzuk, "Preparation and Characterization of Lithium Niobate as a Novel Photocatalyst in Hydrogen Generation" *J. Phys. Chem. Solids* **69** (2007) 236.

U. Ozgur, Y. I. Alivov, C. Liu, A. Teke, M. A. Reshchikov, S. Dogan, V. Avrutin, S.J. Cho, and H. Morkoc, "A comprehensive review of ZnO materials and devices" *J. Appl. Phys.* **98**, (2005) 041301

Z. L. Wang, "Zinc Oxide Nanostructures: Growth, Properties and Applications" *J. Phys. Condens. Matt.* **16**, R829-R858 (2004).

A. Janotti and C. G. V. D. Walle, "Fundamentals of Zinc Oxide as a Semiconductor", *Rep. Prog. Phys.* **72**, 126501 (2009).

Y. Sun, R. J. Nemanich, "Photo-induced Ag deposition on periodically poled lithium niobate: Concentration and intensity dependence" *J. Appl. Phys.* **109**, 104302 (2011).

Y. Sun, B. S. Eller, and R. J. Nemanich, "Photoinduced Ag deposition on periodically poled lithium niobate: Wavelength and polarization screening dependence" *J. Appl. Phys.* **110**, 084303 (2011).

Y. S. Park, J. H. Kim, and W. Yang, "Comparison Study of Metal Nanoparticles Grown on Polarity Patterned Ferroelectrics by Scanning Probe Microscopy" *Surf. Interface Anal.* **44** (2012) 759.

A. Haussmann, P. Milde, C. Erler, and L. M. Eng, "Ferroelectric Lithography: Bottom-up Assembly and Electrical Performance of a Single Metallic Nanowire" *Nano Lett.* **9** (2009) 2.

W. C. Yang, B. J. Rodriguez, A. Gruverman, and R. J. Nemanich, *Appl. Phys. Lett.* **12**, (2004) 2316.

Y. Xu, S. A. A. Schoonen, "The absolute energy positions of conduction and valence bands of selected semiconducting minerals" *American Mineralogist* **85** (2000) 543–556.

P. Barquinha, R. Martins, E. Fortunato, "Advances in GaN and ZnO-based Thin Film, Bulk and Nanostructured Materials and Devices" Vol. *156* (Ed: S. J. Pearton), Springer , New York **2012** , 435.

U. Ozgur, Ya. I. Alivov, C. Liu, A. Teke, M. A. Reshchikov, S. Dogan, V. Avrutin,S. J. Cho, and H. Morkoç, "A comprehensive review of ZnO materials and devices", *Appl. Phys. Rev.* **98** (2005) 041301.

J. C. Moore, R. Louder and C. V. Thompson, "Photocatalytic Activity and Stability of Porous Polycrystalline ZnO Thin-Films Grown via a Two-Step Thermal Oxidation Process", *Coatings* **4**, 651-669 (2014).

T. S. Herng, A. Kumar, C. S. Ong, Y. P. Feng, Y. H. Lu, K. Y. Zeng & J. Ding, "Investigation of the non-volatile resistance change in noncentrosymmetric compounds" *Nature Specific Reports* **2** (2012) 587.

S. M. George, A. W. Ott, and J. W. Klaus, "Surface chemistry for atomic layer growth Source" *J. Phys. Chem.* **100**, 13121 (1996).

H. B. Profijt, S. E. Potts, M. C. M. van de Sanden, and W. M. M. Kessels, "Plasma-Assisted Atomic Layer Deposition: Basics, Opportunities, and Challenges" *J. Vac. Sci. Technol.* **A 29** (2014) 5

E. Fortunato, P. Barquinha, and R. Martins, "Oxide Semiconductor Thin-Film Transistors: A Review of Recent Advances", *Adv. Mater*. **24**, 2945-2986 (2012).

R. L. Hoffman, B. J. Norris and J. F. Wager, "ZnO-based transparent thin-film transistors", *Appl. Phys. Lett*. **82**, 5 (2003).

N. Huby, S. Ferrari, E. Guziewicz, M. Godlewski and V. Osinniy, "Electrical behavior of zinc oxide layers grown by low temperature atomic layer deposition", *Appl. Phys. Lett.* **92**, 023502 (2008).

P. C. Rowlette, C. G. Allen, O. B. Bromley, A. E. Dubetz and C. A. Wolden, "Plasma-Enhanced Atomic Layer Deposition of Semiconductor Grade ZnO Using Dimethyl Zinc", *Chem. Vap. Dep.* **15**, 15-20 (2009).

S. H. Park, C. S. Hwang, H. S. Kwack, J. H. Lee, and H. Y. Chu, "Characteristics of ZnO thin films by means of plasma-enhanced atomic layer deposition", *Electrochem. Solid State Lett.* **9**, G299-G301 (2006).

M. E. Lines and A. M. Glass, *Principles and Applications of Ferroelectrics and Related Materials* (Clarendon, Oxford, 1977).

D. A. Scrymgeour, V. Gopalan, A. Itagi, A. Saxena, and P. J. Swart, "Phenomenological theory of a single domain wall in uniaxial trigonal ferroelectrics: lithium niobate and lithium tantalite," *Phys. Rev. B* **71**, 184110 (2005).

S. C. Abrahams, E. Buehler, W. C. Hamilton, and S. J. Laplaca, "Ferroelectric lithium tantalate—III. Temperature dependence of the structure in the ferroelectric phase and the para-electric structure at 940°K" *J. Phys. Chem. Solids* **34**, 521 (1973).

K. Kitamura, J. K. Yamamoto, N. Iyi, S. Kimura, and T. Hayashi, "Stoichiometric $LiNbO_3$ single crystal growth by double crucible Czochralski method using automatic powder supply system," *J. Cryst. Growth* **116**, 327 (1992).

H. Franke, "Li+ Ionic-Conductivity in $LiNbo_3$" *Phys. Status Solidi A* **83** (1984) K73.

W. C Yang, B. J. Rodriguez, A. Gruverman, and R. J. Nemanich, *J. Phys.: Condens. Matter*, **17**, S1415 (2005).

S. V. Kalinin, D. A. Bonnell, T. Alvarez, X. Lei, J. H. Ferris, Q. Zhang and S. Dunn, "Atomic Polarization and Local Reactivity on Ferroelectric Surfaces: A New Route toward Complex Nanostructures", *Nano Lett.* 2, 589 (2002).

N. V. Burbure, P. A. Salvador, and G. S. Rohrer, "Photochemical Reactivity of Titania Films on $BaTiO_3$ Substrates: Origin of Spatial Selectivity" *Chem. Mater.***22** (2010) 5823.

P. Schwinkendorf, M. Lorenz, H. Hochmuth, Z. Zhang, and M. Grundmann, "Interface charging effects in ferroelectric ZnO–BaTiO3 field-effect transistor heterostructures", *Phys. Status Solidi A* 211 (2014) 166.

E. Cagin, D. Y. Chen, J. J. Siddiqui, and J. D. Phillips, "Hysteretic metal-ferroleectric-semiconductor capacitors based on PZT/ZnO heterostructures" *J. Phys. D* **40** (2007) 2430.

N. V. Burbure, P. A. Salvador and G. S. Rohrer, "Photochemical Reactivity of Titania Films on $BaTiO_3$ Substrates: Influence of Titania Phase and Orienation", *Chem Mater.* **22** (2012) 5831.

S. M. George, "Atomic Layer Deposition: An Overview" *Chem. Rev.* 110 (2010) 111–131

T. Suntola, and J. Antson, U. S. Patent No. 4,058,43015 November, 3 1977.

A. M. Shevjakov, G. N. Kuznetsova, and V. B. Aleskovskii, in Chemistry of High-Temperature Materials, Proceedings of the Second USSR Conference on High-Temperature Chemistry of Oxides, Leningrad, USSR, 26–29 November 1965 (Nauka, Leningrad, USSR, 1967), pp. 2 149–155, in Russian.

T. Suntola, and J. Antson, U. S. Patent No. 4,058,43015 November, 3 1977.

T. S. Suntola, A. J. Pakkala, and S. G. Lindfors, U.S. Patent No. 4,389,973 28 June 1983.

T. S. Suntola, A. J. Pakkala, and S. G. Lindfors, U.S. Patent No. 4,413,022 1 November 1983.

M. Leskel and M. Ritala, "Atomic Layer Deposition Chemistry: Recent Developments and Future Challenges" *Electronic Materials Angew. Chem. Int. Ed*. **42** (2003) 5548 – 5554

H. Kim, "Atomic layer deposition of metal and nitride thin films: Current research efforts and applications for semiconductor device processing" *J. Vac. Sci. Technol.* **B 21** 2003 1071

V. Miikkulainen, M. Leskelä, M. Ritala, and R. L. Puurunen, "Crystallinity of inorganic films grown by atomic layer deposition: Overview and general trends" *Journal of Applied Physics* **113** (2013) 02130.

R. L. Puurunena, "Surface chemistry of atomic layer deposition: A case study for the trimethylaluminum/water process" *J. Appl. Phys.* **97** (2005) 121301.

N. P. Dasgupta, X. Meng, J. W. Elam, and A. B. F. Martinson, "Atomic Layer Deposition of Metal Sulfide Materials" *Acc. Chem. Res.* **48** (2015) 341−348.

J. Hamalainen, M. Ritala, and M. Leskela, "Atomic Layer Deposition of Noble Metals and Their Oxides" *Chem. Mater.* **26 (**2014) 786−801.

T. Tynell and M. Karppinen, "Atomic layer deposition of ZnO: a review" *Semicond. Sci. Technol.* **29** (2014) 043001.

M. Knez, K. Nielsch, and L. Niinisto "Synthesis and Surface Engineering of Complex Nanostructures by Atomic Layer Deposition" *Adv. Mater.* **19** (2007) 3425–3438.

H. Kim, H. Lee, W.J. Maeng, "Applications of atomic layer deposition to nanofabrication and emerging nanodevices", *Thin Solid Films* **517** (2009) 2563–2580.

C. Detavernier, J. Dendooven, S. Pulinthanathu Sree, K. F. Ludwig and J. A. Martens, "Tailoring nanoporous materials by atomic layer deposition" *Chem. Soc. Rev.,* **40** (2011) 5242–5253.

J. R. Bakke, K. L. Pickrahn, T. P. Brennan and S. F. Bent, "Nanoengineering and interfacial engineering of photovoltaics by atomic layer Deposition" *Nanoscale* **3** (2011) 3482–3508.

J. Borges, and J. F. Mano, "Molecular Interactions Driving the Layer-by-Layer Assembly of Multilayers" *Advan. Func. Mater.* **114** (2014) 8883.

Q. Peng, J. S. Lewis, P. G. Hoertz, J. T. Glass, and G. N. Parsons, "Atomic layer deposition for electrochemical energy generation and storage systems" *J. Vac. Sci. Technol.* **A 30 (**2012) 1

D. M. King, X. Liang, A. W. Weimer, "Functionalization of fine particles using atomic and molecular layer deposition" *Powder Technology* **221** (2012) 13–25.

T. Singh, T. Lehnen, T. Leuning, and S. Mathur, "Atomic layer deposition grown MOx thin films for solar water splitting: Prospects and Challenges" *J. Vac. Sci. Technol.* **A 33 (**2015) 1.

T. Wang, Z. Luo, C. Li and J. Gong, "Controllable fabrication of nanostructured materials for photoelectrochemical water splitting via atomic layer deposition" *Chem. Soc. Rev.* **43** (2014) 7469.

X. Jiang and S. F. Bent, "Area-Selective ALD with Soft Lithographic Methods: Using Self-Assembled Monolayers to Direct Film Deposition" *J. Phys. Chem. C* 2009, *113,* 17613–17625.

A. J. M. Mackus, A. A. Bol and W. M. M. Kessels, "The use of atomic layer deposition in advanced Nanopatterning" *Nanoscale* **6** (2014) 10941–10960.

H. C. M. Knoops, M. E. Donders, M. C. M. van de Sanden, P. H. L. Notten, and W. M. M. Kessels, "Atomic layer deposition for nanostructured Li-ion batteries" *J. Vac. Sci. Technol*. **A 30** (2012) 1.

J. Liu and X. Sun, "Elegant design of electrode and electrode/electrolyte interface in lithium-ion batteries by atomic layer deposition" *Nanotechnology* **26** (2015) 024001.

S. M. George, A. W. Ott, and J. W. Klaus, "Surface chemistry for atomic layer growth Source" *J. Phys. Chem.* 100, 13121 (1996).

C. H. L. Goodman and M. V. Pessa, "Title Atomic Layer Epitaxy" J. *Appl. Phys*. **60** (1986) R65.

M. Leskela and M. Ritala, "ALD precursor chemistry: Evolution and future challenges" *J. Phys. IV* **9** (1999) Pr8/837.

M. Leskela and M. Ritala, "Atomic layer deposition (ALD): from precursors to thin film structures" *Thin Solid Films* **409** (2002) 138.

L. Niinisto, M. Ritala, and M. Leskela, "Synthesis of oxide thin films and overlayers by atomic layer epitaxy for advanced applications" *Mater. Sci. Eng. B* **41** (1996) 23.

M. Ritala and M. Leskela, "Atomic layer epitaxy - a valuable tool for nanotechnology?" *Nanotechnology* **10** (1999) 19.

T. Suntola, "Atomic Layer Epitaxy" *Acta Polytechnica Scandinavica-Electrical Engineering Series* **64** (1989) 242-270

S. Haukka, E. L. Lakooma, and T. Suntola, "Adsorption controlled preparation of heterogeneous catalysts" *Stud. Surf. Sci. Catal*. **120A** (1999) 715.

H. B. Profijt, S. E. Potts, M. C. M. van de Sanden, and W. M. M. Kessels, "Plasma-Assisted Atomic Layer Deposition: Basics, Opportunities, and Challenges" *J. Vac. Sci. Technol.* **A 29** (2014) 5.

M. De Keijser and C. Vamn Opdorp, "Atomic Layer Epitaxy of Gallium Arsenide with the use of Atomic Hydrogen" *Appl. Phys. Lett.* **58** (1991) 1187.

M. Verghese, J. W. Maes, and N. Kobayashi, Atomic layer deposition goes mainstream in 22nm logic technologies, http://www.solid-state.com (March 15, 2012).

Tokyo Electron Limited website, http://www.tel.com (March 15, 2012)

S.M. Rossnagel, A. Sherman, F. Turner, "Plasma-enhanced atomic layer deposition of Ta and Ti for interconnect diffusion barriers Source" *J. Vac. Sci. Techn.* B, **18** (2000) 2016-2020.

A. Grill, Cold Plasmas in Materials Fabrication: From Fundamentals to Applications (Wiley-IEEE Press, New York, 1994).

S.E. Potts, W.M.M. Kessels, "Energy-enhanced atomic layer deposition for more process and precursor versatility" *Coordination Chemistry Reviews* **257** (2013) 3254– 3270

H. B. Profijt, P. Kudlacek, M. C. M. Van de Sanden, and W. M. M. Kessels, "Ion and Photon Surface Interaction during Remote Plasma ALD of Metal Oxides" *J. Electrochem. Soc.* **158**, G88 (2011).

S. B. S. Heil, J. L. van Hemmen, C. J. Hodson, N. Singh, J. H. Klootwijk, F. Roozeboom, M. C. M. van de Sanden, and W. M. M. Kessels, J. Vac. Sci. Technol. A 25, 1357 (2007).

S. B. S. Heil, J. L. van Hemmen, C. J. Hodson, N. Singh, J. H. Klootwijk, F. Roozeboom, M. C. M. van de Sanden, and W. M. M. Kessels, "Deposition of TiN and HfO2 in a commercial 200 mm remote plasma atomic layer deposition reactor" *J. Vac. Sci. Technol*. A **25**, 1357 (2007).

MKS website, http://www.mksinst.com (May 31, 2011).

Advanced Energy website, http://www.advanced-energy.com/ (May 31, 2011).

H. Kim and Il-Kwon Oh, "Review of plasma-enhanced atomic layer deposition: Technical enabler of nanoscale device Fabrication" *Jpn. J. Appl. Phys.* **53** (2014) 03DA01.

R. L. Puurunen, W. Vandervorst, W. F. A. Besling, O. Richard, H. Bender, T. Conard, C. Zhao, A. Delabie, M. Caymax, S. D. Gendt, M. Heyns, M. M. Viitanen, M. de Ridder, H. H. Brongersma, Y. Tamminga, T. Dao, T. de Win, M. Verheijen, M. Kaiser, and M. Tuominen, "Island growth in the atomic layer deposition of zirconium oxide and aluminum oxide on hydrogen-terminated silicon: Growth mode modeling and transmission electron microscopy" *J. Appl. Phys.*, **96** (2004) 9.

S. E. Potts, G. Dingemans, C. Lachaud, and W. M. M. Kessels, "Plasma-enhanced and thermal atomic layer deposition of Al2O3 using dimethylaluminum isopropoxide, [Al(CH3)(2)(mu-(OPr)-Pr-i)](2), as an alternative aluminum precursor" *J. Vac. Sci. Technol.* A 30, 021505 (2012).

S. E. Potts,W. Keuning,E. Langereis,G. Dingemans, M.C.M. vandeSanden, and W. M. M. Kessels, "Low Temperature Plasma-Enhanced Atomic Layer Deposition of Metal Oxide Thin Films" *J. Electrochem. Soc.***157** (2010) P66.

J. W. Lim and S. Yun, "Electrical properties of alumina films by plasma-enhanced atomic layer deposition" *Electrochem. Solid-State Lett.* **7** (2004) F45.

S. B. S. Heil, P. Kudlacek, E. Langereis, R. Engeln, M. C. M. van de Sanden, and W. M. M. Kessels, "In situ reaction mechanism studies of plasma-assisted atomic layer deposition of Al2O3" *Appl. Phys. Lett.* **89** (2006) 131505.

J. Yang, B. S. Eller, M. Kaur, and R. J. Nemanich, "Characterization of plasma-enhanced atomic layer deposition of Al2O3 using dimethylaluminum isopropoxide" *J. Vac. Sci. Technol.* A **32** (2014) 2.

J. Koo, S. Kim, S. Jeon, H. Jeon, Y. Kim, and Y. Wen, "Characteristics of Al2O3 thin films deposited using dimethylaluminum isopropoxide and trimethylaluminum precursors by the plasma-enhanced atomic-layer deposition method" *J. Korean Phys. Soc.* **48** (2006) 131.

J. W. Lim and S. Yun "Electrical properties of alumina films by plasma-enhanced atomic layer deposition" *Electrochem. Solid-State Lett*.7, F45 (2004)

E. Langereis, M. Creatore, S. B. S. Heil, M. C. M. van de Sanden, and W. M. M. Kessels, *Appl. Phys. Lett*. **89** (2006) 081915.

B. B. Burton, S. W. Kang, S. W. Rhee, and S. M. George, "SiO2 Atomic Layer Deposition Using Tris(dimethylamino)silane and Hydrogen Peroxide Studied by in Situ Transmission FTIR Spectroscopy" *J. Phys. Chem. C* **113**, 8249 (2009).

P. C. Rowlette, C. G. Allen, O. B. Bromley, A. E. Dubetz and C. A. Wolden, "Plasma-Enhanced Atomic Layer Deposition of Semiconductor Grade ZnO Using Dimethyl Zinc", *Chem. Vap. Dep.* **15** (2009) 15-20.

T. M. Barnes, S. Hand, J. Leaf and C. A. Wolden, "ZnO synthesis by high vacuum plasma-assisted chemical vapor deposition using dimethylzinc and atomic oxygen", J. Vac. Sci. Tech. A **22** (2004)2118.

R. B. Schoolar, J. N. Zemel, "Preparation of Single-Crystal Films of PbS" *J. Appl. Phys.* **35** (1964) 3

J. E. Davey and T. Pankey, "Epitaxial GaAs films deposited by vacuum evaporation" *J. Appl. Phys.* **39** (1968) 1941.

K. L. Lewis, A. M. Pitt, J. A. Savage, A. G. Savage, A. G. Cullis, and N. G. Chew, "Molecular Beam Techniques for optical thin film fabrication, Boulder Damage Symposium, Colorado, 1985.

I. T. Muirhead, A. Miller, K.L. Lewis, J. Staromlynska, and K. Welford, "Molecular Beam Deposited Inteference Filters, *Tech. Dig. Series*, 6, Optical Interference Coatings, Optical Society of America, New York, 1988.

K. L. Lewis, I. T. Muirhead, A. M. Pitt, and A. Miller," Thin Film Ultraclean Environments" *J. Vac. Sci. Technol.* **7** (1989) 3.

K. L. Lewis, I. T. Muirhead, A. M. Pitt, A. G. Cullis, N. G. Chew, A. Miller, and T. J. Wyatt-Davies, "Molecular Beam Deposition of Optical Coatings and their Characterization" *Appl. Opt.* **28** (1989) 2785.

C. Zhu, M. Kaur, F. Tang, X. Liu, D. J. Smith, and R. J. Nemanich, "Band alignment of vanadium oxide as an interlayer in a hafnium oxide-silicon gate stack structure" *J. Appl. Phys.* **112** (2012) 8.

C. C. Fulton, G. Lucovsky and R. J. Nemanich, "Electronic states at the interface of Ti–Si oxide on Si(100)" *J. Vac. Sci. Technol.* **20** (2002) 1726.

M. Vasilopoulou, A. M. Douvas, D. G. Georgiadou, L. C. Palilis, S. Kennou, L. Sygellou, A. Soultati, I. Kostis, G. Papadimitropoulos, D. Davazoglou, and P. Argitis, "The Influence of Hydrogenation and Oxygen Vacancies on Molybdenum Oxides Work Function and Gap States for Application in Organic Optoelectronics" *J. Am. Chem. Soc.* **134** (2012) 16178.

C. Battaglia, S. M. Nicolas, S. D. Wolf, X. Yin, M. Zheng, C. Ballif, and A. Javery, "Silicon heterojunction solar cell with passivated hole selective MoOx contact" *Appl. Phys. Lett.* **104** (2014) 113902.

Scanning Probe Microscopy, Center for probing the nanoscale, Stanford University

G. Binnig, C. F. Quate, and C. Gerber, "Atomic Force Microscope" *Phys. Rev. Lett.* **56** (1986) 930.

N. Jalili, K. Laxminarayana "A review of atomic force microscopy imaging systems: application to molecular metrology and biological sciences", *Mechtronics* **14** (2004) 907.

E. Meyers, "Atomic Force Microscopy", *Progress Surf. Sci.* **41** (1992) 3.

C. B. Prater, P. G. Maivald, K. J. Kjoller and M. G. Heaton, "Tapping Mode Imaging Applications and Technology" *Veeco.*

A. Gruverman, O. Auciello, and H. Tokumoto, "Scanning force microscopy for the study of domain structure in ferroelectric thin films" *J. Vac. Sci. Technol*. B **14** (1996) 602.

A. Gruverman, O. Auciello, and H. Tokumoto, "Scanning force microscopy: Application to nanoscale studies of ferroelectric domains" *Integr*. *Ferroelectrics* **19** (1998) 49.

O. Kolosov, A. Gruverman, J. Hatano, K. Takahashi, and H. Tokumoto, "Nanoscale Visualization and Control of Ferroelectric Domains by Atomic-Force Microscopy" *Phys. Rev. Lett*., **74** (1995) 4309.

J. W. Hong, D. D. Kahng, J. C. Shin, H. J. Kim, and Z. G. Khim, "Detection and control of ferroelectric domains by an electrostatic force microscope" *J. Vac. Sci. Technol*. B **16** (1998) 2942.

J. W. Hong, S. Park, and Z. G. Khim, "Measurement of hardness, surface potential, and charge distribution with dynamic contact mode electrostatic force microscope" *Rev. Sci. Instrum.* **70** (1999) 1735.

M. Nonnenmacher, M. P. O'Boyle, and H. K. Wickramasinghe, "Kelvin Probe Force Microscopy" *Appl. Phys. Lett.* **58** (1991) 2921.

M. Fujihira and H. Kawate, "Structural Study of Langmuir-Blodgett-Films by Scanning Surface-Potential Microscopy" *J. Vac. Sci. Technol.* B **12** (1994) 1604.

M. M. Shvebelman, A. G. Agronin, R. P. Urenski, Y. Rosenwalks, and G. I. Rosenman, "Kelvin probe force microscopy of periodic ferroelectric domain structure in KTiOPO4 crystals" *Nano Lett*. **2** (2002) 455.

C. B. Prater, P. G. Maivald, K. J. Kjoller, and M. G. Heaton, "Scanning Probe Microscopy .2. Scanning Technology and Applications" *Ameri. Lab.* **27** (1995) 50.

P. Guthner, and K. Dransfeld, "Local Poling Of Ferroelectric Polymers by Scanning Force Microscopy" *Appl. Phys. Lett*. **61**, 1137-1139 (1992).

A. Gruverman, O. Kolosov, J. Hatano, K. Takahashi, and H. Tokumoto, "Domain-Structure And Polarization Reversal In Ferroelectrics Studied By Atomic-Force Microscopy" *J. Vac. Sci. Technol.* B **13** (1995) 1095.

A. Gruverman, O. Auciello, and H. Tokumoto, "Scanning force microscopy for the study of domain structure in ferroelectric thin films" *J. Vac. Sci. Technol.* B **14** (1996) 602

J. A. Christman, R. R. Woolcott, A. I. Kingon, and R. J. Nemanich, "Piezoelectric measurements with atomic force microscopy" *Appl. Phys. Lett.* **73** (1998) 3851.

E. Soergel, "Piezoresponse Force Microscopy (PFM)" *J Phys. D: Appl.Phys.* **44** (2011) 464003

T. Jungk, A. Hoffmann, and E. Soergel, "Influence of the inhomogeneous field at the tip on quantitative piezoresponse force microscopy" *Appl. Phys. A* **86** (2007) 353.

P. Niedermann, W. Haenni, N. Blanc, R. Christoph, and J. Burger, "Chemical vapor deposition diamond for tips in nanoprobe experiments" *J. Vac. Sci. Technol.* A **14** (1996) 1233.

S. J. O'Shea, R. M. Atta, and M. E. Welland, "Characterization of Tips for Conducting Atomic-Force Microscopy" *Rev. Sci. Instrum*. **66** (1995) 2508.

C. Harnagea, M. Alexe, D. Hesse and A. Pignolet, "Contact resonances in voltage-modulated force microscopy" *Appl. Phys. Lett.*, **83** (2003) 338.

B. J. Rodriguez, C. Callahan, S. Kalinin, R. Proksch, "Dual-frequency resonance-tracking atomic force microscopy" *Nanotechnology*, **18** (2007) 475504.

S. Kim, V. Gopalan and A. Gruverman, "Coercive fields in ferroelectrics: A case study in lithium niobate and lithium tantalite" *Appl. Phys. Lett.*, **80** (2002) 2740

Piezoresponse force microscopy, *Asylum Research*.

B. J. Rodriguez, S. V. Kalinin, J. Shin, S. Jesse, V. Grichko, T. Thundat, A. P. Baddorf and A. Gruverman, "Electromechanical imaging of biomaterials by scanning probe microscopy" *J. Struct. Biol.*, **153** (2006) 151.

D. Briggs, et. al., Practical Surface Analysis, Vol. 1 Auger and X-ray Photoelectron Spectroscopy, 2nd edition (John Wiley & Sons,West Sussex, 1990).

C. C. Chusuei and D. W. Goodman, *Texas A&M University*.

S. Zhang, L. Li and A. Kumar, "Materials Characterization Techniques" Taylor and Francis (2009).

D. B. Wittry and N. C. Barb, "X-ray Crystal Spectrometers and Monochromators in Microanalysis", *Microsco. Microanal.* **7** (2001) 124.

Z. W. Chen, Walter M. Gibson, and Huapeng, "Huang High Definition X-Ray Fluorescence: Principles and Techniques", *X-Ray Optics and Instrumentation* **2008** (2008) 318171.

J. F. Moulder, W.F. Stickle, P.E. Sobol, K.D. Bomben, Handbook of X-ray photoelectron spectroscopy (Waltham: Perkin-Elmer Corporation, 1992).

D. A. Cole, J. R. Shallenberger, S. W. Novak, R. L. Moore, M. J. Edgell, S. P. Smith, C. J. Hitzman, J. F. Kirchhoff, E. Principe, W. Nieveen, F. K. Huang, S. Biswas, and K. Jones, "SiO2 thickness determination by x-ray photoelectron spectroscopy, Auger electron spectroscopy, secondary ion mass spectrometry, Rutherford backscattering, transmission electron microscopy, and ellipsometry" *J. Vac. Sci. Technol.* B**18** (2000) 440–444.

C. Zhu, M. Kaur, F. Tang, X. Liu, D. J. Smith, and R. J. Nemanich,"Band alignment of vanadium oxide as an interlayer in a hafnium oxide-silicon gate stack structure" *J. Appl. Phys.* **112** (2012) 084105.

F. G. Bell and L. Ley, "Photoemission-Study of SiOx (0 Less-Than-or-Equal-to x Less-Than-or-Equal-to 2) Alloys" *Phys. Rev. B* **37**, 8383 (1988).

H. Nohira, W. Tsai, W. Besling, E. Young, J. Petry, T. Conard, W. Vandervorst, S. De Gendt, M. Heyns, J. Maes, and M. Tuominen, "Characterization of ALCVD-Al2O3 and ZrO2 layer using X-ray photoelectron spectroscopy" *J. Non-Cryst. Solids* **303**, 83 (2002).

M. Bär, M. Rusu, S. Lehmann, Th. Schedel-Niedrig, I. Lauermann, and M. C. Lux-Steiner, "The chemical and electronic surface and interface structure of CuGaSe2 thin-film solar cell absorbers" *Appl. Phys. Lett.* **93**, 232104 (2008).

J. Yang, B. S. Eller, M. Kaur, and R. J. Nemanich, "Characterization of plasma-enhanced atomic layer deposition of Al2O3 using dimethylaluminum isopropoxide" *J. Vac. Sci. Technol. A* **32**, 021514 (2014).

E. Bersch, S. Rangan, R. A. Bartynski, E. Garfunkel, and E. Vescovo, "Energy gap and band alignment for (HfO2)(x)(Al2O3)(1-x) on (100) Si" *Phys. Rev. B* **78** (2008) 085114.

Miyazaki, *J. Vac. Sci. Technol. B* **19** (2001) 2212.

H. Y. Yu, M. F. Li, B. J. Cho, C. C. Yeo, M. S. Joo, D.-L. Kwong, J. S. Pan, C. H. Ang, J. Z. Zheng, and S. Ramanathan, *Appl. Phys. Lett.* **81** (2002) 376.

"UVL Ultra-violet Source," *Thermo Electron Corporation* Application Note: AN30058_E (2008).

Casa XPS, CasaXPS software Ltd. 2013.

R. Smart, S. McIntyre, M. Bancroft, I. Bello *et al., U. Hong Kong, Dept. Phys*.

J. R. Waldrop and R. W. Grant, "Measurement of AlN/GaN (0001) heterojunction band offsets by x-ray photoemission spectroscopy" *Appl. Phys. Lett*. **68** (1996) 2879.

E. A. Kraut, R. W. Grant, J. R. Waldrop and S. P. Kowalczyk, Heterojunction Band Discontinuities: Physics and Device Applications, edited by F. Capasso and G. Margaritondo (Elsevier, New York, 1987).

A. Kudo and Y. Miseki, "Heterogeneous photocatalyst materials for water splitting", *Chem Socie. Rev.* **38** (2009) 253.

L. Li, P. A. Salvador and G. S. Rohrer, "Photocatalysts with internal electric field", *Nanoscale* **6** (2014) 24.

M. Stock and S. Dunn, "$LiNbO_3$ – A New Material for Artificial Photosynthesis", *IEEE Transac. Ultrasonics Ferroelectrics Freq. Contr.* **58**, 0885 (2011)

A. Paracchino, V. Laporte, K. Sivula, M. Gratzel and E. Thimsen, "Highly active oxide photocathode for photoelectrochemical water reduction", Nature Matt. **10** (2011).

Y. Q. Cao, J. Chen, H. Zhou, L. Zhu, X. Li, Z. Y. Cao, D. Wu and A. D. Li, "Photocatalytic activity and photocorrosion of atomic layer deposited ZnO ultrathin films for the degradation of methylene blue", Nanotech. **26**, 024002 (2015).

M. Stock, and S. Dunn, "Influence of the Ferroelectric Nature of Lithium Niobate to Drive Photocatalytic Dye Decolorization under Artificial Solar Light",*J. Phys. Chem.* **116**, 20854 (2012).

Y. Sun, R. J. Nemanich, "Photo-induced Ag deposition on periodically poled lithium niobate: Concentration and intensity dependence" J. Appl. Phys. **109**, 104302 (2011).

Y. Sun, B. S. Eller, and R. J. Nemanich, "Photoinduced Ag deposition on periodically poled lithium niobate: Wavelength and polarization screening dependence" J. Appl. Phys. **110**, 084303 (2011).

K. Saito, K. Koga and A. Kudo, "Lithium Niobate Nanowires for Photocatalytic Water Splitting" *Dalton Trans.* **40** (2011) 3909.

B. Zielinska, E. Borowiak-Palen, R. J. Kalenzuk, "Preparation and Characterization of Lithium Niobate as a Novel Photocatalyst in Hydrogen Generation" *J. Phys. Chem. Solids* **69** (2007) 236.

Y. S. Park, J. H. Kim, and W. Yang, "Comparison Study of Metal Nanoparticles Grown on Polarity Patterned Ferroelectrics by Scanning Probe Microscopy" *Surf. Interface Anal.* **44** (2012) 759.

B. Zielinska, "Photocatalytic hydrogen generation with Ag-loaded $LiNbO_3$" *Mater. Sci.* **37** (2014) 911.

N. V. Burbure, P. A. Salvador, and G. S. Rohrer, "Photochemical Reactivity of Titania Films on $BaTiO_3$ Substrates: Origin of Spatial Selectivity" *Chem. Mater.***22** (2010) 5823.

N. V. Burbure, P. A. Salvador and G. S. Rohrer, "Photochemical Reactivity of Titania Films on $BaTiO_3$ Substrates: Influence of Titania Phase and Orienation", *Chem Mater.* **22** (2012) 5831.

P. Gopal and N. A. Spaldin, "Polarization, piezoelectric constants, and elastic constants of ZnO, MgO, and CdO," *J. Elec. Mat***. 35** (2006).

Y. Sun, J. H. Seo, C. J. Takacs, J. Seifter, and A. J. Heeger, "Inverted Polymer Solar Cells Integrated with a Low-Temperature-Annealed Sol-Gel-Derived ZnO Film as an Electron Transport Layer", *Adv. Mat.* **23**, 1679 (2011).

W. C. Yang, B. J. Rodriguez, A. Gruverman, and R. J. Nemanich, Appl. Phys. Lett. **12**, 2316 (2004).

Q. Gui, Z. Xu, H. Zhang, C.Cheng, X. Zhu, M. Yin, Y. Song, L. Lu, X. Chen, and D. Li, "Enhanced Photoelectrochemical water splitting performance of anodic TiO_2 nanotube arrays by surface passivation", *ACS Appl. Mater. Interfaces* **6** (2014) 17053.

S. V. Kalinin, D. A. Bonnell, T. Alvarez, X. Lei, J. H. Ferris, Q. Zhang and S. Dunn, "Atomic Polarization and Local Reactivity on Ferroelectric Surfaces: A New Route toward Complex Nanostructures", Nano Lett. 2, 589 (2002).

Y. Cui, J. Briscoe, and S. Dunn, "Effect of Ferroelectricity on Solar-Light-Driven Photocatalytic Activity of $BaTiO_3$ --- Influence on the Carrier Separation and Stern Layer Formation" *Chem. Mater.* **25** (2013) 4215.

A. Janotti and C. G. V. D. Walle, "Fundamentals of Zinc Oxide as a Semiconductor", Rep. Prog. Phys. **72**, 126501 (2009).

U. Ozgur, Ya. I. Alivov, C. Liu, A. Teke, M. A. Reshchikov, S. Dogan, V. Avrutin,S. J. Cho, and H. Morkoç, "A comprehensive review of ZnO materials and devices", *Appl. Phys. Rev.* **98** (2005) 041301.

A. Haussmann, P. Milde, C. Erler, and L. M. Eng, "Ferroelectric Lithography: Bottom-up Assembly and Electrical Performance of a Single Metallic Nanowire" Nano Lett. **9** (2009) 2.

Y. Xu, S. A. A. Schoonen, "The absolute energy positions of conduction and valence bands of selected semiconducting minerals" *American Mineralogist* **85** (2000) 543–556.

P. C. Rowlette, C. G. Allen, O. B. Bromley, A. E. Dubetz and C. A. Wolden, "Plasma-Enhanced Atomic Layer Deposition of Semiconductor Grade ZnO Using Dimethyl Zinc", Chem. Vap. Dep. **15**, 15-20 (2009).

S. E. Potts, G. Dingemans, C. Lachaud, and W. M. M. Kessels, *J. Vac. Sci. Technol. A* **30**, (2012) 021505.

M. G. Cain, S. Dunn and P. Jones, "The measurement of ferroelectric thin films using piezo force microscopy", *NSTI-Nanotech.* **3** (2004)

C. H. M. Chuang, P. R. Brown, V. Bulovic and M. G. Bawendi, "Improved performance and stability in quantum dot solar cells through band alignment engineering", *Nature Mater.* **13** (2014) 796.

L. Yang, R. Zhou, J. Lan, Q. Zhang, G. Cao and J. Zhu, "Efficient band alignment for $Zn_xCd_{1-x}Se$ QD-sensitized TiO_2 solar cells", *J. Mater. Chem. A* **2** (2014) 3669.

X. Lin, J. Xing, W. Wang, Z. Shan, F. Xu, and F. Huang, "Photocatalytic Activities of Heterojunction Semiconductors $Bi_2O_3/BaTiO_3$: A Strategy for the Design of Efficient Combined Photocatalysts" *J. Phys. Chem. C* **111** (2007)18288.

D. Henderson and D. Boda, "Insights from theory and simulation on the electrical double layer", *Phys.Chem.Chem.Phys.* 11 (2009) 3822.

P. Schwinkendorf, M. Lorenz, H. Hochmuth, Z. Zhang, and M. Grundmann, "Interface charging effects in ferroelectric ZnO–BaTiO3 field-effect transistor heterostructures", *Phys. Status Solidi A* 211 (2014) 166.

E. Cagin, D. Y. Chen, J. J. Siddiqui, and J. D. Phillips, "Hysteretic metal-ferroleectric-semiconductor capacitors based on PZT/ZnO heterostructures" *J. Phys. D* **40** (2007) 2430.

N. V. Burbure, P. A. Salvador and G. S. Rohrer, "Photochemical Reactivity of Titania Films on $BaTiO_3$ Substrates: Influence of Titania Phase and Orienation", *Chem Mater.* **22** (2012) 5831.

N. V. Burbure, P. A. Salvador, and G. S. Rohrer, "Photochemical Reactivity of Titania Films on $BaTiO_3$ Substrates: Origin of Spatial Selectivity" *Chem. Mater.***22** (2010) 5823.

L. Li, P. A. Salvador and G. S. Rohrer, "Photocatalysts with internal electric field", *Nanoscale* **6** (2014) 24.

M. Stock, and S. Dunn, "Influence of the Ferroelectric Nature of Lithium Niobate to Drive Photocatalytic Dye Decolorization under Artificial Solar Light",*J. Phys. Chem.* **116**, 20854 (2012).

Y. Cui, J. Briscoe, and S. Dunn, "Effect of Ferroelectricity on Solar-Light-Driven Photocatalytic Activity of $BaTiO_3$ --- Influence on the Carrier Separation and Stern Layer Formation" *Chem. Mater.* **25** (2013) 4215.

W. C. Yang, B. J. Rodriguez, A. Gruverman, and R. J. Nemanich, Appl. Phys. Lett. **12**, 2316 (2004).

S. Calnan, "Applications of Oxide Coatings in Photovoltaic Devices" *Coatings* **4** (2014) 162.

E. Palomares , J. N. Clifford , S. A. Haque , T. Lutz , and J. R. Durrant, "Control of Charge Recombination Dynamics in Dye Sensitized Solar Cells by the Use of Conformally Deposited Metal Oxide Blocking Layers" *J. Am. Chem. Soc.* **125** (2003) 475.

Y.W. Chen, J.D. Prange, S. Dühnen, Y. Park, M. Gunji, C.E. Chidsey, P.C. McIntyre, Atomic layer-deposited tunnel oxide stabilizes silicon photoanodes for water oxidation, Nature materials. 10 (2011) 539-544. (SiO2 and TiO2).

S. Lattante, "Electron and Hole Transport Layers: Their Use in Inverted Bulk Heterojunction Polymer Solar Cells", Electronics **3**, 132-164 (2014).

S. R. Ferreira, P. Lu, Y. J. Lee, R. J. Davis, and J. W. P. Hsu, "Effect of Zinc Oxide Electron Transport Layers on Performance and Shelf Life of Organic Bulk Heterojunction Devices" *J. Phys. Chem. C* **115** (2011) 13471.

K. Stella, D. A. Kovacs, D. Diesing, W. Brezna, and J. Smoliner, "Charge Transport Through Thin Amorphous Titanium and Tantalum Oxide Layers" J. Electrochem. Society **158** (2011) 65.

Y. J. Noh, S. I. Na, and S. S. Kim, "Inverted polymer solar cells including ZnO electron transport layer fabricated by facile spray pyrolysis", *Sol. Energ. Mat. Sol. C.* **117**, 139 (2013).

Y. J. Kang, K. Lim, S. Jung, D. G. Kim, J. K. Kim, C. S. Kim, S. H. Kim and J. W. Kang, "Spray-coated ZnO electron transport layer for air-stable inverted organic solar cells", Solar Energy Mat. Solar Cells. **96,** 137-140, (2012).

R. Sapkal, S. Shinde, T. Waghmode, S. Govindwar, K. Rajpure, C. Bhosale, "Photo-corrosion inhibition and photoactivity enhancement with tailored zinc oxide thin films" *Journal of Photochemistry and Photobiology B: Biology* **110** (2012) 15-21.

L. Cattin, F. Dahou, Y. Lare, M. Morsli, R. Tricot, S. Houari, A. Mokrani, K. Jondo, A. Khelil, K. Napo and J. C. Bernede, "MoO3 surface passivation of the transparent anode in organic solar cells using ultrathin films" *J. Appl. Phys.* **105** (2009) 034507.

J. Meyer, S. Hamwi, M. Kroger, W. Kowalsky, T. Riedl, A. Kahn, "Transition Metal Oxides for Organic Electronics: Energetics, Device Physics and Applications" *Adv. Mater.* 2012, 24, 5408.

J. Meyer, S. Hamwi, T. Bulow, H. H. Johannes, T. Riedl, W. Kowalsky, "Highly efficient simplified organic light emitting diodes" Appl. Phys. Lett. 2007, 91, 113506.

C. Zhu, M. Kaur, F. Tang, X. Liu, D. J. Smith, and R. J. Nemanich,"Band alignment of vanadium oxide as an interlayer in a hafnium oxide-silicon gate stack structure" *J. Appl. Phys.* **112** (2012) 084105.

J. Yang, B. Eller, M. Kaur, and R. J. Nemanich, "Characterization of plasma-enhanced atomic layer deposition of Al2O3 using dimethylaluminum isopropoxide" *J. Vac. Sci. Technol.* **A 32** (2014) 021514.

C. Thierfelder , S. Sanna, Arno Schindlmayr, and W. G. Schmidt, "Do we know the band gap of lithium niobate?" *Phys. Status Solidi* C **7** (2010) 362.

G. Campet, J. Manaud, C. Puprichitkun, Z. Sun, P. Salvador, "Protection of photoanodes against photo-corrosion by surface deposition of oxide films: criteria for choosing the protective coating" *Active and Passive Electronic Components* **13** (1989) 175-189.

A. Mang, K. Reimann, and St Rubenacke, "Band-Gaps, Crystal-Field Splitting, Spin-Orbit-Coupling, And Exciton Binding-Energies In Zno Under Hydrostatic-Pressure" Solid State Commun. 94, 251(1995).

A. Janotti and C. G. V. D. Walle, “Fundamentals of Zinc Oxide as a Semiconductor”, Rep. Prog. Phys. **72**, 126501 (2009).

C. Ko and S. Ramanathan, “Observation of electric field-assisted phase transition in thin film vanadium oxide in a metal-oxide-semiconductor device geometry” *Appl. Phys. Lett.* **93** (2008) 252101.

B. Zielinska, E. Borowiak-Palen, R. J. Kalenzuk, “Preparation and Characterization of Lithium Niobate as a Novel Photocatalyst in Hydrogen Generation” *J. Phys. Chem. Solids* **69** (2007) 236.

M. Stock and S. Dunn, “$LiNbO_3$ – A New Material for Artificial Photosynthesis”, *IEEE Transac. Ultrasonics Ferroelectrics Freq. Contr.* **58**, 0885 (2011).

K. Saito, K. Koga and A. Kudo, “Lithium Niobate Nanowires for Photocatalytic Water Splitting” *Dalton Trans.* **40** (2011) 3909.

M. Kaur, Q. Liu, P. Crozier, R. Nemanich, “Photochemical Reaction Patterns on Heterostructures of ZnO on Polarity Patterned Lithium Niobate”

Y. Sun, R. J. Nemanich, “Photo-induced Ag deposition on periodically poled lithium niobate: Concentration and intensity dependence”, J. Appl. Phys. **109**, 104302 (2011).

Y. Sun, B. S. Eller, and R. J. Nemanich, “Photoinduced Ag deposition on periodically poled lithium niobate: Wavelength and polarization screening dependence”, J. Appl. Phys. **110**, 084303 (2011).

A. Haussmann, P. Milde, C. Erler, and L. M. Eng, “Ferroelectric Lithography: Bottom-up Assembly and Electrical Performance of a Single Metallic Nanowire” Nano Lett. **9** (2009) 2.

Y. S. Park, J. H. Kim, and W. Yang, “Comparison Study of Metal Nanoparticles Grown on Polarity Patterned Ferroelectrics by Scanning Probe Microscopy” *Surf. Interface Anal.* **44** (2012) 759.

J. Waldrop, R. Grant, “Measurement of AlN/GaN (0001) heterojunction band offsets by x-ray photoemission spectroscopy” *Appl. Phys. Lett.* **1996**, 68, 2879-2881.

S. Kohiki, “Electron-energy-loss function of LiTaO3 and LiNbO3 by x-ray photoemission spectroscopy: Theory and experiment" *Physic. Rev. B* **57** (1998) 23.

R. Courths, P. Steiner, H. Hochst, S. Hufner, “ Photoelectron-Spectroscopy Investigation And Electronic-Properties Of $LiNbO_3$ Crystal-Surfaces” *Appl. Phys.* **21** (1980) 345.

C. Zhu, D. J. Smith, R. J. Nemanich, “Band alignment of zinc oxide as a channel layer in a gate stack structure grown by plasma enhanced atomic layer deposition” *J. Vacc. Sci. Techn.* **30** (2012) 5.

A. K. Chandiran, M. Abdi-Jalebi, M. K. Nazeeruddin, and M. Gratzel, "Analysis of Electron Transfer Properties of ZnO and TiO_2 Photoanodes for Dye-Sensitized Solar Cells" *ACS Nano* **8** (2014) 2661.

Q. Zhang, C. S. Dandeneau, X. Zhou, G. Cao, "ZnO Nano-structures for Dye-Sensitized" *Solar Cells. Adv. Mater*. **21** (2009) 4087–4108.

D. Eitan Barlaz and Edmund G. Seebauer, "Manipulation of carrier concentration, crystallite size and density in polycrystalline anatase TiO_2 via amorphous-phase medium range atomic order" *Cryst Eng Comm* **17 (**2015) 2101.

M. Quintana, T. Edvinsson, A. Hagfeldt, G. Boschloo, "Comparison of Dye-Sensitized ZnO and TiO2 Solar Cells: Studies of Charge Transport and Carrier Lifetime" *J. Phys. Chem*. C**111** (2006) 1035–1041.

Baxter, J. B.; Aydil, E. S. "Nanowire-Based Dye-Sensitized Solar Cells" *Appl. Phys. Lett.* 2005, 86, 53114.

Hagfeldt, A.; Boschloo, G.; Sun, L.; Kloo, L.; Pettersson, H. "Dye-Sensitized Solar Cells" *Chem. Rev*. 2010, 110, 6595–6663.

Ozgur, U.; Alivov, Y. I.; Liu, C.; Teke, A.; Reshchikov, M. A.; Dogan, S.; Avrutin, V.; Cho, S. J.; Morkoç, H. "A comprehensive review of ZnO materials and devices," *Appl. Phys. Rev.* 2005, **98**, 041301.

D. Ruzmetov, D. Heiman, B. B. Claflin, V. Narayanamurti, and S. Ramanathan, "Hall carrier density and magnetoresistance measurements in thin-film vanadium dioxide across the metal-insulator transition" *Physical Review* B **79** (2009) 153107.

K. Maeda, K. Teramura, D. Lu, T. Takata, N. Saito, Y. Inoue, K. Domen, "Photocatalyst releasing hydrogen from water" *Nature* **440** (2006) 295-295.

M. Grätzel, "Photoelectrochemical cells" *Nature* **414** (2001**)** 338-344.

Y. Sasaki, H. Nemoto, K. Saito, A. Kudo, "Solar water splitting using powdered photocatalysts driven by Z-schematic interparticle electron transfer without an electron mediator" *J. Physical Chem*. C **113** (2009) 17536-17542.

M. G. Walter, E. L. Warren, J. R. McKone, S. W. Boettcher, Q. Mi, E. A. Santori, N. S. Lewis, "Solar water splitting cells" *Chem*. *Rev*. **110** (2010) 6446-6473.

C. Han, M. Yang, B. Weng, Y. Xu, "Improving the photocatalytic activity and anti-photocorrosion of semiconductor ZnO by coupling with versatile carbon" *Physical Chem Chemical Phy*. **16** (2014) 16891-16903.

A. Paracchino, V. Laporte, K. Sivula, M. Grätzel, E. Thimsen, "Highly active oxide photocathode for photoelectrochemical water reduction", *Nature materials*. **10** (2011) 456-461.

Y. Wang, J. Liu, L. Liu, D.D. Sun, "Enhancing stability and photocatalytic activity of ZnO nanoparticles by surface modification of graphene oxide," *J nanosci nanotech*. **12** (2012) 3896-3902.

Y. Cao, J. Chen, H. Zhou, L. Zhu, X. Li, Z. Cao, D. Wu, A. Li, "Photocatalytic activity and photocorrosion of atomic layer deposited ZnO ultrathin films for the degradation of methylene blue," *Nanotech*. **26** (2015) 024002.

T. Singh, T. Lehnen, T. Leuning, S. Mathur, "Atomic layer deposition grown MOx thin films for solar water splitting: Prospects and challenges" *J. Vac. Sci. Tech.* A **33 (**2015**)** 010801.

R. Sapkal, S. Shinde, T. Waghmode, S. Govindwar, K. Rajpure, C. Bhosale, Photo-corrosion inhibition and photoactivity enhancement with tailored zinc oxide thin films, Journal of Photochemistry and Photobiology B: Biology. 110 (2012) 15-21.

S. Hu, N. S. Lewis, J. W. Ager, J. Yang, J. R. McKone, N. C. Strandwitz, "Thin-Film Materials for the Protection of Semiconducting Photoelectrodes in Solar-Fuel Generators" *J. Physic. Chem* C **119 (**2015) 24201-24228.

N. G. Carratala, M. S. Prévot, K. Sivula, "Surface modification of semiconductor photoelectrodes" *Physical Chem*. *Chemical Phys.* **2015**.

M. F. Lichterman, K. Sun, S. Hu, X. Zhou, M. T. McDowell, M. R. Shaner, M. H. Richter, E. J. Crumlin, A. I. Carim, F. H. Saadi, "Protection of inorganic semiconductors for sustained, efficient photoelectrochemical water oxidation" *Cataly. Today* **262 (**2016) 11-23.

A. Abdulagatov, Y. Yan, J. Cooper, Y. Zhang, Z. Gibbs, A. Cavanagh, R. Yang, Y. Lee, S. George, "Al_2O_3 and TiO_2 atomic layer deposition on copper for water corrosion resistance", *ACS Appl. Mater. Interf.* 3 (2011) 4593-4601.

C. Li, T. Wang, Z. Luo, D. Zhang, J. Gong, "Transparent ALD-grown Ta2O5 protective layer for highly stable ZnO photoelectrode in solar water splitting" *Chemic. Communic.* **51 (**2015) 7290-7293.

Q. Gui, Z. Xu, H. Zhang, C. Cheng, X. Zhu, M. Yin, Y. Song, L. Lu, X. Chen, D. Li, "Enhanced photoelectrochemical water splitting performance of anodic TiO2 nanotube arrays by surface passivation" *ACS appl. Mat. Interf.* **6 (**2014**)** 17053-17058.

M. Liu, C. Nam, C. T. Black, J. Kamcev, L. Zhang, "Enhancing water splitting activity and chemical stability of zinc oxide nanowire photoanodes with ultrathin titania shells" *J. Physical Chem.* C **117 (**2013) 13396-13402.

Y. J. Hwang, C. Hahn, B. Liu, P. Yang, "Photoelectrochemical properties of TiO2 nanowire arrays: a study of the dependence on length and atomic layer deposition coating" *Acs Nano* **6 (**2012) 5060-5069.

M. H. Lee, K. Takei, J. Zhang, R. Kapadia, M. Zheng, Y. Chen, J. Nah, T. S. Matthews, Y. Chueh, J. W. Ager, "p-Type InP Nanopillar Photocathodes for Efficient Solar-Driven Hydrogen Production" *Angewandte Chemie* **124 (**2012) 10918-10922.

S. Hu, M. R. Shaner, J. A. Beardslee, M. Lichterman, B. S. Brunschwig, N. S. Lewis, "Amorphous TiO_2 coatings stabilize Si, GaAs, and GaP photoanodes for efficient water oxidation" *Science* **344 (**2014) 1005-1009.

Y. Yang, D. S. Kim, Y. Qin, A. Berger, R. Scholz, H. Kim, M. Knez, U. Gösele, "Unexpected Long-Term Instability of ZnO Nanowires "Protected" by a TiO2 Shell" J. *Am. Chem. Soc.* **131 (**2009) 13920-13921.

Y. Li, X. Zhang, S. Jiang, H. Dai, X. Sun, Y. Li, "Improved photoelectrochemical property of a nanocomposite NiO/CdS@ ZnO photoanode for water splitting" *Solar Energy Mater. Solar Cells* **132 (**2015) 40-46.

F. L. Formal, N. Tétreault, M. Cornuz, T. Moehl, M. Grätzel, K. Sivula, "Passivating surface states on water splitting hematite photoanodes with alumina overlayers" *Chemical Sci* **2 (**2011) 737-743.

W. Kim, T. Tachikawa, D. Monllor-Satoca, H. Kim, T. Majima, W. Choi, "Promoting water photooxidation on transparent WO3 thin films using an alumina overlayer" *Energy Env. Sci* **6 (**2013) 3732-3739.

D. Barpuzary, Z. Khan, N. Vinothkumar, M. De, M. Qureshi, "Hierarchically grown urchinlike CdS@ ZnO and CdS@ Al2O3 heteroarrays for efficient visible-light-driven photocatalytic hydrogen generation" *J. Physical Chem.* C **116 (**2011) 150-156.

S. M. George, "Atomic layer deposition: an overview" *Chem. Rev.* **110 (**2009) 111-131.

B. Coppa, C. Fulton, P. Hartlieb, R. Davis, B. Rodriguez, B. Shields, R. Nemanich, "In situ cleaning and characterization of oxygen-and zinc-terminated, n-type, ZnO {0001} surfaces", *J. Appl. Phys.* **95** (2004) 5856-5864.

J. Waldrop, R. Grant, "Measurement of AlN/GaN (0001) heterojunction band offsets by x-ray photoemission spectroscopy", *Appl. Phys. Lett.* **68** (1996) 2879-2881.

H. Moormann, D. Kohl, G. Heiland, "Variations of work function and surface conductivity on clean cleaved zinc oxide surfaces by annealing and by hydrogen adsorption," *Surf. Sci*. **100** (1980) 302-314.

J. Yang, B.S. Eller, M. Kaur, R.J. Nemanich, "Characterization of plasma-enhanced atomic layer deposition of Al2O3 using dimethylaluminum isopropoxide" *J. Vac. Sci. Tech.* A. **32** (2014) 021514..

J. Yang, B. Eller, and R. Nemanich "Surface band bending and band alignment of plasma enhanced atomic layer deposited dielectrics on Ga- and N-face gallium nitride" J. Appl. Phys. **116** (2014) 123702.

G. Campet, J. Manaud, C. Puprichitkun, Z. Sun, P. Salvador, "Protection of photoanodes against photo-corrosion by surface deposition of oxide films: criteria for choosing the protective coating," *Active Passive Electronic Comp*. **13** (1989) 175-189..

A. Abdulagatov, Y. Yan, J. Cooper, Y. Zhang, Z. Gibbs, A. Cavanagh, R. Yang, Y. Lee, S. George, "Al2O3 and TiO2 atomic layer deposition on copper for water corrosion resistance," *ACS appl. Mater. Interf.* **3** (2011) 4593-4601.

M. Tomkiewicz, J.M. Woodall,"Photoelectrolysis of water with semiconductor materials," J. *Electrochem. Soc*. **124** (1977) 1436-1440.

A. J. Nozik, "Photoelectrochemistry: applications to solar energy conversion," *Annu. Rev. Phys. Chem*. **29** (1978) 189-222.

A. Topkar, R. Lal, "Effect of electrolyte exposure on silicon dioxide in electrolyte-oxide-semiconductor structures," *Thin Solid Films*. **232** (1993) 265-270.

H. B. Profijt, S. E. Potts, M. C. M. van de Sanden, and W. M. M. Kessels, "Plasma-Assisted Atomic Layer Deposition: Basics, Opportunities, and Challenges" *J. Vac. Sci. Technol.* **A 29** (2014) 5.

H. Kim and Il-Kwon Oh, "Review of plasma-enhanced atomic layer deposition: Technical enabler of nanoscale device Fabrication" *Jpn. J. Appl. Phys.* **53** (2014) 03DA01.

Janotti, A.; Walle, C. G. V. D. Fundamentals of Zinc Oxide as a Semiconductor, *Rep. Prog. Phys.* 2009, **72**, 126501.

Ozgur, U.; Alivov, Y. I.; Liu, C.; Teke, A.; Reshchikov, M. A.; Dogan, S.; Avrutin, V.; Cho, S. J.; Morkoç, H. A comprehensive review of ZnO materials and devices, *Appl. Phys. Rev.* 2005, **98**, 041301.

J. Yang, B. S. Eller, M. Kaur, and R. J. Nemanich, "Characterization of plasma-enhanced atomic layer deposition of Al2O3 using dimethylaluminum isopropoxide". Vac. Sci. Technol. A **32** 2014 (2).

E. Bersch, S. Rangan, R. A. Bartynski, E. Garfunkel, and E. Vescovo, "Band offsets of ultrathin high-kappa oxide films with Si" *Phys. Rev.* B **78**, 085114 (2008).

S. Lee, S. Bang, J. Park, S. Park, W. Jeong, and H. Jeon, "The effect of oxygen remote plasma treatment on ZnO TFTs fabricated by atomic layer deposition" *Phys. Status Solidi* A **207** (2010) 1845.

H. Kind, H. Yan, B. Messer, M. Law, and P. Yang, "Nanowire Ultraviolet Photodetectors and Optical Switches" *Adv. Mater*. **14** (2002) 158.

S. Song, W. K. Hong, S. S. Kwon, and T. Lee "Passivation effects on ZnO nanowire field effect transistors under oxygen, ambient, and vacuum environments" *Applied Physics Letters* **92** (2008) 263109.

R. Kawakami, A. Takeichi, M. Niibe, T. Inaoka, and K. Tominaga "Damage Characteristics of TiO2 Thin Film Surfaces Etched by Capacitively oupled Radio Frequency Helium Plasmas" *Jap. J. App. Phy.* **50** (2011) 08KD01.

F. Tang, C. Zhu, D. J. Smith, and R. J. Nemanich, "Low temperature growth of high-k Hf–La oxides by remote-plasma atomic layer deposition: Morphology, stoichiometry, and dielectric properties" *J. Vac. Sci. & Tech. A* **30** (2012) 01A147.

L. Li, P. A. Salvador and G. S. Rohrer, "Photocatalysts with internal electric field", *Nanoscale* **6** (2014) 24.

M. Stock, and S. Dunn, "Influence of the Ferroelectric Nature of Lithium Niobate to Drive Photocatalytic Dye Decolorization under Artificial Solar Light",*J. Phys. Chem.* **116**, 20854 (2012).

Y. Cui, J. Briscoe, and S. Dunn, "Effect of Ferroelectricity on Solar-Light-Driven Photocatalytic Activity of $BaTiO_3$ --- Influence on the Carrier Separation and Stern Layer Formation" *Chem. Mater.* **25** (2013) 4215.

N. V. Burbure, P. A. Salvador, and G. S. Rohrer, "Photochemical Reactivity of Titania Films on $BaTiO_3$ Substrates: Origin of Spatial Selectivity" *Chem. Mater.***22** (2010) 5823.

J. Yang, B. S. Eller, M. Kaur, and R. J. Nemanich, "Characterization of plasma-enhanced atomic layer deposition of Al2O3 using dimethylaluminum isopropoxide" . Vac. Sci. Technol. A 32(2) 2014

H. Kind, H. Yan, B. Messer, M. Law, and P. Yang, "Nanowire Ultraviolet Photodetectors and Optical Switches" *Adv. Mater*. **14** (2002) 158.